Ultrastructural study of synaptic vesicle dynamics in murine inner hair cell ribbon synapses under sustained stimulation

Dissertation

for the award of the degree

"Doctor of Philosophy" (PhD)
Division of Mathematics and Natural Sciences

of the Georg-August-Universität Göttingen

within the doctoral program Sensory and Motor Neuroscience (SMN)

of the Georg-August University School of Science (GAUSS)

submitted by

Magdalena Redondo Canales

from Madrid, Spain

Göttingen, 2022

Thesis Committee

Prof. Dr. Carolin Wichmann

Molecular architecture of synapses group, Institute for Auditory Neuroscience, Inner Ear Lab and Centre for Biostructural Imaging of Neurodegeneration, University Medical Center Göttingen

Prof. Dr. Tim Gollisch

Department of Sensory Processing in the Retina, University Medical Center Göttingen

Prof. Dr. Nils Brose

Department of Molecular Neurobiology, Max-Planck Institute for Multidisciplinary Sciences

Members of the Examination Board

1st Referee: Prof. Dr. Carolin Wichmann

Molecular architecture of synapses group, Institute for Auditory Neuroscience, Inner Ear Lab and Centre for Biostructural Imaging of Neurodegeneration, University Medical Center Göttingen

2nd Referee: Prof. Dr. Tim Gollisch

Department of Sensory Processing in the Retina, University Medical Center Göttingen

Further members of the Examination Board

Prof. Dr. Rubén Fernández-Busnadiego

Institute for Neuropathology, University Medical Center Göttingen

Prof. Dr. med. Christine Stadelmann-Nessler

Institute for Neuropathology, University Medical Center Göttingen

Prof. Dr. Silvio O. Rizzoli

Department of Neuro- and Sensory Physiology and Centre for Biostructural Imaging of Neurodegeneration, University Medical Center Göttingen

Date of oral examination: 21st April 2023

Declaration

I hereby declare that this dissertation has been written independenly and with no other sources and aids than cited.

Magdalena Redondo Canales

Göttingen, December 2022

TABLE OF CONTENTS

TABLE OF FIGURES

ABSTRACT

Transmission of auditory information relies in the correct functioning of inner hair cell (IHC) ribbon synapses, which mediate synaptic vesicle release in an indefatigable manner. The name-giving synaptic ribbon and the formation of tethers at the active zone membrane are key to maintain coordinated and sustained exocytosis. Furthermore, endocytosis, which has been identified to happen as clathrin-mediated and bulk endocytosis, is essential to retrieve material upon prolonged stimulation. This thesis focuses on the study of the ribbon synapse ultrastructure upon sustained stimulation to elucidate the role of otoferlin (Otof) and RIBEYE (RBE) in the synaptic vesicle cycle. On the one hand, Otof is a protein essential for exocytosis, where it has been proposed to be a tether component, as well as being suggested to be involved in endocytosis. On the other hand, RBE is the most abundant constituent of the synaptic ribbon, whose disruption results in ribbon-less synapses and a mild impairment of the ribbon synapse function. Hence, the availability of synaptic vesicles and a fully functional vesicle cycle is required for normal ribbon synapse function. Therefore, the vesicle dynamics in Otof and RBE mutant ribbon synapses was studied via strong and prolonged chemical stimulation followed by high-pressure freezing and electron tomography. Vesicles were classified into different pools, according to their position within the ribbon synapse, as well as vesicle subpools, according to the presence of tethers that are thought to mediate vesicle recruitment for release. In addition, precise millisecond stimulation of IHCs has been recently achieved via optogenetics by expressing channelrhodopsin 2 (ChR2) in IHCs, allowing to observe the early stages of exocytosis. Therefore, I investigated the contribution of Ca^{2+} influx to exocytosis passing through ChR2 upon prolonged stimulation. In this regard, I established a 500 ms light stimulation paradigm, which was followed by high-pressure freezing and electron tomography, where the different vesicle pools and subpools were analysed.

The role of Otof as an actor in exocytosis and endocytosis was investigated using a 15-minute, chemical stimulation paradigm and tomogram analysis. Morphological correlates of exocytosis and endocytosis were analysed and compared in two Otof mutants, namely *Otof* knockout (KO) and *pachanga* ($Otof^{pga/pga}$) to better propose a role of Otof in the vesicle cycle. Vesicle subpool analysis revealed that the presence of Otof is necessary for vesicles to establish initial tethering with the active zone membrane. Conversely, endocytic correlate data make Otof remain unclear, since more endocytic structures were found in resting $Otof^{KO/KO}$ ribbon synapses compared to stimulated $Otof^{KO/KO}$, as well as resting wild-type and $Otof^{pga/pga}$ synapses. This vesicle clusters might indicate an impairment in the endocytic pathway. Furthermore, clusters of large vesicles were observed in some mutant ribbon synapses, although their molecular identity remains unknown. Overall, these data indicate Otof to be essential in the approach of tethered vesicles upon prolonged stimulation to the plasma membrane until docking.

Second, the role of the synaptic ribbon was studied using *RBE*$^{KO/KO}$ IHCs, which resulted ribbonless active zones. I used a 15-minute chemical stimulation paradigm and followed by tomogram analysis to compared stimulated and inhibited wild-type and mutant samples. Vesicle subpool analysis showed that the synaptic ribbon seems to be involved in the approach of vesicles to the active zone membrane. Furthermore, lack of synaptic ribbon appears to affect the topography of docked vesicles laterally to the active zone membrane, which might be indicative of an alteration in the coupling of Ca^{2+}influx-to-vesicle. Importantly, due to the partial dataset is not possible to draw any final conclusion from this work. In summary, the preliminary ultrastructural data suggest that the ribbon might be a key structure modulating the approach of vesicles to the plasma membrane and their position prior to release.

Third, the contribution of ChR2 in Ca^{2+} influx for exocytosis in optogenetically stimulable IHCs was assessed applying a 500 ms light stimulation paradigm and subsequent vesicle subpool analysis. To this end, blockage of IHC constitutive Ca^{2+} channels was performed using isradipine in stimulatory conditions, which was compared to inhibited and stimulated (in the absence of isradipine) conditions. No significant differences were found here, and future experiments will need to be done to confirm the preliminary observations. However, my study revealed long term ChR2 expression, which did not affect the synaptic progression along adulthood.

In conclusion, the study of the morphological correlates of exocytosis and endocytosis upon prolonged stimulation suggest that docked vesicles greatly depend on the presence of Otof to reach such state, and the synaptic ribbon to localise them normally along the active zone membrane. Completion of the study on Ca^{2+} influx through ChR2, as well as the creation of optogenetically stimulable IHCs lacking Otof or the synaptic ribbon will allow to obtain temporally precise ultrastructural information of the synaptic vesicle cycle.

ABBREVIATIONS (ALPHABETICAL ORDER)

AMPA	α-amino-3 hydroxy-5-methyl-4-isoxazolepropionic acid
AP-2	Adaptor protein 2
AZ	AZ
Bsn	Bassoon
CCV	Clathrin-coated vesicle
ChR2	Channelrhodopsin 2
CME	Cathrin-mediated endocytosis
CNS	Central nervous system
EGTA	Ethyleneglycol-*bis*(β-aminoethyl)-N,N,N′,N′-tetraacetic acid
ELV	Endosomal-like vacuole
EPON	Epoxy resin
EPSC	Excitatory postsynaptic currents
GSDB	Goat serum dilution buffer
HC	Hair cell
HPF	High-pressure freezing
HPM	High-pressure freezing machine
IHC	Inner hair cell
KI	Vglut3-ires-cre-knock-in
KO	knock-out
MP	Membrane proximal
Myo6	Myosin VI
N	Number of animals used
n	Number of replicates
OHC	Outer hair cell
Opto-HPF	Optical stimulation of tissue combined with high-pressure freezing

Otof	Otoferlin
P	Postnatal day
PBS	Phosphate buffered saline
PD	Presynaptic density
PDA	Presynaptic density associated
periRA	Peripherally ribbon-associated
PFA	Paraformaldehyde
PKCα	Protein kinase Cα
PSD	Postsynaptic density
RA	Ribbon-associated
RBE	*RIBEYE*
RIM	Rab3-interacting molecule
RIM-BP	Rab3-interacting molecule-binding protein
ROI	Region of interest
RRP	Readily releasable pool
S.E.M	Standard error of the mean
SGN	Spiral ganglion neuron
SNAP-25	Synaptosomal-associated protein, 25kDa
SNARE	Soluble N-ethylmaleimide-sensitive-factor attachment protein receptor
STED	Stimulated emission depletion
SV	Synaptic vesicle
TES	Tubular endocytic structure
VC	Vglut3-cre
vglut3	Vesicular glutatamet transporter 3
WT	Wild-type

1 INTRODUCTION

Sound surrounds us and makes hearing an important sense to navigate the environment, not only by collecting crucial information that keeps us safe, but also through the various interactions with others that help to define the social landscape. The conversion of sound to neuronal signal happens in the cochlea, a spiral-shaped structure where the sensory cells, called hair cells (HCs), are found (Dallos, 1992). These cells encode information about pitch and loudness that is ultimately sent to upstream centres of the brain where the auditory information is further processed and interpreted (Dallos, 1992).

However, hearing must not be taken for granted, since it can be diminished or non-existent due to age, genetic disorders or other reasons (Liberman and Kujawa, 2017; Moser and Starr, 2016). Then, navigating daily situations, such as crossing a road or establishing a conversation with a neighbour, might become a challenge leading to a decrease in the quality of life. Therefore, studying the mechanisms of auditory information reception and transmission at the level of HCs are key to understand the pathology.

Audiograms presenting high hearing thresholds indicate a dysfunction in cochlear synaptic transmission, called cochlear synaptopathy, although the process of synaptic dysfunction or degeneration may start in a non-detectable manner (Liberman and Kujawa, 2017). Different animal models have been used to deepen the understanding of physiological and molecular mechanisms underlying hearing loss, although analysis of the synaptic landscape with nm-resolution may provide valuable information about the different causes of cochlear synaptopathies. Hence, the ultrastructural implications in HCs of aberrant transmission of auditory information have been studied in mammalian animal models via electron microscopy techniques. In this label-free approach, the individual subcellular HC components involved in signal transmission can be distinguished, which allows to draw a picture of the synapse architecture and its changes under the event of signal transmission in health and impaired conditions. Recent electron tomography research efforts in this field attain to the understanding of the functioning of the molecular machinery in healthy conditions (Chakrabarti et al., 2018; Lenzi et al., 2002), as well as to aging (Sergeyenko et al., 2013; Stamataki et al., 2006) or deafness-related questions (Becker et al., 2018; Chakrabarti et al., 2022; Jean et al., 2018; Jung et al., 2015b; Strenzke et al., 2016).

In the next subsections I will explain with detail the anatomy of the mammalian ear and the sensory cells of interest, morphological correlates of signal transmission events and the molecular players, and the state-of-the-art of techniques that connect function and structure. Finally, the hypotheses and connected aims underlying this thesis will be outlined.

1.1 THE MAMMALIAN INNER EAR

Sound information, which can be decoded into pitch (frequency-specific information) and intensity (sound pressure), is quickly and faithfully converted into neuronal signals for correct hearing. The auditory information is captured, amplified and transduced into electrical signals in the inner ear, namely the cochlea (*Neuroscience, 3rd ed.*, 2004) (Fig. 1.1a), from where the information is conveyed to higher brain centres during the hearing process (Dallos, 1992). The cochlea is found in the temporal bone as a spiral, bony layer enclosing three fluid-filled ducts or *scalae* that maintain the ionic imbalance, which is key for depolarisation of the sensory cells upon sound reception (Wangemann, 2002). The upper and lower *scalae*, called *scala tympani* and *scala vestibuli*, are filled with a fluid poor in K^+ (4.2-6 mM) and rich in Na^+ (141-148 mM) called perilymph; while the central duct, called *scala media*, is filled with a high K^+ (157 mM), low Na^+ (1.3 mM) fluid called endolymph (Wangemann, 2006). This ionic imbalance between the *scalae* results in the so-called endocochlear potential, which maintains sensory transduction in the cochlea (Wangemann, 2006). The sensory organ called organ of Corti is found within the *scala media* sitting on the basilar membrane that transmits the vibration of the perilymph to the organ of Corti upon sound arrival (Fig. 1.1b). Altogether, the organ of Corti, supported by the surrounding structures in the cochlea, converts a physical stimulus into an electric signal.

The organ of Corti is composed of several rows of HCs and a variety of supporting cells (Fig. 1.1c), that are involved in the homeostasis of the organ of Corti (Wan et al., 2013). HCs are classified into inner hair cells (IHCs), which are lined in one row; and outer hair cells (OHCs), that are found in three rows. OHCs perform a mechanical amplification function via stereociliary deflection followed by cellular contraction mediated by the protein prestin (Zheng et al., 2000). In contrast, the transmission of frequency-specific information relies on the location of IHCs along the basilar membrane, resulting in the so-called tonotopic organisation of the cochlea (*Neuroscience, 3rd ed.*, 2004). High frequency sounds are detected at the base of the cochlea, where the basilar membrane is narrow and stiff; while low frequency sounds are detected at the apex of the cochlea where the basilar membrane is wide and flexible (Oghalai, 2004). IHCs transmit the information to the cochlear nucleus through monosynaptic connections with type I spiral ganglion neuron (SGN) fibres (*Neuroscience, 3rd ed.*, 2004). Consequently, the tonotopic distribution of auditory information achieved at the level of IHCs is transmitted to the cochlear nucleus and higher brains centres (*Neuroscience, 3rd ed.*, 2004).

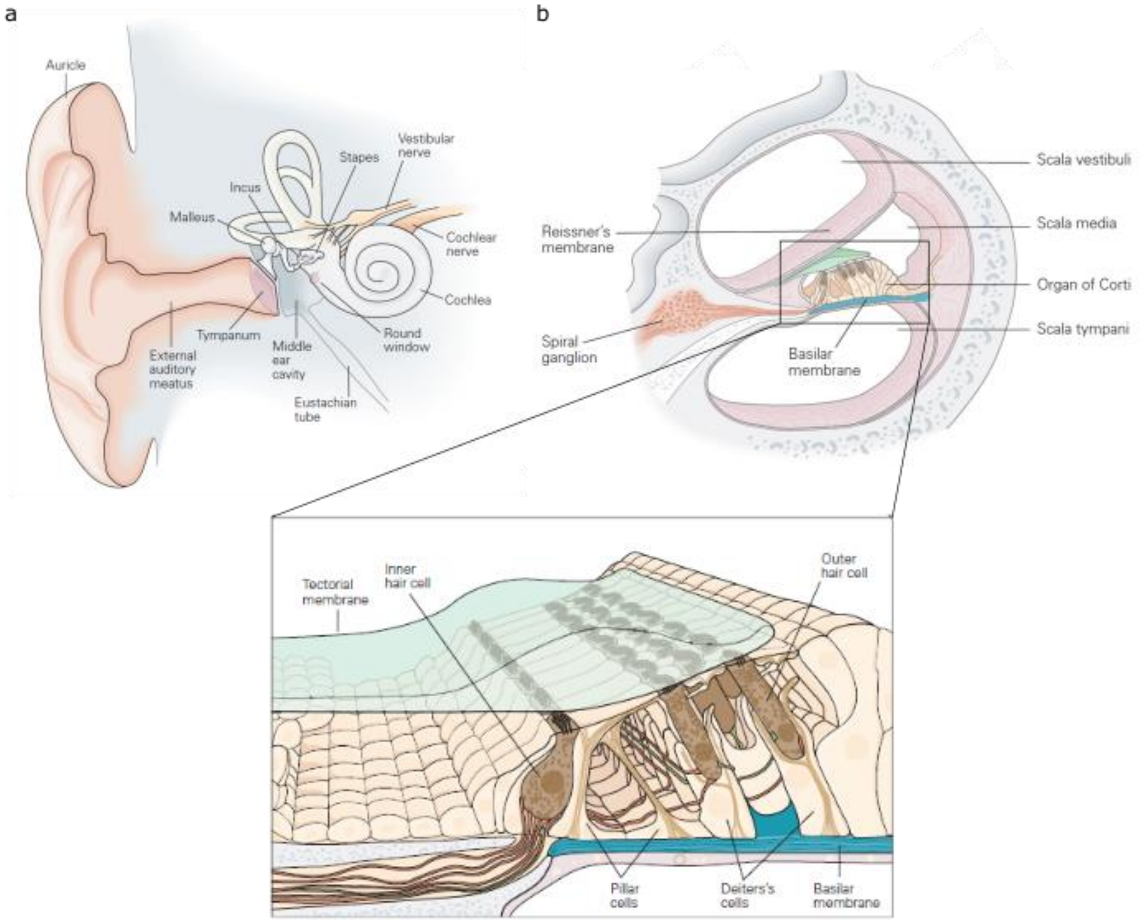

Fig. 1.1: The mammalian inner ear anatomy. a, Schematic representation of the auditory pathway. Sound information is received at the ear and conducted to the middle ear via the external auditory meatus. The eardrum or tympanic membrane produces the vibration of the ossicle chain, which culminates in the oval window of the cochlea. Neuronal connections are made between the sensory cells at the cochlea and the cochlear nerve that conveys the signal to the cochlear nucleus. **b**, Diagram of a cross-section of the cochlea. A close look to the interior of the cochlea reveals three ducts, in which the *scala tympani* and *scala vestibuli* are filled with perilymph, while the *scala media* is filled with endolymph. In the *scala media* the sensory organ, called organ of Corti, is found. (inset) The organ of Corti is composed by a row of inner hair cells (IHCs), several rows of outer hair cells (OHCs) and multiple types of supporting cells (pillar and Deiter's cells) that sit on the basilar membrane. Stereocilia of OHCs are embedded in the tectorial membrane, while IHC stereocilia are surrounded by endolymph. OHCs and IHCs establish synaptic connections with spiral ganglion neuron fibres, which convey the information to the cochlear nucleus. Figure adapted from *Neuroscience, 3rd ed, 2004* (with permission of McGraw Hill LLC).

IHC relay of auditory information requires precise synaptic transmission, which culminates with the interpretation of sound in the brain. The motion of the basilar membrane ultimately leads to the opening of the mechanotransduction channels that is followed by K^+ influx. The depolarisation wave travels along the IHC until reaching the basolateral region where the 10-20 ribbon synapses are found (Meyer et al., 2009; Wong et al., 2014). The depolarisation of the active zone (AZ) membrane elicits the opening of an L-type, voltage-gated Ca^{2+} channels, named $Ca_V1.3$, that allow Ca^{2+} influx in the presynapse and fusion of glutamate-filled synaptic vesicles (SVs). Finally, glutamate binds to α-amino-3 hydroxy-5-methyl-4-isoxazolepropionic acid (AMPA) receptors at the postsynaptic membrane of SGN fibres, triggering action potentials (*Neuroscience, 3rd ed.*, 2004).

1.2 ANATOMY OF IHC RIBBON SYNAPSES

Ribbon synapses are a specialised type of chemical synapses that support tonic activity of sensory cells, such as cochlear and vestibular HCs (Ginzberg and Gilula, 1980; Sobkowicz et al., 1982), photoreceptors (Rao-Mirotznik et al., 1995), retinal bipolar cells (tom Dieck and Brandstätter, 2006) and pinealocytes (McNulty and Fox, 1992). These synapses contain a prominent structure, called synaptic ribbon that is proposed to participate in AZ zone organisation of ribbon synapses and in the recruitment of SVs to support release.

Ribbon synapses undergo a process of maturation in which some of its components (i.e., synaptic ribbon) are transported and assembled (Michanski et al., 2019; Regus-Leidig et al., 2009, p.; Zhai et al., 2001), although the mechanism remains unknown (Voorn and Vogl, 2020). Electron microscopy studies in murine IHCs show that mature synaptic ribbons present diverse shapes, whereby round, oval and droplet-shaped tend to be the commonest types (Sobkowicz et al., 1982; Wong et al., 2014). Regardless of the variety of the morphology, young mature synaptic ribbons reach a height of ~ 190 nm, a width of ~ 150 nm and depth of 400 nm (Michanski et al., 2019; Moser et al., 2019; Payne et al., 2021); and are mostly found as single ribbons per AZ (Hua et al., 2021; Michanski et al., 2019). Moreover, IHC ribbons are anchored to the AZ membrane through a structure termed presynaptic density (PD). In addition, after hearing onset most of $Ca_V1.3$ channels cluster at the AZ in a strip-like formation (Wong et al., 2014). Synaptic ribbons appear as electron-dense structures in electron microscopy that are surrounded by numerous SVs (Smith and Sjöstrand, 1961) (Fig. 1.2), which establish filamentous connections with different elements of the ribbon synapse, such as the ribbon, the PD or other SVs (Bullen et al., 2015; Chakrabarti et al., 2018).

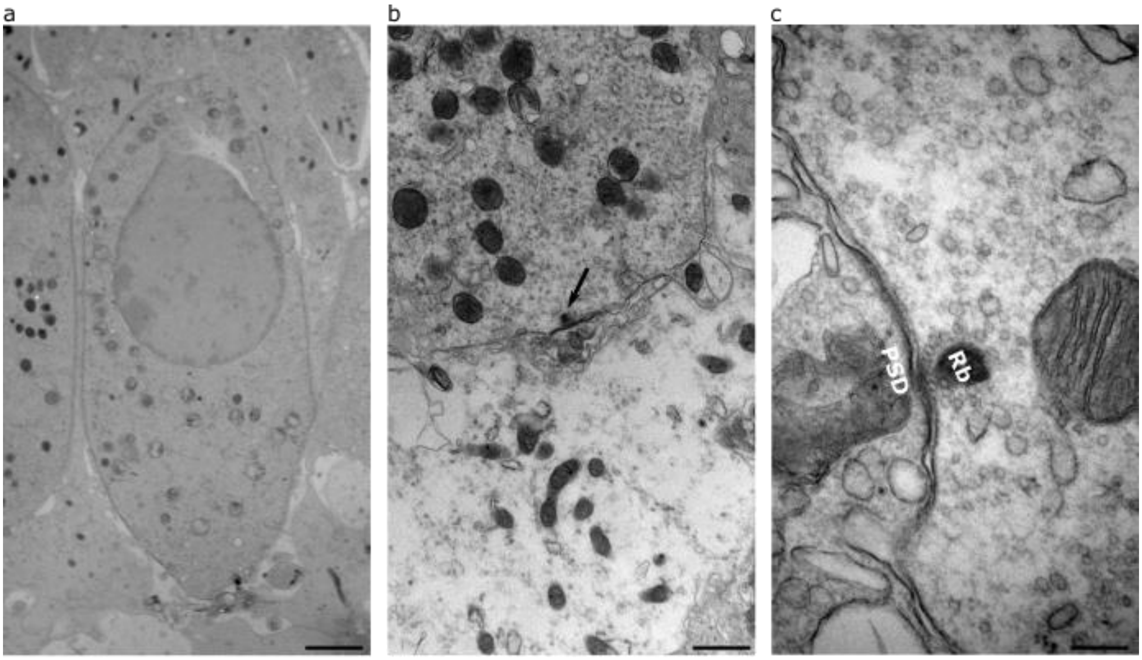

Fig. 1.2: Inner hair cell ribbon synapse morphology. Representative transmission electron microscopy images of **a**, an inner hair cell, in which some synaptic boutons are found in the basal region. Scale bar, 2 µm; **b**, a close-up of a portion of the basal region where a synaptic ribbon is found (arrow). Scale bar, 1 µm; and **c**, a ribbon synapse, in which a droplet-shaped synaptic ribbon (Rb) is seen at the active zone membrane surrounded by synaptic vesicles. Opposite to the active zone, the postsynaptic density (PSD) can be observed. Scale bar, 200 nm.

1.3 SYNAPTIC VESICLE CYCLE IN IHCS

Various SV pools have been identified in relation to their mobilisation from the beginning of stimulation, in which SV release, recycling and turnover are essential for neurotransmission. Electrophysiological experiments in central nervous system (CNS) synaptic terminals upon strong stimulation (> 10 Hz) have allowed the classification of SVs into following pools: the readily releasable pool (RRP), that refers to the SVs that are immediately released upon stimulation (Rosenmund and Stevens, 1996; Stevens and Tsujimoto, 1995); the recycling pool, that replenishes the RRP upon moderate stimulation (Denker and Rizzoli, 2010); and the reserve pool, which is mobilised upon intense stimulation after the recycling pool has been depleted (Denker and Rizzoli, 2010). However, hours-long, low frequency stimulations (2-5 Hz) have unveiled a much more dynamic interaction among SVs, whereby the distinction of the reserve and recycling pools is less obvious (Denker and Rizzoli, 2010). Counterbalancing the increase in cell size due to exocytosis, slow and fast mechanisms of endocytosis have been identified (Ceccarelli et al., 1972; Clayton and Cousin, 2009; Heuser and Reese, 1973; Watanabe et al., 2013b, 2013a). In addition to electrophysiological and immunofluorescence data, modern electron microscopy techniques permit the specific identification of SVs into a functional pool, whereby synapse architecture is a differentiator factor for morphological SV pool classification in CNS and ribbon synapses (Chakrabarti et al., 2018; Imig et al., 2014; Lagnado et al., 1996; Lenzi et al., 2002).

1.3.1 Exocytosis

CNS neurotransmission accurately transmits information in a phasic or tonic manner, in which differences in recruitment of SVs to the AZ membrane define the ability of a synapse to adapt to a change in stimulation (Maus et al., 2020). Early ultrastructural data from conventional synapses upon intense stimulation showed that SV cycle related changes (i.e., SV fusion/invagination, SV depletion and cisternae formation) could be tracked (Ceccarelli et al., 1972; Heuser and Reese, 1973). Minutes-long strong stimulation followed by resting time in the frog's neuromuscular junction showed that exocytosis depletes SVs at the AZ, while there is an increase in the morphological correlates that undergo a process of SV reformation (Heuser and Reese, 1973). Recently, monitoring changes in the distance of SVs to the AZ membrane has allowed to visually identify and measure the size of the RRP in murine hippocampal synapses, which accounts for ~ 6-9 docked SVs per AZ that functionally correspond to primed SVs (Imig et al., 2014). Subsequently, morphologically docked SVs fuse with the AZ membrane forming a characteristic omega-shape (Fernández-Busnadiego et al., 2010).

In contrast, IHC ribbon synapses precisely transmit frequency information in a fast, indefatigable manner to support graded, sustained stimulation (Moser and Beutner, 2000). Capacitance measurements of the IHC ribbon synapse showed a fast and a slow components of exocytosis (Moser and Beutner, 2000; Schnee et al., 2005; Spassova et al., 2004), which ultimately correlate to the RRP and a slowly releasable pool. Functional approaches to study SV dynamics make use of Ca^{2+} chelator buffers, whereby the slow Ca^{2+} chelator ethyleneglycol-*bis*(β-aminoethyl)-N,N,N',N'-tetraacetic acid (EGTA) suppresses the slow component of exocytosis and allows to estimate the temporal range of the fast component (RRP) (Beutner et al., 2001; Goutman and Glowatzki, 2007; Moser and Beutner, 2000). Moreover, an approximate number of SVs (~ 280 SVs) can be inferred from these capacitance recordings (Beutner et al., 2001), which result in ~ 15-21 SVs per ribbon synapse when considering the ribbon count data reported in the literature (Meyer et al., 2009; Pangšrič et al., 2010; Wong et al., 2014). Therefore, a RRP formed by 15-21 SVs per ribbon would deplete in ~ 20-30 ms from the start of stimulation (Beutner and Moser, 2001; Goutman and Glowatzki, 2007).

Studying exocytosis from the ultrastructural point of view combines anatomical and functional information to classify SVs into different pools (Chakrabarti et al., 2022, 2018; Lenzi et al., 2002, 1999). SVs are categorised according to their location at a prominent structure, either plasma membrane or to the ribbon (Lenzi et al., 2002, 1999). Early observations of SV traffic upon strong stimulation in saccular ribbon synapses showed that SVs close to the membrane were depleted and replenished by SVs surrounding the ribbon, which presented a positive gradient of SVs towards the membrane (Lenzi et al., 2002). Overall, SVs close to the membrane are quickly released, while SVs around the ribbon have a replenishment role, allowing to sustain exocytosis for prolonged amounts of time (Lenzi et al., 2002, 1999).

SVs have been classified according to their distance to the membrane as MP-SVs and distance to the ribbon surface into the ribbon-associated (RA) pool, despite the differences in criteria due to the sample type (Chakrabarti et al., 2022, 2018; Jean et al., 2018; Lenzi et al., 2002; Michanski et al., 2019). More recently, strong stimulation of IHC ribbon synapses have shown an increase in the docked SVs, which are part of the so-called membrane proximal (MP) pool (Chakrabarti et al., 2018). The application of these ultrastructural criteria on stimulated IHCs ribbon synapses has revealed the response of the ribbon synapse to exocytosis to an unprecedented extent (Chakrabarti et al., 2022, 2018).

Tethering of SVs to the ribbon or the AZ membrane has recently been shown to play a role in exocytosis (Chakrabarti et al., 2018). Tether formation is suggested to mediate the recruitment of SVs from the different pools (Chakrabarti et al., 2018; Imig et al., 2020, 2014; Maus et al., 2020), so that a change in activity is likely portrayed as a change in SV tethering. Cochlear ribbon synapse SVs have been found establishing connexions with other SVs, termed interconnected (Bullen et al., 2015; Chakrabarti et al., 2018); connected to the AZ membrane, named tethered (Chakrabarti et al., 2018); and forming thin looking tethers or filaments with the ribbon (Chakrabarti et al., 2018). Strong, sustained exocytosis of ribbon synapses is thought to require SVs transport along the ribbon via filaments until reaching the PD (Chakrabarti et al., 2018), where thick tethers are established (see section 3.1). Furthermore, SV tethered to the PD may also form tethers with the plasma membrane, possibly before approaching the AZ membrane (Chakrabarti et al., 2018). Therefore, the complexity involved in SV tethering is shown by the different tethering partners of SVs along their descent for release.

1.3.1.1 Ribbon-associated SVs and exocytosis

Electron microscopy studies of IHC ribbon synapses have classified RA-SVs as those vesicles found up to 80 nm in first line from the ribbon surface. The size of the RA pool ranges between ~ 20-40 SVs, based on ultrastructural studies of unstimulated and stimulated young, mature ribbon synapses (Chakrabarti et al., 2022, 2018; Jean et al., 2018; Michanski et al., 2019). These SVs are thought to move along the ribbon towards the plasma membrane providing a continuous supply of SVs to be release upon sustained stimulation (Chakrabarti et al., 2018). The mechanism of RA-SV transport is not clear, but it likely involves SVs forming tethers of low affinity that would support fast SV probably via diffusion.

Previous structure-function analysis of the IHC ribbon synapse has revealed the dynamism of filament formation depending on activity. Upon stimulation, RA-SVs without filaments become less abundant, while SVs establishing filaments increase, especially with the ribbon and other SVs at the upper half of the ribbon where SV join the supply chain (Chakrabarti et al., 2018). In addition, measurements of the average filament length showed a shortening (< 30 nm), although filaments on the upper half of the ribbon were longer than in the lower half (Chakrabarti et al., 2018). Therefore, it can be concluded that shorter filaments and a more intricate filament network make RA-SVs available to support MP pool resupply (Chakrabarti et al., 2018).

1.3.1.2 Membrane-proximal SVs and exocytosis

Prolonged, strong stimulation has also shown alterations within the MP-SV pool. For example, an increase in the SV presenting single tethers to the AZ membrane, which was interpreted as an initial recruitment for release (Chakrabarti et al., 2018). Based on these findings, a sequence for MP-SV release has been recently proposed whereby single tethered SVs are recruited to the PD and the AZ membrane where they will establish multiple tethers and dock (Chakrabarti et al., 2022, 2018) (Fig. 1.3.1.3). MP-SVs have been ultrastructurally defined in IHC ribbon synapses as SVs found up to 50 nm from the AZ membrane and up to 100 nm from the PD (Chakrabarti et al., 2018; Jean et al., 2018), since tethers were found to reach up to ~ 60 nm in length (Jung et al., 2015b; Vogl et al., 2015). Stimulation results in the extreme abundance of single tethered MP-SVs, especially tethered to the AZ membrane, while multiple tethered SVs are a transient state that results in SV docking (Chakrabarti et al., 2018).

SVs dock at the AZ release sites, which are near $Ca_V1.3$ channels that permit Ca^{2+} entry to trigger priming and fusion. Recent studies proposed that young, mature IHC ribbon synapses follow a Ca^{2+} nanodomain-like model (Moser et al., 2019; Takago et al., 2019; Wong et al., 2014) (see more in section 1.4.3), whereby SVs within 14-30 nm from a $Ca_V1.3$ channel cluster (Spassova et al., 2004) would be susceptible to fuse at their release sites. Currently, the number of release sites per IHC ribbon is still unknown due to the lack of a solid ultrastructural definition for RRP (Beutner and Moser, 2001; Chakrabarti et al., 2018). The maximal number of release sites in CNS synapses is usually obtained knowing the RRP size (i.e., ~ 6-9 SVs in hippocampal synapses) (Byczkowicz et al., 2018; Imig et al., 2014). If applying the same definition to calculate the number of release sites in conventional synapses, the number of release sites in IHC ribbon synapses would range between 1-10, depending on the experimental origin of the RRP size.

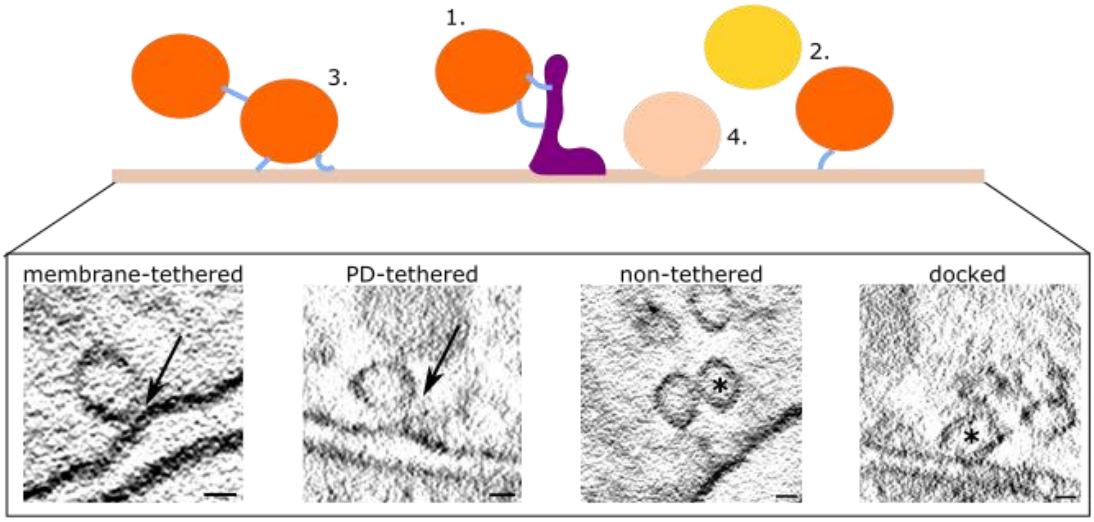

Fig. 1.3.1.2.1: Recruitment of SVs to the AZ membrane. SVs are recruited to the membrane proximal pool via the (1) presynaptic density (magenta), from which they remain in this pool as (2) non-tethered (yellow) or establishing a single tether with the AZ membrane (orange). Next, (3) multiple tethers are formed and finally (4) they dock (light orange). (insets) Representative examples of membrane proximal vesicles. The arrow indicates the presence of a tether and the asterisk indicates the SVs of interest among other SVs present in the virtual slice. Scale bar, 20 nm.

Once SVs are docked in their release sites, fusion may happen in a Ca^{2+}-dependent manner. Excitatory postsynaptic currents (EPSCs) of SGN boutons display a high variability in amplitudes and shapes, namely multiphasic (temporally non-compact) and monophasic (temporally compact) EPSCs (Goutman and Glowatzki, 2007; Neef et al., 2007). Three hypotheses have been proposed to explain the variability in behaviours: coordinated multiquantal release, whereby a group of SVs fuse with variable precision producing monophasic or multiphasic EPSCs (Edmonds et al., 2004; Takago et al., 2019); multiquantal release, whereby a group of SVs fuse with each other before/during release (Edmonds et al., 2004); and uniquantal release, whereby a single SV opens a flickering pore with the plasma membrane through which different amounts of glutamate would be released by regulating the opening-closing dynamics of the pore according to the stimulation strength (Chapochnikov et al., 2014). This latter hypothesis seems to be more plausible in young, mature IHC ribbon synapses (Takago et al., 2019), although no electron microscopy images of the pore have been obtained so far. Understanding the mode of SV fusion is key to clarify how information propagates from IHCs to the first brain centre in the auditory pathway.

1.3.2 Endocytosis

Coupling exocytosis and endocytosis is important to maintain plasma membrane surface under different stimulation frequencies, preserving its resistor-like properties. Partial or full collapse of a SV into the AZ membrane is generally followed by cofactor recruitment to induce membrane retrieval (Rizzoli, 2014). The determination of the endocytic pathway seems to be highly dependent on the intracellular Ca^{2+} levels, which seems to be true for sensory and conventional synapses (Beutner et al., 2001). Electrophysiological studies, confocal microscopy of vesicle trafficking and electron microscopy have been used to identify and validate the presence of the different pathways for membrane retrieval in CNS (Watanabe et al., 2013b, 2013a; Wu et al., 2014), as well as retinal (Paillart et al., 2003; Pelassa et al., 2014) and IHC ribbon synapses (Beutner et al., 2001; Jung et al., 2015a; Kamin et al., 2014; Kroll et al., 2019; Neef et al., 2014).

Various modes of endocytosis have been proposed for CNS synapses to cope with endocytosis at different speeds, although the triggers for these mechanisms are still under debate. Release site clearance (Neher, 2010) and changes in membrane tension have been hypothesised to couple exocytosis and endocytosis (Watanabe et al., 2013b, 2013a), but the molecular machinery behind it remains largely unknown (Neher, 2010; Watanabe et al., 2013b, 2013a). In addition, intracellular Ca^{2+} concentrations might be coupling exocytosis and endocytosis, as well as regulating endocytosis kinetics (Leitz and Kavalali, 2011). Therefore, fast and slow endocytosis seem to depend to some extent in membrane tension, intracellular Ca^{2+} levels and release site availability.

Slow endocytosis mechanisms of CNS synapses, which include clathrin-mediated endocytosis (CME) and bulk endocytosis, retrieve membrane areas of different sizes depending on the presynaptic terminal activity. CME has been classically considered the main endocytic pathway of conventional synapses in which membrane retrieval is mediated by the formation of a clathrin-coated vesicle (CCV) over tens of seconds (room temperature measurements, t= 10-20 s; physiological temperature measurements, t= 7-10 s) (Granseth et al., 2006; Granseth and Lagnado, 2008). CCVs are one of the earliest correlates of membrane retrieval processes to be identified by electron microscopy, where vesicles surrounded by a spiky coat could be distinguished (Heuser and Reese, 1973). Simultaneously to CCV identification, clear core vacuoles at the cytoplasm and budding from the plasma membrane were also observed (Heuser and Reese, 1973). These structures are the morphological correlates of bulk endocytosis (Clayton and Cousin, 2009), in which big portions of membrane are retrieved in seconds (t= 1-15 s, depending on the sample type) upon strong stimulation of CNS synapses (Clayton et al., 2008; Clayton and Cousin, 2009). These clear core structures, called endosomal-like vacuoles (ELVs), present protrusions in their surface where SVs are reformed. ELV generation is clathrin- and dynamin-independent, but the specific molecular players remain to be identified (Wu et al., 2014).

Fast endocytosis pathways, which include kiss-and-run and ultrafast endocytosis, retrieve vesicles in less than a second, making them candidate mechanisms for single vesicle retrieval. Kiss-and-run involves the retrieval of a SV upon quick opening and closure of a fusion (t< 1 s) (Ceccarelli et al., 1972), although its existence is controversial in the different conventional synapses due to the caveats in visual and electrophysiological information (He and Wu, 2007). For instance, micrographs of possible kiss-and-run events from an early study (Heuser and Reese, 1973) prevent from accurately knowing the SV origin due to a lack of temporal resolution in the experiment. In addition, variations in electrophysiological recordings protocols show that using electrophysiological temperatures yields time constants of ~ 50 ms (He and Wu, 2007), which resemble the ones from ultrafast endocytosis (Watanabe et al., 2013b, 2013a). Ultrafast endocytosis has recently been observed peripherally to the AZ of murine hippocampal synapses and *C. elegans* neuromuscular junctions using optogenetic stimulation combined with electron microscopy (Watanabe et al., 2013b, 2013a). Ultrafast endocytosis events have been observed to start at 20 ms and peak at 100 ms after stimulation in an actin and dynamin-dependent manner (Watanabe et al., 2013b, 2013a). As a result of endocytosis, large vesicles (diameter > 70 nm) are formed, which is equivalent of retrieving membrane material of 4 SVs (Watanabe et al., 2013b, 2013a). These fast endocytosis mechanisms retrieve small portions of membrane in close temporal proximity to the exocytosis events, although distinguishing between exocytosis and endocytosis morphological correlates is still an issue.

In contrast, IHC high release rates of SVs require endocytic mechanisms that can cope with the recycling of large number of exocytic components. Styryl dye-based photo-oxidation in IHCs revealed tubular and vesicular structures of different sizes, which are morphological correlates endocytosis (Kamin et al., 2014). Upon 5-30 min of recovery from stimulation, IHCs showed an increase in the abundance of smaller sized vesicles (diameter < 100 nm) on the detriment of tubular structures, especially at the basal region. These morphological-functional observations suggest that recycling processes are more important in the basal zone, where ribbon synapses are found, than in the nuclear and apical regions of IHCs (Kamin et al., 2014).

Two functional components of endocytosis that are Ca^{2+} dependent have been identified in IHC ribbon synapses, in which the linear component shows Ca^{2+} and clathrin-dependence (Beutner et al., 2001; Neef et al., 2014). Rising levels of intracellular Ca^{2+} (10-50 µM) caused an earlier onset of endocytosis along with larger portions of retrieved membrane (0-2.5 pF/s). Ca^{2+} influx into the ribbon synapse is regulated by endophilins, which might couple exocytosis and endocytosis (Kroll et al., 2019). The increase in speed of endocytosis might reflect the action of the different endocytic mechanisms, namely CME and bulk endocytosis (Beutner and Moser, 2001).

Sustained stimulation of IHC ribbon synapses results in the activation of slow and fast endocytosis, namely CME bulk endocytosis (Neef et al., 2014) and kiss-and-run (Beutner et al., 2001). Bulk endocytosis has been observed upon strong stimulations in which tubular-like invaginations of the plasma membrane produce a vacuolar structure from where SVs are reformed (Chakrabarti et al., 2018; Jung et al., 2015a; Kroll et al., 2019; Neef et al., 2014). CME happens at a constant pace upon sustained stimulation (1-2fF/s) in a process that produces CCVs, which have been visualised as small vesicles (inner diameter, ~ 54 nm) with the characteristic spiky coat (Neef et al., 2014). Fast endocytosis (kiss-and-run, τ≈ 300 mn) has also been proposed to occur in IHC ribbon synapses under high Ca^{2+} concentrations (Beutner et al., 2001), although morphological correlates of these events remain to be reported. Ultrastructural clarification of the types of endocytic pathways and their molecular players that IHC ribbon synapses use is necessary to understand recycling under different stimulation paradigms.

1.4 MOLECULAR PLAYERS IN IHC RIBBON SYNAPSES

The distinct architecture of ribbon synapses (see section 1.2) hints towards a particular molecular composition due to a difference in protein composition and/or in protein assembly compared to CNS synapses. For instance, bassoon (Bsn) is a protein found in CNS and IHC ribbon synapses (Uthaiah and Hudspeth, 2010) that is involved in the assembly of the elements required for signal transmission (Dresbach et al., 2001; Khimich et al., 2005). In CNS synapses Bsn organises the cytomatrix at the AZ and interacts with other components of the cytomatrix (tom Dieck et al., 1998; Zhai et al., 2001), while in ribbon synapses it is found organising elements at the AZ membrane (Dick et al., 2003; Frank et al., 2010; Khimich et al., 2005). In contrast, specifically at IHC ribbon synapses one protein plays an important role in synaptic transmission, called Otoferlin (Otof, see more in section 1.4.2), while it is lacking (and not needed) in CNS synapses (Reisinger et al., 2011; Wichmann and Moser, 2015). Such particularities in the molecular composition of IHCs that might translate into a specific presynaptic architecture, finely tune these ribbon synapses for reliable signal transmission.

Some proteins are necessary to comply with the functional demands of ribbon synapses by having an active role in SV cycling and its modulation. Multiple studies have found differences in proteins involved in signal transmission in IHC ribbon synapses, photoreceptor ribbon synapses and CNS synapses. IHC ribbon synapses express VAMP1/synaptobrevin 1, which is also found in CNS synapses (Uthaiah and Hudspeth, 2010). Conversely, cochlear ribbon synapses appear to lack proteins such as syntaxin 1, synaptosomal-associated protein 25kDa (SNAP-25), complexin 1, 2, synapsin 1, 2a, synaptotagmin 1, 2, synaptophysin 1, 2, and Munc 13 (Nouvian et al., 2011;

Uthaiah and Hudspeth, 2010); although mature IHCs seem to express, among other proteins, synaptotagmin 4 (Safieddine and Wenthold, 1999), Otof (Roux et al., 2006) (see subsection 1.4.2) and the voltage-gated Ca^{2+} channel $Ca_V1.3$ (Platzer et al., 2000) (see section 1.4.3), which play key roles in exocytosis.

Other proteins act as landscape organisers by interacting with each other, while serving as platform for SV traffic. Large scaffolding proteins found in ribbon synapses include Bsn (Dick et al., 2003; Khimich et al., 2005), piccolino (Müller et al., 2019; Regus-Leidig et al., 2014) and Ribeye (RBE) (Schmitz et al., 2000), the latter one is exclusive of ribbon synapses (Moser et al., 2019; Wichmann and Moser, 2015) (see section 1.4.1). For example, the scaffolding role of Bsn in IHC ribbon synapses includes anchoring the ribbon to the plasma membrane (Dick et al., 2003) -- it constitutes the PD--, recruiting SVs to the AZ membrane and mediating $Ca_V1.3$ channel clustering (Frank et al., 2010). The presence of these proteins is necessary for correct SV recruitment to MP pool and replenishment of MP-SVs that supports sustained neurotransmission (Becker et al., 2018; Frank et al., 2010; Jean et al., 2018; Müller et al., 2019).

1.4.1 RBE, the main component of the ribbon

RBE is the commonest scaffolding protein constituting the synaptic ribbon (Schmitz et al., 2000; Zenisek et al., 2004) that contains two domains mediating RBE-RBE interactions (Magupalli et al., 2008). The N-terminal A domain has no homology to any other protein, while the C-terminal B domain is highly similar to the transcription repressor CtBP2 (Schmitz et al., 2000). RBE A domain establishes homotypic interactions that result in the assembly of multiple RBE molecules (Magupalli et al., 2008; Schmitz et al., 2000). In contrast, the B domain of RBE establishes interactions with the A domain, which allows the three dimensional growth of the ribbon under the modulation of NAD^+/NADH concentration (Magupalli et al., 2008). In addition to the enlargement of the ribbon structure, the B domain of RBE promotes the interaction with SVs (Schwarz et al., 2011), fulfilling its role as a structural element that facilitates the movement of SVs towards the AZ membrane.

Intense stimulation of ribbon synapses has pointed towards the ability of the synaptic ribbon to cope with high rates of SV supply for release and continuous replenishment (Holt et al., 2004; Lenzi et al., 2002; Maxeiner et al., 2016). Testing the role of the IHC ribbon makes use of *RBE*$^{KO/KO}$, in which ribbon loss translates into a mild reduction in hearing (Becker et al., 2018; Jean et al., 2018). Micrograph analysis of ribbon-less synapses have revealed long (~ 600 nm) post-synaptic densities (PSD) and the increase in multiple PDs per AZ, compared to wild-type (Jean et al., 2018). Quantifications of the ribbon-less synapses revealed a 20-50% smaller PD-associated (PDA) and MP pools compared to wild-type in unstimulated experiments. Despite the small size of these pools, IHCs can manage normal sustained exocytosis (Becker et al., 2018; Jean et al., 2018), likely compensated by the large number of PDs per AZ. Furthermore, it might be possible that they present more SVs in the periphery of the PDA pool than *RBE*$^{wt/wt}$ to facilitate SV recruitment to the PD.

Functional data from these ribbon-less synapses show defects in sound encoding, which might be the consequence of the depolarised voltage shift of $Ca_V1.3$ channels and a smaller RRP (Jean et al., 2018). For instance, EPSCs recordings from single SGNs have revealed an asynchronous firing pattern and a reduced adapted firing rate that points to a failure in SV replenishment (Jean et al., 2018). These findings suggest that MP-SVs might show some impairment in their recruitment to the AZ membrane, which would lead to few SVs docking at the release sites.

In summary, the lack of severe functional deficits upon ribbon loss fails to clearly answer the explicit role(s) of this prominent structure name-giving of ribbon synapses. As mentioned above, a potential source for normal activity of ribbon-less IHCs might be the increase in the formation of multiple PDs per AZ (Jean et al., 2018), which might provide enough SVs to maintain normal exocytosis upon strong stimulation. Thus, analysis of the ultrastructural effects of the lack of ribbon upon strong, sustained stimulation might help clarify how the recruitment of SV to the AZ membrane occurs.

1.4.2 Otof, necessary for signal transmission

Otof is a protein from the ferlin family whose numerous mutation are linked to non-syndromic human deafness (DFNB9) (Rodríguez-Ballesteros et al., 2008; Yasunaga et al., 2000), some of which exhibit a temperature-dependent nature (Strenzke et al., 2016). Mouse models are key to understand the physiological and ultrastructural basis of the auditory synaptopathy that the different mutations of *Otof* produce. Otof has been proposed to bind to Ca^{2+} ions and membrane lipids: C_2B to C_2G domains are proposed to bind Ca^{2+} (Dominguez et al., 2022; Michalski et al., 2017), while C_2C and C_2F have lipid binding properties (Marty et al., 2013; Padmanarayana et al., 2014). Therefore, it is likely that, in presence of Ca^{2+}, Otof undergoes a conformational change that results in a shorter structure that allows the C_2C and C_2F domains to bind to a membrane (Pangšrič et al., 2010). Such mechanism would support the role of Otof in SV release (Roux et al., 2006) by allowing the approach of SVs to the AZ membrane.

Otof is mostly distributed below the cuticular plate of IHCs at the apical zone and at the basal zone (Roux et al., 2006). Immunogold labelling has pointed Otof to be present in the AZ membrane and in the membrane of components of the endosomal compartment of mature IHC ribbon synapses (Strenzke et al., 2016). Furthermore, Otof has also been proposed to localise in the membrane of SVs (Roux et al., 2006), although its presence in SVs remains to be confirmed. The broad distribution of Otof hints the importance of its functioning for signal transmission.

Functional Otof is key for exocytosis after hearing onset, when multiple interacting partners have been identified (Safieddine et al., 2012). *In vivo* experiments have shown functional IHCs upon blockage of soluble N-ethylmaleimide-sensitive-factor attachment protein receptor (SNARE) proteins such as SNAP-25 and syntaxin 1A (Nouvian et al., 2011), although *in vitro* interaction of Otof with these proteins via Otof C_2F domain served to suggest a role for Otof in docking and priming of SVs to the AZ membrane (Ramakrishnan et al., 2009). Moreover, $Ca_V1.3$ channels have been shown to interact *in vitro* mainly with the C_2D domain of Otof (Ramakrishnan et al., 2009), hinting a possible regulatory role for SV release (Ramakrishnan et al., 2009). Furthermore, other interactions with proteins involved in the endocytic pathway and retrograde transport have also been identified in IHC ribbon synapses, such as AP-2 (Duncker et al., 2013; Jung et al., 2015a), myosin VI (myo6) (Heidrych et al., 2009), endophilin (Kroll et al., 2019) and protein kinase Cα (PKCα) (Cepeda et al., 2019). Therefore, these interacting partners suggest that the essential and universal role of Otof for signal transmission is based on the correct functioning of the exocytic and endocytic pathways.

Special effort has been made into understanding the consequences in ribbon synapse functioning upon total lack of Otof (*Otof*$^{KO/KO}$) (Roux et al., 2006; Vogl et al., 2015) and upon missense mutation of the C_2F domain whose mouse model is called *pachanga* (*Otof*$^{Pga/Pga}$) (Chakrabarti et al., 2018; Pangšrič et al., 2010; Schwander et al., 2007). Both mouse models show severe hearing impairment, whereby defects in Ca^{2+} sensing that translate into almost completely abolished or poor stimulation-triggered exocytosis (Takago et al., 2019). In depth understanding of the role of Otof requires the acquisition of functional and structural data, as well as the combination of both.

Functional recordings of different Otof mutants are key to understand how signal propagation is affected. IHC capacitance measurements of Otof mutants of the C_2F and C_2C domains have shown defects in sustained exocytosis by a failure in RRP replenishment (Michalski et al., 2017; Pangšrič et al., 2010). In contrast, deletion of Otof disrupts exocytosis almost fully (Pangšrič et al., 2010; Roux et al., 2006; Vogl et al., 2015). More recently Otof has been suggested to control the flickering pore that SVs form for neurotransmitter release, according to the uniquantal release hypothesis (Takago et al., 2019). Therefore, signal transmission in IHCs highly depends on Otof to sustain the engagement of SV at the AZ membrane and modulate glutamate release.

Ultrastructural studies reported ribbon synapses to maintain their normal morphology (Chakrabarti et al., 2018; Roux et al., 2006; Vogl et al., 2015), although MP-SV tether length and endocytic pathways are affected (Chakrabarti et al., 2018; Heidrych et al., 2009; Jung et al., 2015b, 2015b). In relation to exocytosis *Otof*$^{KO/KO}$ present a lack of short tethers, which suggests an impairment of MP-SVs to approach to the AZ membrane upon stimulation, while short tethers are more commonly found in *Otof*$^{pga/pga}$ IHC synapses. Recently, strong and prolonged stimulation of *Otof*$^{pga/pga}$ ribbon synapses have been shown to accumulate multiple tethered and docked SVs, presumably caused by the lack of release site clearance (Chakrabarti et al., 2018). In contrast, for *Otof*$^{KO/KO}$ ribbon synapses no such structure-function study have been performed to date. Furthermore, Otof has been shown to interact with AP-2 (Duncker et al., 2013; Jung et al., 2015a) and myo6 (Heidrych et al., 2009), suggesting a link to CME and SV reformation (Duncker et al., 2013; Jung et al., 2015a). Thus, disruption of Otof might abolish endocytosis and SV reformation, while Otof C_2F domain mutation (*Otof*$^{pga/pga}$) might result in an impairment of these processes.

In summary, Otof has been proposed to act as Ca^{2+} sensor and mediate in the SV cycle (Chakrabarti et al., 2018; Jung et al., 2015a; Pangšrič et al., 2010; Roux et al., 2006; Strenzke et al., 2016; Takago et al., 2019). Potential roles for Otof include participation in tether formation and shortening (Chakrabarti et al., 2018; Vogl et al., 2015), coupling exocytosis and endocytosis (Jung et al., 2015a; Michalski et al., 2017; Pangšrič et al., 2010), and SV recycling and replenishment (Jung et al., 2015a; Pangšrič et al., 2010). Thus, the analysis of ultrastructural effects in exocytosis and endocytosis of the lack of Otof under strong, prolonged stimulation, as well as the analysis of the ultrastructural correlates of endocytosis in *Otof*$^{pga/pga}$ ribbon synapses might help clarify the involvement of Otof in SV release and material retrieval.

1.4.3 $Ca_V1.3$ channels

$Ca_V1.3$ channels are an isoform of L-type Ca^{2+} channels that are essential for IHC response upon depolarisation (Brandt et al., 2003; Platzer et al., 2000). Mature IHCs mostly display $Ca_V1.3$ channels in a strip-like cluster at the ribbon synapse, while few of them are found extrasynaptically (Wong et al., 2014). $Ca_V1.3$ channels exhibit a relatively hyperpolarised (-65 mV) and depolarised (-25 mV) activation/inactivation potentials (Platzer et al., 2000; Xu and Lipscombe, 2001) that are combined with fast activation (~ 1 ms) and slow inactivation (~ 20 ms) kinetics (Fuchs et al., 1990; Spassova et al., 2004). These characteristics make $Ca_V1.3$ channels essential to elicit a response under small and large stimulation while preserving the temporal accuracy of the signal and maximising the time for neurotransmitter release.

The ribbon synapse response upon stimulation highly depends on the spatial relationship between the source of Ca^{2+} ($Ca_V1.3$) and the Ca^{2+} sensing machinery. Two models of SV exocytosis have been proposed upon electrophysiological experiments using Ca^{2+} chelator buffers. As a result, the number of channels involved in SV release and their distance to the Ca^{2+} sensors can be inferred, which lead to the proposal of Ca^{2+}-microdomain and Ca^{2+}-nanodomain models (Wong et al., 2014). The Ca^{2+}-microdomain model suggests that a group of $Ca_V1.3$ channels in proximity from a given SV are required to elicit its fusion (Eggermann et al., 2011). Conversely, the Ca^{2+}-nanodomain models suggests that a single $Ca_V1.3$ channel in very close proximity (~ 30 nm) to a SV triggers its fusion (Eggermann et al., 2011; Moser et al., 2019; Wong et al., 2014). Young, mature IHC ribbon synapses seem to follow a Ca^{2+}-nanodomain-like coupling for exocytosis, whereby a the Ca^{2+} influx from a few $Ca_V1.3$ channels in very close proximity of a SV, trigger the fusion of such SV (Moser et al., 2019).

1.5 METHODS FOR CORRELATING STRUCTURE AND FUNCTION

Early studies on exocytosis and endocytosis from the ultrastructural perspective allowed to broadly observe changes in the synapse of interest that led to correlate certain structures with products of exocytosis and endocytosis (Ceccarelli et al., 1972; Heuser and Reese, 1973). These experiments combined strong stimulations followed by different resting times, after which the tissue was preserved using fixatives (Heuser and Reese, 1973). Despite obtaining high tissue contrast, artifacts of chemical origin (e.g., protein aggregation or collapsed structures) are a big deterrent for fine studies of the ultrastructure of dynamic processes. Therefore, these studies provide valuable information about the general changes that synapses undergo upon activity and recovery.

An improvement in the tissue preservation method translates into an increase in the reliability of visual information – specifically of fine structures like filaments –, which was achieved via various sample freezing techniques. The key hurdle for sample preservation is to achieve freezing without the formation of hexagonal ice (Dubochet, 1995), since it would dramatically alter and disrupt the tissue ultrastructure. Early freezing techniques, such as freeze fracture, relied on the use of thin tissue that could also be chemically stimulated (Heuser and Reese, 1981). Later, the development of high-pressure freezing (HPF) allowed to preserve a given tissue in near-to-native-conditions combining fast freezing with liquid nitrogen and pressure build-up (Dubochet, 1995). On the one hand, ice crystal nucleation is avoided, and water molecules vitrify due to the rapid dip in temperature caused by liquid nitrogen (Kanno et al., 1975). On the other hand, high pressure facilitates freezing of ≤ 200-µm-thick samples with liquid nitrogen at less cold temperatures than without the use of pressure (Leunissen and Yi, 2009). Therefore, HPF is an appropriate technique to preserve the organ of Corti. As a result, a sample with good structural preservation, but with poor tissue contrast is obtained (Fig. 1.5).

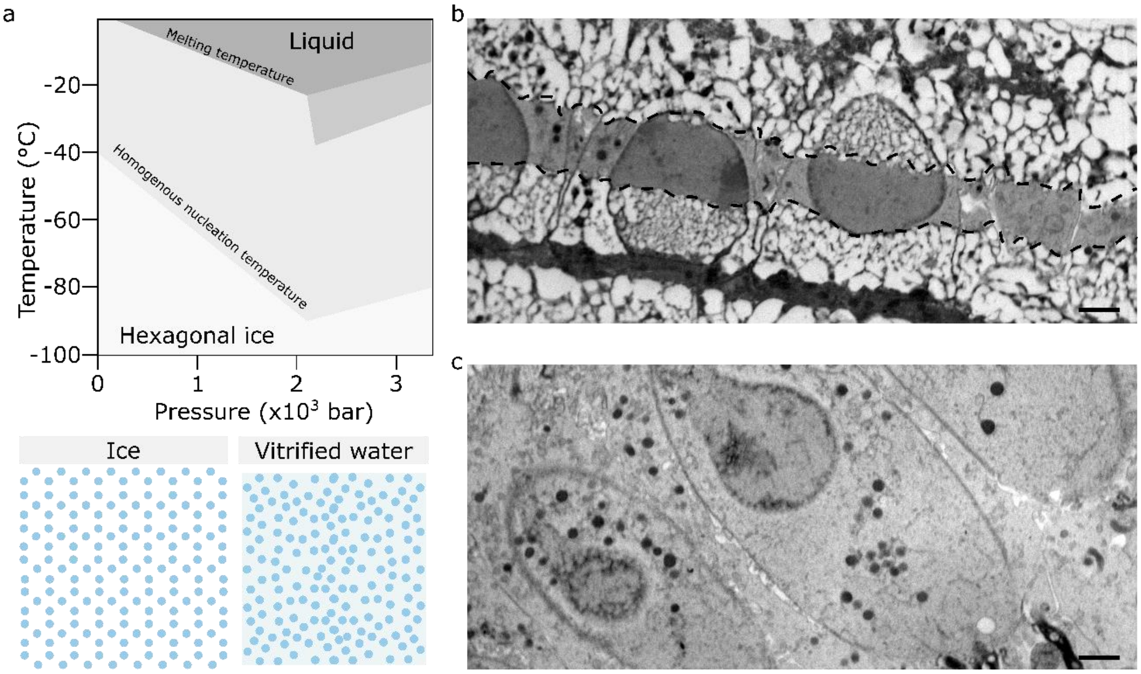

Fig. 1.5: High-pressure freezing. a, Diagram of the correlation between temperature and pressure regulating the water states. There is an inverse relationship between temperature and pressure, whereby lower temperatures are needed for crystal ice formation (left panel) and vitrification ("homogeneous nucleation"; right panel) with higher pressure values. At around 2000 bar, water vitrification is achieved at -90°C. **b-c**, Representative examples the possible outcomes after high-pressure freezing. If freezing is not optimal, the tissue shows severe freezing artifacts, and can even break. Alternatively, the sample is preserved in near-to-native conditions. Note that **b** contains a central stripe of well-preserved tissue (between dotted lines). Scale bar, 2µm.

However, studying the SV cycle via HPF together with chemical stimulation lacks fine temporal resolution, since the control for tissue preservation is manually given by the experimenter (Chakrabarti et al., 2018). High-pressure frozen organs of Corti yielded valuable information about prolonged activity-driven changes in the IHC ribbon synapse ultrastructure, which revealed a SV subpool organisation where different tether patterns precede SV docking (Chakrabarti et al., 2018). Therefore, the combination of optogenetic stimulation and HPF provides the most accurate temporal resolution to date, which allows to obtain answers about the very early stages of exocytosis and endocytosis (Chakrabarti et al., 2022; Watanabe et al., 2013b, 2013a). For instance, early studies establishing this technique revealed ultrafast endocytosis as a new mode of membrane retrieval in conventional synapses (Watanabe et al., 2013b, 2013a). More recently, optogenetic stimulation combined with HPF was applied for the first time in the murine organ of Corti, which revealed changes in the number of docked SVs providing additional evidence into defining the size of the RRP in IHC ribbon synapses (Chakrabarti et al., 2022). Furthermore, the combination of HPF upon light stimulation and electron tomography has permitted the study of the SV cycle and phenomena related to adaptation to a stimulus in CNS (Imig et al., 2020) and ribbon synapses (Chakrabarti et al., 2022). Therefore, data accuracy for the study of dynamic processes increases with better sample preservation and stimulation control.

Coupling light stimulation and HPF requires optogenetically-stimulable IHCs, that express channelrhodopsin 2 (ChR2) for light-to-electrical signal transduction. ChR2 is a light-gated cation channel that has been used to precisely depolarise a variety of cells to better study signal transmission (Borges-Merjane et al., 2020; Madisen et al., 2012; Nagel et al., 2003; Stahlberg et al., 2019; Watanabe et al., 2013b, 2013a). ChR2 shows fast opening (0.2 ms) and desensitisation (20 ms) kinetics (Nagel et al., 2003), which can be further adjusted for the desired experimental approach by modifying ChR2 molecular structure (Dieter et al., 2020; Stahlberg et al., 2019). ChR2 expression in the IHC has recently been allowed to study the ribbon synapse ultrastructure upon tens of milliseconds that provided some answers regarding the early changes in ribbon synapse architecture (Chakrabarti et al., 2022). However, whether a contribution of ChR2 in Ca^{2+} influx that ultimately triggers exocytosis exists is still unknown.

1.6 AIMS OF THE STUDY

This thesis focuses on the analysis of the morphological correlates of exocytosis and endocytosis upon prolonged stimulation of mature IHC ribbon synapses. I aimed to (I) investigate the role of the RBE and Otof, as key proteins in IHC ribbon synapses; (II) to investigate the contribution of ChR2 in Ca^{2+} influx in optogenetically stimulated IHCs; and to (III) introduce a new light-stimulation paradigm of 500 ms. Special focus is put in investigating the changes in SV subpools and endocytosis correlates to achieve these aims.

1.6.1 Comparative study of activity-based changes in synaptic vesicle organisation in ribbon synapses from two Otof mutants

Disruption of Otof produces severe deafness and mostly abolished exocytosis (Pangšrič et al., 2010; Roux et al., 2006; Vogl et al., 2015), although the impaired step(s) of the SV sequence affected remain not fully known. In addition, Otof has been proposed to be necessary for SV release (Chakrabarti et al., 2018; Pangšrič et al., 2010; Roux et al., 2006) and reformation (Jung et al., 2015a), whose morphological correlates remain to be studied. Therefore, incubation for 15 min in a strong stimulatory, resting or inhibitory solution of *Otof*$^{KO/KO}$ and *Otof*$^{wt/wt}$ organs of Corti combined with HPF and electron tomography, as well as further analysis of tomograms used in publication (Chakrabarti et al., 2018), are used to test the following hypotheses:

1. Deletion of Otof results in a severe impairment of the tethering steps necessary for SV release. Thus, little variation in MP subpools combined with failure in the approach of SVs to the AZ membrane might be observed upon stimulation of *Otof*$^{KO/KO}$ ribbon synapses. Consequently, docked SVs might be sparsely observed. This hypothesis is tested by quantifying the MP subpools and the distances of MP-SVs to the AZ membrane in ribbon synapses of *Otof*$^{KO/KO}$.
2. Disruption of Otof hinders MP pool replenishment. Mutant ribbon synapses might present fewer MP-SVs tethered to the PD compared to wild-type. Therefore, assessing this premise requires the quantification of SVs tethered to the PD out of the tethered MP-SVs.
3. Deletion of Otof and mutation of Otof C$_2$F domain alters in different degrees the endocytic pathway. These two mutations of Otof have been shown to impact exocytosis differently, whereby SV replenishment is impaired in *Otof*$^{pga/pga}$ (Pangšrič et al., 2010) and almost null exocytosis occurs in *Otof*$^{KO/KO}$ ribbon synapses. Therefore, a reduction in endocytosis correlates is expected in *Otof*$^{pga/pga}$ IHCs, while sparse endocytic structures are expected in *Otof*$^{KO/KO}$ ribbon synapses. Hence, this hypothesis is evaluated by quantifying the endocytic structures.

1.6.2 Ultrastructural correlates of exocytosis and endocytosis in ribbon-occupied and ribbon-less synapses

Lack of synaptic ribbons results in normal exocytosis (Becker et al., 2018; Jean et al., 2018), but the mechanism of SV recruitment upon stimulation remains unknown. Therefore, incubation for 15 minutes in a strong stimulatory, resting or inhibitory solution of the organ of Corti combined with HPF and electron tomography allowed to test the following hypotheses:

1. Stimulation of *RBE*$^{KO/KO}$ synapses results in normal recruitment of MP and PDA-SVs, despite the small size of these pools (Jean et al., 2018). This premise is tested by quantifying the size of the PDA pool, as well as quantifying the MP-SVs, their subpools and their distances to the AZ membrane at different activity states.
2. Stimulated ribbon-less synapses present few docked SVs, suggesting changes in the readiness of SV for fusion. This hypothesis is inspected by quantifying docked SVs, as well as their relative abundance over the total of MP-SVs.

1.6.3 Effects of ChR2 expression in ribbon synapse ultrastructure for an optogenetic model

Optogenetic stimulation of IHCs has been recently achieved, which has revealed the ultrastructural changes in ribbon synapse architecture upon phasic and sustained stimulation (Chakrabarti et al., 2022). Being this an early study into the consequences of ChR2 expression in IHCs, the following hypothesis were tested:

1. ChR2 is expressed towards adulthood without interfering with the synaptic progression upon aging. This premise is evaluated via immunohistochemical labelling of ChR2 in the plasma membrane and ribbon count of high-resolution confocal images.
2. ChR2 has a small effect in Ca^{2+} influx to the ribbon synapse upon stimulation. This hypothesis is tested by blocking the $Ca_V1.3$ channels with isradipine (see section 2.3.3) and quantifying the SV pools and MP subpools via electron tomography.
3. Optogenetic stimulation over hundreds of milliseconds produces an increase in docked SVs at the AZ membrane, due to SV replenishment upon sustained stimulation. This hypothesis is analysed by quantifying docked SVs and their fraction out of the total of MP-SVs.

2 MATERIALS AND METHODS

2.1 MATERIALS

Workflow stage	**Component**	**Company, location**	**ID number/Model**
Dissection	Micro curette	F.S.T.	10082-15
Immunohistochemistry	Paraformaldehyde (PFA)	Carl Roth	0335.1
Immunohistochemistry	Goat serum	Merck	S26-100ML
Immunohistochemistry	Phosphate buffer	Sigma Aldrich	P5244-100ML
Immunohistochemistry	Triton X-100	Sigma-Aldrich	X-100
Immunohistochemistry	Chicken anti-GFP	Abcam	Ab13970 RRIID: AB_300798
Immunohistochemistry	Mouse anti-CtBP2	BD Biosciences	612044 RRID: AB_399431
Immunohistochemistry	Rabbit anti-myo6	Sigma	N5389 RRID: AB_260781
Immunohistochemistry	Goat anti-chicken (AlexaFluor 488)	Invitrogen	A11039; RRID: AB_2534096
Immunohistochemistry	Goat conjugated anti-mouse (Abberior STAR 635p)	Abberior (Germany)	2-0002-007-5 RRID: AB_2893232
Immunohistochemistry	Goat conjugated anti-rabbit (Abberior STAR 580)	Abberior (Germany)	0012-005-8 RRID: AB_2810981
Immunohistochemistry	Mowiol 4-88	Carl Roth	0718
Immunohistochemistry	Glass slides	ThermoFisher Scientific (Germany)	76 x 26 mm
Immunohistochemistry	775nm 2-color stimulated emission depletion (STED) microscope	Abberior Instruments Expert Line (Germany)	

Solutions	KCl	Sigma Aldrich	P504
Solutions	NaCl	Carl Roth	3957.1
Solutions	$MgCl_2$	Sigma Aldrich	M1028-10X1ML
Solutions	$MgSO_4*7H_2O$	Sigma Aldrich	63140-500g-F
Solutions	HEPES	Sigma Aldrich	H3375-500g
Solutions	$CaCl_2$	Fluka	63020-1L
Solutions	$Na_2HPO_4*H_2O$	Sigma Aldrich	71643-250ML
Solutions	KH_2PO_4	Sigma Aldrich	I6658-5MG
Solutions	Ethylene glicol-bis(β-aminoethyl ether)-N,N,N’,N’-tetraacetic acid (EGTA)	Roth	3054.3
Solutions	Isradipine	Sigma Aldrich	I6658-5MG
Solutions	Glucose	Sigma Aldrich	G8270-1kg
Solutions	L-Glutamine	Sigma Aldrich	G3126-100g
High-pressure freezing	High-pressure freezing machine	Leica Microsystems (Germany)	HPM100
High-pressure freezing	Sample holder half cylinder cartridge	Leica Microsystems (Germany)	16771849 16771846
High-pressure freezing	Sample holder middle plate (Ø, 3 mm)	Leica Microsystems (Germany)	16771833
High-pressure freezing	Planchette type A (Ø, 3 mm x 0.5 mm)	Leica Microsystems (Germany)	16770141
High-pressure freezing	Planchette type B (Ø, 3 mm x 0.5 mm)	Leica Microsystems (Germany)	16770142
High-pressure freezing	1-hexadecene	Sigma Aldrich	H2131-100ML
Optogenetic stimulation combined with high-pressure freezing	Sample holder middle plate (Ø, 6 mm)	Leica Microsystems (Germany)	16770160
Optogenetic stimulation combined with high-pressure freezing	Planchette type A (Ø, 6 mm)	Leica Microsystems (Germany)	16770126
Optogenetic stimulation combined	Saphire disc (Ø, 6 mm)	Leica Microsystems (Germany)	16770158

with high-pressure freezing			
Optogenetic stimulation combined with high-pressure freezing	Spacer rings (Ø, 6 mm)	Leica Microsystems (Germany)	16770180
Optogenetic stimulation combined with high-pressure freezing	LED blue light source	Schott and Moritex (Germany)	LLS-3 A20955 473 nm
Optogenetic stimulation combined with high-pressure freezing	PCI 6221 interface card	National Instruments (Germany)	6221 37 pins
Optogenetic stimulation combined with high-pressure freezing	Pneumatic pressure sensor	WIKA (Germany)	Pressure sensor type A-10
Optogenetic stimulation combined with high-pressure freezing	Microphone	Sennheiser electronic GmbH & Co (Germany)	MKE2
Optogenetic stimulation combined with high-pressure freezing	Accelerometer	Disynet GmbH (Germany)	
Optogenetic stimulation combined with high-pressure freezing	*HPMacquire* (version 9)	Gerhard Hoch (Institute for Auditory Neuroscience, Göttingen)	Custom made Matlab script (Chakrabarti et al., 2022)
Freeze-substitution	AFS	Leica Microsystems (Germany)	EM AFS 2
Freeze-substitution	AFS simple containers, aluminium	Leica Microsystems (Germany)	16702735
Freeze-substitution	AFS simple containers, plastic D13xH18 mm, mesh base	Leica Microsystems (Germany)	16702734
Freeze-substitution	Tannic acid	Sigma Aldrich	W304204
Freeze-substitution	Acetone (≥ 97%)	Sigma Aldrich	W332615

Freeze-substitution	OsO_4 solid	Sigma Aldrich	75632
Freeze-substitution	EPON pre-mix kit	Plano	R1140
Grid making	Formvar	Plano	R1202
Grid making, trimming and sectioning	Mesh grids	Plano	G27075C G2220C-X
Trimming and sectioning	Leica Ultramicrotome	Leica Microsystems	UC7
Trimming and sectioning	45° diamond knife	DiAtome	DTB45
Trimming and sectioning	35˚ diamond knife	DiAtome	DU3530
Post-staining	UranylLess	EMS	#22409
Fiducial staining	Protein A (10 nm), gold particle colloid	BB solutions	EM.GC10
Electron microscopy	Transmission electron microscope	JEOL	JEM 1011
Electron microscopy	CCD camera	GATAN	Orius SC1000
Electron microscopy	Electron tomography transmission electron microscope	JEOL	JEM 2100
Electron microscopy	Serial-EM	https://bio3d.colorado.edu/SerialEM/ (Mastronarde, 2005)	PMID: 16182563
Tomogram reconstruction	etomo	https://bio3d.colorado.edu/imod/	RRID: SCR_003297
Data analysis	FIJI	https://imagej.net/software/fiji/	RRID: SCR_002285
Data analysis	IMARIS custom plug-in	Gerhard Hoch (Institute for Auditory Neuroscience, Göttingen)	(Chakrabarti et al., 2022)
Data analysis	Imod	https://bio3d.colorado.edu/imod/ (Kremer et al., 1996)	RRID: SCR_003297
Preprocessing data	Tomogram analysis	Python https://www.python.org/downloads/	RRID: SCR_008394

Statistical analysis	GraphPad Prism software	GraphPad Prism (https://graphpad.com)	RRID: SCR_002798

Table 2.1: List of materials used in experiments.

2.2 SOLUTIONS

HEPES-Hanks' balanced salt solution	
KCl	5.36 mM
NaCl	141.7 mM
$MgCl_2$	1 mM
$MgSO_4*7H_2O$	0.5 mM
HEPES	10 mM
pH =	7.2
Osm ≤	300 mmol/kg

Table 2.2.1: HEPES-Hanks for tissue dissection in electron microscopy experiments.

Freshly addition of 2 mg/ml of glucose and 0.5 mg/ml of L-glutamine before procedure.

Phosphate buffered saline (PBS)	
NaCl	137 mM
KCl	2.7 mM
Na_2HPO_4	8 mM
KH_2PO_4	0.2 mM
pH =	7.4

Table 2.2.2: PBS for tissue dissection in immunohistochemistry experiments.

Goat serum dilution buffer (GSDB)	
Goat serum	16%
NaCl	450 mM
Triton X-100	0.3%
Phosphate buffer	20 mM
pH =	7.4

Table 2.2.3: Goat serum dilution buffer for immunohistorchemistry.

Wash buffer	
Phosphate buffer	20 mM
Triton X-100	0.3%
NaCl	1.3 mM
pH =	7.4

Table 2.2.4: Wash buffer for immunohistochemistry.

Inhibitory solution	
KCl	5 mM
NaCl	130 mM
$MgCl_2$	3 mM
EGTA	5 mM
HEPES	10 mM
pH =	7.2
Osm ≤	300 mmol/kg

Table 2.2.5: Inhibitory solution for tissue incubation in electron microscopy experiments.

Freshly addition of 2 mg/ml of glucose before experiment

Resting solution	
KCl	5 mM
NaCl	136.5 mM
$MgCl_2$	1 mM
$CaCl_2$	1.3 mM
HEPES	10 mM
pH =	7.2
Osm ≤	300 mmol/kg

Table 2.2.6: Resting solution for 15-minute tissue incubation in electron microscopy experiments.

Freshly addition of 2 mg/ml of glucose before experiment

Stimulatory solution	
KCl	50 mM
NaCl	95 mM
$MgCl_2$	1 mM
$CaCl_2$	5 mM
HEPES	10 mM
pH =	7.2
Osm ≤	300 mmol/kg

Table 2.2.7: Stimulatory solution for 15-minute tissue incubation in electron microscopy experiments. Freshly addition of 2 mg/ml of glucose before experiment.

Isradipine solution	
KCl	5 mM
NaCl	136.5 mM
$MgCl_2$	1 mM
$CaCl_2$	1.3 mM
HEPES	10 mM
Isradipine	5 mM
pH =	7.2
Osm ≤	300 mmol/kg

Table 2.2.8: Isradipine solution for tissue mounting in optogenetic stimulation electron microscopy experiments. Freshly addition of 2 mg/ml of glucose before experiment.

Opto stimulatory solution	
KCl	5 mM
NaCl	136.5 mM
$MgCl_2$	1 mM
$CaCl_2$	1.3 mM
HEPES	10 mM
pH =	7.2
Osm ≤	300 mmol/kg

Table 2.2.9: Stimulatory solution for tissue mounting in optogenetic stimulation electron microscopy experiments. Freshly addition of 2 mg/ml of glucose before experiment.

2.3 ANIMALS AND EXPERIMENTAL CONDITIONS

Animals were bred in the animal facility of the University Medical Centre Göttingen (UMG) and the Max-Planck-Institute for Multidisciplinary Sciences, City Campus. Mice were housed in groups in ventilated cages where they had access to water and food *ad libitum*. Genotyping was performed before hearing onset and verified after the experiment by Sandra Gerke and Christiane Senger-Freitag (Institute for Auditory Neuroscience). All experiments were performed complying with the animal welfare regulations of the University of Göttingen and the state of Lower Saxony (Table 2.3.1, Table 2.3.2, Table 2.3.3).

Mouse line	Genotype	Source
Constitutive Otof knock-out, C57BL6 background	*Otof*$^{wt/wt}$ (*Otof*, +/+)	PMCID: PMC3083821
	Otof$^{KO/KO}$ (*Otof*, -/-)	
Constitutive RBE knock-out, C57BL6/J background	*RBE*$^{wt/wt}$ (*CtBP*, +/+)	PMID: 26929012
	RBE$^{wt/wt}$ (*CtBP*, -/-)	
Ai32	*fl/+* *fl/fl*	PMCID: PMC283525
	+/+	
Vglut3-Cre, C57BL6 background	*cre*$^{-}$	PMCID: PMC4475996
	cre^{+}	
Vglut3-ires-Cre knock-in, C57BL6 background	*cre*$^{+}$/*cre*$^{-}$	PMCID: PMC5283584
AI32KI	*fl/fl; cre*$^{-}$/*cre*$^{-}$ *fl/+; cre*$^{-}$/*cre*$^{-}$	Chakrabarti et al., 2022
	fl/fl; cre^{+}/*cre*$^{-}$ *fl/+; cre*$^{+}$/*cre*$^{-}$	
Ai32VC	*fl/fl; cre*$^{+}$ *fl/+; cre*$^{+}$	Chakrabarti et al., 2022

Table 2.3.1: Animal source summary.

Mouse line	Primers
Constitutive Otof knock-out, C57BL6 background	$^{5'}$CATGCTGTCCTTCACAGATTATGC$^{3'}$ $^{5'}$GGAACAAAGACAGGGTGGTCAGA$^{3'}$ $^{5'}$TCATGACCCATTTCCCTAGCTTCT$^{3'}$
Constitutive RBE knock-out, C57BL6/J background	*RBE*$^{wt/wt}$: $^{5'}$CTTGTGGCTGTGTACAGTTAGCTACATG$^{3'}$
	RBE$^{KO/KO}$: $^{5'}$GCCATCCAACCGAACTAGAGAACCACC$^{3'}$

Ai32	Wild-type: $^{5'}$AAGGGAGCTGCAGTGGAGTA$^{3'}$ $^{5'}$CCGAAAATCTGTGGGAAGTC$^{3'}$
	Mutant: $^{5'}$ACATGGTCCTGCTGGAGTTC$^{3'}$ $^{5'}$GGCATTAAAGCAGCGTATCC$^{3'}$
	Recombinant: $^{5'}$GTGCTGTC TCATCATTTTGGC$^{3'}$ $^{5'}$TCCATAATCCATGGTGGCAAG$^{3'}$
Vglut3-Cre/ Vglut3-ires-Cre knock-in	vglut3-Cre: $^{5'}$CCCGTGGGCTGGAGTTGAG$^{3'}$ $^{5'}$GCGCAGCAGGGTGTTGTAGG$^{3'}$
	vglut3-ires-Cre knock-in: $^{5'}$CTACAGCGGAGTCATCTTCTACG$^{3'}$ $^{5'}$ACCAAGGTCCATATTCCCATCT$^{3'}$
	Recombinant (vglut3-Cre): $^{5'}$CTGCTAACCATGTTCATGCC$^{3'}$ $^{5'}$TTCAGGGTCAGCTTGCCGTA$^{3'}$

Table 2.3.2: Genotyping primers

Research question	**Experiment**	**Genotype**	**Age**	**$N_{animals}$**	**n**
Role of Otof in exo-/endocytosis	Chemical stimulation High-pressure freezing Electron tomography	*Otof*$^{wt/wt}$ inhibitory	P16-19	4	23 ribbons
		Otof$^{wt/wt}$ resting	P19-20	2	20 ribbons
		Otof$^{wt/wt}$ stimulatory	P17-19	3	18 ribbons
		Otof$^{KO/KO}$ inhibitory	P17-21	2	20 ribbons
		Otof$^{KO/KO}$ resting	P19-20	2	20 ribbons
		Otof$^{KO/KO}$ stimulatory	P17	3	17 ribbons
	Tomogram analysis (Chakrabarti et al., 2018)	B6J inhibitory	P14-P16	3	10 ribbons
		B6J resting	P14-P16	2	7 ribbons
		B6J stimulatory	P14-P16	3	10 ribbons

		Otof$^{pga/pga}$ inhibitory	P14-19	2	10 ribbons
		Otof$^{pga/pga}$ resting	P14-19	2	8 ribbons
		Otof$^{pga/pga}$ stimulatory	P14-19	2	10 ribbons
Role of the ribbon in exo-/ endocytosis	Chemical stimulation High-pressure freezing Electron tomography	*RBE*$^{wt/wt}$ inhibitory	P15	1	7 ribbons
		RBE$^{wt/wt}$ resting	P19	2	6 ribbons
		RBE$^{wt/wt}$ stimulatory	P18-19	2	7 ribbons
		RBE$^{KO/KO}$ inhibitory	P18-22	2	6 PDs
		RBE$^{KO/KO}$ stimulatory	P17-20	2	6 PDs
Long-term ChR2 expression in IHCs	Immunohisto-chemistry (Chakrabarti et al., 2022)	Ai32KI *cre*$^{+}$	Group 1: 4-5 months old	3	170 cells
		Ai32KI *cre*$^{+}$	Group 2: 6-7 months old	2	116 cells
		Ai32KI *cre*$^{+}$	Group 3: 9-12 months old	2	129 cells
		WT	Group 1: 4-5 months old	2	99 cells
		WT	Group 2: 6-7 months old	2	87 cells
		WT	Group 3: 9-12 months old	2	49 cells
Ca^{2+} influx through ChR2 in IHCs	Optogenetic stimulation High-pressure freezing Electron tomography	Ai32VC *cre*$^{+}$ inhibitory	P15	3	15 ribbons
		Ai32VC *cre*$^{+}$ isradipine	P19	3	9 ribbons
		Ai32VC *cre*$^{+}$ opto-stimulatory	P15	3	7 ribbons

Table 2.3.3: Summary of experiments, animal genotypes, and sample size.

2.3.1 Otof mutants and littermate controls

7 *Otof*$^{KO/KO}$ and 8 littermate *Otof*$^{wt/wt}$ between postnatal day (P)16-21 were used to clarify the ultrastructural effects of the disruption of Otof, which leads to almost abolished exocytosis (Roux et al., 2006). The apical turn of the cochlea of *Otof*$^{wt/wt}$ and *Otof*$^{KO/KO}$ mice was incubated in either inhibitory (Table 2.2.5), resting (Table 2.2.6) or stimulatory (Table 2.2.7) solution. These mice were divided into the following conditions: *Otof*$^{wt/wt}$ inhibition mice, N= 4 from which 23 ribbons were acquired; *Otof*$^{wt/wt}$ resting mice, N= 2 from which 20 ribbons were imaged; *Otof*$^{wt/wt}$ stimulation mice, N= 3 where 18 ribbons were obtained; *Otof*$^{KO/KO}$ inhibition mice, N= 2 from which 20 ribbons were acquired; *Otof*$^{KO/KO}$ resting mice, N= 2 from which 20 ribbons were imaged; *Otof*$^{KO/KO}$ stimulation mice, N= 3 where 17 ribbons were obtained (Table 2.3.3). These mice were used for section 3.1.1 and section 3.1.3 of my thesis.

In addition, *Otof*$^{pga/pga}$ tomograms and data already used in publication (Chakrabarti et al., 2018) were further analysed to obtain information about endocytosis (Table 2.3.3). These mice were used for the result section 3.1.2 of my thesis.

2.3.2 RBE$^{KO/KO}$ mice and non-littermate controls

5 *RBE*$^{KO/KO}$ and 4 littermate *RBE*$^{wt/wt}$ at P15-22 were used to shed light into the role of the ribbon as a SV hub. The apical turn of the cochlea of *RBE*$^{wt/wt}$ and *RBE*$^{KO/KO}$ mice was incubated in either an inhibitory, a resting or a stimulatory solution. These mice were categorised into five conditions: *RBE*$^{wt/wt}$ inhibition mice, N= 1 from which 7 ribbons were acquired; *RBE*$^{wt/wt}$ resting mice, N= 1 from which 6 ribbons were imaged; *RBE*$^{wt/wt}$ stimulation mice, N= 2 where 7 ribbons were obtained; *RBE*$^{KO/KO}$ inhibition mice, N= 2 from which 6 PDs were acquired; and *RBE*$^{KO/KO}$ stimulation mice, N= 2 where 6 PDs were obtained (Table 2.3.3). These mice were used for section 3.2 of my thesis.

2.3.3 Optogenetically stimulable mouse lines

The creation of mouse lines for optogenetic stimulation of IHCs was based in the loxP/cre recombination system. One mouse line, called Ai32 (Table 2.3.1), carries the *ChR2-H134-eYFP* construct (B6;129S-Gt(ROSA)26Sor$^{tm32(CAG-COP4*H134R/EYFP)Hze}$/J) that is preceded by a STOP codon, which is flanked by *loxP* sequences (Madisen et al., 2012; Nagel et al., 2003). The Ai32 mouse line was bred with either of two mouse lines that contain the Vglut3-cre construct whereby upon cre recombinase expression *ChR2* is transcribed in IHCs (Jung et al., 2015b). A first line of mice for optogenetic experiments called Ai32VC was done by breeding Ai32 mice with a previously reported line containing Vglut3-cre (VC) construct (Jung et al., 2015b) (Table 2.3.1). Another line of mice for optogenetic experiments called Ai32KI was achieved by breeding Ai32 mice with Vglut3-ires-cre-knock-in mice (KI) (Lou et al., 2013; Vogl et al., 2016) (Table 2.3.1). As a result, the following genotypes from the Ai32VC and Ai32KI lines were used for experiments: *fl/fl; cre*$^+$, which was termed Ai32VC *cre*$^+$; *fl/fl; cre*$^+$*/cre*$^-$ or *fl/+; cre*$^+$*/ cre*$^-$, which were called Ai32KI *cre*$^+$; and *fl/fl; +/+* or *fl/+; +/+*, which were named wild-type (WT).

7 Ai32KI *cre*$^+$ and 6 WT of three age groups were used to verify a stable, long-term ChR2 expression in IHCs. Ai32KI mice were divided into three age groups: group 1 (G1) includes 4-5-month-old Ai32KI *cre*$^+$ mice, N= 3 from which 170 cells were screened; and WT mice, N= 2 from which 99 cells were imaged. Group 2 (G2) contains 6-7 months-old Ai32KI cre$^+$ mice, N= 2 from which 116 cells were screened; and WT mice, N= 2 from which 87 cells were imaged. Finally, group 3 (G3) includes 9-12 months-old Ai32KI cre$^+$ mice, N= 2 from which 129 cells were screened; and WT mice, N= 2 from which 49 cells were imaged (Table 2.3.3). These data were used for publication (see our paper, Chakrabarti et al., 2022) and the results from this line can be found in section 3.3.1 of my thesis.

8 Ai32VC *cre*$^+$ at P15-19 were used to evaluate changes in ribbon synapse architecture upon Ca^{2+} influx through ChR2 in IHCs. Isolating the action of ChR2 was performed by using 5 µM of isradipine, which abolishes IHC exocytosis by blocking $Ca_V1.3$ channels (Brandt et al., 2003). Organs of Corti of Ai32VC *cre*$^+$ were incubated in either inhibitory solution (Table 2.2.5), isradipine solution (Table 2.2.8) or stimulatory solution for optogenetic experiments (Table 2.2.9). Ai32VC *cre*$^+$ mice were classified into three experimental conditions: Ai32VC *cre*$^+$ opto, N= 2 from which 7 ribbons were acquired; *cre*$^+$ isradipine, N= 3 from which 9 ribbons were obtained; Ai32VC *cre*$^+$ inhibitory, N= 3 mice from which 13 ribbons were imaged (Table 2.3.3). Some Ai32VC mice showed recombination of ChR2 construct due to unspecific cre activity (see Table 2.3.2), which results in ectopic expression of ChR2 in the cochlea. Due to problems in breeding, 2 Ai32VC *cre*$^+$ Ai32 recombinant mice were used in the isradipine condition. The results corresponding these mice were used for section 3.3 of my thesis.

2.4 METHODS

2.4.1 Tissue dissection

Mice were deeply anesthetised using CO_2 and decapitated. The skull was cleaned from the skin and cut along the sagittal plane into halves, which were transferred into ice cold HEPES-Hanks buffer (Table 2.2.1) or x1 phosphate buffered saline (PBS, Table 2.2.2). The brain was removed, and the bony labyrinth was isolated from the occipital and temporal bones. A small hole was made at the apex of the cochlea, which was used to uncover at least 1.5 turns of the cochlear duct. Then, the 1.5 apical turns of the cochlear duct (referred in this thesis the "apical turn of the cochlea") was gently detached from the modiolus and cut with micro-scissors. Finally, the tissue was transferred with a micro curette to the next required location, which varies depending on the research question.

2.4.2 Immunohistochemistry

Ai32KI mice were used in this protocol with the aim to observe long-term ChR2 expression in the IHCs. The apical turn of the cochlea was dissected in 1x PBS and was fixed in 4% paraformaldehyde (PFA) on ice for 1 hour. Next, PFA was removed and the samples washed with PBS 3x for 10 min. Subsequently, the tissue was blocked with goat serum dilution buffer (GSDB, Table 2.2.3) at room temperature for 1 hour. Then, the samples were placed in a wet chamber and incubated overnight at 4°C with the primary antibodies diluted in GSDB, which include chicken anti-GFP (1:500), rabbit anti-CtBP2 (1:200) and rabbit anti-myo6 (1:200) (Table 2.1). The primary antibody solution was removed and the tissue was washed with wash buffer (Table 2.2.4) 3x for 10 min. Afterwards, the organs of Corti were incubated at room temperature for 1 hour with the secondary antibodies diluted in GSDB, which contained goat anti-chicken AlexaFluor 488 (1:200), AbberiorStar 635p conjugated anti-mouse (1:200) and AbberiorStar 580 conjugated anti-rabbit (1:200) (Table 2.1). Next, a washing step was performed 3x for 10 min with wash buffer. Finally, the samples were mounted onto a glass coverslip in a drop of mounting medium Mowiol and covered with a glass coverslip.

Confocal images were acquired using a stimulated emission depletion (STED) microscope with a 1.4NA 100x oil immersion objective and excitation lasers at 488, 594 and 633 nm. Information about the materials can be found in Table 2.1.

2.4.3 High-pressure freezing for chemical stimulation

RBE$^{KO/KO}$ and their non-littermate controls, as well as *Otof*$^{KO/KO}$ and their littermate controls were used for this procedure with the aim to observe ultrastructural changes in the ribbon synapse upon minutes-long chemical stimulation. The apical turn of the organ of Corti was dissected in freshly prepared HEPES-Hanks solution and incubated in either inhibitory, resting or stimulatory solution (Table 2.2.5, Table 2.2.6, Table 2.2.7) during 15 min at room temperature (Chakrabarti et al., 2018).

Meanwhile, the 3 mm system (Fig. 2.4.3) that will hold the sample was prepared onto the loading station of the high-pressure freezing machine (HPM). Here, two half cylinders were placed on either side and a middle plate that contains a 3 mm hole was put on top of one of the half cylinders. About 2-1.5 min until the incubation time finished, the organ of Corti was placed in the deepest side (200 µm) of a 3 mm planchette A, while still embedded in the pertinent incubation solution. Then, the flat side of a planchette B is lightly coated in 1-hexadecene and pressed on the planchette A to avoid any air bubbles and seal the 3 mm system. This planchette sandwich was dried on the edges and was placed in the hole of the middle plate (Fig. 2.4.3). Then, the cylinder was closed and, when the incubation time finished, the sample was inserted into the freezing chamber for freezing. Finally, frozen samples were transferred in liquid nitrogen into a cryo-vial for storage (Chakrabarti et al., 2018). Information about the material can be found in Table 2.1.

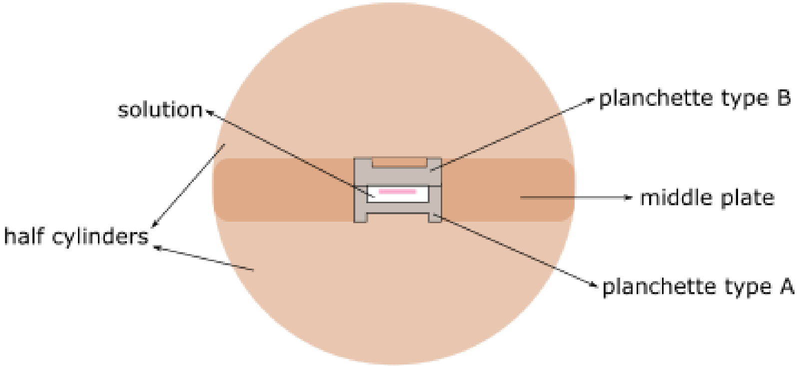

Fig. 2.4.3: Diagram of the 3 mm system used in high-pressure freezing. The apical turn of the organ of Corti (pink) is embedded in either stimulatory, resting, or inhibitory solution in between the planchette A and B. These enclosed by the middle plate and two half cylinders.

2.4.4 Optical stimulation combined with HPF

Optical stimulation of tissue combined with HPF (opto-HPF) allows precise stimulation in milliseconds time range to study early phenomena of exocytosis and endocytosis (Chakrabarti et al., 2022; Imig et al., 2020; Watanabe et al., 2014, 2013b, 2013a).

Ai32VC mice were used for opto-HPF with the aim of evaluating the basal activity of ChR2 on IHCs by detecting any possible contribution from Ca^{2+} influx through ChR2 to exocytosis. The apical turn of the organ of Corti was mounted in a 6 mm planchette system in either inhibitory (Table 2.2.5), isradipine (Table 2.2.8) or opto-stimulation solution (Table 2.2.9). Part of the data shown in this thesis are the result of Julius Bahr's Masters' dissertation project, which was supervised by me. His contributions to this thesis are detailed in section 3.3.

Samples were mounted onto a middle plate that contains a 6 mm hole with a small rim where there a sapphire disc was placed, which will later allow light stimulation of the tissue. After putting a spacer ring, a drop of the pertinent solution is pipetted, and the organ was placed on the right side of the sapphire disc for optimal light stimulation (Chakrabarti, 2018). The sandwich was sealed by placing a 6 mm planchette A and a second spacer ring (Fig. 2.4.4). Then, the cylinder was closed and the sample was loaded into the HPM, whose freezing mechanism was coupled with the blue light source that stimulated the sample for 500 ms with a maximum irradiance of 6 mW/mm^2 (Chakrabarti et al., 2022). Finally, frozen samples were transferred into a cryo-vial in liquid nitrogen for storage. Information about the materials can be found in Table 2.1.

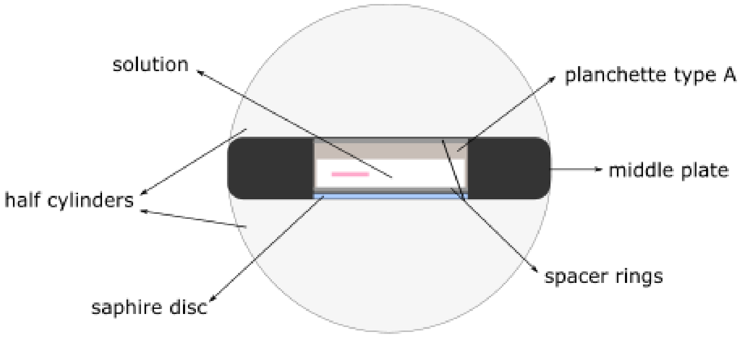

Fig. 2.4.4: Diagram of the 6 mm system used for opto-high-pressure freezing. On a half cylinder and the middle plate, the apical turn of the organ of Corti (pink) is placed on a sapphire disc with a spacer ring, and embedded in either an inhibitory, isradipine or stimulatory solution for optogenetic experiments. A planchette A with a spacer ring is used to seal the tissue. Finally, another half cylinder is used to close the system.

Opto-HPF requires a precise control of the light stimulation of the sample right before freezing, which was achieved by coupling several devices and sensors to the HPM. The first device was the trigger box that allowed the user to manually control the start of the stimulation and freezing paradigm. Then, a blue light optical fibre reaching the freezing chamber with an external control was also coupled to the HPM to provide the stimulation source and control the intensity. This system was connected to the computer via PCI 6221 interface card and a RS-232 interface cable for user control of the stimulation length and intensity (Chakrabarti et al., 2022). Further information about the materials can be found in Table 2.1.

As reported in Chakrabarti et al. (2022), recording the pressure and the temperature in the freeze chamber, as well as their ratio was achieved by the internal pressure sensor and thermal sensor that the HPM had integrated from assembly. However, a precise monitorisation of the pressure-to-freezing curve was possible only after reaching 65 bar in the freezing chamber. The lack of prior temporal information prevented from identifying the beginning of the liquid nitrogen entry, the exact freezing time point and, by extension, the length of the light stimulation in an objective timescale. Therefore, other sensors were installed to monitor the freezing process and precisely determine the light stimulation time, namely microphone, accelerometer, and pneumatic pressure sensor (Table 2.1). Importantly, the pneumatic pressure sensor was installed on the pneumatic valve preceding the freezing chamber, which opens when the liquid nitrogen pressure reaches 7 bar on this valve. Consequently, the pneumatic pressure drops, and the liquid nitrogen enters the freezing chamber resulting in sample freezing within 6.52 ms (Chakrabarti et al., 2022).

It is important to note the timing in the high-pressure freezing process, since there are several delays that determine the length of the light stimulation (Chakrabarti et al., 2022). The first delay refers to the time that takes to pressurise the liquid nitrogen into the freezing chamber ($T_{\text{pressurised N2}}$) that by default in the stimulation paradigm is ~400 ms. The next delay is mechanical ($T_{\text{mechanics}}$) and refers to the values of the internal pressure sensor in context of the absolute timescale given by the pneumatic pressure sensor. The $T_{\text{mechanics}}$ values vary with each freezing. The last delay refers to the time that takes for the sample to be frozen ($T_{\text{sample at 0}}$), which is the summation of the time that takes the freezing chamber to reach 0°C ($T_{\text{chamber at 0}}$), the time for the sapphire disc to reach 0°C ($T_{\text{sapphire disc at 0}}$) and the time for the sample centre to reach 0°C ($T_{\text{sample centre at 0}}$). The $T_{\text{chamber at 0}}$ is the ratio between internal pressure and the internal thermal sensor read outs, which vary between freezings and it is on average 5.41 ms ± 0.26 (SD). The $T_{\text{sapphire disc at 0}}$ was estimated to be 0.01 ms (Watanabe et al., 2013b) and the $T_{\text{sample centre at 0}}$ was estimated to be 1.1 ms (Watanabe et al., 2013b). Therefore, $T_{\text{sample at 0}}$ is ~6.25 ms and the delay of the HPM to start ($T_{\text{HPM delay to START}}$) is ~406.25 ms, plus the $T_{\text{mechanics}}$ (Chakrabarti et al., 2022).

In preparation to perform opto-HPF, the *pause* button in the trigger box had to be pressed preventing the sample from being immediately frozen after shooting it into the freezing chamber. Then, using *HPMacquire* (Chakrabarti et al., 2022), a Matlab-based program (Table 2.1) developed by Gerhard Hoch (Institute for Auditory Neuroscience, UMG, Göttingen), we could select the type of light stimulation (blue light), the intensity (80 mV) and the stimulation paradigm (“stimulation”), as well as the length of light stimulation in ms and the delay to stimulus onset. The light stimulation and freezing of the sample only happen after clicking “HPM start” in the *HPMacquire* software.

In the current stimulation paradigm, the light stimulation was set to 500 ms and there was no delay to stimulus onset, which meant that the actual light stimulation period equalled the $T_{\text{HPM delay to START}}$. To determine the actual light stimulation interval, an excel file and an HPM file were required to correlate the freezing information per freezing, which were acquired from the HPM and the output of the HPM software. The actual light stimulation for this set of experiments including all samples was 442.49 ms ± 3.32 (SD).

2.4.5 Freeze substitution

The objective of this protocol was to dehydrate the tissue at low temperatures to prevent the formation of ice while increasing the sample contrast and making it available to be manipulated at room temperature. Freeze-substitution is a process in which the vitrified water is gently exchanged with an organic solvent, while introducing heavy metals (i.e., osmium) in the tissue at low temperatures. Consequently, high contrast within the tissue is achieved. Avoidance of dehydration artifacts and embedding in a resin enable to preserve the structural features of the sample.

This protocol was performed using an EM AFS machine in which 2-3 aluminium sample containers were loaded with four AFS plastic simple containers. ~ 1.5 ml of pre-cooled 0.1% tannic acid in acetone were placed in each aluminium container. Then, high-pressure frozen samples were loaded from the cryo-vials to the correspondent AFS plastic simple container. The samples were incubated for 73 hours in pre-cooled 0.1% tannic acid in acetone at -90°C. Then, washing with 100% acetone was performed 3x for 30-60 min at -90°C and was followed by application of 2% OsO_4 in acetone for 7 hours. The tissue was incubated in OsO_4 for an additional 36.4 hours in which the temperature gradually increased: first, the temperature increased until reaching -20°C for 14 hours and maintaining the temperature stable at -20°C for 17 hours; then, the temperature increased for 2.4 hours until reaching 4°C and maintained at that temperature for 3 hours. At this point, the OsO_4 was washed 3x for 30-60 min with 100% acetone and the samples were brought to room temperature (Table 2.4.5).

Next, infiltration with epoxy resin (EPON) started by incubating for 90 min in a 1:1 EPON: acetone solution. Then, it was changed to 100% EPON, in which was infiltrated overnight. Upon refreshing the resin in the morning and incubating for 3-5 hours, the samples were mounted in EPON blocks. Polymerisation of the blocks was performed at 70°C for 72 hours (Chakrabarti et al., 2022, 2018; Jean et al., 2018; Kroll et al., 2019; Michanski et al., 2019) (Table 2.4.5). Information about the materials can be found in Table 2.1.

Day	Starting time	Temperature	Duration	Solution
Friday	14.00	-90°C	82 hours	0.1% tannic acid
Monday	9.00	-90°C	2 hours	3x 30-60 min 100% Acetone wash
	17.00	-90°C	7 hours	2% OsO_4

	00.00	-90°C to -20°C	14 hours	2% OsO_4
Tuesday	14.00	-20°C	17 hours	2% OsO_4
Wednesday	07.00	-20°C to 4°C	2.4 hours	2% OsO_4
	09.30	4°C	3 hours	x3 30-60 min 100% Acetone wash
	13.30	RT	1.5 hours	EPON:Acetone (1:1)
	16.00	RT	Overnight	EPON
Thursday	09.00	RT	3-6 hours	EPON
	15.00	70°C	72 hours	Polymerisation

Table 2.4.5: Freeze substitution summary.

2.4.6 Grid making

A coat of 1% formvar (w/v in water free chloroform) was applied to the grids before any further sample processing. First, the 1% formvar was poured into a 50 ml dropping funnel. Then, a glass slide was thoroughly clean of any dust and dipped into the formvar. Subsequently, the tap of the dropping funnel was fully opened, creating a coat of formvar on each side of the slide. After drying for a few minutes in a dust-free environment, the edges of the slide were scratched with a razor blade to remove the excess of formvar coating the glass. Then, a rectangle was delineated with the razorblade on each side of the slide, which was slowly dipped in distilled water in a 1 l beaker. The formvar sheets detached and its thickness could be evaluated, whereby the optimal thickness (80-90 nm) presents a silver and golden colour. After, mesh grids were placed on the formvar with their smooth surface facing up. Finally, the formvar coated grids were covered and picked up with parafilm paper, pressed gently against it to avoid the formation of air bubbles, and left to dry on a Petri dish. Information about the materials can be found in Table 2.1.

2.4.7 Trimming and sectioning

Polymerised EPON blocks were trimmed with a filer parallel to the block surface to approach the tunnel of Corti, where after it the row of IHCs lays. Then, using first the filer and then a razorblade, the tip of the EPON block was shaped into a small trapezoid prism. Subsequently, the blocks were mounted in a Leica UC7 Ultramicrotome where their surface was smoothened with a 45° trimming knife and semi-thin sections (250 nm) were acquired using the ultramicrotome and a 35° diamond knife. Line of 8-12 semi-thin sections were placed on the rough side of mesh grids. Information about the materials can be found in Table 2.1.

2.4.8 Transmission electron microscopy

The usability of a sample was evaluated by the tissue integrity and the freezing quality in a JEOL 1011 transmission electron microscope (Table 2.1) (Fig. 2.4.7). Additionally, the region of interest (ROI) was identified, the integrity of the membrane was evaluated, and micrographs of the ribbon synapse were obtained at x12,000 magnification.

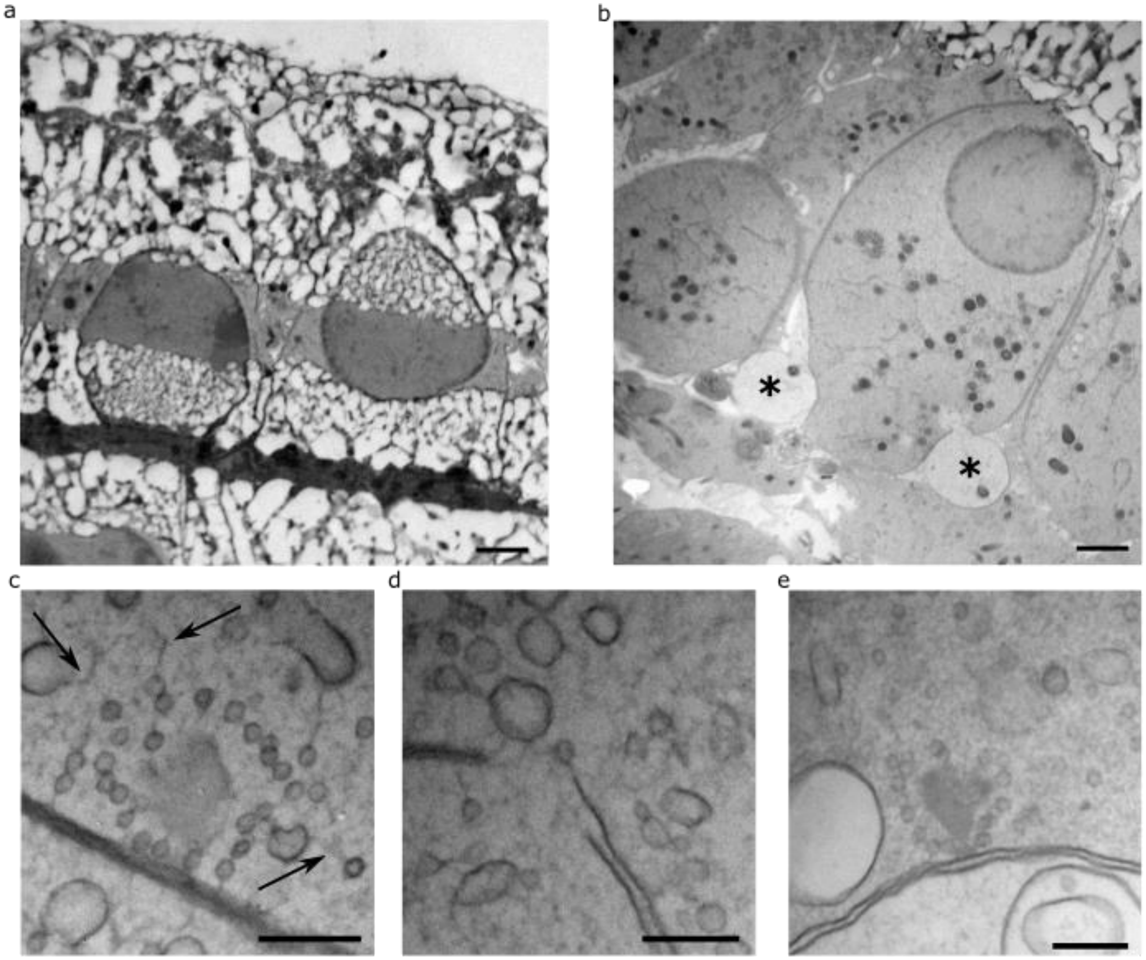

Figure 2.4.8: Sample quality check. Semi-thin sections showing **a**, a row of IHCs with severe freezing artifacts (scale bar, 2 µm); **b**, IHCs with a slightly better structural preservation. The basolateral region shows postsynaptic boutons (*) (scale bar, 2 µm); **c**, a ribbon synapse presenting freezing artifacts, which look like filaments in the cytoplasm (arrows); **d**, broken AZ membrane; **e**, ribbon synapse with good tissue preservation and continuous AZ membrane (scale bar, 200 nm).

2.4.9 Post-staining and application of gold particles

Grids containing ribbon synapses were post-stained using 4% UranylLess, which is a uranyl acetate replacement solution. The rough side of the grids was incubated for 20 min on a drop of UranylLess and then wash them on a distilled water droplet 6x for 1 min, respectively. After air-drying under the fumehood, each side of the grid was incubated for 6-7 min in a protein A gold particle colloid. Finally, the excess of gold colloid was removed was removed with filter paper and left to fully dry in a dust-free environment. Information about the materials can be found in Table 2.1.

2.4.10 Tomogram acquisition

Tomograms were acquired in a 200 kV, JEOL 2100 electron microscope (Table 2.1) with a tilting stage. A single tilt axis series with 1° increment at x12,000 magnification was acquired using the Serial-EM software (Table 2.1), which uses the gold particles (fiducials) for general alignment in the ROI over the tilt series. The tilt axis was established first from -60° to +60°; and, due to mechanical issues with the stage from the electron tomograph, -55° to +55° or from -50° to +50° using. A few tomograms were acquired from -45° to +50° due to the proximity to a grid bar and these tomograms were taken for data analysis if they had sufficient quality (see section 2.4.8 for quality criteria).

The first steps in tomogram acquisition were to align the electron beam and find the z position of the sample. After identifying the ROI, the fiducials were focused on the *z* axis in order to be tracked properly during the tomogram acquisition, which positively impacts the tomogram quality. Next, the tilt axis was established by following and centring a remarkable feature in the ROI from 0 to +60°/55° and from 0 to -60°/-55° in steps of 20°. Finally, the step was set to 1° and tomogram file with all its metadata was saved as *.mrc*.

2.4.11 Tomogram generation

Tomograms were reconstructed using etomo (Table 2.1), an imod package using a Cygwin environment for Windows. The file type was changed to *.st* in order for etomo to read it. First, the file header was read, whereby the pixel size (1.188 nm) and fiducial marker size were obtained. After specifying the image rotation per step as 2.2, the x-rays were eliminated since they produce very bright or dark pixels when hitting the microscope's CCD camera and may produce artifacts during tomogram reconstruction. Then, the coarse alignment started by calculating the cross-correlation of the individual images of the stack. Subsequently, the gold fiducial markers were identified, which are used as seed to track them over the tomogram sections. After ensuring that each fiducial marker was tracked over the stack of images, the fine alignment was performed, which ultimately reduced the error in gold particle alignment between consecutive images. Then, delimiting the volume of the tomogram was performed by increasing the tomogram thickness to 1,000 virtual sections and marking the actual tomogram volume in its bottom, middle and top regions. Next, the final alignment was performed. Finally, the tomogram was back projected, trimmed to the ROI volume and the *y* and *z* axis were swapped so that movement between slices in the final file was performed in depth direction.

2.4.12 Data visualisation and analysis

The FIJI software (Table 2.1) was used to visualise confocal images. Data analysis was performed using a custom made IMARIS plug-in for counting ribbons in the ROI (Chakrabarti et al., 2022) (Table 2.1), by using the Spots function. Then, the average number of ribbons per IHC was calculated by dividing the total number of ribbons by the number of IHCs in the ROI.

HPManalyse (Table 2.1), which is a MATLAB-based program, was used for determining the actual light stimulation per sample during opto-HPF (Chakrabarti et al., 2022). *HPManalyse* required the excel data table from the *HPMacquire* programme that contains the information of the time (ms), internal pressure and internal temperature, and the HPM file of the corresponding shot that contained the information of all the sensors. The information was displayed in a graph where the opening of the pneumatic valve, as well as the beginning of the internal pressure and internal thermal sensor curves were identified. Consequently, the position of the cursor over the pneumatic sensor curve provides the temporal information from sample shot until the lowering of the pneumatic valve when the liquid nitrogen pressure reaches 7 bar. In addition, the $T_{\text{sample at 0}}$ (see section 2.4.4) is also provided. As a result, the actual light stimulation interval could be calculated (Chakrabarti et al., 2022) (Table 2.4.4, Fig. 2.4.12.1).

Condition	**Time of stimulation (ms)**
Inhibition	440.15
Inhibition	440.55
Isradipine	442.15
Isradipine	440.65
Isradipine	440.3
Stimulation	450.25
Stimulation	443.65
Stimulation	440.2
Total (average and standard deviation)	442.49 ± 3.32

Table 2.4.12: Optogenetical stimulation intervals.

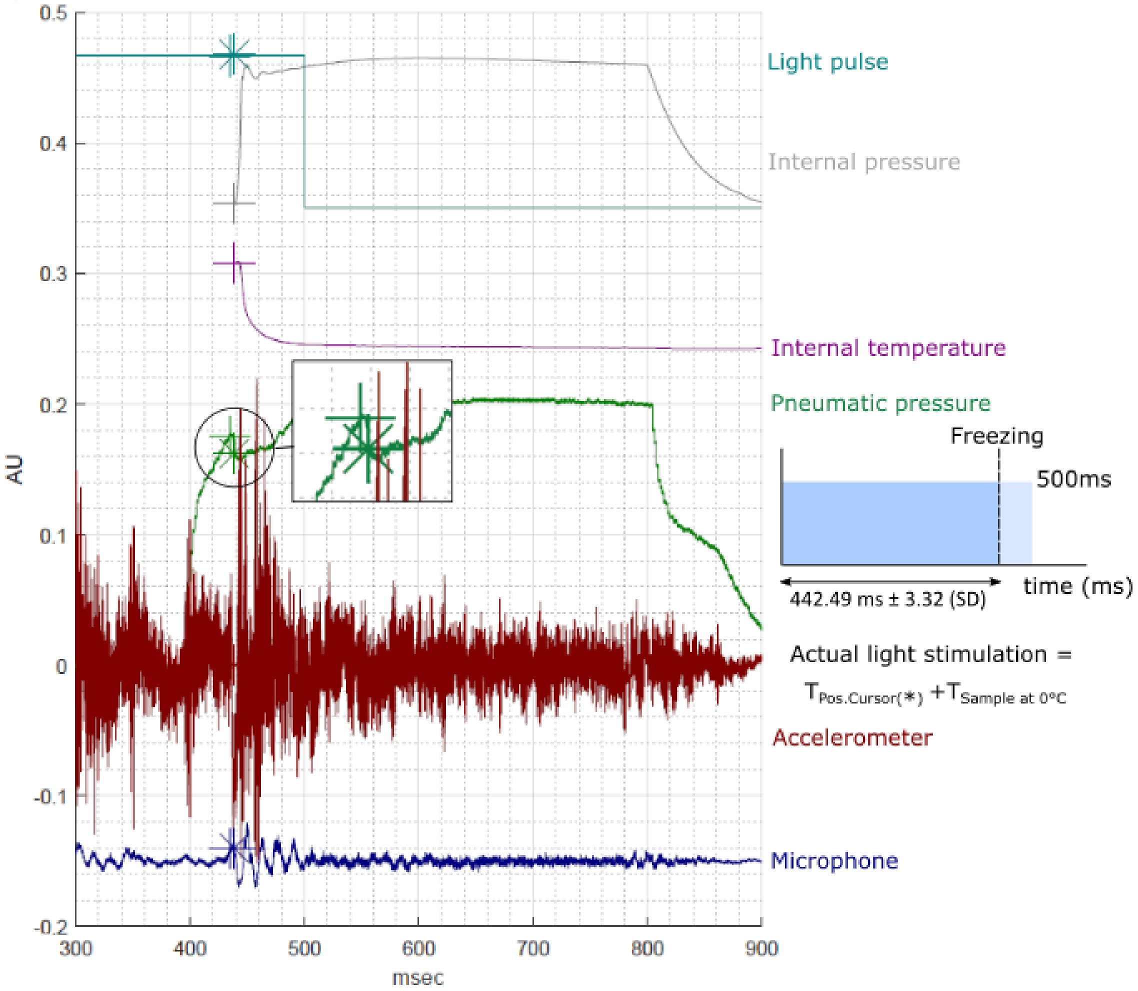

Fig. 2.4.12.1: Calculation of the current light stimulation upon 500 ms stimulation. Example of output graph from *HPManalyse* where sensor information is found. The time until the lowering of the pneumatic pressure valve was determined by positioning the asterisk cursor (green asterisk) at the point of pressure drop, as well as the cross-like cursor at the beginning of the internal pressure and temperature curves. Calculating the actual light stimulation per shot is the sum of the position of the cursor (Pos.Cursor) and the time for the sample to reach 0°C ($T_{sample\ at\ 0}$). A 500 ms light stimulation yields an average actual light stimulation of 442.49 ms ± 3.32 (SD).

Imod (3dmod software, Table 2.1) was used to segment semi-automatically tomograms(Kremer et al., 1996), whose pixel size is 1.188 nm. The AZ membrane was defined in relation to a clear synaptic cleft and postsynaptic density. Segmentation of the AZ was performed by assigning a closed object and drawing manually its contour over 10 consecutive virtual sections every 10-15 virtual sections. The synaptic ribbon was categorised as a closed object and its segmentation was done over 5 consecutive virtual sections every 7-10 virtual sections. Finally, the PD was also defined as a closed object and its segmentation was done over 5 consecutive virtual sections every 5 virtual sections. Then, the full contour of the AZ membrane, ribbon and PD was interpolated using the interpolator tool in the smooth mode. The contour of each object was corrected to ensure accuracy with the tomogram data.

SV were classified into different morphological pools according to their position respect to the ribbon surface or the AZ membrane and PD surface as well as their tethering state. Each SV pool was defined as a spherical scattered object whereby the object may contain multiple contours and each contour corresponded to a single point. The categorisation of each SV into a specific pool was determined by the distance to a prominent structure, which can be either the ribbon surface or the PD surface and the AZ membrane (Chakrabarti et al., 2018; Jean et al., 2018). Ribbon associated (RA) SVs included vesicles located in the first row from the ribbon surface in ≤ 80 nm (Chakrabarti et al., 2022, 2018; Jean et al., 2018). In *RBE*$^{KO/KO}$ ribbon synapses, where there is no synaptic ribbon, PD-associated (PDA) SVs included vesicles in the first row from the PD surface in a distance of ≤ 80 nm (Jean et al., 2018). An additional SV pool, which was called peripherally RA/PDA (periRA/PDA) SVs, was identified by including the SVs that were not annotated to the first row but found in a distance from the ribbon's surface up to 160 nm. The quantification of this pool aimed to estimate the number of SVs close to RA-SVs, which might play a role in replenishing the RA pool (Fig. 2.4.12.2a).

Membrane proximal (MP) SVs were defined as vesicles located in direct line to the AZ membrane in ≤ 100 nm from the PD and ≤ 50 nm from the AZ membrane from its (Chakrabarti et al., 2018). Morphological subpool classification of MP-SVs was performed according to the tether presence/absence and distance to the AZ membrane. These include non-tethered, single tethered, multiple tethered and docked SVs (Chakrabarti et al., 2018) (Fig. 2.4.12.2b).

Finally, endocytic structures were classified as ELVs, CCV and, exclusively in the Otof datasets, tubular endocytic structures (TESs). From these structures, all round structures were defined as scattered objects, while the non-round structures were segmented closed objects and interpolated afterwards. Endocytic structures were included in ≤ 400 nm from the ribbon surface (Kroll et al., 2019) (Fig. 2.4.12.2a). Non round endocytic structures were included in the analysis if a major portion of its volume could be observed in the tomograms.

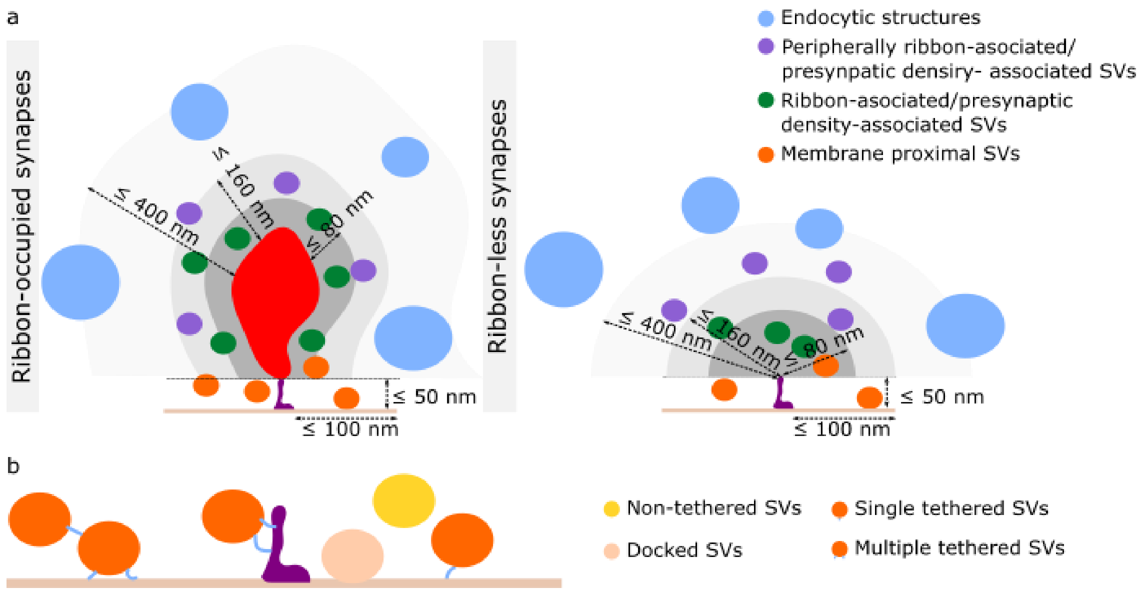

Fig. 2.4.12.2: Ribbon synapse analysis criteria. a, SV pools in ribbon-occupied and ribbon-less synapses. Membrane proximal (MP) SVs are found ≤ 50 nm from the AZ membrane and ≤ 100 nm from the PD (magenta) surface. Ribbon-associated/ presynaptic-density-associated (RA/PDA) SVs are found beyond 50 nm from the AZ membrane, in direct line with the ribbon/PD surface in ≤ 80 nm distance. Peripherally RA/PDA SVs refer to SVs behind RA/PDA-SVs and/or in ≤ 160 nm from the ribbon/PD surface. Lastly, endocytic structures are quantified ≤ 400 nm from the ribbon/PD surface. **b**, MP-SV subpool classification according to the presence of tethers. MP-SVs can be found non-tethered, establishing single or multiple tethers and docked SVs.

An additional analysis of ribbon synapses in *RBE*$^{wt/wt}$ and *RBE*$^{KO/KO}$ was performed using similar criteria as for conventional synapses in order to observe SV changes in relation to the distance from the AZ membrane. SVs were quantified in a distance of ≤ 100 nm from the PD, and ≤ 400 nm vertically from the plasma membrane, which is divided into 40 nm bins. Further, 5 nm subdivision of the first 40 nm bin was performed, in which docked SVs were also classified ≤ 2 nm from the AZ membrane (Fig. 2.4.12.3).

Finally, radii of scattered objects, such as SVs, round ELVs and CCVs, were obtained in Cygwin using the option -p and -f of the imod package. In contrast, for closed objects like non-round ELVs, TESs and budding CCVs, the volume was obtained in the *object information* option in imod and used to infer an approximate radius (“effective radius”). Notably for SVs, the SV diameter was calculated from the radius to make it comparable to other studies. Importantly, the effective radius of any closed object that is used for statistical analysis and graphical representation may not correspond to the maximal diameter of such structure in the stack of virtual sections.

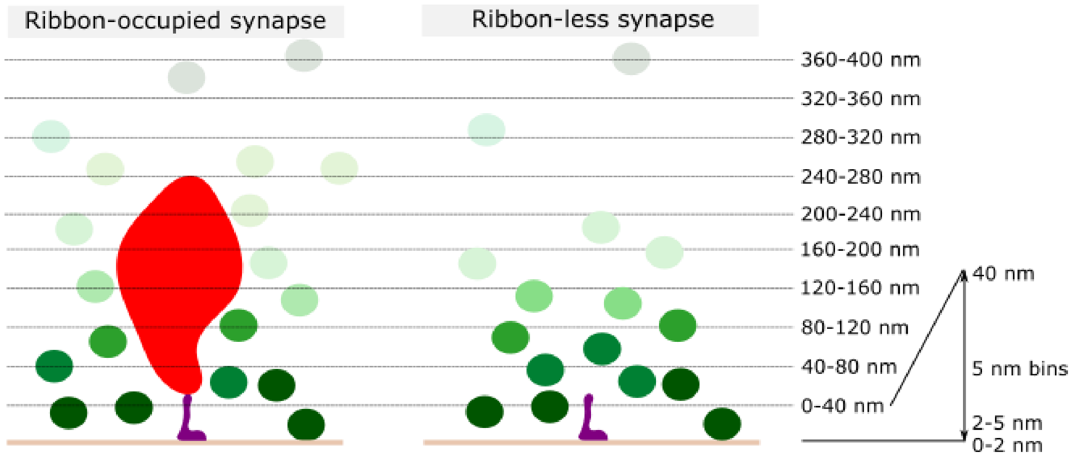

Fig. 2.4.12.3: Conventional synapse analysis criteria. 40 nm bins are drawn from the AZ membrane up to 400 nm within 100 nm from the PD surface. Further subdivision in 5nm bins of 0-40 nm bin is performed, where docked SVs are found ≤ 2 nm from the plasma membrane.

2.4.13 Statistical analysis

The number of animals used (N) and the number of replicates (n) from each dataset is indicated in the figure legend, as well as in Table 2.3.1. Data were collected in Excel and pre-processed using a Python script (Table 2.1) for automatically counting and calculating the SV fractions.

Statistical analysis and graph production was performed in GraphPad Prism (Table 2.1). First, shape of the distribution was assessed with Saphiro-Wilk test. If normality was verified, presence of outliers was checked by ROUT method, whereby data are fit in a non-linear regression and analysed to identified outliers. No outliers were removed from any samples. In addition, the frequency distribution of the SV and endocytic structure radii was done setting a 10 nm bin for SVs and round endocytic structures, while a 20 nm bin for non-round endocytic structures.

Datasets with normal distribution were analysed with either a one-way ANOVA followed by Šídák's multiple comparison post-test, a two-way ANOVA with Tukey multiple comparisons post-test, or a Brown-Forsythe and Welch ANOVA followed by Dunnett's post-test. Datasets with not normal distribution were analysed via Kruskal-Wallis followed by Dunn's multiple comparisons test. Multiple comparison tests were set to compare the means of the essential, minimum factors to avoid falsely accept or reject the null hypothesis. Data are presented in this thesis as mean ± standard error of the mean (S.E.M).

3 RESULTS

This thesis focuses on the analysis the architectural changes that ribbon synapses undergo upon prolonged stimulation. This thesis presents three result sections: the first and second parts of this thesis are centred on the impact of the lack of two central IHC ribbon AZ proteins, Otof and RBE on morphological SV pools in an activity context. Though disruption of Otof results in almost abolished exocytosis, the ultrastructural consequences for morphological exo- and endocytosis correlates upon stimulation compared to inhibition and control conditions are unknown. The last part of this thesis focuses on the study of the effects of ChR2 expression in IHCs. I wanted to clarify the effect of its long-term expression on IHCs and use it to study millisecond precise, which might contribute to clarify the modes of SV release and events of the SV cycle upon sustained, but short stimulation. Finally, these results constitute a first approach into the use of ChR2 for a potential contribution to study mutations, such as $RBE^{KO/KO}$ or $Otof^{KO/KO}$, upon precise, milliseconds stimulation.

In this thesis I employed high-pressure freezing coupled with electron tomography to study ultrastructural changes in the ribbon synapse in different activity paradigms. The quality of the tomograms and the number of ribbons per active zone was assessed prior to any analysis. The analysed structures consist of morphometric parameters of the whole SV cycle: endocytic structures, peripherally ribbon-associated (periRA) SVs, ribbon-associated (RA) SVs and membrane-proximal (MP) SVs, including the different tethered-based morphological subpools (see section 2.4.12). The data in this thesis appear as a quantification, in which the graph represent the average number of certain structures (e.g., number of MP-SVs); or as a fraction, in which case the graph represents the relative abundance of certain structure (e.g., number of tethered MP-SVs over the total number of MP-SVs). The fraction was first calculated per tomogram using the total numbers obtained during SV pool and subpool quantification per sample; then the average per condition was obtained.

In section 3.1, I present $Otof^{KO/KO}$, $Otof^{pga/pga}$ data, and their comparison to achieve a better understanding of the role of Otof in the SV cycle. These samples were incubated for 15 minutes in either an inhibitory (EGTA, 5 mM), resting (KCl, 5 mM) or stimulatory (KCl, 50 mM) solutions (see section 2.2) until high-pressure frozen. 2D electron microscopy of semi-thin section was used to initially check the morphology of the IHCs, while electron tomography allowed to obtain detailed information of the ribbon synapse architecture in the different activity states of $Otof^{KO/KO}$ ribbon synapses (section 3.1.1). First, I analysed the fraction of the different vesicle pools and endocytic structures found in any conditon to elucidate the ribbon synapse structural organization at different activity states.

Then, I focused on analysing the different SV subpools of the MP pool according to the presence of tethers, SV location, and their distances to the AZ membrane and PD surface; finally, I analysed in detail the different morphological types and sizes of endocytic structures found in the ribbon synapse proximity.

I partially reanalysed already existing *Otof*$^{pga/pga}$ tomograms that were generated and used in a previous study by Chakrabarti et al. (2018). This study focused on examining the SV subpool organisation for exocytosis, not on morphological correlates of endocytosis (Chakrabarti et al., 2018). Therefore, partial analysis of *Otof*$^{pga/pga}$ ribbon synapses was performed to obtain data of periRA-SVs and endocytic structures to help understand the extent of the effect of mutation in the C_2F domain in endocytosis (section 3.1.2). First, I quantified the fractions of the analysed structures per tomogram. Revision of published raw (Chakrabarti et al., 2018) was conducted to accurately obtain and plot each fraction of endocytic structures and each SV pool (see section 2.4.13). Then, the endocytic structures numbers, types were analysed.

Finally, a comparison between *Otof*$^{KO/KO}$ and *Otof*$^{pga/pga}$ data was performed (section 3.1.3) in which I compared the fractions of all analysed structures combining novel data from both *Otof* mutants and raw data used in publication for *Otof*$^{pga/pga}$ (Chakrabarti et al., 2018). I focused on the MP pool by studying the number of non-docked and docked SVs to elucidate the impact of each mutation to exocytosis (Chakrabarti et al., 2018). Finally, I compared the number and types of endocytic structures to investigate if the different mutations interfere in different phases of the SV cycle.

In section 3.2, I present electron tomography data from *RBE*$^{wt/wt}$ and *RBE*$^{KO/KO}$ ribbon synapse architecture upon 15 min chemical stimulation following the analysis parameters for ribbon synapses (Chakrabarti et al., 2022, 2018; Jean et al., 2018; Michanski et al., 2019; Strenzke et al., 2016) (also see section 2.4.12) and conventional synapses, as done for the endbulb of Held (Hintze et al., 2021) (also see section 2.4.12), since ribbon-less synapses resemble to a certain extent conventional synapses. When following the analysis criteria for ribbon synapses (section 3.2.1), I calculated the fractions of all analysed structures. Next, I focused specifically on the RA/PDA and MP pool and its SVs according to their tethered state with the aim of understanding how under exhaustive stimulation conditions exocytosis is maintained. I finally analysed the abundance of different endocytic structures. In contrast, when following similar analysis criteria as for conventional synapses (section 3.2.2), SVs were categorized into BINs from which their relative abundance was plotted. Special focus was made in the analysis of 0-40 nm SVs from the AZ membrane, in which docked SVs are included.

In section 3.3, I first present Ai32KI *cre*$^+$ data as to measure the impact of ChR2 in synapse progression of aging organs of Corti using immunohistochemistry. Then, I present data on Ai32VC *cre*$^+$ mice under optogenetic stimulation to investigate ultrastructural changes upon sustained stimulation. I used three different conditions: the organs of Corti were mounted in either inhibitory, isradipine or stimulatory extracellular solutions, and precisely stimulated with blue light before high-pressure freezing (see section 2.4.4).

3.1 COMPARATIVE STUDY OF ACTIVITY-BASED CHANGES IN SYNAPTIC VESICLE ORGANISATION IN RIBBON SYNAPSES FROM TWO OTOFERLIN MUTANTS

3.1.1 Ultrastructural effects of Otoferlin disruption at inner hair cell ribbon synapses upon prolonged activity changes

Lack of Otof in cochlear ribbon synapses results in severe hearing impairment and almost nulled exocytosis (Roux et al., 2006), which seems to correlate with the location of Otof at SVs and components of the endosomal compartment (Dulon et al., 2009; Roux et al., 2006; Strenzke et al., 2016). However, the effects of lack of Otof in ribbon synapse ultrastructure upon prolonged, strong stimulation are poorly understood. First, I determined the orientation of the ribbon within a given tomogram, since it contributes to the variability of my data along with the proportion of the ribbon included in the semi-thin section. The direction of ribbon position, which usually shows an elongated shape, during acquisition of the tomograms, although not controllable, may have effects on the quantification of structures as it determines the visible surface of the synaptic ribbon. Hence, the direction for synaptic ribbon appearance can be from a cross-section, longitudinally or in between. All conditions show similar acquisition perspectives (Table 5.1.1).

Values of quantifications and fractions presented in this section can be found in section 5.1.

3.1.1.1 Anatomy of Otof$^{KO/KO}$ inner hair cells

IHCs were screened via transmission electron microscopy to identify ribbon synapses and, during this process, clusters of vesicles of various sizes were identified in some of the mutant IHCs (Table 3.1.1.1). These vesicle cluster were mostly identified in the cytoplasm, and few of them in the ribbon synapse proximity (Fig. 3.1.1.1).

Experimental condition		No. tomograms with SV clusters	No. tomograms without SV clusters
Otof$^{wt/wt}$ inhibition	20 tomograms	0	20
Otof$^{wt/wt}$ resting	20 tomograms	0	20
Otof$^{wt/wt}$ stimulation	18 tomograms	0	18
Otof$^{KO/KO}$ inhibition	18 tomograms	2 (< 400 nm and > 400 nm)	16
Otof$^{KO/KO}$ resting	20 tomograms	1 (> 400 nm)	19
Otof$^{KO/KO}$ stimulation	17 tomograms	0	17

Table 3.1.1.1: Number of tomograms presenting vesicle clusters in the proximity of the ribbon synapse.

The vast majority of analysed tomograms did not present vesicle clusters, while only in *Otof*$^{KO/KO}$ under inhibition and rest showed vesicle clusters below and beyond 400 nm from the synaptic ribbon surface.

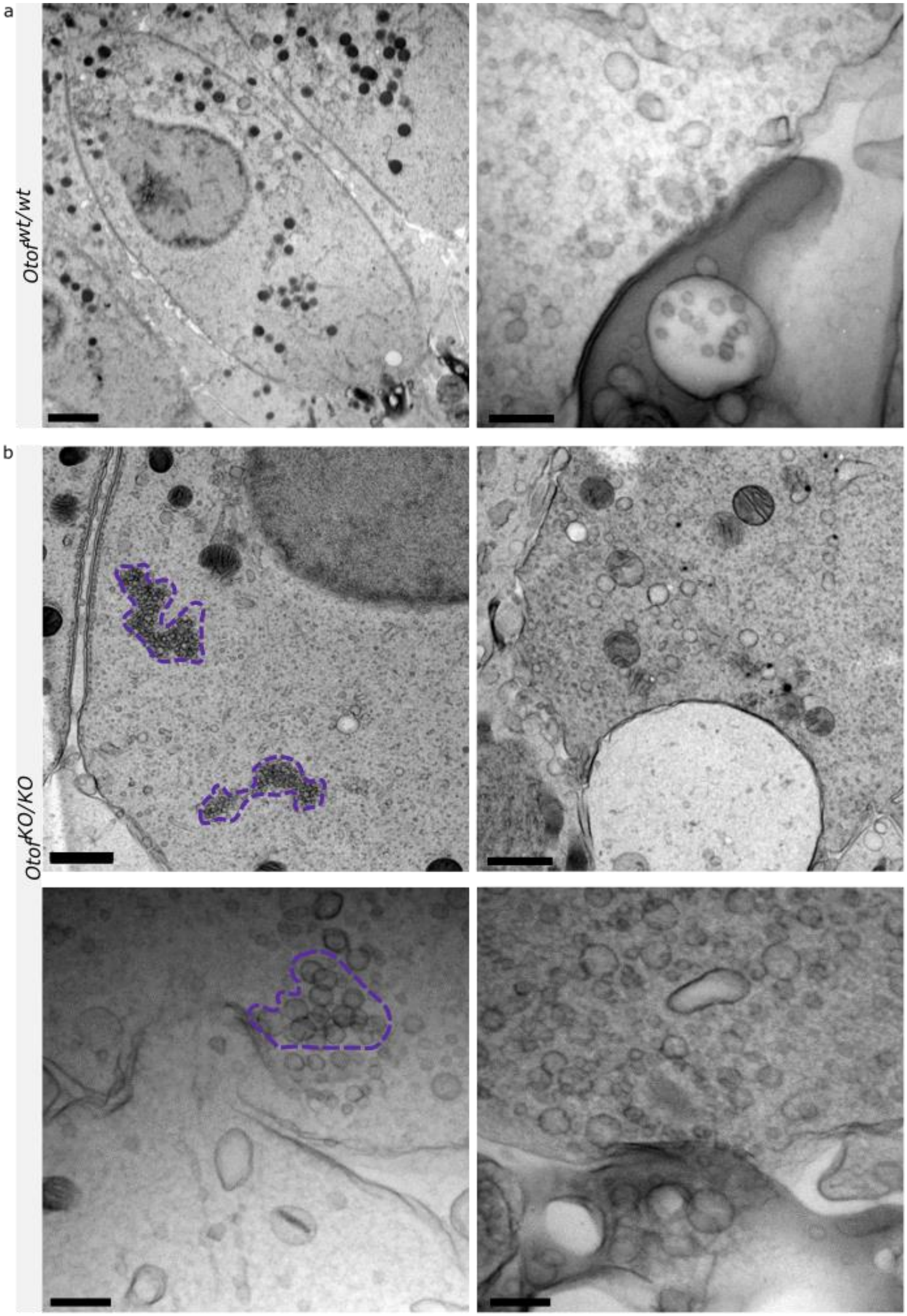
a
Otof^wt/wt
b
Otof^KO/KO

Fig. 3.1.1.1: Inner hair cell anatomy. Representative semi-thin sections for morphology screening of *Otof*$^{wt/wt}$ and *Otof*$^{KO/KO}$ from (**a**) the basolateral region and ribbon synapse of *Otof*$^{wt/wt}$, where no SV clusters are observed. Magnification, (left) x2500, (right) x12000; scale bar, (left) 2 µm, (right) 200 nm. **b**, (upper row) Micrographs of semi-thin section from *Otof*$^{KO/KO}$ IHC basolateral region. Some cells presented in this region vesicle clusters (outlined). Magnification, x2500; scale bar, 1 µm. (Lower row). Representative micrographs of *Otof*$^{KO/KO}$ ribbon synapses in which vesicles of different sizes are found loose around the ribbon or forming clusters (outlined). Magnification, x12000; scale bar, 200 nm. (Figure above)

3.1.1.2 Structure organisation in Otof$^{KO/KO}$ *and Otof*$^{wt/wt}$ *ribbon synapses*

Otof has been hypothesised to be a Ca^{2+} sensor (Michalski et al., 2017) that is involved in tethering SVs to the AZ membrane (Vogl et al., 2015), serving as a Ca$_V$1.3 channel organiser (Heidrych et al., 2009) and coupling exocytosis and endocytosis (Pangšrič et al., 2010). Immunogold labelling point Otof to be found in the AZ membrane, SV membrane and in the endosomal compartment (Roux et al., 2006; Strenzke et al., 2016). Otof ubiquitous localisation in IHCs and its role in exo-/endocytosis, hint towards the disruption in the SV organisation in *Otof*$^{KO/KO}$ synapses upon prolonged activity. First, I confirmed *de visu* that the lack of Otof did not affect the morphology of the ribbon synapses (Fig. 3.1.1.2.1), as previously reported (Dulon et al., 2009; Roux et al., 2006; Vogl et al., 2015).

An additional anatomical observation of the SV pools is the appearance of the different filaments and tethers connecting the RA and MP-SVs, which is linked to the recruitment of SVs upon activity (Chakrabarti et al., 2018). On the one hand, filaments connecting RA-SVs look thin; on the other hand, thicker tethers are found connecting MP-SVs, especially when tethering SVs to the AZ membrane. Notably, the subset of tethers connecting MP-SVs to the PD appear to have a triangular shape (Fig.3.1.1.2.2).

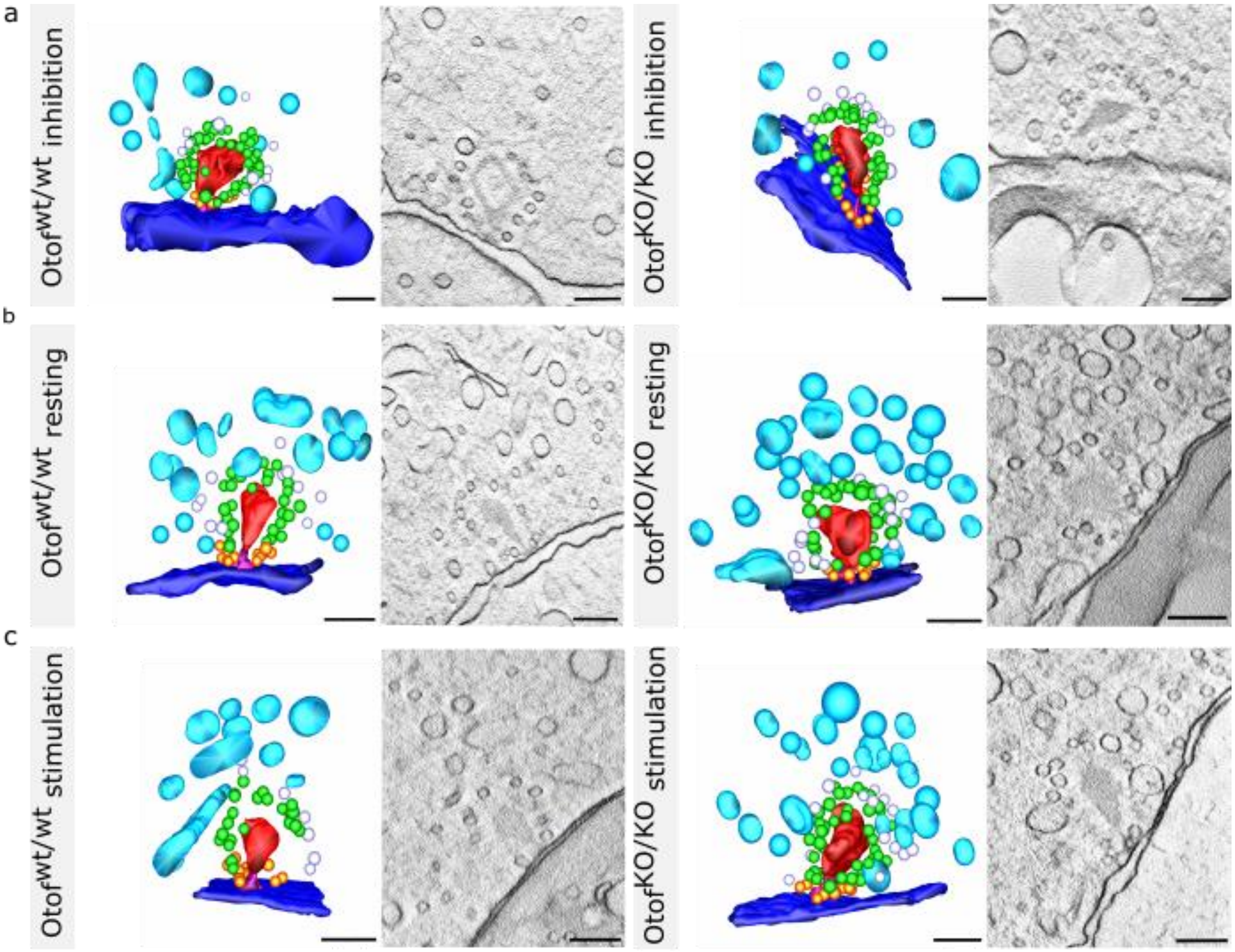

Fig. 3.1.1.2.1: Quantification of the structures found at ribbon synapses after 15-minute stimulation. a-c, Representative models and virtual section of *Otof*$^{wt/wt}$ and *Otof*$^{KO/KO}$ upon inhibitory, resting, and stimulatory conditions. Endocytic structures are presented in blue; peripherally RA (periRA) SVs are shown in white; green SVs are RA pool; and MP-SVs are shown in orange. This colour-code will be maintained for any future depictions of each pool. Magnification, x12000; scale bar, 200 nm.

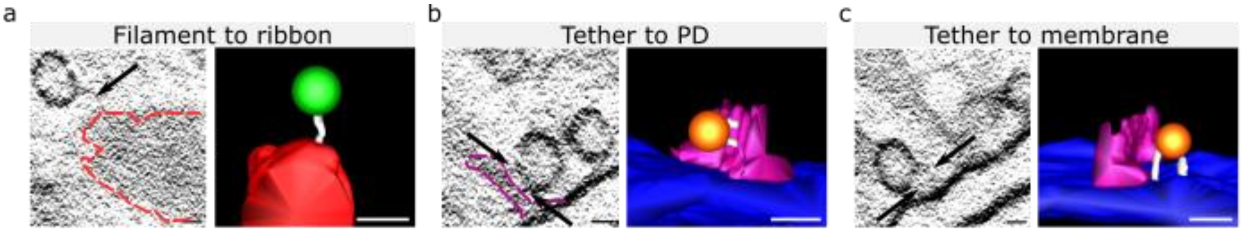

Fig. 3.1.1.2.2: Tether appearance for RA and MP-SVs in wild-type ribbon synapses. a, Thin filaments connect RA-SVs (green), while MP-SVs (orange) establish thicker tethers with the (**b**) PD and the (**c**) AZ membrane. Tethers with the PD appear to have a triangular shape compared to the tethers linking SVs and the AZ membrane. Scale bar, 20 nm.

Activity-dependent changes were studied by quantifying the fractions of SVs per pool and endocytic structures, which serves to track changes upon stimulation compared to inhibition and rest in wild-type and mutants. I found that in *Otof*$^{KO/KO}$ resting condition the fraction of endocytic structures was statistically significantly larger compared to inhibitory and stimulatory conditions in the *Otof*$^{KO/KO}$, as well as with *Otof*$^{wt/wt}$ upon rest (*Otof*$^{wt/wt}$ resting, 0.17 ± 0.02; *Otof*$^{KO/KO}$ inhibition, 0.14 ± 0.02; *Otof*$^{KO/KO}$ resting, 0.28 ± 0.02; *Otof*$^{KO/KO}$ stimulation, 0.16 ± 0.03. Kruskall-Wallis followed by Dunn's post-test, ***, $p < 0.001$; **, $p < 0.01$). Conversely, the fraction of RA-SVs was significantly smaller in *Otof*$^{KO/KO}$ resting compared to the inhibitory conditions (*Otof*$^{KO/KO}$ inhibition, 0.52 ± 0.02; *Otof*$^{KO/KO}$ resting, 0.43 ± 0.02. One-way ANOVA followed by Šidák's post-test, **, $p < 0.01$) (Fig. 3.1.1.2.3, Table 5.1.2).

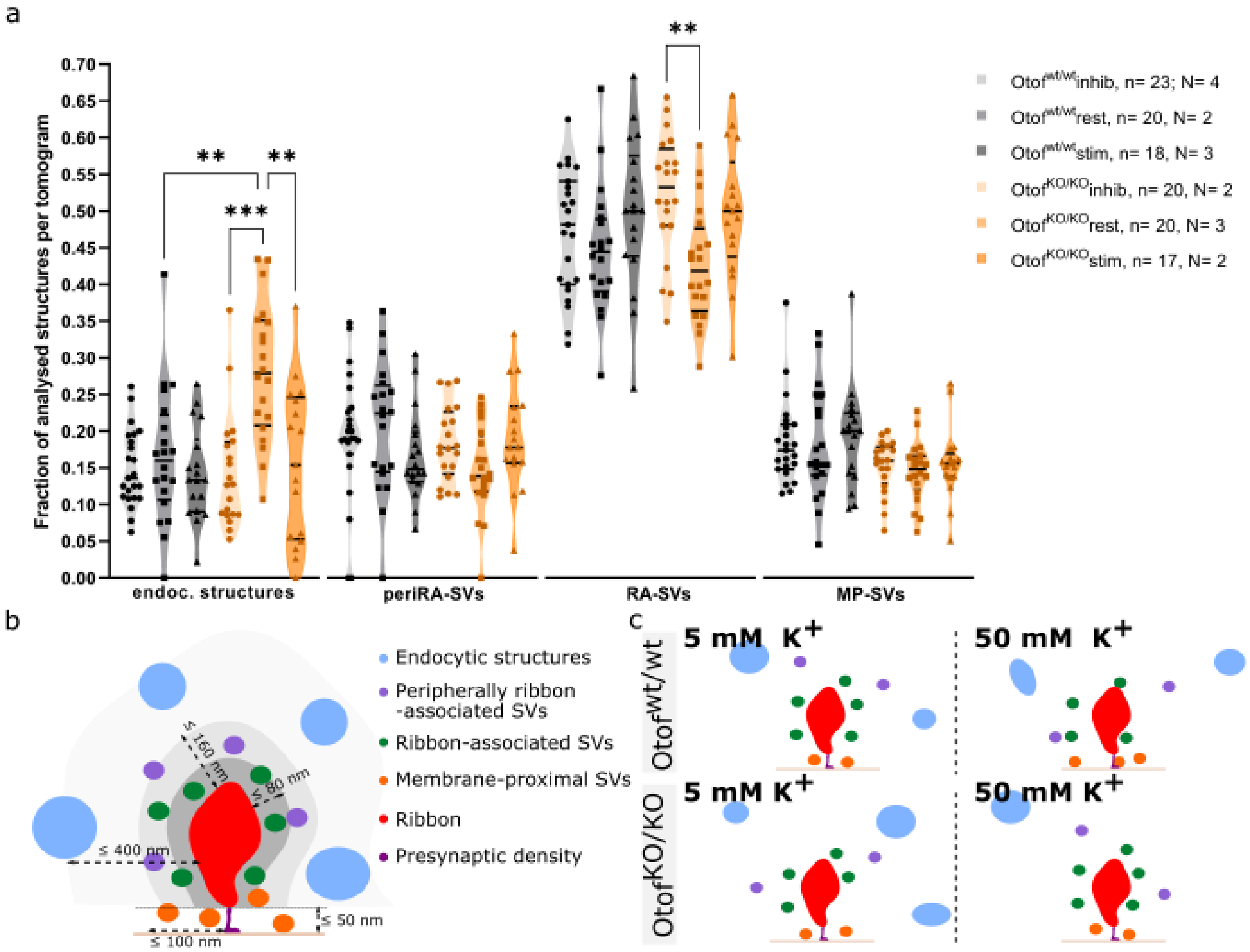

Fig. 3.1.1.2.3: Quantification of the structures found at ribbon synapses after 15-minute stimulation. a, Average fraction of analysed structures per tomogram. A larger fraction of endocytic structures was found in *Otof*$^{KO/KO}$ in rest compared to any other *Otof*$^{KO/KO}$ activity state, as well as to *Otof*$^{wt/wt}$ in rest. Conversely, the fraction of RA-SVs was reduced in *Otof*$^{KO/KO}$ upon rest compared to the other *Otof*$^{KO/KO}$ activity states. Data are presented as mean ± S.E.M. Kruskal-Wallis followed by Dunn's post-test and one-way ANOVA followed by Šidák's post-test, **, $p < 0.01$; ***, $p < 0.001$. Values: Table 5.1.2. **b**, Diagram of the criteria to classify SVs and endocytic structures at the ribbon synapse: membrane-proximal (MP, orange) SVs include SVs in the first row from the AZ membrane in a ≤ 50 nm from the membrane and ≤ 100 from the PD surface; ribbon-associated (RA, green) SVs contain SVs in direct line with the surface of the ribbon in a ≤ 80 nm distance; peripherally RA (periRA, lillac) SVs are SVs beyond the first row of RA-SVs within ≤ 160 nm from the ribbon surface; and endocytic structures (blue) are quantified in a distance of ≤ 400 nm from the ribbon surface. **c**, Schematic summary of the effects of resting (5 mM K^+) and stimulated conditions (50 mM K^+). (Figure above)

3.1.1.3 Ribbon-associated and membrane-proximal pool characteristics

Classically, the sizes of the RA and MP morphological SV pools have been quantified to determine the availability of SVs for release and the dynamism of these pools (Chakrabarti et al., 2022, 2018; Lenzi et al., 2002). The RA pool corresponds, by definition, to those SVs in the first row around the ribbon up to 80 nm away from the ribbon surface (see section 2.4.12), which are thought to replenish MP-SVs upon sustained stimulation (Chakrabarti et al., 2018). In contrast, the MP pool is defined as those SVs in first line and up to 50 nm from the AZ membrane and laterally up to 100 nm from the PD surface (see section 2.4.12). Please note that these definitions were established for IHC ribbon synapses preserved via high-pressure freezing in accordance with observed tether length at the membrane and distances of SV to the ribbon under these near to native conditions (Chakrabarti et al., 2018; Jung et al., 2015b). As previously described, I found a smaller RA-SV fraction in *Otof*$^{KO/KO}$ under resting compared to the inhibitory conditions. Therefore, I first analysed the average size of the RA pool in all conditions and genotypes to verify whether the decrease in the fraction of RA-SVs in resting *Otof*$^{KO/KO}$ was caused by a significant change in the number of RA-SVs. Similar numbers of RA-SVs were found in *Otof*$^{KO/KO}$ and *Otof*$^{wt/wt}$ regardless of the activity state. Next, and despite the lack of significant differences in the fraction of MP-SVs in *Otof*$^{KO/KO}$ and littermate controls, quantification of the MP pool size was done since Otof might affect the release performance of these SVs. The quantification of the MP pool showed no significant differences between mutant and control ribbon synapses in any of the activity states (Fig. 3.1.1.3.1; Table 5.3.3).

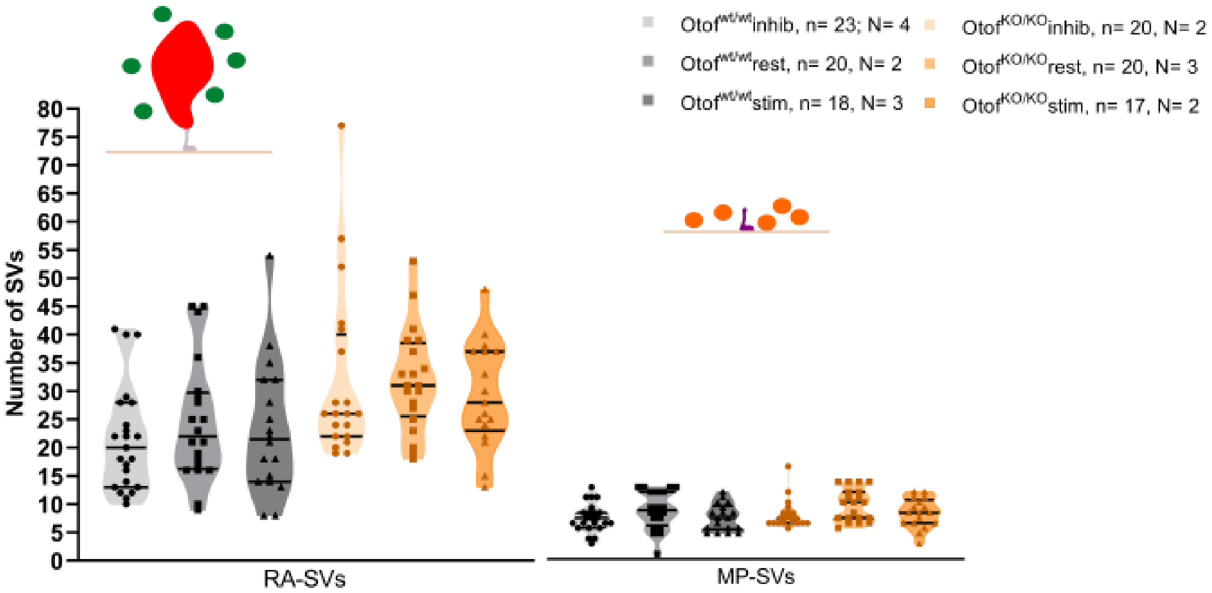

Fig. 3.1.1.3.1: Quantification of the size of RA and MP pools per ribbon synapse after 15-minute stimulation. Total count of RA-SVs (green) in up to 80 nm from the ribbon surface, and MP-SVs (orange) in up to 100 nm from the PD surface and up to 50 nm from the AZ membrane. Data are presented as mean ± S.E.M. Kruskal-Wallis followed by Dunn's multiple comparison post-test, ns, p > 0.05. Values: Table 5.1.3.

Furthermore, the sizes of SVs might be altered by activity and/or disruption of Otof, because in the latter case disruption in SV reformation might be reflected in an in an uneven size distribution of RA-SVs (Chakrabarti et al., 2018; Strenzke et al., 2016). In contrast, quantification of MP-SV sizes could indicate the manner in which SV fusion events might happen (i.e., universicular release or multivesicular fusion events) in ribbon synapses. The outer diameter of the SVs was obtained as described in the method section (see section 2.3.12). Significantly larger diameters were found in RA and MP-SVs in *Otof*$^{KO/KO}$ compared to *Otof*$^{wt/wt}$ (RA-SVs: *Otof*$^{wt/wt}$ inhibition, 46.51 ± 0.16; *Otof*$^{wt/wt}$ resting, 47.76 ± 0.16; *Otof*$^{wt/wt}$ stimulation, 47.14 ± 0.16; *Otof*$^{KO/KO}$ inhibition, 48.29 ± 0.17; *Otof*$^{KO/KO}$ resting, 48.78 ± 0.18; *Otof*$^{KO/KO}$ stimulation, 48.85 ± 0.19. Kruskall-Wallis followed by Dunn's post-test, **, $p < 0.01$; ****, $p < 0.0001$. MP-SVs: *Otof*$^{wt/wt}$ inhibition, 44.34 ± 0.24; *Otof*$^{wt/wt}$ resting, 45.82 ± 0.28; *Otof*$^{wt/wt}$ stimulation, 45.85 ± 0.21; *Otof*$^{KO/KO}$ inhibition, 45.18 ± 0.29 ; *Otof*$^{KO/KO}$ resting, 46.58 ± 0.29; *Otof*$^{KO/KO}$ stimulation, 47.47 ± 0.29 Kruskall-Wallis followed by Dunn's post-test, *, $p < 0.05$; **, $p < 0.01$; ***, $p < 0.001$; ****, $p < 0.0001$) (Fig. 3.1.1.3.2a; Table 5.1.4). However, the frequency distribution of RA and MP-Svs in 10 nm bins showed that the vast majority of RA and MP-SVs presented a radius of 40-50 nm, in which no statistically significant differences were found within each bin regardless the genotype and the activity state (Fig. 3.1.1.3.2b).

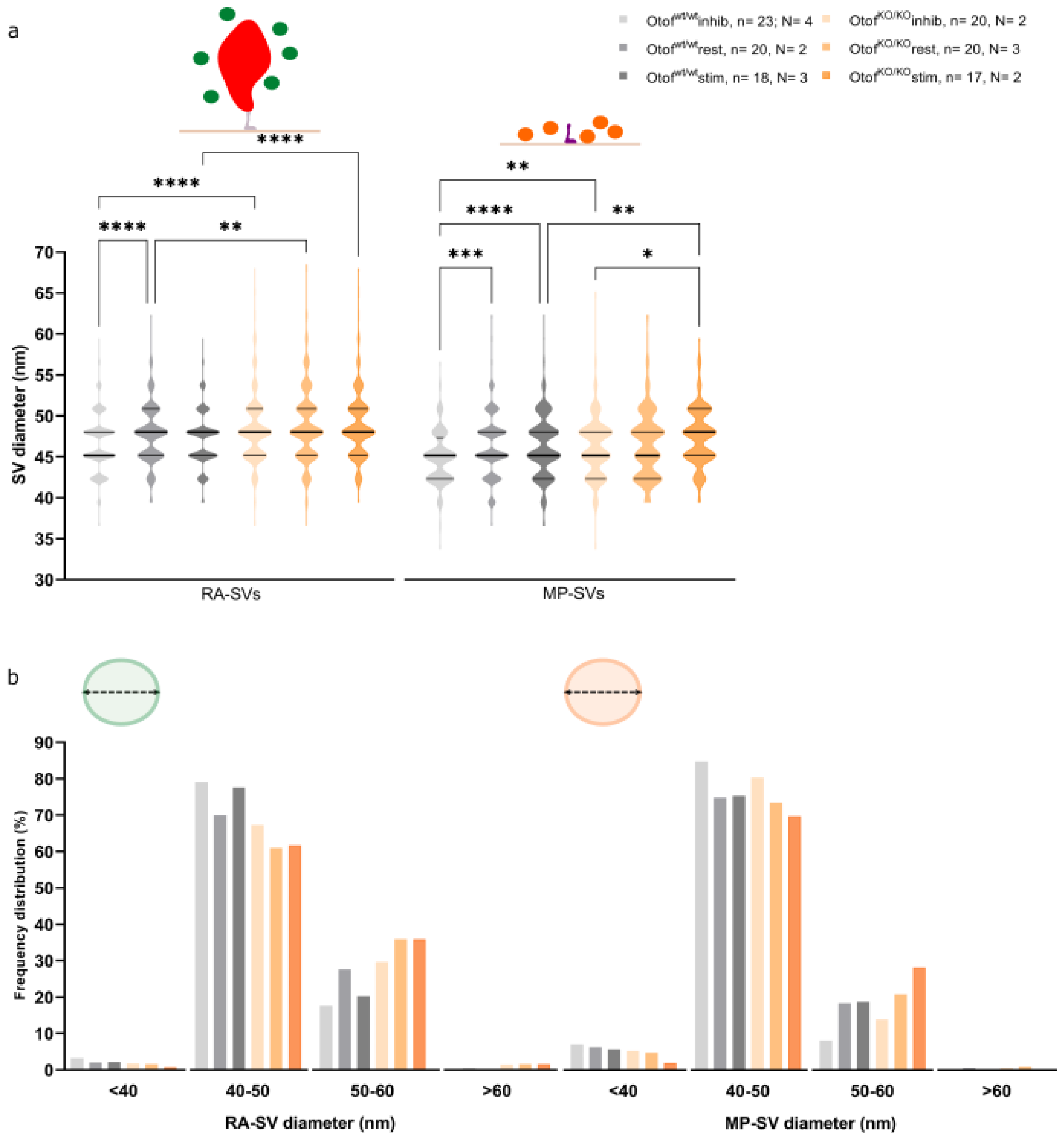

Fig. 3.1.1.3.2: Quantification of the diameters of RA and MP-SV per ribbon synapse after 15-minute stimulation. **a**, The diameter of RA and MP-SVs was significantly smaller in mutants compared to wild-type. Kruskal-Wallis followed by Dunn's post-test, *, p< 0.05; **, p< 0.01; ***, p< 0.001; ****, p< 0.0001. Values: Table 5.1.4. Data are presented as mean ± S.E.M. **b**, Frequency distribution of RA and MP-SV diameters per 10 nm bin. No statistically significant differences are observed between wild-type and mutant. Two-way ANOVA followed by Tukey's post-test, ns, p > 0.05.

The recruitment of SVs to support sustained release might also be translated into distances of SVs to the ribbon surface or AZ membrane. SVs that are closer to the ribbon/AZ membrane might also have shorter tethers (Chakrabarti et al., 2018). At the ribbon, 15 min stimulation was shown to result in an overall shorter tether length. Therefore, I determined the distances of the SVs to the AZ membrane as well as to the ribbon. In addition, the distance of MP-SVs to the PD surface was also measured, which might be an indicator for a close SV coupling to Ca^{2+} channels (Fig, 3.1.1.3.3a).

The distance of RA-SVs to the ribbon surface showed a significantly decrease in *Otof*$^{KO/KO}$ upon inhibition compared to *Otof*$^{KO/KO}$ in rest (*Otof*$^{KO/KO}$ inhibition, 44.22 nm ± 0.72; *Otof*$^{KO/KO}$ resting, 47.27 nm ± 0.71. Kruskal-Wallis followed by Dunn's post-test, *, $p < 0.05$) (Fig, 3.1.1.3.3b; Table 5.1.5).

Upon stimulation, MP-SVs in *Otof*$^{wt/wt}$ approached the AZ membrane and remained distant to the PD, as already reported in the literature (Chakrabarti et al., 2018). In contrast, stimulation did not lead to the approach of MP-SVs to the AZ membrane in *Otof*$^{KO/KO}$ but revealed a significantly closer distance to the PD in *Otof*$^{KO/KO}$ upon stimulation compared to rest (Distance to AZ membrane: *Otof*$^{wt/wt}$ inhibition, 22.78 ± 1.096; *Otof*$^{wt/wt}$ resting, 22.20 ± 1.04; *Otof*$^{wt/wt}$ stimulation, 15.49 ± 1.07; *Otof*$^{KO/KO}$ inhibition, 27.04 ± 1.00; *Otof*$^{KO/KO}$ resting, 23.13 ± 1.05; *Otof*$^{KO/KO}$ stimulation, 23.32 ± 1.14. Kruskal-Wallis followed by Dunn's post-test, *, $p < 0.05$; ***, $p < 0.001$; ****, $p < 0.0001$. Distance to PD surface: *Otof*$^{KO/KO}$ inhibition, 30.03 nm ± 1.64; *Otof*$^{KO/KO}$ resting, 39.75 nm ± 1.86; *Otof*$^{KO/KO}$ stimulation, 29.12 nm ± 2.22. Kruskal-Wallis followed by Dunn's post-test, **, $p < 0.01$; ****, $p < 0.0001$) (Fig, 3.1.1.3.3 c, d; Table 5.1.5).

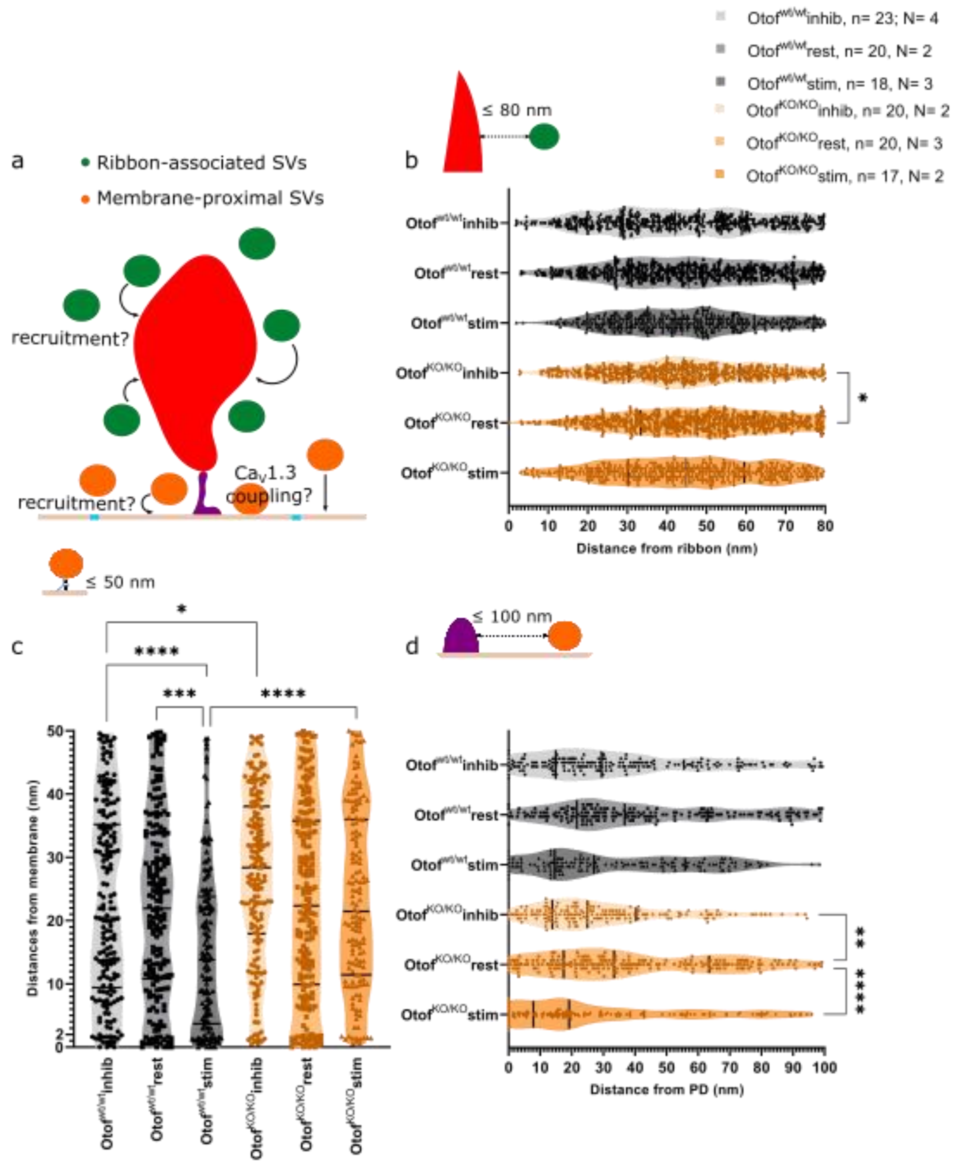

Fig. 3.1.1.3.3: Quantification of the distance of RA and MP-SVs per ribbon after 15-minute stimulation. a, Quantification of the distance to the ribbon and AZ membrane might serve as an indicator of the recruitment of SVs for exocytosis. The distance of MP-SVs to the PD may be used as an indicator for the coupling of SVs to Ca^{2+} channels. **b**, The distance of RA-SVs to the ribbon was measured up to 80 nm from the ribbon surface in the virtual section with the maximal SV diameter. Statistically significant differences are found between *Otof*$^{KO/KO}$ upon inhibition and resting conditions. Kruskal-Wallis followed by Dunn's post-test, *, $p < 0.05$. Values: Table 5.1.5. **c-d**, The distance to the AZ membrane was measured in up to 50 nm range, while the distance from the PD was measured up to 100 nm in the virtual section with the maximal diameter of a SV. The distance to the plasma membrane of MP-SVs decreases upon stimulation in *Otof*$^{wt/wt}$, while the distance to the PD remains comparable in all activity states. In contrast, the distance to the AZ membrane of MP-SVs in *Otof*$^{KO/KO}$ is significantly larger than in wild-type. Kruskal-Wallis followed by Dunn's post-test, *, $p < 0.05$; **, $p < 0.01$; ***, $p < 0.001$; ****, $p < 0.0001$. Values: Table 5.1.5. Each sample point of the violin plot corresponds to the average distance measurement of a SVs. All data are presented as mean ± S.E.M.

Furthermore, prolonged stimulation requires a constant supply of SVs to the AZ membrane, in which the morphologically docked SVs might represent fusion-competent, primed SVs, as shown for conventional synapses (Imig et al., 2014). Chakrabarti et al. (2018) suggested that docked SVs might also constitute the RRP at IHC ribbon synapses, although cell capacitance recordings point to a more abundant SV pool (Beutner and Moser, 2001; Goutman and Glowatzki, 2007; Moser and Beutner, 2000). Therefore, the subdivision of the MP pool into non-docked and docked SVs might contribute to define what constitutes the RRP in ribbon synapses. Significantly fewer docked SVs are found in the mutant compared to the wild-type (*Otof*$^{wt/wt}$ stimulation, 1.61 ± 0.20; *Otof*$^{KO/KO}$ stimulation, 0.71 ± 0.24. Kruskal-Wallis followed by Dunn's post-test, *, p< 0.05) (Fig, 3.1.1.3.4, Table 5.1.6).

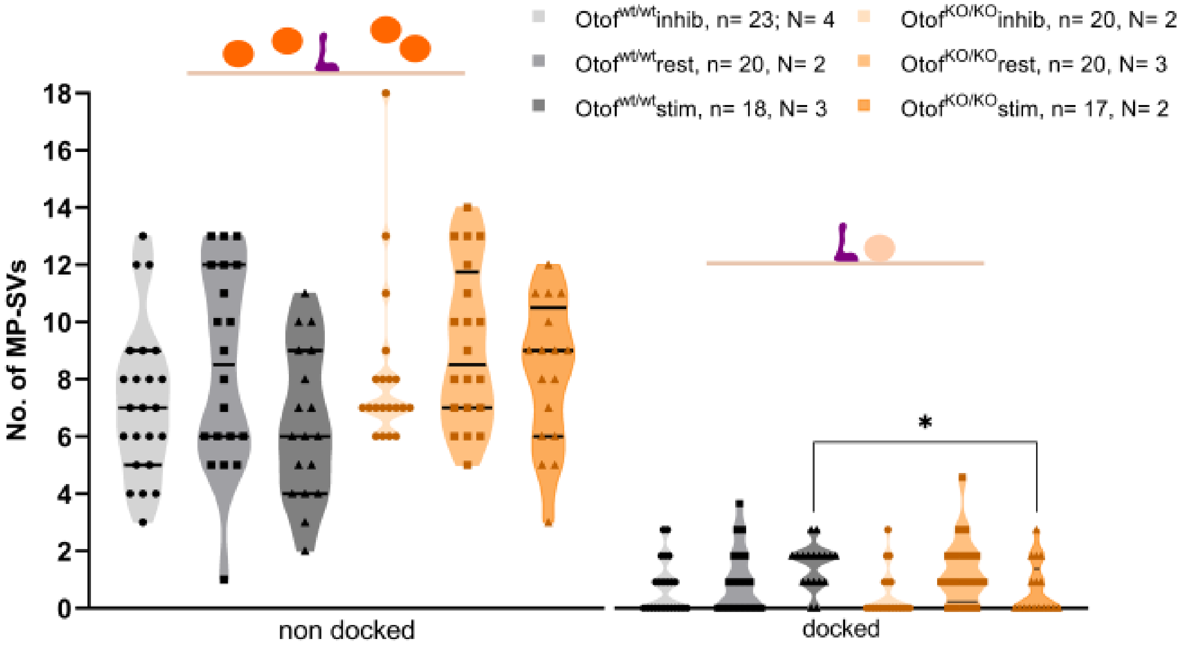

Fig. 3.1.1.3.4: Quantification of non-docked and docked MP-SVs per ribbon synapse. Average number of MP-SVs categorised into non-docked and docked, in which significantly fewer docked SVs are found in the mutant compared to the wild-type upon stimulation. Data are presented as mean ± S.E.M. Kruskal-Wallis followed by Dunn's multiple comparison test, *, p < 0.05. Values: Table 5.1.6.

Since I included the docked SVs in the distance measurement of the MP pool, a possible effect of docked SVs in the average distance of MP-SVs cannot be excluded. Therefore, the distances of non-docked and docked SVs were plotted separately for all conditions and genotypes. Similarly to the findings for the whole MP pool, non-docked SVs in *Otof*$^{wt/wt}$ approached the membrane upon stimulation (*Otof*$^{wt/wt}$ inhibition, 25.11 ± 1.06; *Otof*$^{wt/wt}$ resting, 24.85 ± 0.99; *Otof*$^{wt/wt}$ stimulation, 19.13 ± 1.10. Kruskal-Wallis followed by Dunn's post-test, **, p <0.01), while only upon rest non-docked SVs were found closer to the PD compared to inhibition (*Otof*$^{wt/wt}$ inhibition, 34.88 ± 2.01; *Otof*$^{wt/wt}$ resting, 43.51 ± 2.10; *Otof*$^{wt/wt}$ stimulation, 36.91 ± 2.27. Kruskal-Wallis followed by Dunn's post-test, *, p <0.05). Similarly to the overall behaviour of MP-SVs, stimulation failed to trigger the approach of non-docked SVs to the AZ membrane in the mutant (*Otof*$^{KO/KO}$ inhibition, 28.60 ± 0.93; *Otof*$^{KO/KO}$ resting, 26.59 ± 1.00; *Otof*$^{KO/KO}$ stimulation, 25.21 ± 1.10. Kruskal-Wallis, **, p <0.01), although they were significantly closer to the PD compared to rest (*Otof*$^{KO/KO}$ inhibition, 30.59 ± 1.65; *Otof*$^{KO/KO}$ resting, 39.82 ± 2.00; *Otof*$^{KO/KO}$ stimulation, 30.18 ± 2.31. Kruskal-Wallis followed by Dunn's post-test, *, p <0.05; **, p <0.01). In addition, docked SVs showed similar distances to the membrane and AZ membrane in wild-type and mutant, as expected due to the morphological definition. Instead, docked SVs were found significantly closer to the PD surface in *Otof*$^{KO/KO}$ upon stimulation compared to rest (*Otof*$^{KO/KO}$ resting, 38.63 ± 5.10; *Otof*$^{KO/KO}$ stimulation, 16.91 ± 7.48. Kruskal-Wallis followed by Dunn's post-test, *, p <0.05; **, p <0.01) (Fig. 3.1.1.3.5, Table 5.1.7).

To summarise, this subsection showed that the MP pool size remained constant in wild-type and mutant IHCs. Moreover, upon stimulation *Otof*$^{wt/wt}$ MP-SVs were found closer to the AZ membrane, which could not be observed in *Otof*$^{KO/KO}$, including non-docked and docked SVs. Instead, non-docked and docked SVs were found closer to the PD in the mutants. In the next subsection I will dissect the MP subpools into non-tethered, tethered and docked SVs.

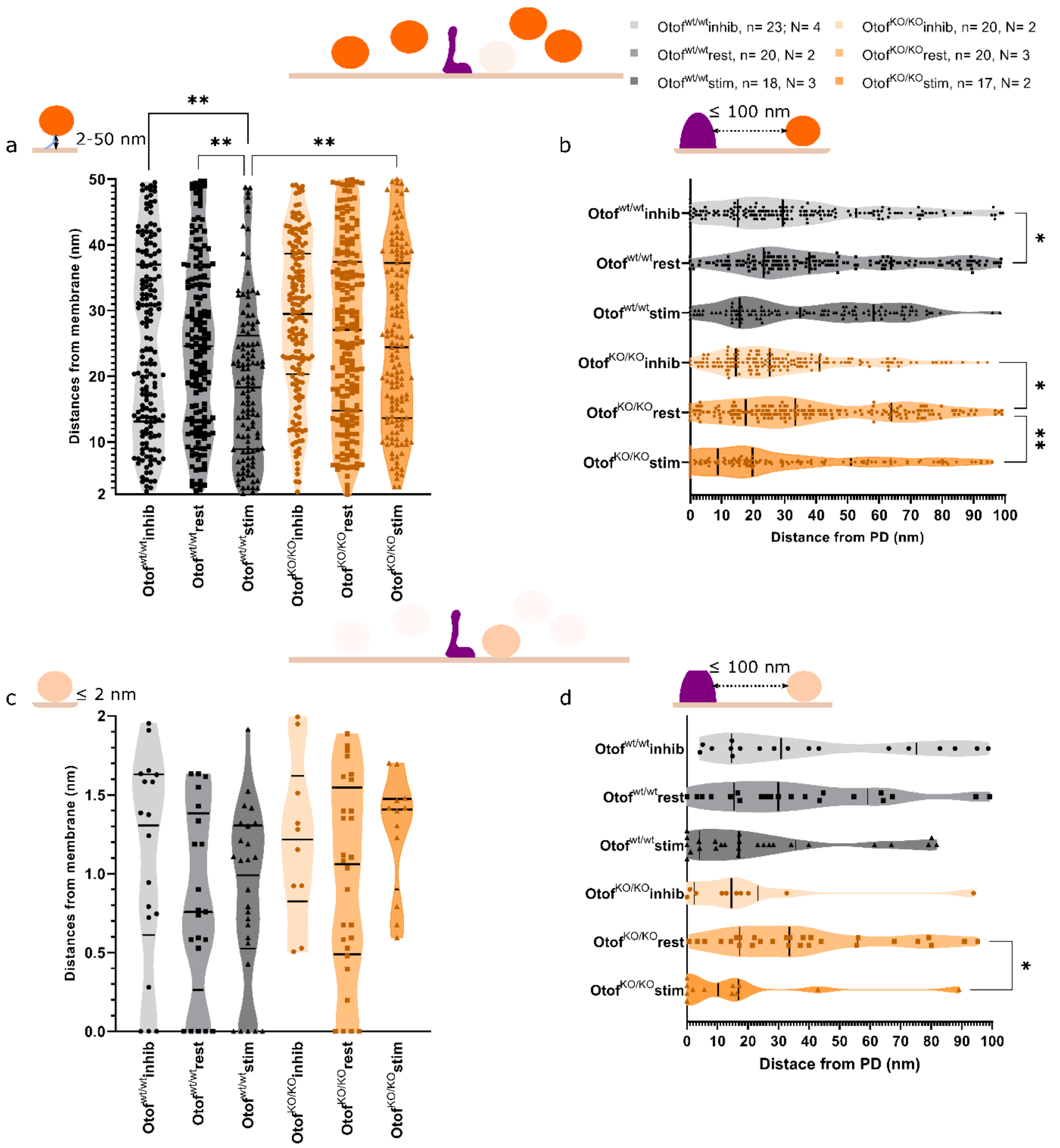

Fig. 3.1.1.3.5: Distance of non-docked and docked MP-SVs per ribbon synapse. a, Non-docked MP-SVs are statistically significantly closer to the AZ membrane in stimulated *Otof*$^{wt/wt}$ ribbon synapses compared to other activity states and upon *Otof*$^{KO/KO}$ stimulation. **b**, *Otof*$^{KO/KO}$ resting synapses present non-docked SVs further away from the PD surface compared to stimulatory and inhibitory conditions. **c**, Distances of docked SVs to the AZ membrane remain similar across genotypes and activity states. **d**, Docked SVs in stimulated *Otof*$^{KO/KO}$ are significantly closer to the PD surface than in rest. Kruskal-Wallis followed by Dunn's multiple comparisons test, ns, $p > 0.05$; *, $p < 0.05$; **, $p < 0.01$. Values: Table 5.1.7. Each sample point of the violin plot corresponds to the average distance measurement of a SVs. All data are shown as mean ± S.E.M.

3.1.1.4 Analysis of membrane-proximal SV subpools

Recent ultrastructural studies draw a parallelism between the readiness for release of a given SV, and the presence and number of tethers (Bullen et al., 2015; Chakrabarti et al., 2022, 2018; Lenzi et al., 2002, 1999). Ultrastructural studies of the synaptic ribbon in IHCs have shown that MP-SVs establish tethers with structures such as the synaptic ribbon, the presynaptic density, the active zone membrane and other SVs. MP-SVs can be classified according to the presence of tethers and distance to the AZ membrane as non-tethered, tethered and docked. MP-SVs in IHC ribbon synapses can be found forming one tether, which presumably represents the first tethered step prior to fusion; and multiple tethers, which are likely a transient step prior to docking (Chakrabarti et al., 2018) (Fig. 3.1.1.4.1a). Ultrastructural analysis of the MP subpools upon prolonged stimulation of ribbon synapses may highlight the relevance of Otof in certain tethering steps of the release sequence.

Stimulation resulted in a significant decrease of non-tethered SVs in wild-type (*Otof*$^{wt/wt}$ inhibition, 0.16 ± 0.04; *Otof*$^{wt/wt}$ resting, 0.32 ± 0.05; *Otof*$^{wt/wt}$ stimulation, 0.14 ± 0.03. Kruskal-Wallis followed by Dunn's post-test, *, $p < 0.5$), while the fraction of tethered MP-SVs remains comparable to rest. Moreover, single and multiple tethered SVs were found in similar abundances in all activity states. *Otof*$^{wt/wt}$ ribbon synapses presented a greater fraction of docked MP-SVs upon stimulation compared to inhibitory condition (*Otof*$^{wt/wt}$ inhibition, 0.09 ± 0.02; *Otof*$^{wt/wt}$ stimulation, 0.22 ± 0.03. Kruskal-Wallis followed by Dunn's post-test, *, $p < 0.5$) (Fig. 3.1.1.4.1b, Table 3.1.4.7). Conversely, the fraction of non-tethered, tethered and docked SVs in *Otof*$^{KO/KO}$ was comparable across the three activity states. The fraction of tethered MP-SVs was slightly higher than in any of the *Otof*$^{wt/wt}$ conditions, especially when compared to the resting and stimulatory conditions. In addition, single and multiple tethered SVs remained in comparable proportions. Stimulated *Otof*$^{KO/KO}$ ribbon synapses showed statistically significantly fewer docked SVs than stimulated *Otof*$^{wt/wt}$ (*Otof*$^{wt/wt}$ stimulation, 0.22 ± 0.03.; *Otof*$^{KO/KO}$ stimulation, 0.07 ± 0.02. Kruskal-Wallis followed by Dunn's post-test, *, $p < 0.05$) (Fig. 3.1.1.4.1b, Table 5.1.8).

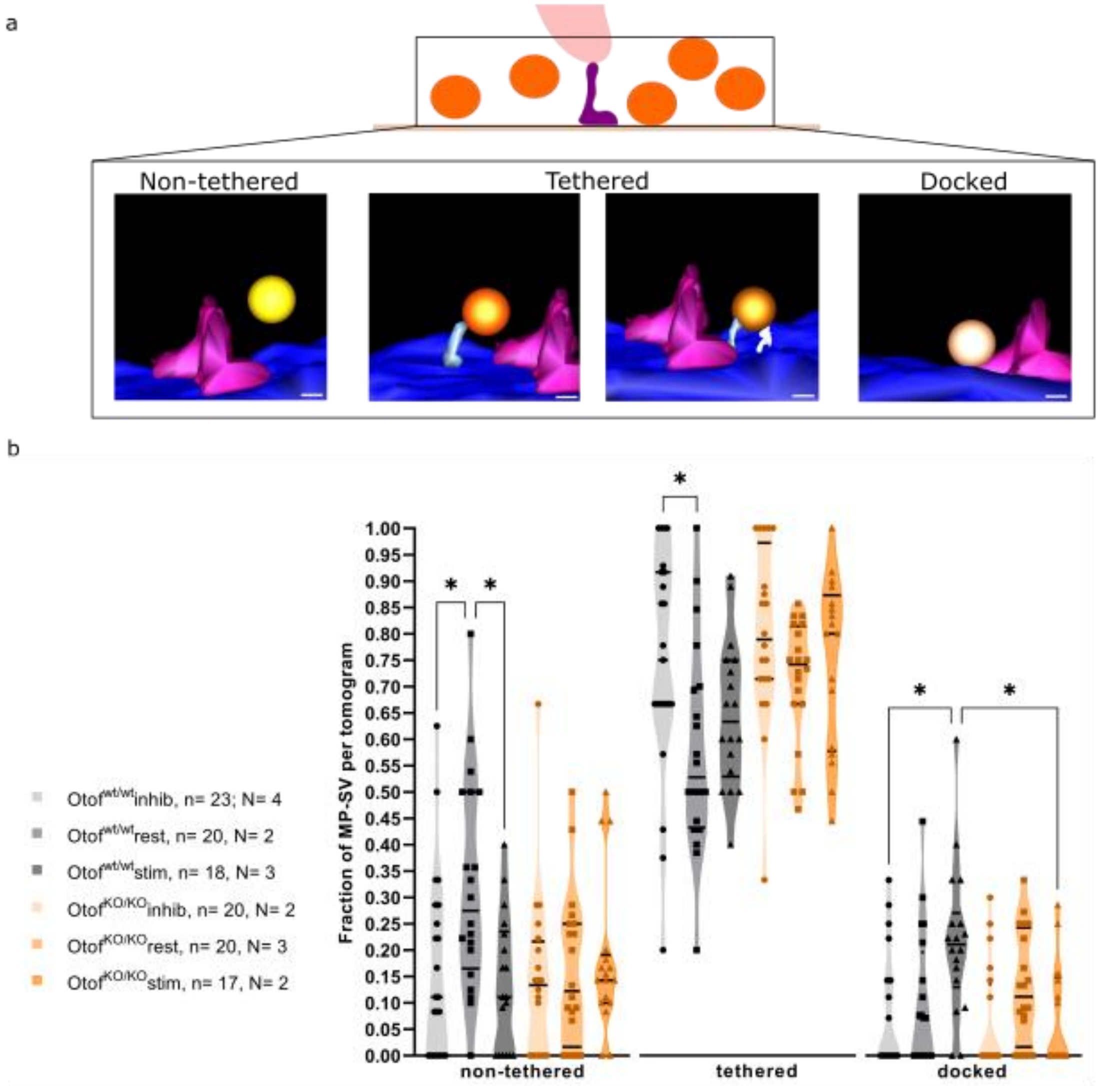

Fig. 3.1.1.4.1: MP-SV subpools in wild-type and *Otof*$^{KO/KO}$ ribbon synapses. a, Diagram showing the classification of MP-SVs according to the presence of tethers and the distance to the membrane, namely non-tethered (yellow), tethered (orange) and docked (light orange). Scale bar, 20 nm. **b**, Average fraction of MP-SVs per tomogram according to their tethered status. Significantly higher fraction of non-tethered SVs is found in *Otof*$^{wt/wt}$ in resting conditions compared to inhibitory and stimulatory states. Fewer tethered SVs are observed in rest than in resting *Otof*$^{wt/wt}$ compared to inhibition. Docked SVs are significantly more abundant in stimulated *Otof*$^{wt/wt}$ ribbon synapses than upon inhibition and stimulated *Otof*$^{KO/KO}$. Kruskal-Wallis, *, $p < 0.05$. Values: Table 5.1.8. All data are presented as mean ± S.E.M.

Then, the distances to the AZ membrane were measured in each MP-SV and classified according to the presence of tethers to analyse the recruitment for release of each SV subpool in the different activity states. Upon stimulation, only single tethered SVs in *Otof*$^{wt/wt}$ ribbon synapses became significantly closer to the membrane compared to *Otof*$^{wt/wt}$ upon inhibition and stimulated *Otof*$^{KO/KO}$ (*Otof*$^{wt/wt}$ inhibition, 24.62 ± 1.17; *Otof*$^{wt/wt}$ stimulation, 17.79 ± 1.13; *Otof*$^{KO/KO}$ stimulation, 25.12 ± 1.19. Kruskal-Wallis followed by Dunn's post-test, **, p <0.01). Subsequently, the distance of MP-SVs to the PD surface per SV subpool was plotted and were found to be comparable across genotypes upon stimulation (Fig. 3.1.1.4.2, Table 5.1.9).

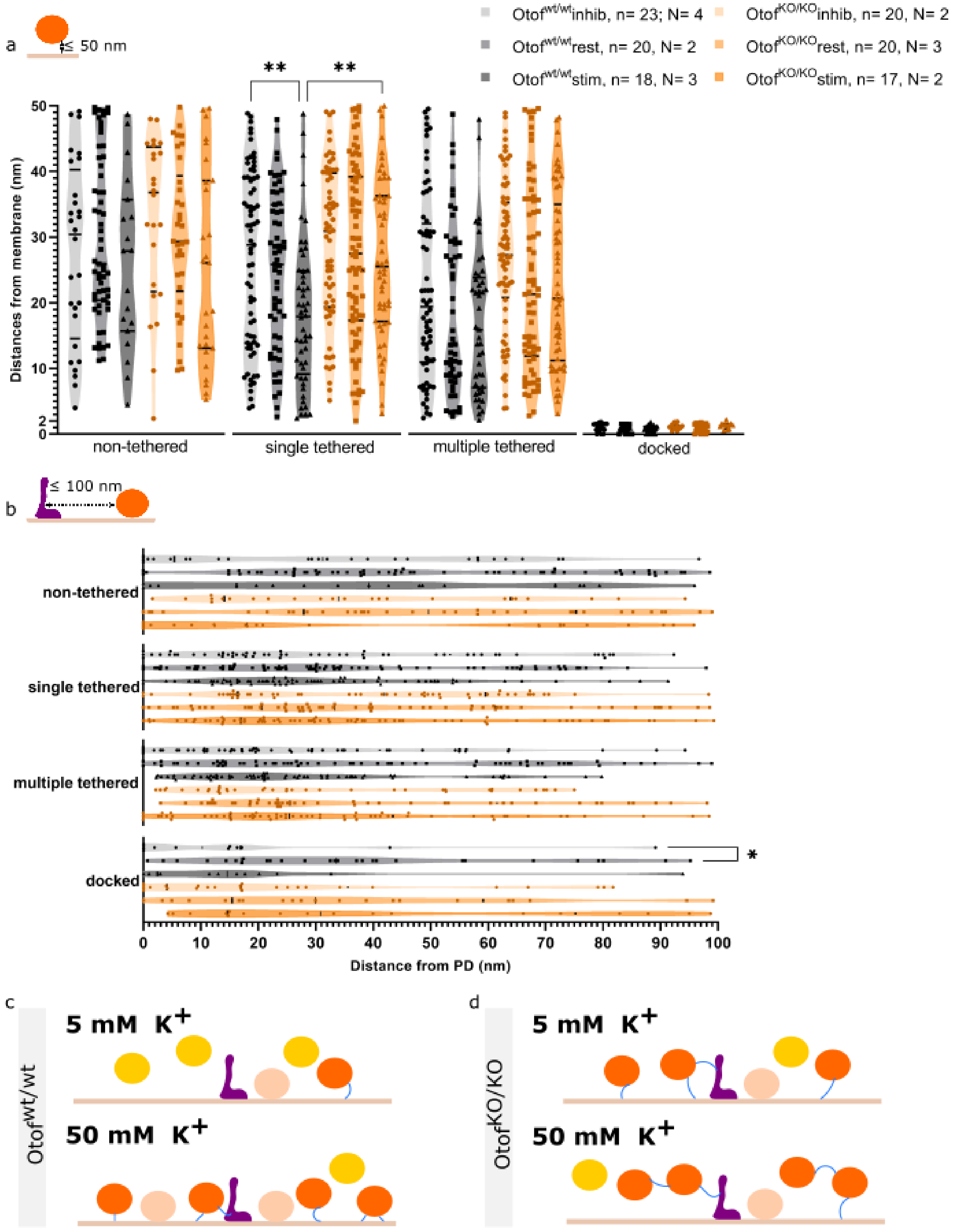

Fig. 3.1.1.4.2: Distances of MP-SVs per subpool. a, Average distance of MP-SVs from the AZ membrane. Tethered SVs in *Otof*$^{wt/wt}$ are closer to the membrane upon stimulation than inhibition and stimulation in *Otof*$^{KO/KO}$. Kruskal-Wallis followed by Dunn's post-test, **, p< 0.01. **b**, Average distance from PD of MP-SVs. Statistically significant differences can be found docked SVs between inhibitory and resting *Otof*$^{wt/wt}$ ribbon synapses. Kruskal-Wallis followed by Dunn's multiple comparison test, ns, p> 0.05. Each sample point of the violin plot corresponds to the average distance measurement of a SVs. All data are presented as mean ± S.E.M. Values: Table 5.1.9. **c-d**, Summary schematics of tether changes in the MP pool from rest to stimulation. On the one hand, in *Otof*$^{wt/wt}$ the abundance of non-tether SVs decreases, while tether SVs increase and are found closer to the membrane upon stimulation. On the other hand, in *Otof*$^{KO/KO}$ similar amount of non-tethered and tethered SVs at similar distances from the plasma membrane upon stimulation. (Figure above)

Furthermore, tethered MP-SVs can be sub-categorized according to the structure with whom the tether is established: membrane, PD or ribbon, other SV (called interconnected), and any combination of the previous. Analysis of the tethering the MP-SVs per tethering partner(s) may give insight into any alteration in the MP pool recruitment, since a function-structure study proposed that SVs tether to the PD before establishing connections with the AZ membrane (Chakrabarti et al., 2018). No statistically significant differences were observed across genotypes and activity states (Fig. 3.1.1.4.3, Table 5.1.10).

This subsection shows that non-tethered SVs become less abundant, while the fraction of tethered SVs slightly increased upon stimulation in the *Otof*$^{wt/wt}$, especially with the AZ membrane. These tethered SVs, which seem to approach the AZ membrane in their pathway to release, culminating their approach when docking. Conversely, tethered SVs upon deletion of Otof were not found to be closer to the AZ membrane. Altogether, these data indicate that Otof might be necessary to bring SVs close to the AZ membrane upon prolonged stimulation.

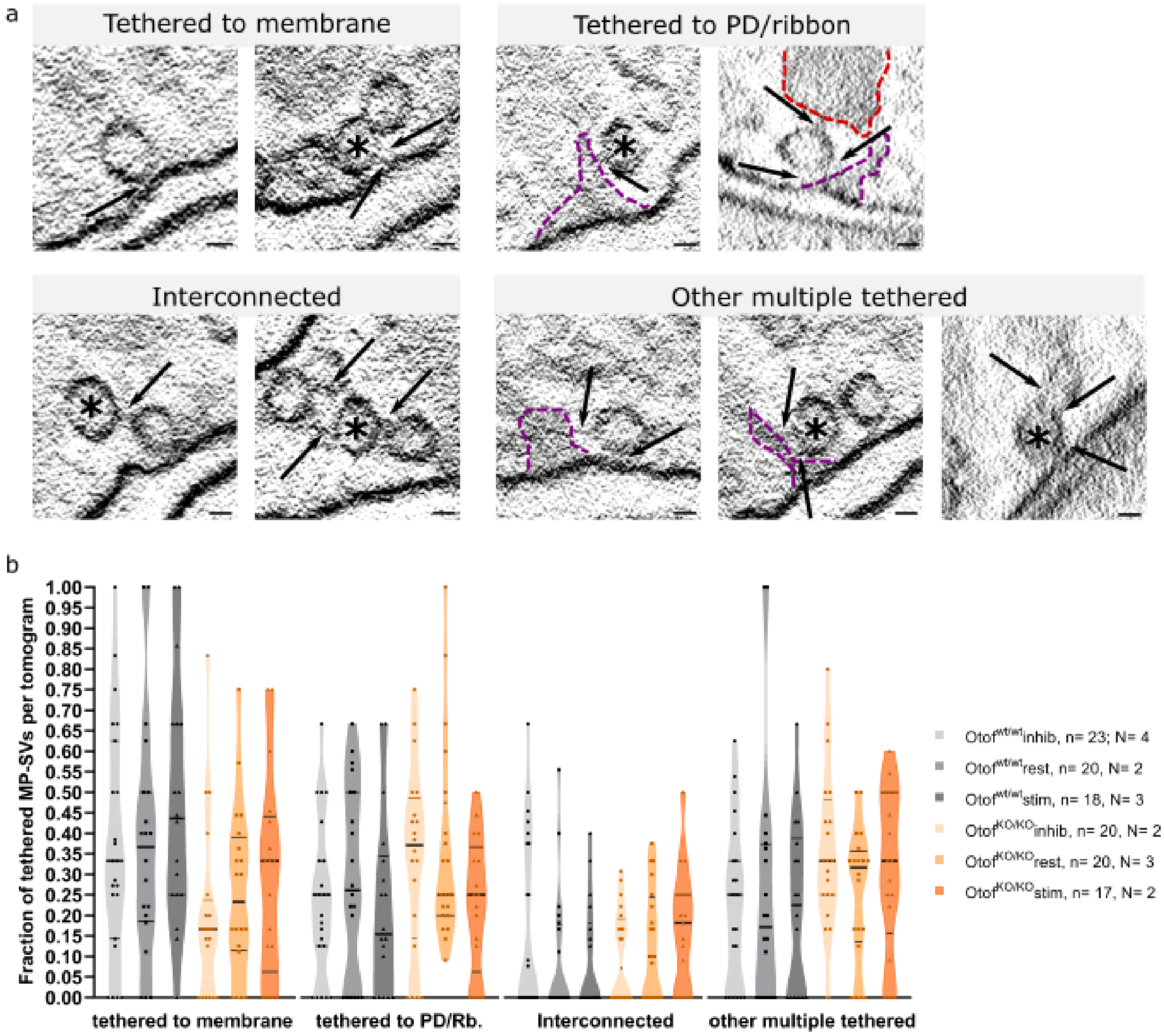

Fig. 3.1.1.4.3: Fractions of MP-SVs classified according to their tethering companion. a, Examples of virtual sections from MP-SVs from *Otof*$^{wt/wt}$ under rest. Single or multiple tethers can be established with the membrane, PD/ribbon (Rb.) and to other SVs (interconnected). In addition, SVs can establish multiple tethers with other structures ("other multiple tethered"), such as the PD and membrane; PD and other SVs; and membrane and other SVs. The arrow points to the tethers and the asterisk indicates multiple tethered MP-SVs from each category. **b**, No statistically significant differences are found in any of the genotypes in any of the activity states. Kruskal-Wallis followed by Dunn's multiple comparison post-test, ns, p> 0.05. Values: Table 5.1.10. All data are presented as mean ± S.E.M.

3.1.1.5 Analysis of endocytic structures

Previous studies have shown bulk endocytosis and clathrin-mediated endocytosis to happen in the proximity of the AZ membrane of ribbon synapses (Chakrabarti et al., 2018; Neef et al., 2014). In addition, tubular or cisternae-like structures of endocytic origin have been mostly observed at the apical and nuclear regions of IHCs, while fewer in the basal region, which become more abundant upon stimulation (Kamin et al., 2014). In this study, I quantified the endocytic structures in close proximity to ribbon synapses comparing *Otof*$^{wt/wt}$ and *Otof*$^{KO/KO}$mice. The quantified endocytic structures include endosomal-like vacuoles (ELVs), which are clear-core, round- or oval-shaped vesicles with diameter bigger than 70 nm by definition (Kroll et al., 2019); clathrin-coated vesicles (CCVs), which can be identified by the clathrin coat; and tubular endocytic structures (TESs), which are tubular/cisternae-like structures in the proximity of the ribbon synapses. In addition to the total number and the fractions of endocytic structures, their sizes were analysed.

Otof is thought to be involved in clathrin-mediated endocytosis, due to its interaction with AP-2μ (Jung et al., 2015a); as well as in SV reformation because of its presence in non-coated endosomal vacuoles (Strenzke et al., 2016). Therefore, a reduction in the number of endocytic structures was expected in stimulated *Otof*$^{KO/KO}$ ribbon synapses compared to wild-type. The number of endocytic structures in resting *Otof*$^{KO/KO}$ was significantly higher than inhibitory and stimulatory condition, as well as compared to *Otof*$^{wt/wt}$ in rest (*Otof*$^{wt/wt}$ resting, 9.75 ± 1.47; *Otof*$^{KO/KO}$ inhibition, 9.50 ± 1.81; *Otof*$^{KO/KO}$ resting, 21.85 ± 2.29; *Otof*$^{KO/KO}$ stimulation, 10.47 ± 2.12. Kruskal-Wallis followed by Dunn's post-test, **, $p< 0.01$; ***, $p< 0.001$) (Fig. 3.1.1.5.1, Table 5.1.3).

Furthermore, quantifying the sizes of endocytic structures may contribute to understand whether disruption of Otof results in impaired endocytosis and/or SV reformation due to almost nulled exoytosis. As described in section 2.4.12, I determined the effective radii in order to be able to compare the sizes of irregular structures. All endocytic structures presented comparable effective radii across genotypes and conditions (Fig. 3.1.1.5.1c, Table 5.1.11). Subsequently, endocytic structures were divided into round and non-round structures (see section 2.4.12), to determine whether any of them had a greater impact in determining the average effective radius of all endocytic structures. Round endocytic structures in inhibited condition showed significantly smaller radii in *Otof*$^{wt/wt}$ than *Otof*$^{KO/KO}$ synapses, while *Otof*$^{wt/wt}$ non-

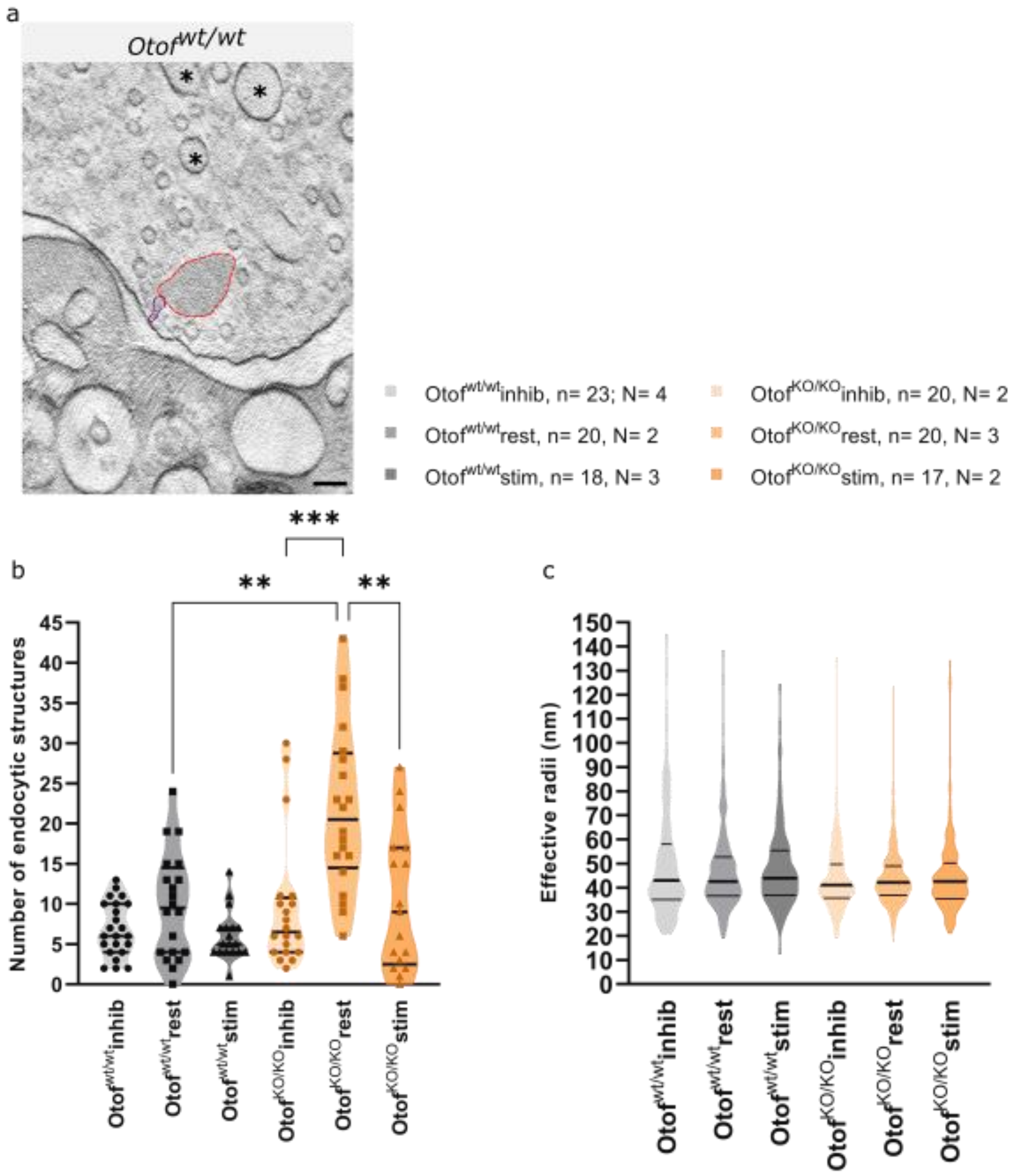

Fig. 3.1.1.5.1: Quantification of endocytic structures. a, Example of virtual slices from MP-SVs from *Otof*$^{wt/wt}$ where endocytic structures (*) were quantified. **b**, No statistically significant differences are found in any of the genotypes in any of the activity states. Kruskal-Wallis followed by Dunn's post-test, **, $p< 0.01$; ***, $p< 0.001$. **c**, The effective radii of the endocytic structures remained comparable across genotypes and conditions. Kruskal-Wallis followed by Dunn's post-test, ns, $p> 0.05$. Values: Table 5.1.3 and Table 5.1.11. All data are shown as mean ± S.E.M.

round endocytic upon inhibition displayed significantly bigger effective radii than in *Otof*$^{KO/KO}$ synapses (round endocytic structures: *Otof*$^{wt/wt}$ inhibition, 39.22 ± 1.48; *Otof*$^{KO/KO}$ inhibition, 43.94 ± 0.92. Kruskal-Wallis followed by Dunn's post-test, *, $p< 0.05$; non-round endocytic structures: *Otof*$^{wt/wt}$ inhibition, 57.26

± 2.79; *Otof*$^{KO/KO}$ inhibition, 42.97 ± 1.92. Kruskal-Wallis,*, $p < 0.05$). Structures between 30-50 nm of effective radii were the most abundant (Fig.5.1.1.5.2).

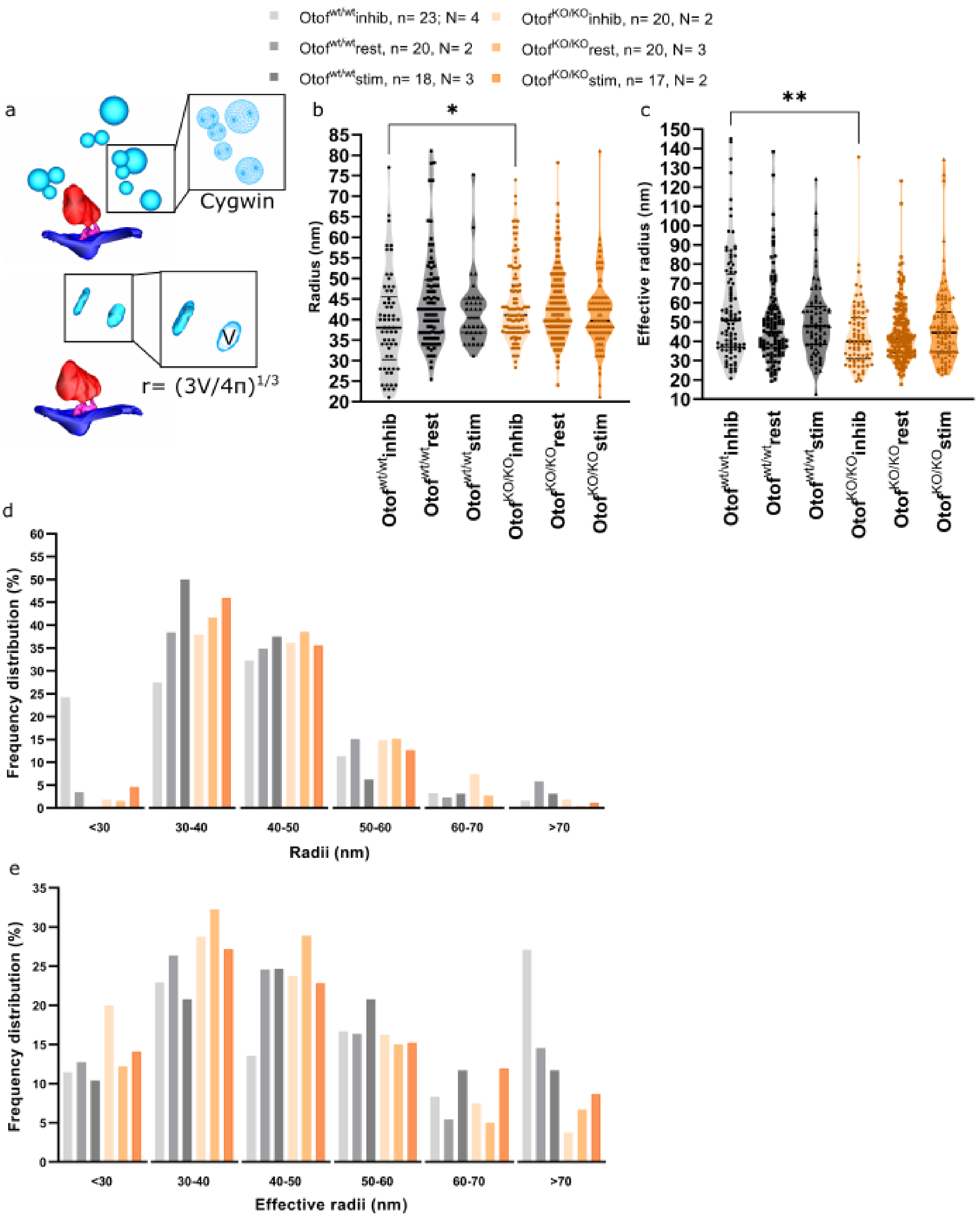

Fig. 3.1.1.5.2: Sizes of endocytic structures per ribbon synapse according to their shape. a, Summary diagram of the method for calculating the radii of round and non-round endocytic structures. The radii of round endocytic structures are directly obtained from Cygwin, while the radii of non-round endocytic structures are inferred from the volume of such structures (hence named “effective radius”). **b-c**, Average radius of round structures and effective radius of non-round structures. Statistically significant differences are found between inhibited *Otof*$^{wt/wt}$ and *Otof*$^{KO/KO}$ ribbon synapses. Kruskal-Wallis followed by Dunn’s multiple comparison test, *, $p< 0.05$. Values: Table 5.1.11. Each sample point corresponds to the average distance measurement of a SVs. All data are shown as mean ± S.E.M. **d-e**, Frequency distribution of (left) round and (right) non-round endocytic structures whose bin width is 10 nm. Two-way ANOVA followed by Tukey’s post-test, ns, $p> 0.05$. (Figure above)

Absence of Otof might disrupt the formation of endocytic structures, such as CCVs due to its interaction with AP-2µ, which could affect the abundance of either endocytic structure. Therefore, the relative abundances of CCVs and TESs were calculated per tomogram and averaged. This quantification showed ELVs to be the most abundant endocytic structure, although similar fractions of ELVs, CCVs and TESs were found among genotypes and activity states (Fig. 3.1.1.5.3; Table 5.1.12). In addition, size measurements showed that non-round ELVs are larger in inhibited *Otof*$^{wt/wt}$ and stimulated *Otof*$^{KO/KO}$ ribbon synapses than in *Otof*$^{KO/KO}$ upon inhibition tomograms (non-round: *Otof*$^{wt/wt}$ inhibition, 58.50 ± 3.35; *Otof*$^{KO/KO}$ inhibition, 39.24 ± 2.16; *Otof*$^{KO/KO}$ stimulation, 47.70 ± 2.32. Kruskal-Wallis followed by Dunn’s post-test, *, $p< 0.05$; ****, $p< 0.0001$). Round CCVs sizes inhibitory condition were significantly larger in *Otof*$^{KO/KO}$ than in *Otof*$^{wt/wt}$ (*Otof*$^{wt/wt}$ inhib, 31.41 ± 1.75; *Otof*$^{KO/KO}$ inhibition, 43.72 ± 2.37. Kruskal-Wallis followed by Dunn’s post-test, ***, $p< 0.001$). The effective radius of TESs was similar in all genotypes and activity states (Fig. 3.1.1.5.3, Table 5.1.13).

Ultrastructural data investigating the morphological correlates of endocytosis was presented in this subsection. The number of endocytic structures was significantly increased in resting *Otof*$^{KO/KO}$ compared to other activity states and its control. However, the overall size of these endocytic structures upon stimulation remained comparable in resting and stimulatory conditions, despite the diversity in shapes (i.e., round and not round) and the differences per endocytic structure type (i.e., ELVs, CCVs and TESs). The comparable sizes of endocytic structures in rest and stimulation suggests that Otof might play a minor role in SV reformation.

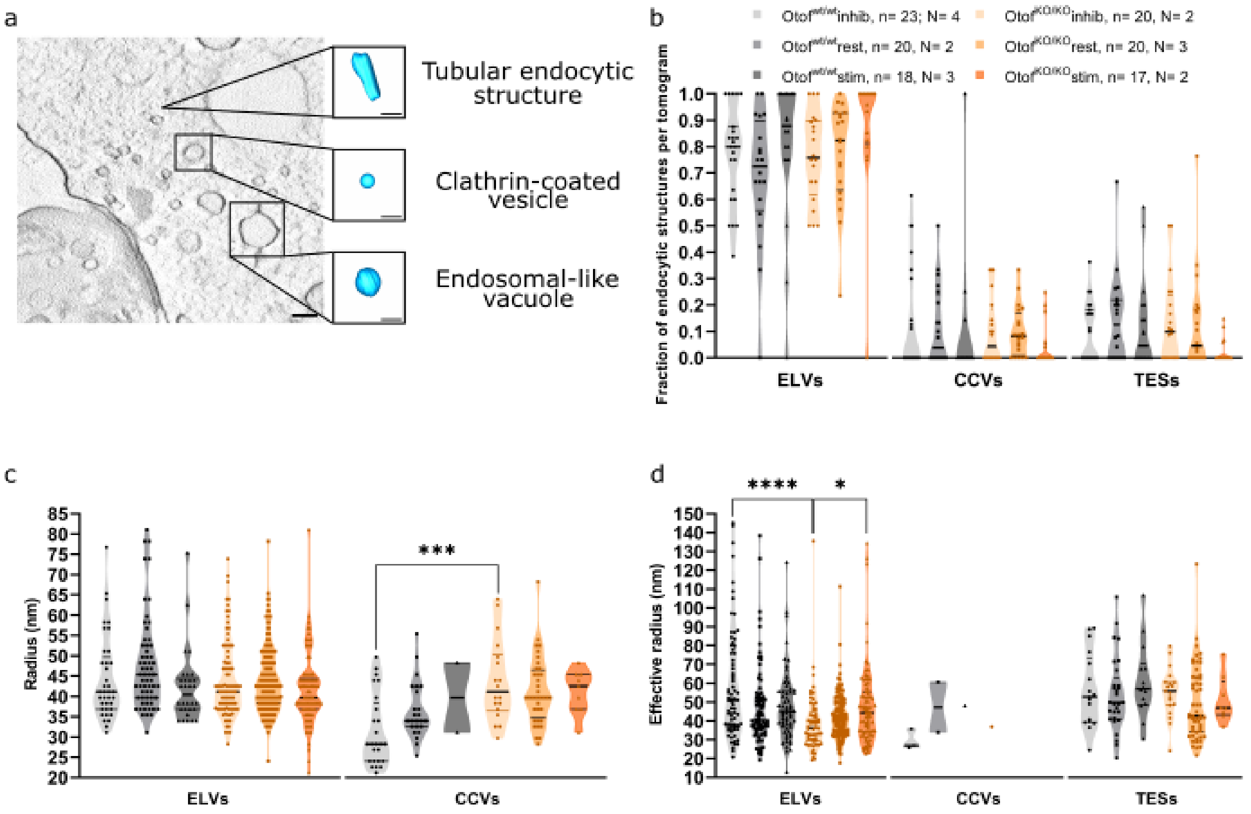

Fig. 3.1.1.5.3: Types of endocytic structures per ribbon synapse. a, Representative virtual section of a wild-type ribbon synapse that contains tubular endocytic structures (TESs), clathrin-coated vesicles (CCVs) and endosomal-like vacuoles (ELVs). b, Fraction of endocytic structures per ribbon synapse. Comparable proportions of ELVs, CCVs and TESs are found in all genotypes and activity states. Kruskal-Wallis, ns, $p > 0.05$. Values: Table 5.1.12. **c**, Average radii of round ELVs and CCVs. Statistically significant differences are found in wild-type and mutant in ELVs radii upon rest, as well as in CCV radii upon inhibition. Kruskal-Wallis followed by Dunn's post-test, *, $p < 0.05$; ***, $p < 0.001$. Values: Table 5.1.13. Each sample point of the violin plot corresponds to the average distance measurement of a SVs. Data are shown as mean ± S.E.M. d, Average effective radii of non-round endocytic structures. Statistically significant differences are found in *Otof*$^{wt/wt}$ and *Otof*$^{KO/KO}$ in ELVs, CCVs and TESs upon inhibition. Each sample point of the violin plot corresponds to the average distance measurement of a SVs. Kruskal-Wallis followed by Dunn's post-test, ***, $p < 0.001$. Values: Table 5.1.13. Data are presented as mean ± S.E.M.

3.1.2 Ultrastructural study of *Otof*$^{pga/pga}$ ribbon synapse endocytic structures

OTOF gene is found in the locus DFNB9, whose mutations results in a type of non-syndromic deafness (Yasunaga et al., 2000). Physiological and molecular understanding of one of its mutations has been performed using a mouse model called *pachanga* (*Otof*$^{pga/pga}$) (Schwander et al., 2007), in which the truncated Otof is still expressed, although with strongly diminished levels specifically at IHC membranes (Pangšrič et al., 2010). Here, the C$_2$F domain of Otof contains a missense mutation that results in severe hearing impairment (Pangšrič et al., 2010).

Briefly, functional data from *Otof*$^{pga/pga}$ ribbon synapses show a reduction in sustained SV release, which indicates a defect in SV replenishment (Pangšrič et al., 2010). Ultrastructural data from mutant ribbon synapses reveal an accumulation of multiple tethered and docked MP-SVs (Chakrabarti et al., 2018).

However, capacitance measurements did not show an impairment in endocytosis, whose morphological correlates are yet to be investigated in *Otof*$^{pga/pga}$ ribbon synapses. Therefore, an additional analysis of tomograms already used in publication (Chakrabarti et al., 2018) was performed for a subsequent comparison of *Otof*$^{KO/KO}$ and *Otof*$^{pga/pga}$ data (see section 3.1.3).

Data of endocytic structures and peripherally RA (periRA) SVs was obtained from tomograms used in Chakrabarti et al. (2018). Conversely, data related to RA and MP pools were obtained from the supplementary tables from the publication; and data related to docked and non-docked MP-SVs was obtained from the raw data spreadsheets used in the aforementioned publication (Chakrabarti et al., 2018). Values of quantifications and fractions presented in this section can be found in section 5.1.

3.1.2.1 *Structure organisation in C57B6/J and Otof*$^{pga/pga}$ *ribbon synapses upon 15-minute chemical stimulation*

Quantification of the fractions of endocytic structures and the different morphological SV pools constitutes a holistic approach to study the effects of the mutation in *Otof*$^{pga/pga}$ ribbon synapses. I compared the abundance of the different morphological correlates of the SV cycle in *Otof*$^{pga/pga}$ and C57Bl6/J controls (tomograms were acquired from Chakrabarti et al., 2018). Here, comparable fractions of each analysed structure were found in all genotypes and activity states (Fig. 3.1.2.1, Table 5.1.14).

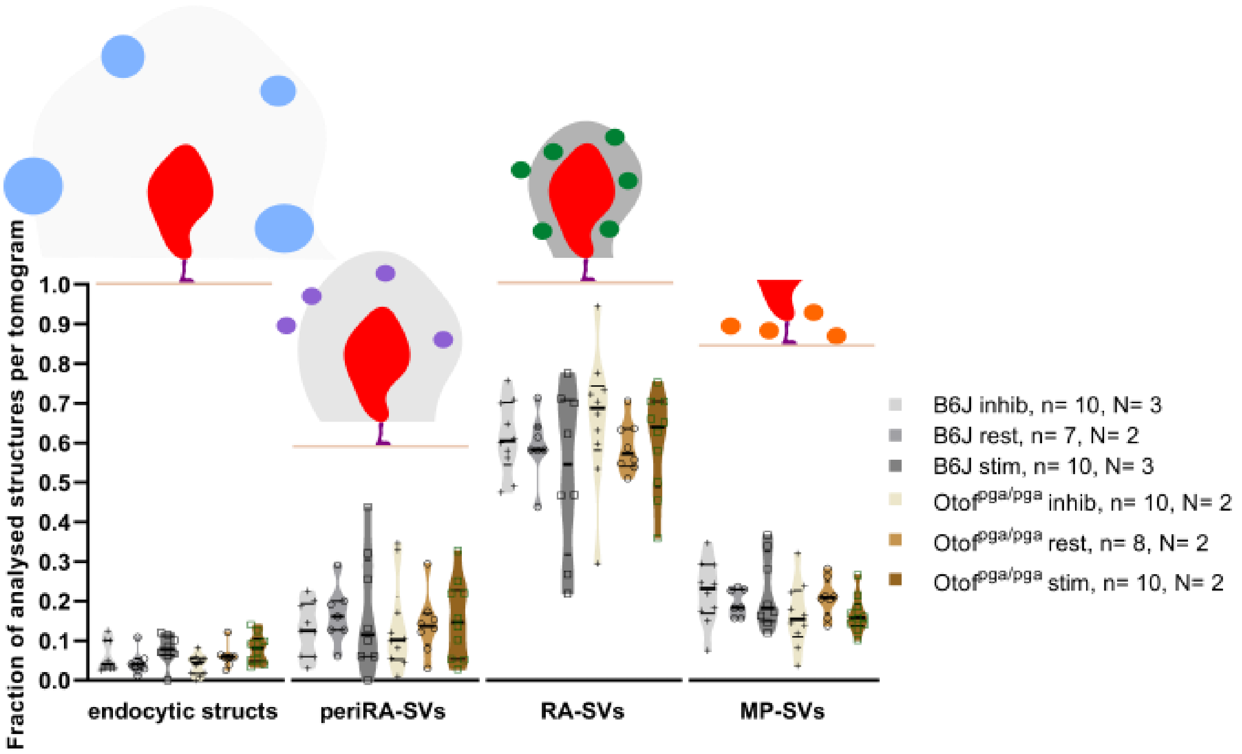

Fig. 3.1.2.1: Fractions of analysed structures in wild-type and *Otof$^{pga/pga}$* ribbon synapses. No statistically significant differences were found in the fractions of endocytic structures, periRA-SVs, RA nor MP-SVs. Kruskal-Wallis followed by Dunn's post-test and one-way ANOVA followed by Šidák's post-test, ns, p> 0.05. Values: Table 5.1.14. All data are shown as mean ± S.E.M.

3.1.2.2 Analysis of endocytic structures

The complete lack of Otof has previously revealed an abnormal number of endocytic structures in resting conditions, while their sizes remained relatively constant among conditions (see section 3.1.1.5). Large plasma membrane invaginations, which are thought to be bulk endocytosis morphological correlates, have been observed in the proximity of the ribbon in wild-type samples, but have not been reported for *Otof$^{pga/pga}$* synapses (Chakrabarti et al., 2018). Similar number of endocytic structures and fractions of the different endocytic structures were found in both genotypes regardless of the activity state (Fig. 3.1.2.2, Table 5.1.15, Table 5.1.16). This suggests that, at least on the ultrastructural level, defects in SV replenishment are not caused by massive impairment of SV reformation.

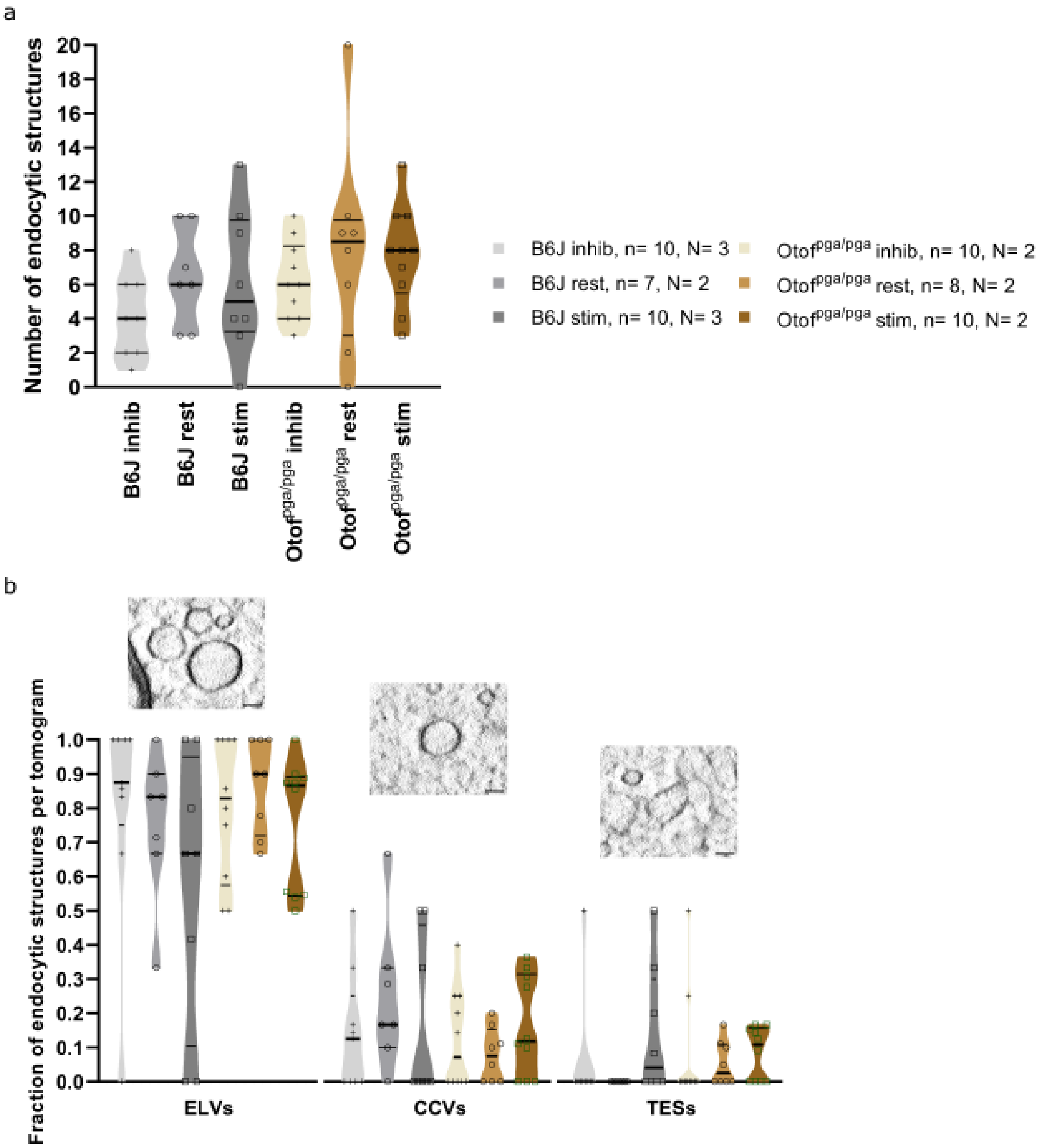

Fig. 3.1.2.1.2: Quantification of endocytic structures in wild-type and *Otof*$^{pga/pga}$ tomograms. a, Quantification of endocytic structures showed not significant differences between wild-type and mutant. Kruskal-Wallis followed by Dunn's post-test, ns, p> 0.05. Values: Table 5.1.15. **b**, Fractions of analysed structures. Not significant differences were found between B6J and *Otof*$^{pga/pga}$ ribbon synapses per endocytic structure type. Insets, virtual sections depicting (left) an endosomal-like vacuole (ELV), (middle) a clathrin-coated vesicle and (right) a tubular endocytic structure (TES). Scale bar, 50 nm. Kruskal-Wallis followed by Dunn's post-test, ns, p> 0.05. Values: Table 5.1.16. All data are shown as mean ± S.E.M.

3.1.3 Comparison $Otof^{KO/KO}$ and $Otof^{pga/pga}$ ribbon synapse architecture upon chemical stimulation

Deletion of Otof and truncation of the final domains of Otof result in severe hearing impairment, although the underlying ultrastructural causes differ (see section 3.1.1, section 3.2.1 and Chakrabarti et al., 2018). On the one hand, SV replenishment of the RRP seemed impaired in $Otof^{pga/pga}$ ribbon synapses (Pangšrič et al., 2010), whose cause has been suggested to be a defect in release site clearance due to the accumulation of multiple tethered and docked SVs (Chakrabarti et al., 2018). On the other hand, almost completely abolished exocytosis is seen in $Otof^{KO/KO}$ IHCs (Pangšrič et al., 2010; Roux et al., 2006; Vogl et al., 2015) that resulted in an impairment in MP-SV tethering, but not in SV accumulation at the AZ zone (see section 3.1.1.4. A comparison of the SV pools and endocytic pathway from these Otof mutants might contribute to elucidate the effect of Otof in the SV cycle.

In this section I compare the ribbon synapse architecture of both mutants upon strong and prolonged stimulation with especial emphasis on the MP pool and endocytic structures. As stated before, $Otof^{pga/pga}$ data that is used here is a combination of already available data (Chakrabarti et al., 2018) and a further analysis of those tomograms. Values of quantifications and fractions presented in this section can be found in section 5.1.

3.1.3.1 Structure organisation in $Otof^{KO/KO}$ and $Otof^{pga/pga}$ ribbon synapse upon 15 min stimulation

General changes in ribbon synapse architecture in different activity states were quantified via fractions of endocytic structures and SV pools. Previously, the lack of Otof revealed statistically significant differences in the fraction of endocytic structures upon stimulation, while the remaining SV pools behaved similarly to each other. In $Otof^{pga/pga}$ mutants the fraction of analysed structures was comparable between genotypes in all activity states. Differences in the impact over the SV cycle of each mutant might be observed comparing both samples.

The comparison revealed a significantly smaller fraction of endocytic structures of $Otof^{pga/pga}$ compared to $Otof^{KO/KO}$ in inhibitory and resting states ($Otof^{KO/KO}$ inhibition, 0.14 ± 0.02; $Otof^{KO/KO}$ resting, 0.28 ± 0.02; $Otof^{pga/pga}$ inhibition, 0.04 ± 0.01; $Otof^{pga/pga}$ resting, 0.06 ± 0.01. Kruskal-Wallis followed by Dunn's multiple comparison test, *, $p< 0.05$; **, $p< 0.01$; ****, $p< 0.0001$). Conversely, a significant increase in the fraction of RA-SVs was found in $Otof^{pga/pga}$ compared to $Otof^{KO/KO}$ upon inhibition and rest ($Otof^{KO/KO}$ inhibition, 0.52 ± 0.02; $Otof^{KO/KO}$ resting, 0.43 ± 0.02; $Otof^{pga/pga}$ inhibition, 0.66 ± 0.05; $Otof^{pga/pga}$ resting, 0.59 ± 0.02. One-way ANOVA followed by Šidák's post-test, *, $p< 0.05$; ***, $p< 0.001$; ****, $p< 0.0001$). Finally, the proportion of the MP pools is larger in resting $Otof^{pga/pga}$ than in $Otof^{KO/KO}$ ribbon synapses ($Otof^{KO/KO}$

resting, 0.1558 ± 0.0122; *Otof$^{pga/pga}$* resting, 0.1665 ± 0.01474. Kruskal-Wallis, *, $p < 0.05$) (Fig. 3.1.3.1, Table 5.1.17).

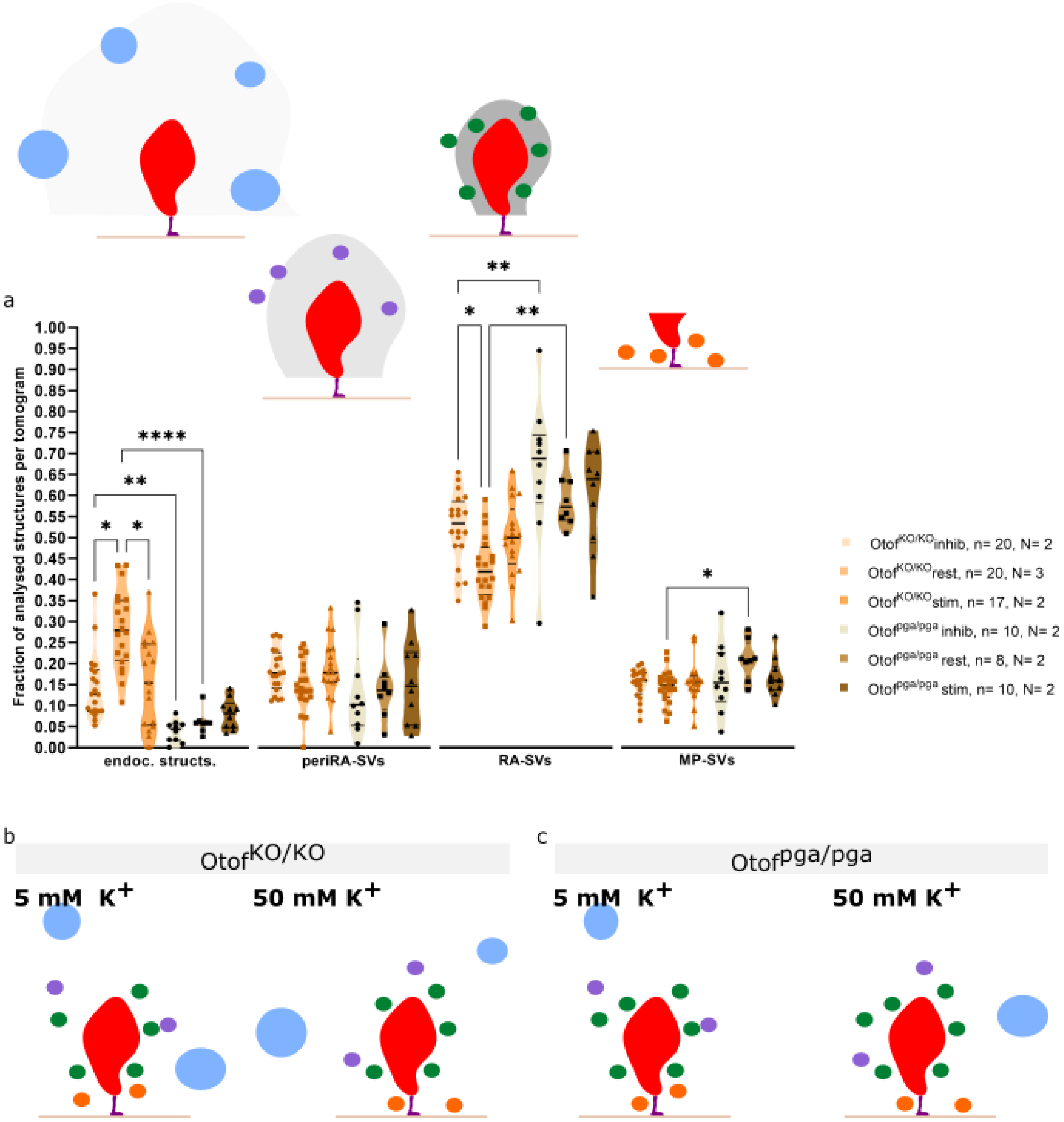

Fig. 3.1.3.1: Comparison of the fraction of analysed structures in *Otof*$^{KO/KO}$ and *Otof*$^{pga/pga}$. a, The fraction of endocytic structures was significantly smaller between inhibited and resting *Otof*$^{KO/KO}$ and *Otof*$^{pga/pga}$ synapses. In contrast, the proportion of RA-SVs was significantly larger *Otof*$^{pga/pga}$ in than in *Otof*$^{KO/KO}$ tomograms. The MP pool was larger in resting condition in *Otof*$^{pga/pga}$ in than in *Otof*$^{KO/KO}$ samples. One -way ANOVA followed by Šidák's post-test and Kruskal-Wallis followed by Dunn's post-test, *, $p < 0.05$; **, $p < 0.01$; ***; $p < 0.001$; ****, $p < 0.0001$. Values: Table 5.1.17. All data are shown as mean ± S.E.M. **b-c**, Schematic summary of the effects of activity in Otof$^{KO/KO}$ and *Otof*$^{pga/pga}$ ribbon synapses. Stimulation (50 mM K^+) in *Otof*$^{KO/KO}$ ribbon synapses results in a proportional mild increase of endocytic structures (blue) and a mild decrease in RA-SVs (green) and MP-SVs (orange) compared to *Otof*$^{pga/pga}$ ribbon synapses. (Figure above)

3.1.3.2 Ribbon-associated and membrane-proximal pools characteristics

Sustained stimulation requires strong mechanisms for SV replenishment, in which reformed SV feed the RA pool and RA-SVs replenish the MP pool. *Otof*$^{KO/KO}$ tomograms revealed similar sizes of the RA and MP pools when compared to wild-type ribbon synapses (Chakrabarti et al., 2018) (see section 3.1.1.3), hence no major differences are expected to be found between mutants. Verification of this hypothesis is done by comparing both pools in *Otof*$^{KO/KO}$ and *Otof*$^{pga/pga}$ synapses. Similar number of RA-SV were found in both mutants across different activity states, despite the significant differences in their fractions. Conversely, the size of the MP pool was significantly smaller in *Otof*$^{KO/KO}$ compared to *Otof*$^{pga/pga}$ upon inhibition and stimulation (*Otof*$^{KO/KO}$ inhibition, 8.650 ± 0.6168; *Otof*$^{KO/KO}$ stimulation, 8.882 ± 0.6907.; *Otof*$^{pga/pga}$ inhibition, 12.30 ± 1.82; *Otof*$^{pga/pga}$ stimulation, 11.10 ± 0.9. Brown-Forsythe and Welch ANOVA followed by Dunnett's post-test, ****, $p < 0.0001$) (Fig. 3.1.3.2.1, Table 5.1.18).

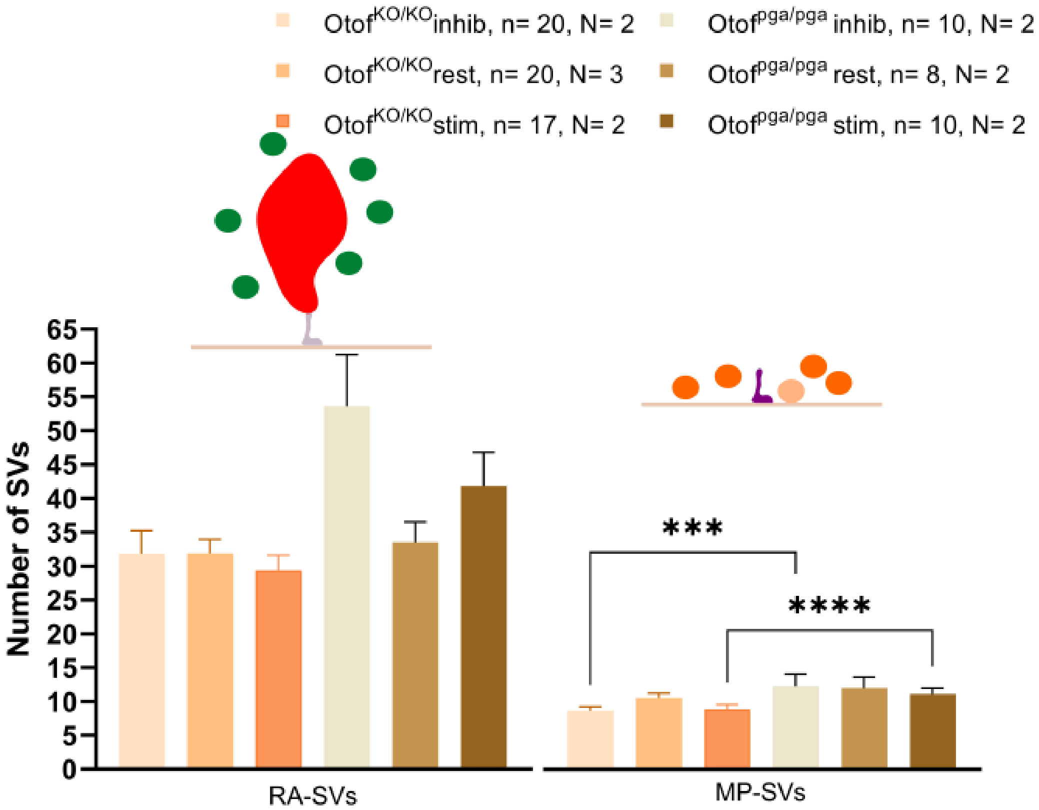

Fig. 3.1.3.2.1: Comparison of RA and MP pools sizes between *Otof$^{KO/KO}$* and *Otof$^{pga/pga}$*. RA- and MP-SV quantification. Similar RA pool sizes were found in both mutants, while statistically significantly smaller MP pool was found in *Otof$^{KO/KO}$* upon inhibition and stimulation. Brown-Forsythe and Welch ANOVA followed by Dunnett's post-test, ***, $p< 0.001$; ****, $p< 0.0001$. Values: Table 5.1.18. All data are shown as mean ± S.E.M.

Moreover, the essential supply of MP-SVs to the release sites is known to be impaired in *Otof$^{pga/pga}$* mutants, whereby impaired release site clearance prevents newly supplied SVs from becoming competent for release (Chakrabarti et al., 2018). Stimulated *Otof$^{KO/KO}$* ribbon synapses contain few docked SVs, possible due to an impairment of MP-SVs in tethering progression until docking. Therefore, differences in SV recruitment for docking between the two mutants might be observed by comparing the non-docked and docked SVs. This comparison revealed similar numbers in non-docked and docked SVs regardless the genotype and activity state (Fig. 3.1.3.2.2, Table 5.1.19).

In summary, this subsection has shown that disruption of Otof results in a smaller MP pool than in *Otof$^{pga/pga}$* synapses. However, the number of non-docked and docked SVs remained similar, which argues against these SVs being the cause for almost abolished (*Otof$^{KO/KO}$*) or the strong impairment in exocytosis (*Otof$^{pga/pga}$*). Instead, differences in MP-SV subpools and their distances to the PD might explain the different severy in exocytosis impairment.

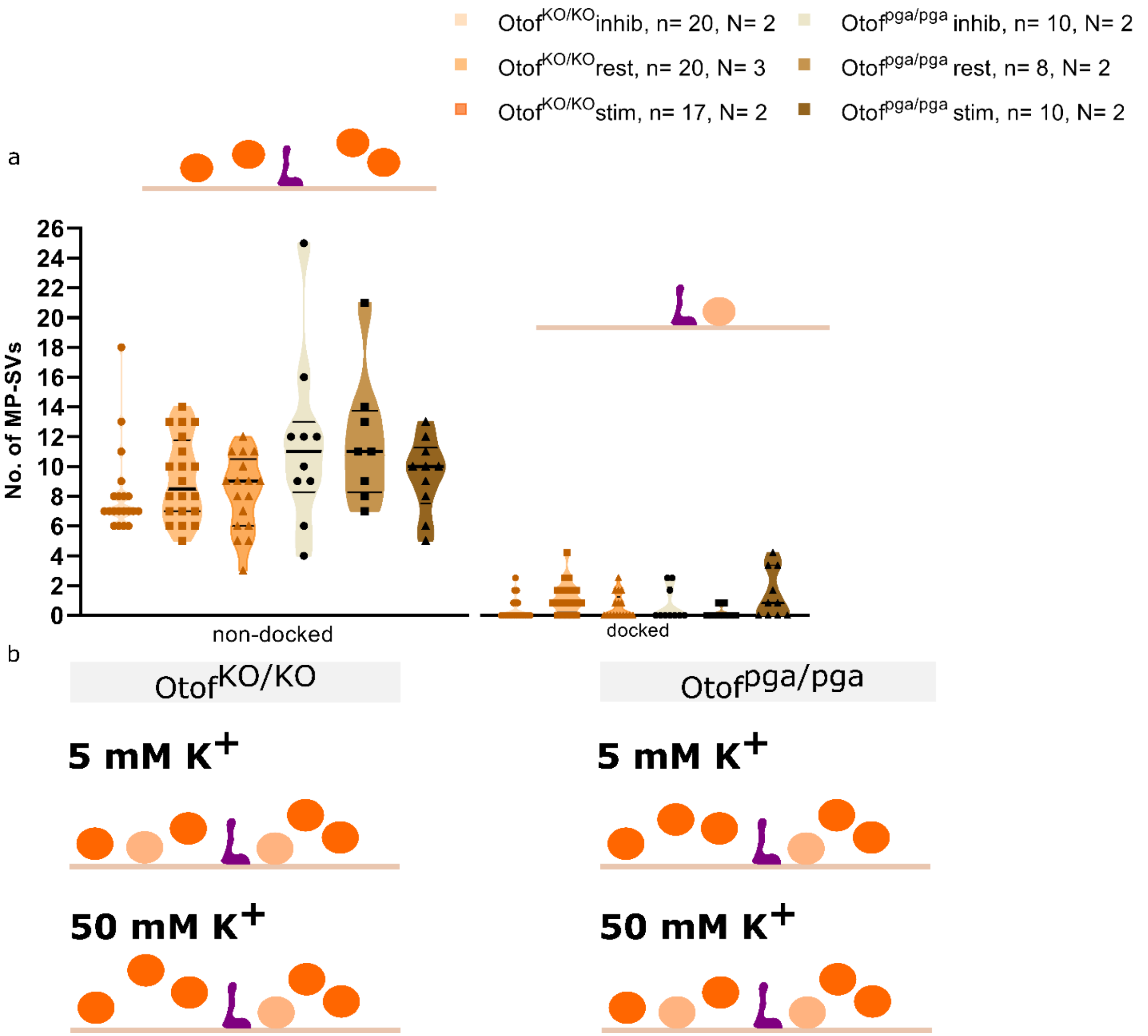

Fig. 3.1.3.2.2: Comparison of non-docked and docked SVs between *Otof*$^{KO/KO}$ and *Otof*$^{pga/pga}$. a, Non-docked (orange) and docked MP-SV (light orange) quantification. No statistically significant differences were observed in the number of non-docked SVs regardless the genotype and activity state. Kruskal-Wallis followed by Dunn's multiple comparison test, *, $p < 0.05$. Values: Table 5.1.19. All data are presented as mean ± S.E.M. **b**, Summary scheme of the effects of activity in the MP pool in *Otof*$^{KO/KO}$ and *Otof*$^{pga/pga}$. Similar number of non-docked (orange) and docked (light orange) SVs are found in both mutants, despite that the MP pool is smaller upon deletion of Otof than in *Otof*$^{pga/pga}$ mutants. Resting condition, 5 mM K^+; stimulatory condition, 50 mM K^+.

3.1.3.3 Analysis of endocytic structures

Previous data has shown that the disruption of Otof results in an increase of endocytic structures in resting conditions (see section 3.1.1.5), while *Otof*$^{pga/pga}$ data behaves similarly to wild-type (see section 3.1.2.2). Comparison of the endocytic structures *Otof*$^{KO/KO}$ in *Otof*$^{pga/pga}$ and permits identifying the difference in impact on the endocytic pathway caused by the lack of Otof and truncation of its full length. Endocytic structures were significantly more abundant in *Otof*$^{KO/KO}$ compared to *Otof*$^{pga/pga}$ in resting conditions (*Otof*$^{KO/KO}$ resting, 21.85 ± 2.29. N= 2, n= 20; *Otof*$^{pga/pga}$ resting, 8.00 ± 2.13. N= 2, n= 8. Kruskal-Wallis, **, p< 0.01). A deeper analysis of the types of endocytic structures showed similar fractions regardless the type, genotype and activity state (Fig. 3.1.3.3, Table 5.1.17, Table 5.1.20).

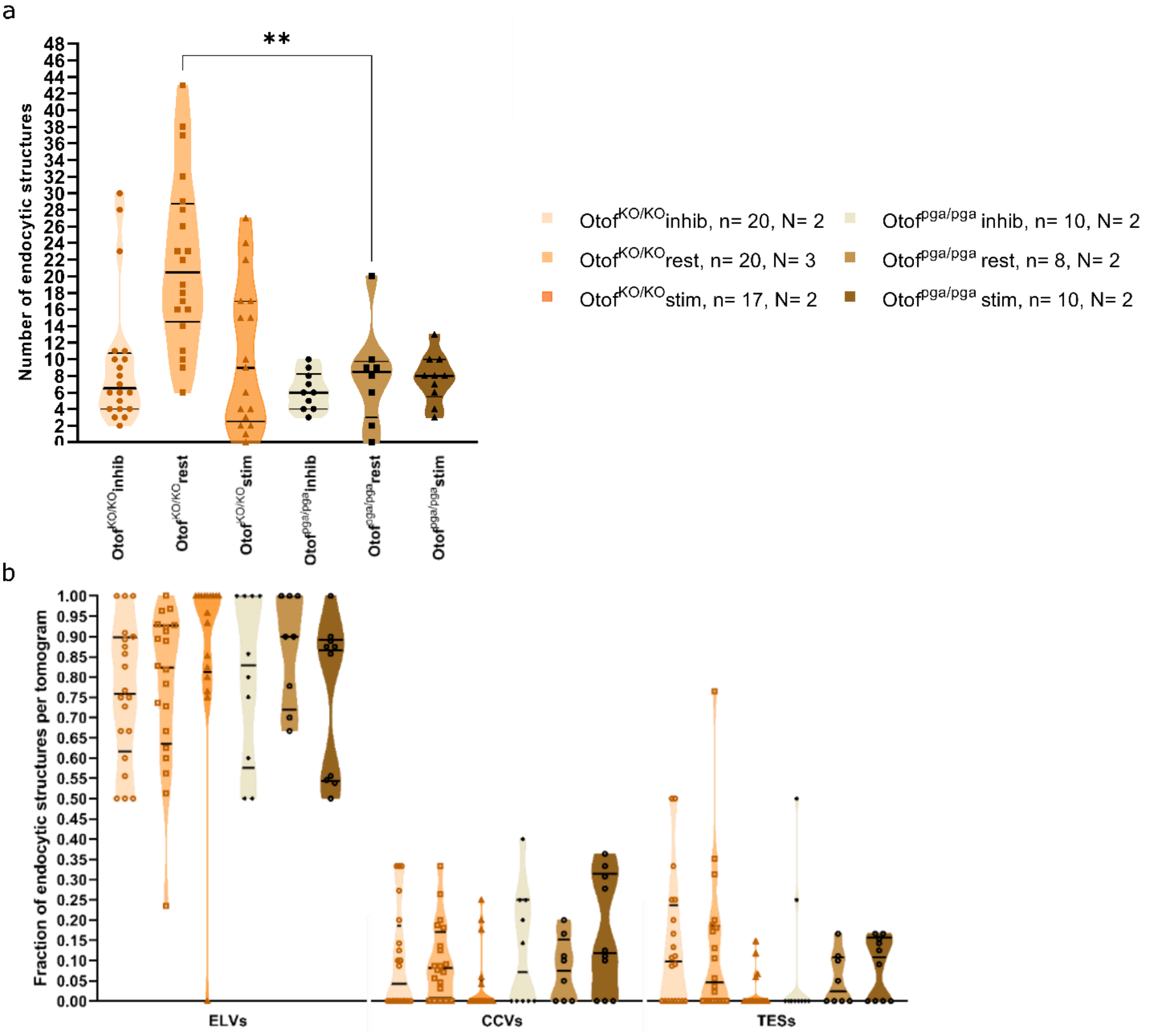

Fig. 3.1.3.3: Comparison of endocytic structures in *Otof*$^{KO/KO}$ and *Otof*$^{pga/pga}$. a, Quantification of endocytic structures. Statistically significant differences were found between *Otof*$^{KO/KO}$ and *Otof*$^{pga/pga}$ in rest. Kruskal-Wallis followed by Dunn's post-test, **, p< 0.01. Values: Table 5.3.17. **b**, Fractions of endocytic structures. Comparable fractions of ELVs, CCVs and TESs were found in both genotypes across condition. Kruskal-Wallis followed by Dunn's post-test, ns, p> 0.05. Values: Table 5.1.20. All data are shown as mean ± S.E.M. (Figure above)

Summary

This section reveals ultrastructural changes in the SV pools and endocytic structures in different activity states in *Otof*$^{KO/KO}$ ribbon synapses with special focus in the MP pool. In addition, this section also contains information about endocytic structures in *Otof*$^{pga/pga}$, and a comparison between *Otof*$^{KO/KO}$ and *Otof*$^{pga/pga}$ ultrastructural data.

Briefly, stimulated *Otof*$^{KO/KO}$ showed that the recruitment of MP-SVs to the AZ membrane and the release sites might be severely reduced, as inferred from the increased distance of single tethered SVs to the plasma membrane. Conversely, stimulated *Otof*$^{KO/KO}$ synapses results in the formation of a normal number of endocytic structures, which is comparable to stimulated *Otof*$^{pga/pga}$ synapses. Notably, resting of *Otof*$^{KO/KO}$ ribbon synapses present more endocytic structures than *Otof*$^{pga/pga}$ ribbon synapses

In a nutshell, the results from this section show that Otof is essential in the approach of tethered SVs to the AZ membrane during activity, which leads to SV docking. In contrast, the quantification of endocytic structures in both mutants do not contribute to clarify the role of Otof in endocytosis and SV reformation.

3.2 ULTRASTRUCTURAL CORRELATES OF EXOCYTOSIS AND ENDOCYTOSIS IN RIBBON-OCCUPIED AND RIBBON-LESS SYNAPSES

In the first part of my thesis, I investigated two Otof mutants that interfered with the SV cycle. In the following subsections, I will analyse the ultrastructural consequences of a drastic disturbance in the AZ structure, the lack of the synaptic ribbon due to the disruption of RBE. These mutants showed a mild reduction in hearing and unaltered exocytosis under strong stimulation (Becker et al., 2018; Jean et al., 2018). However, the ultrastructural effects upon activity of the absence of ribbon are poorly understood. Therefore, I studied *RBE*$^{wt/wt}$ and *RBE*$^{KO/KO}$ ribbon synapse architecture upon 15 minutes stimulation and applied two different analysis criteria to understand how the lack of ribbon affects the distribution of the different SV pools and endocytic structures.

In the appendix, I disclose the tomogram orientation due to impact on the access to visual data for analysis. Tomograms were classified as cross-section, longitudinal an in-between (Table 5.2.1).

Values of quantifications and fractions presented in this section can be found in section 5.2.

3.2.1 Ultrastructural effects of *RBE*$^{KO/KO}$ synapses following ribbon synapse analysis criteria

Previous ultrastructural studies have classified the SVs surrounding the ribbon into different pools, whose classification parameters vary depending on the sample or the method of immobilisation for electron microscopy (Chakrabarti et al., 2018; Gersdorff et al., 1996; Lenzi et al., 1999; Michanski et al., 2019). These morphological SVs pools, and more recently subpools, allow to correlate structure and function for ribbon synapses. For instance, RA-SVs replenish the MP pool being the SV source upon prolonged stimulation, as observed by chemically forcing the release machinery to work exhaustively in saccular and cochlear ribbon synapses (Chakrabarti et al., 2018; Lenzi et al., 2002). Therefore, determining similar morphological pools (see section 2.4.12) in *RBE*$^{wt/wt}$ and *RBE*$^{KO/KO}$ ribbon synapses permits to understand whether stimulation results into depletion of specific SV pools in the mutant.

3.2.1.1 Structure organisation in RBE$^{KO/KO}$ *and RBE*$^{wt/wt}$ *ribbon synapses upon 15-minute stimulation*

Previous studies have pointed the ribbon/RBE to act as a SV reservoir that replenishes MP-SV upon stimulation, as well as having a role in the organisation and inactivation dynamics of $Ca_V1.3$ channels in the AZ membrane (Becker et al., 2018; Frank et al., 2010; Jean et al., 2018; Khimich et al., 2005). Removing such a prominent structure like the ribbon might lead to morphological changes in the SV pools and subpools upon strong and prolonged stimulation. As reported in the literature (Becker et al., 2018; Jean et al., 2018;

Maxeiner et al., 2016), *RBE*$^{KO/KO}$ results in the absence of the synaptic ribbon (Fig. 3.2.1.1) and the formation of multiple PDs per AZ (Table 3.2.1.1). Despite that some AZ in my tomograms presented two PDs, the SV pool analysis was performed individually per PD.

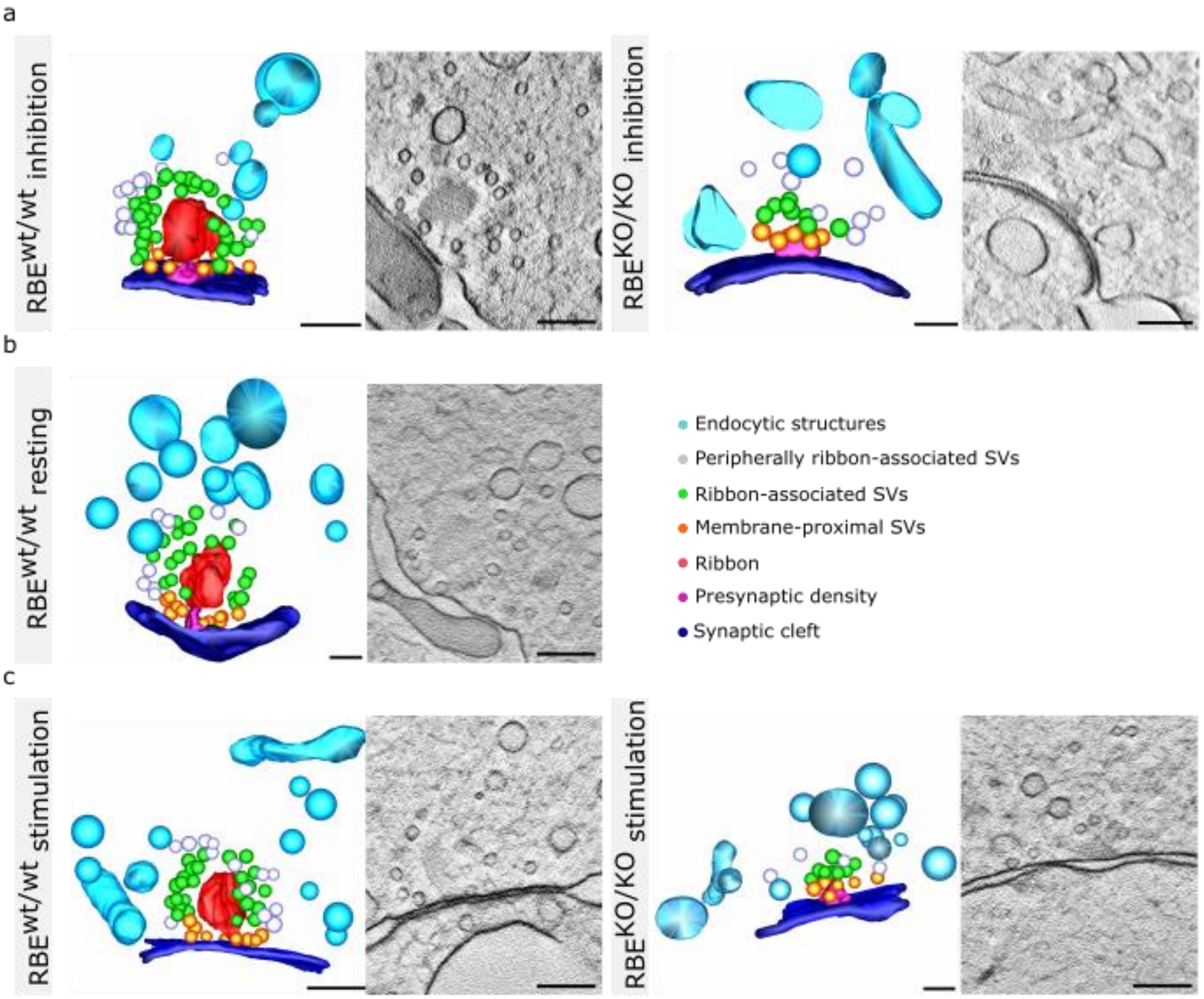

Fig. 3.2.1.1.1: Quantified structures found in ribbon-occupied and ribbon-less synapse after 15 minutes stimulation. a-c, Representative models and virtual section of *RBE*$^{wt/wt}$ and *RBE*$^{KO/KO}$ synapses upon inhibition, rest and stimulation. Endocytic structures are presented in blue, periRA-SVs are shown in white, RA/PDA-SVs are depicted in green and MP -SVs are coloured in orange. This colour code will be maintained along the figures of the next subsections. Magnification, x12,000; virtual section scale bars, 200 nm; wild-type model scale bar, 200 nm; mutant model scale bar, 100 nm.

Experimental condition		Single	Double
RBE$^{wt/wt}$ inhibition	N= 1, n= 7	7	0
RBE$^{wt/wt}$ resting	N= 1, n= 6	6	0
RBE$^{wt/wt}$ stimulation	N= 2, n= 7	7	0
RBE$^{KO/KO}$ inhibition	N= 2, n= 6	4	1
RBE$^{KO/KO}$ stimulation	N= 2, n= 6	4	1

Table 3.2.1.1: Number of tomograms containing single or multiple synaptic ribbons or PDs per AZ.

Single synaptic ribbons were only observed in wild-type tomograms, while one tomogram per condition in $RBE^{KO/KO}$ samples presented double PDs.

Functional studies in ribbon-less IHCs have shown normal sustained exocytosis (Becker et al., 2018; Jean et al., 2018; Maxeiner et al., 2016), since the formation of multiple PDs per AZs functionally seems to compensate for the phenotype (Jean et al., 2018). It is unknown how the recruitment of SVs by a given PD happens to maintain exocytosis upon stimulation. Therefore, the fractions of endocytic structures, peripherally RA/PDA (periRA/PDA), RA/PDA and MP-SVs were quantified. Statistically significant differences were found in the fraction of RA-SVs in inhibitory conditions comparing $RBE^{wt/wt}$ and $RBE^{KO/KO}$ ($RBE^{wt/wt}$ inhibition, 0.50 ± 0.04; $RBE^{KO/KO}$ inhibition, 0.31 ± 0.03. One-way ANOVA followed by Šidák's post-test, *, $p < 0.05$) (Fig. 3.2.1.2, Table 5.2.2).

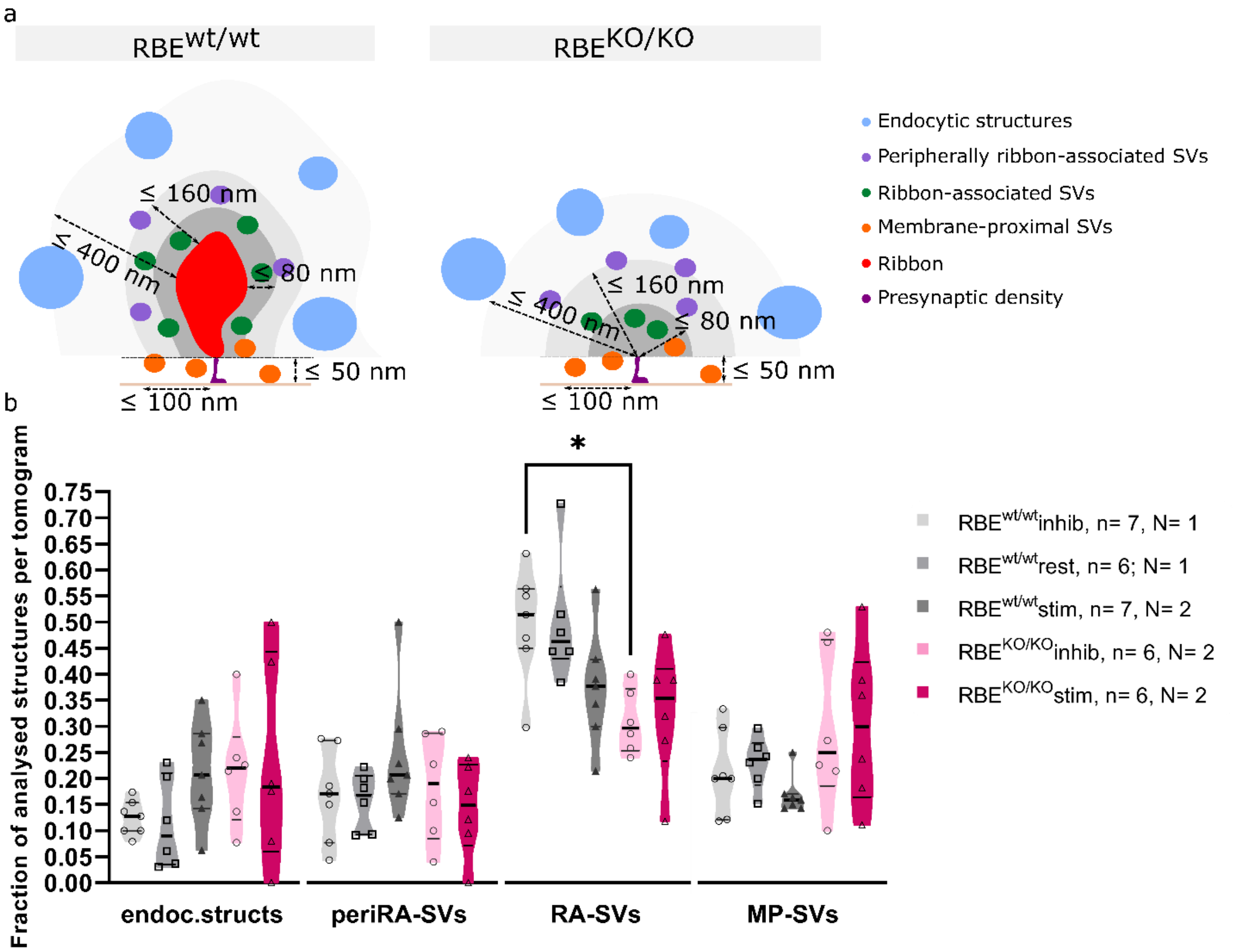

Fig. 3.2.1.1.2: Quantification of analysed structures in the ribbon synapse after 15 minutes stimulation. a, Summary diagram of ribbon-occupied and ribbon-less synapse analysis criteria. **b**, Fraction of analysed structures in RBE$^{wt/wt}$ and RBE$^{KO/KO}$ in different activity states. Significant differences are found between RBE$^{wt/wt}$ and RBE$^{KO/KO}$ in inhibitory conditions. One-way ANOVA followed by Šidáks's post-test and Kruskal-Wallis followed by Dunn's post-test, *, $p < 0.05$. Values: Table 5.2.2. Data are show in mean ± S.E.M.

3.2.1.2 Ribbon-associated and membrane-proximal pool characterisation

Prolonged stimulation requires fast SV replenishment provided by MP and RA-SVs to replace the fused SVs (Chakrabarti et al., 2018; Lenzi et al., 2002; Lenzi and von Gersdorff, 2001). However, the lack of ribbon in *RBE$^{KO/KO}$* synapses produces a change in the definition of RA pool, whereby these SVs are now categorised as PDA-SVs (see section 2.3.12). The fraction of RA-SVs previously showed comparable amounts of RA/PDA-SVs per ribbon/PD, except in inhibited condition. Therefore, quantification of the number of RA/PDA was performed to confirm previous results on the smaller pool of SVs at the PD compared to the RA pool (Jean et al., 2018). In addition, this quantification might also reveal whether PDA-SVs are depleted upon prolonged stimulation. Furthermore, since replenishing the MP is required for sustained stimulation, the MP pool size was also quantified. The RA/PDA and MP pools are significantly smaller in *RBE*$^{KO/KO}$ compared to *RBE*$^{wt/wt}$ upon inhibition (RA/PDA-SVs: *RBE*$^{wt/wt}$ inhibition, 30.71 ± 4.05; *RBE*$^{wt/wt}$ stimulation, 14.14 ± 3.13; *RBE*$^{KO/KO}$ inhibition, 7.00 ± 0.68. Kruskal-Wallis followed by Dunn's post-test, ***, p< 0.001. MP-SVs: *RBE*$^{wt/wt}$ inhibition, 8.00 ± 0.57; *RBE*$^{wt/wt}$ stimulation, 8.06 ± 0.61; *RBE*$^{KO/KO}$ inhibition, 8.65 ± 0.62, Kruskal-Wallis, *, p< 0.05) (Fig. 3.2.1.2.1, Table 5.2.3).

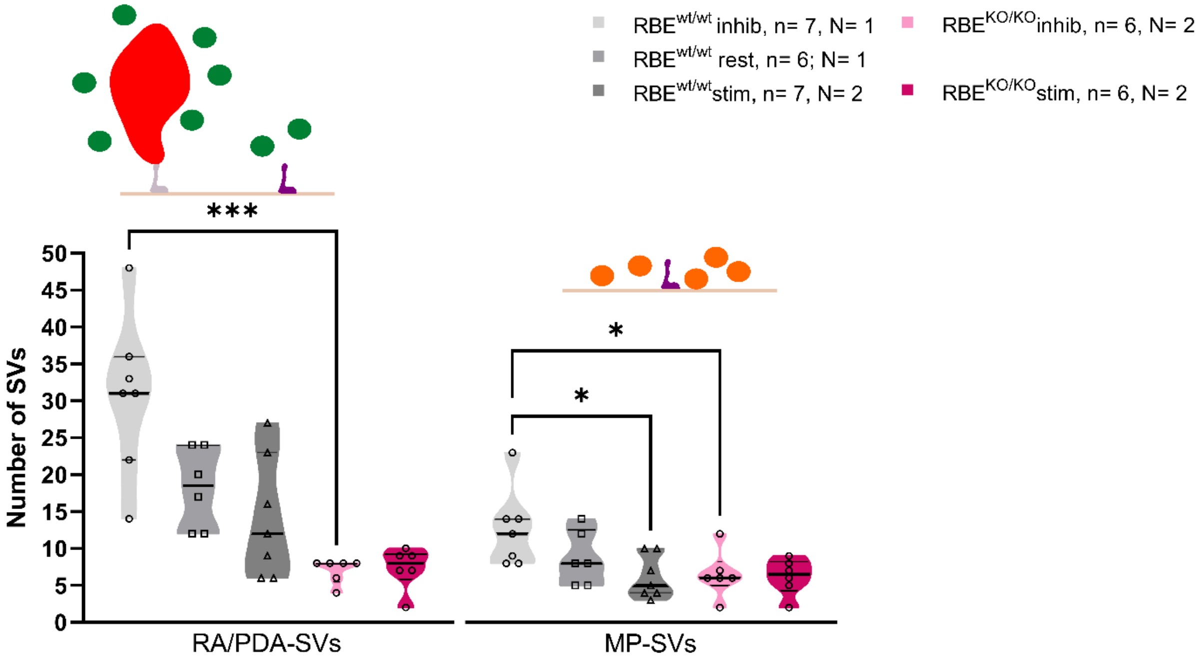

Fig. 3.2.1.2.1: RA/PDA and MP pool quantification per tomogram. Statistically significantly smaller RA/PDA pool is found in RBE$^{KO/KO}$ upon inhibition, and significantly fewer MP-SVs are counted in inhibited RBE$^{wt/wt}$ ribbon synapses compared to stimulated ones and RBE$^{KO/KO}$ inhibited synapses. Kruskal-Wallis followed by Dunn's post-test, *, p< 0.05; ***, p< 0.001. Values: Table 5.2.3. All data are shown as mean ± S.E.M.

Recruitment of these SVs for release can be assessed by measuring the distances to either prominent structure (ribbon or AZ membrane). Stimulation likely triggers a shortening of filaments, especially at the lower half of the ribbon (Chakrabarti et al., 2018), which may be translated as a decrease in the distance to the ribbon. Engagement of SVs to the PD and the AZ is expected to happen, since exocytosis is maintained in ribbon-less synapses (Becker et al., 2018; Jean et al., 2018; Maxeiner et al., 2016). Furthermore, the observed abnormal distribution of Ca_V1.3 channels (Jean et al., 2018) may impact on the coupling between Ca_V1.3 channels and MP-SVs, which might have ultrastructural consequences on the topographic distribution of MP-SVs, especially on docked SVs (Fig. 3.2.1.2.2a). Quantifying the lateral distance of MP-SVs to the PD surface might provide information in this regard.

RA/PDA-SVs were found at comparable distances from the surface of the ribbon or PD regardless the condition (Fig. 3.2.1.2.2b). Notably, MP-SVs are found significantly closer to the AZ membrane in $RBE^{wt/wt}$ in resting and stimulatory conditions compared to inhibition. Conversely, stimulation impairs MP-SV approach to the plasma membrane in $RBE^{KO/KO}$ compared to $RBE^{wt/wt}$ ($RBE^{wt/wt}$ inhibition, 23.81 ± 1.46; $RBE^{wt/wt}$ resting, 17.07 ± 2.23; $RBE^{wt/wt}$ stimulation, 15.16 ± 2.16; $RBE^{KO/KO}$ stimulation, 24.77 ± 2.51. Kruskal-Wallis followed by Dunn's post-test, *, $p < 0.05$; **, $p < 0.01$). Lastly, MP-SVs are found at similar distances from the PD in all genotypes and activity states (Fig. 3.2.1.2.2c, d, Table 5.2.4).

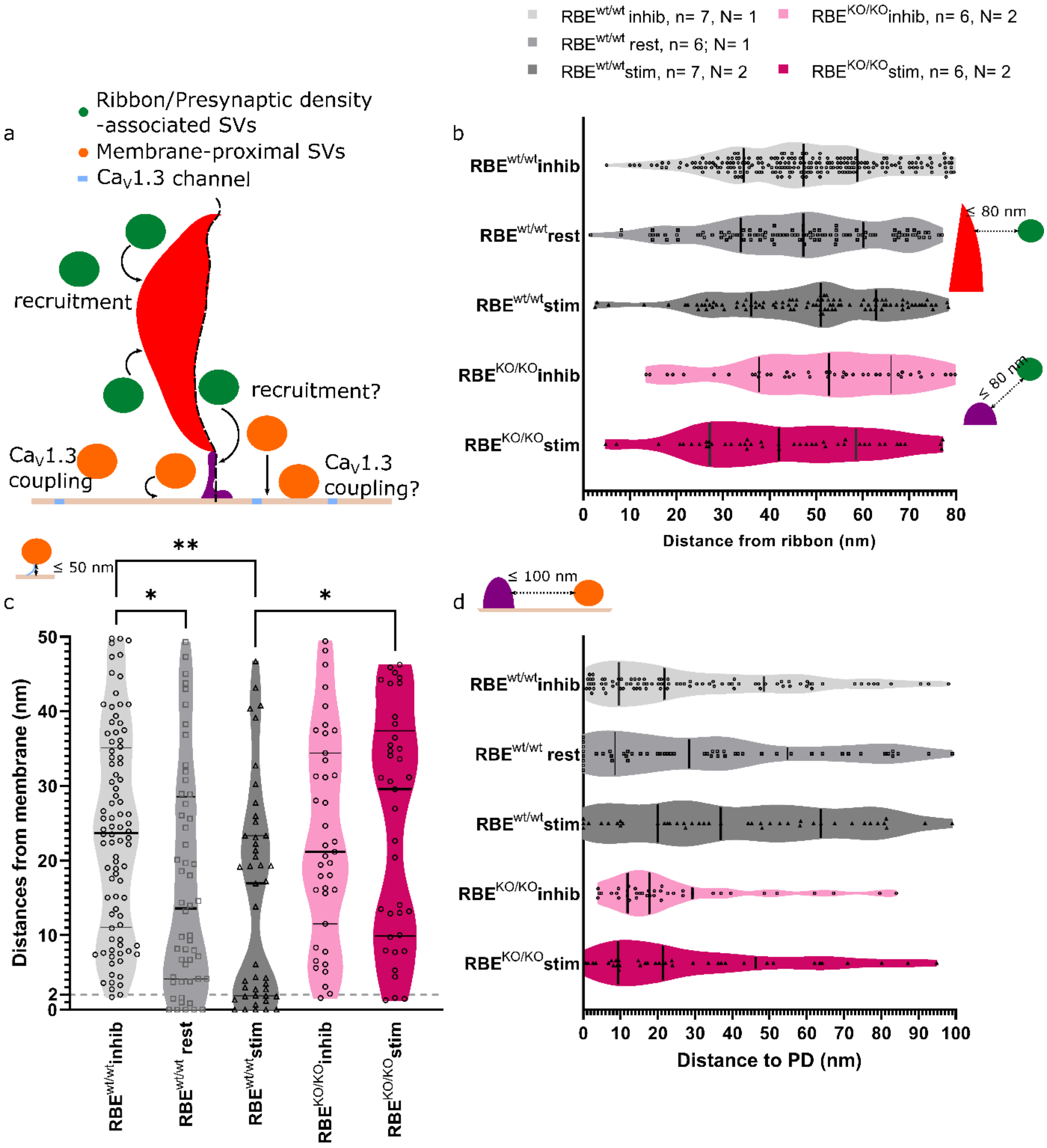

Fig. 3.2.1.2.2: Quantification of the distance measurements of RA/PDA-SVs and MP-SVs. a, The distance of RA/PDA-SVs might indicate the recruitment of SVs for replenishment of the MP pool, while the distance to the AZ membrane indicates the recruitment of MP-SVs to be released later. The transient spatial coupling between Ca^{2+} and SVs might differ between the wild-type and mutant conditions, which changes in the distance of MP-SVs to the PD surface might be observed. **b**, The distance of RA/PDA-SVs to the ribbon/PD surface reveals no significant differences in any of the conditions. Kruskal-Wallis by Dunn's multiple comparisons test, ns, p> 0.05. **c**, The distance to the AZ membrane of MP-SVs is significantly smaller upon rest and stimulation than inhibition in RBE$^{wt/wt}$ ribbon synapses. This distance is larger in RBE$^{KO/KO}$ than in RBE$^{wt/wt}$ upon stimulation. Kruskal-Wallis followed by Dunn's post-test, ns, p> 0.05; **, p< 0.01. d, No statistically significant differences are found in the distance of MP-SVs to the PD surface in any of the genotypes in any of the activity states. Kruskal-Wallis followed by Dunn's multiple comparisons test, *, p< 0.05; **, p< 0.01. Values: Table 5.2.4. Each sample point of the violin plot corresponds to the average distance measurement of a SVs. Each sample point of the violin plot corresponds to the average distance measurement of a SVs. All data are presented as mean ± S.E.M. (Figure above)

Previous studies in ribbon-less synapses have shown that fewer AZ present single PDs (80%), while the there is an increase in double and triple PDs per AZ (20%) compared to wild-types (Jean et al., 2018). IHCs with these ultrastructural features can maintain exocytosis indefatigably, hence the number of docked SV might be similar between *RBE*$^{KO/KO}$ and *RBE*$^{wt/wt}$ synapses. The number of docked SVs remained constant in all conditions, while non-docked SVs were significantly fewer *in RBE*$^{wt/wt}$ upon stimulation compared to inhibition (*RBE*$^{wt/wt}$ inhibition, 12.29 ± 1.94; *RBE*$^{wt/wt}$ stimulation, 4.43 ± 0.72. Kruskal-Wallis followed by Dunn's post-test, **, p< 0.01) (Fig. 3.2.1.2.3, Table 5.2.5).

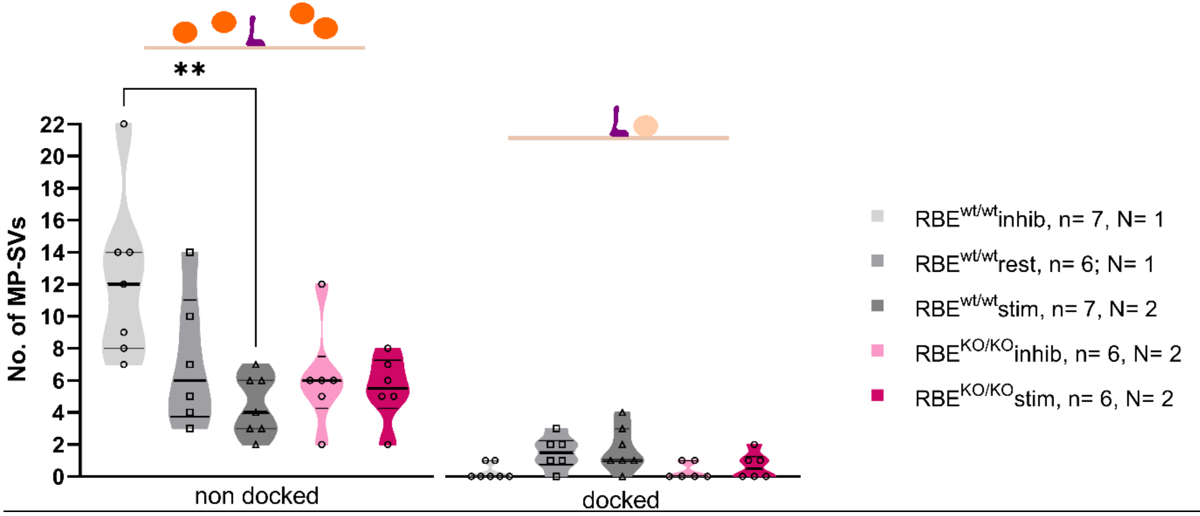

Fig. 3.2.1.2.3: Quantification of non-docked and docked SVs in *RBE*$^{wt/wt}$ and *RBE*$^{KO/KO}$. Average count of non-docked (orange) and docked (light orange) MP-SVs. Significantly fewer non-docked SVs are found in the wild-type upon stimulation compared to inhibition. Kruskal-Wallis, **, p< 0.01. Values: Table 5.2.5. Data are presented as mean ± S.E.M.

The distances to the AZ membrane as well as to the PD of MP-SVs give an indication of the topographic distribution of the SVs. This is an important read-out for docked SVs this is an important since they might represent the release ready SVs. Non-docked SVs in *RBE*$^{wt/wt}$ ribbon synapses were found significantly further away from the PD upon stimulation compared to inhibition (*RBE*$^{wt/wt}$ inhibition, 30.62 ± 2.77; *RBE*$^{wt/wt}$ stimulation, 48.04 ± 4.88. Kruskal-Wallis followed by Dunn's post-test, **, p< 0.01). Docked SVs are defined by their distances to the AZ membrane of 0-2 nm, so that their distances are uniform between all conditions. We refrained from perfoming statistical analysis in the docked SVs distances due to the reduced SV numbers (Fig. 3.2.1.2.4, Table 5.2.6).

This subsection shows that stimulation results in a slightly smaller PDA and MP pools in *RBE*$^{KO/KO}$ compared to *RBE*$^{wt/wt}$. Despite that continuous exocytosis can be maintained in *RBE*$^{KO/KO}$ IHCs (Becker et al., 2018; Jean et al., 2018; Maxeiner et al., 2016), the recruitment of MP-SVs to the AZ membrane is smaller than than in wild-type conditions.

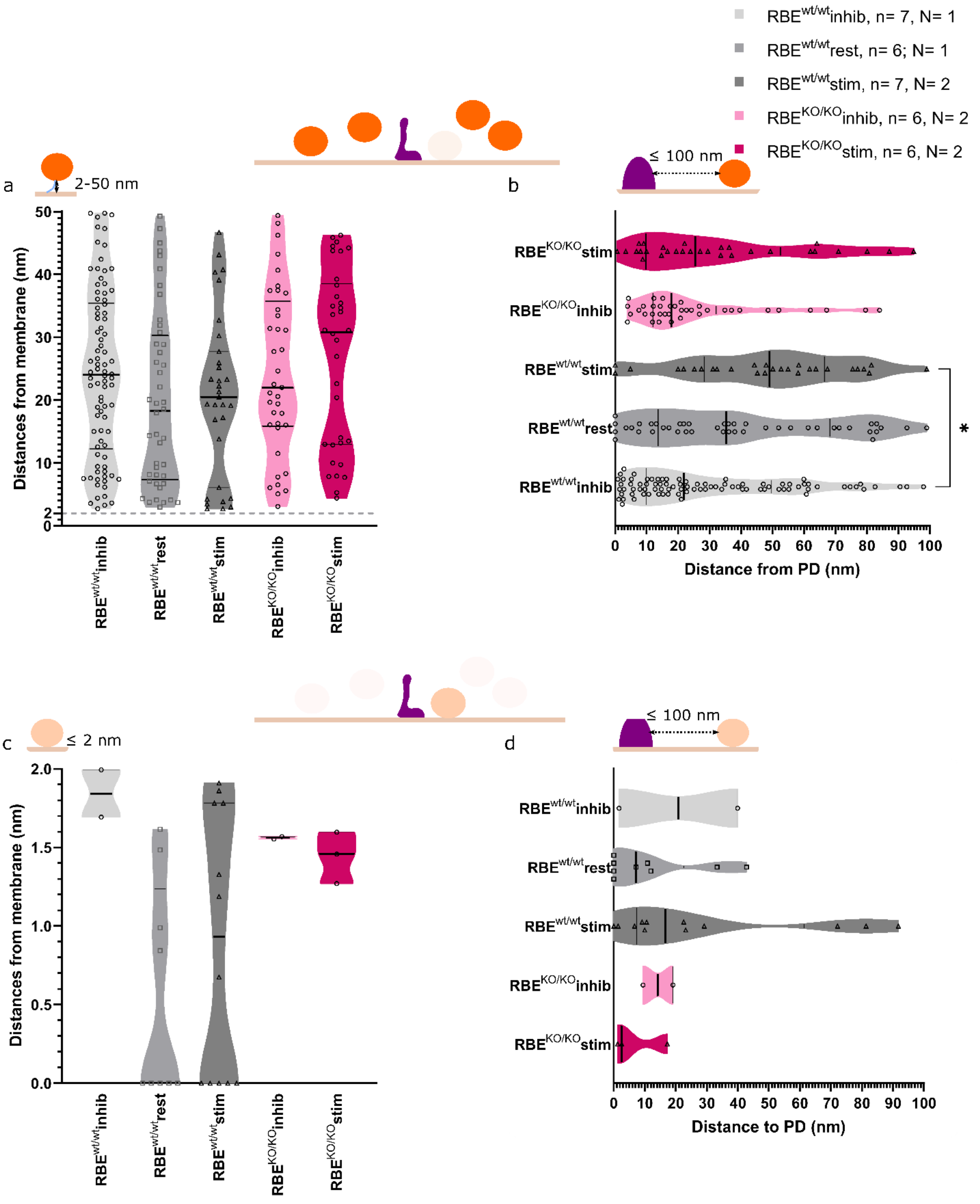
RBE^wt/wt inhib, n= 7, N= 1
RBE^wt/wt rest, n= 6; N= 1
RBE^wt/wt stim, n= 7, N= 2
RBE^KO/KO inhib, n= 6, N= 2
RBE^KO/KO stim, n= 6, N= 2
a
2-50 nm
Distances from membrane (nm)
50
40
30
20
10
2
0
RBE^wt/wt inhib
RBE^wt/wt rest
RBE^wt/wt stim
RBE^KO/KO inhib
RBE^KO/KO stim
b
≤ 100 nm
RBE^KO/KO stim
RBE^KO/KO inhib
RBE^wt/wt stim
RBE^wt/wt rest
RBE^wt/wt inhib
*
0
10
20
30
40
50
60
70
80
90
100
Distance from PD (nm)
c
≤ 2 nm
Distances from membrane (nm)
2.0
1.5
1.0
0.5
0.0
RBE^wt/wt inhib
RBE^wt/wt rest
RBE^wt/wt stim
RBE^KO/KO inhib
RBE^KO/KO stim
d
≤ 100 nm
RBE^wt/wt inhib
RBE^wt/wt rest
RBE^wt/wt stim
RBE^KO/KO inhib
RBE^KO/KO stim
0
10
20
30
40
50
60
70
80
90
100
Distance to PD (nm)

Fig. 3.2.1.2.4: Quantification of the distances of non-docked and docked MP-SVs to membrane and PD in *RBE*$^{wt/wt}$ and *RBE*$^{KO/KO}$. a, Distances of non-docked SVs to the AZ membrane. No statistically significant differences are found in any condition. Kruskal-Wallis followed by Dunn's post-test, *, $p < 0.05$. Values: Table 5.2.6. **b**, Distances of non-docked MP-SVs to the PD surface, whereby their distance is reduced in wild-type upon inhibition compared to stimulation. Kruskal-Wallis followed by Dunn's post-test, *, $p < 0.05$. Values: Table 5.2.6. **c-d**, Distances of docked SVs to the plasma membrane and the PD surface. Comparable distances are found in all genotypes and activity states. Each sample point of the violin plot corresponds to the average distance measurement of a SVs. All data are shown as mean ± S.E.M. (Figure above)

3.2.1.3 Membrane-proximal SV subpool analysis

Tether formation in MP-SVs seems required for them to achieve competence for fusion, since tethering engages SVs to a release site at the AZ membrane. The proposed SV release sequence entails SVs to establish single tethers with the PD and then the AZ membrane, followed by the formation of multiple tethers and docking to the membrane (Chakrabarti et al., 2018). Analysis of the SV subpools might indicate the importance of the ribbon for the normal advance of SVs towards their release. Stimulation produced a significant decrease in the fraction of tethered SVs compared to inhibition in *RBE*$^{wt/wt}$ (*RBE*$^{wt/wt}$ inhibition, 0.84 ± 0.053; *RBE*$^{wt/wt}$ stimulation, 0.55 ± 0.11. Kruskal-Wallis followed by Dunn's post-test, *, $p < 0.05$), (Fig. 3.2.1.3.1, Table 5.2.7). Furthermore, tethered SVs can be classified into single tethered and multiple tethered, whose relative proportions remained similar across genotypes and activity states (Table 5.2.7, Table 5.4.9).

Subsequently, the distances of MP-SVs to the AZ membrane revealed that SVs in wild-type and mutant behave similarly in all conditions per SV subpool. The distance of MP-SVs to the PD surface showed that tethered MP-SVs in inhibited *RBE*$^{wt/wt}$ are closer than upon stimulation (*RBE*$^{wt/wt}$ inhibition, 29.93 ± 2.90 *RBE*$^{wt/wt}$ stimulation, 46.30 ± 5.063. Kruskal-Wallis followed by Dunn's post-test, *, $p < 0.05$) (Fig. 3.2.1.3.2, Table 5.2.8).

To summarise, this subsection showed that SV subpools were comparable between wild-type and mutant. Moreover, the distances of MP-SVs to the AZ membrane and the PD surface was similar between *RBE*$^{wt/wt}$ and *RBE*$^{KO/KO}$ synapses. A bigger sample size is necessary to draw a conclusive statement about the recruitment of MP-SVs to the AZ membrane upon stimulation.

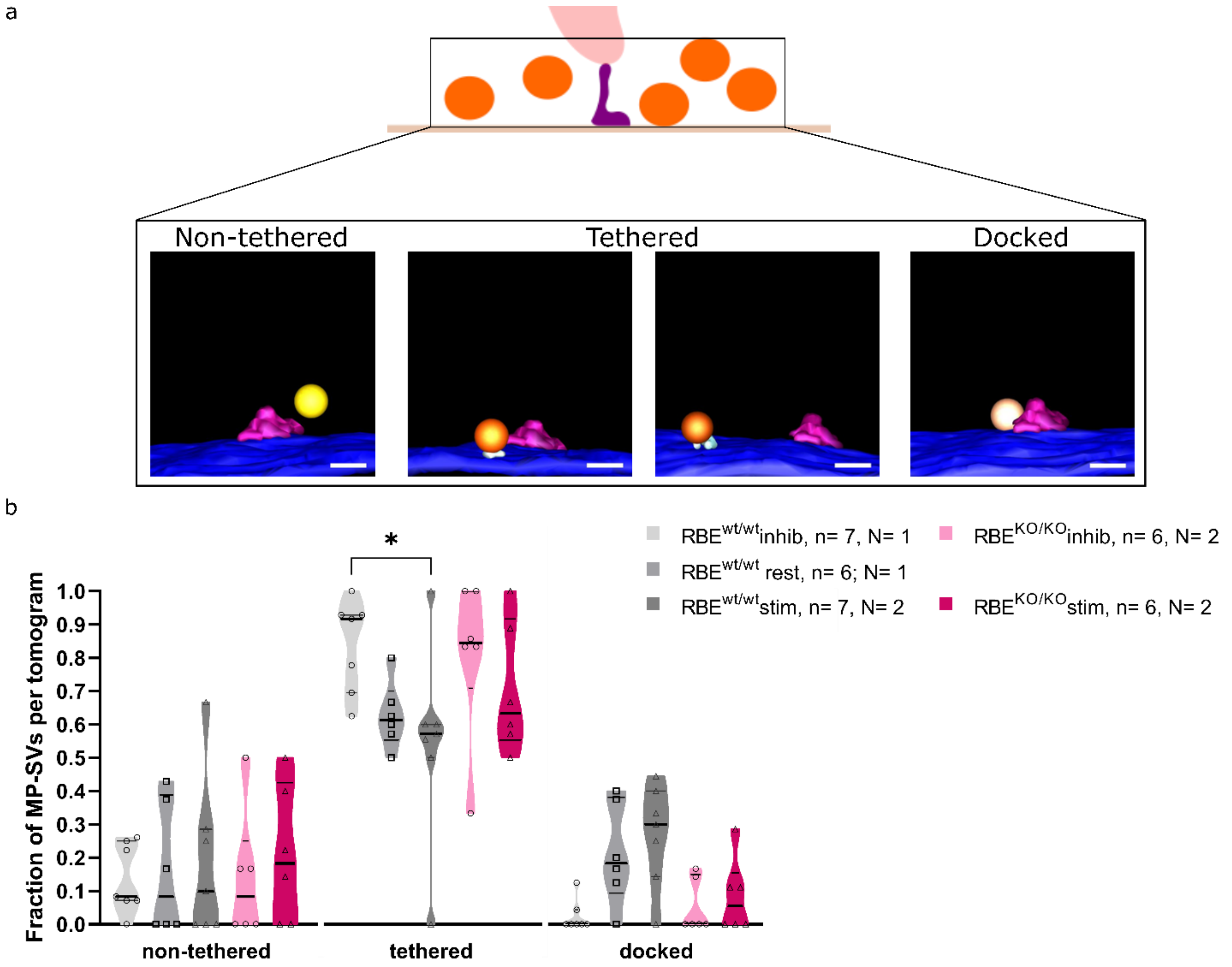

Fig. 3.2.1.3.1: Classification of MP-SVs according to the tethering state. a, Diagram of MP-SV types according to the presence of tethers and proximity to the AZ membrane. SVs can be found non-tethered, tethered and docked. Scale bar, 50 nm. **b**, Fraction of non-tethered, tethered and docked MP-SVs. A significantly smaller fraction of tethered MP-SVs is found in RBE$^{wt/wt}$ upon stimulation compared to inhibition. Kruskal-Wallis followed by Dunn's post-test, *, $p < 0.05$. Values: Table 5.2.7. All data are shown as mean ± S.E.M.

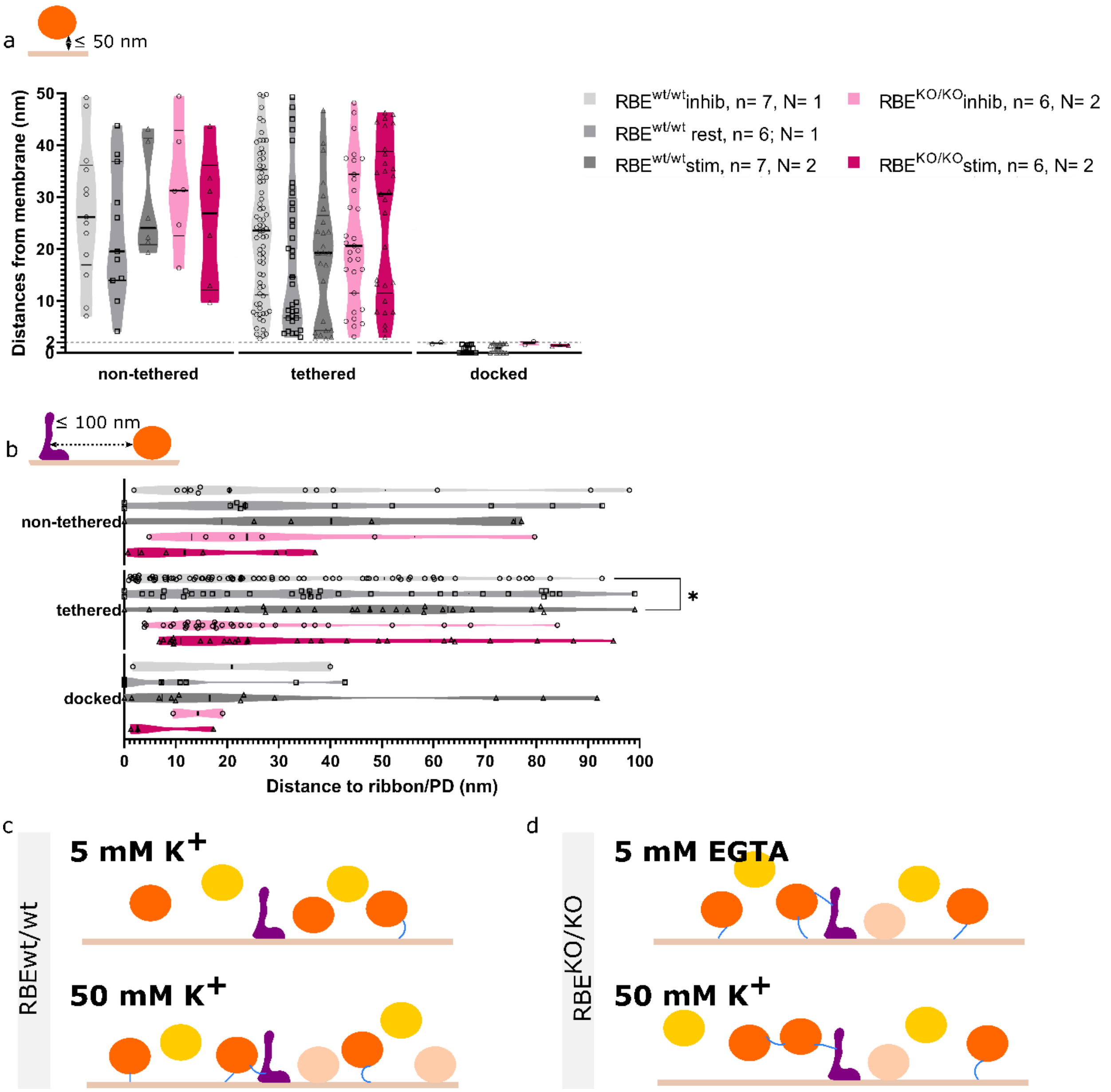

Fig. 3.2.1.3.2: Distance to membrane and PD of MP-subpools. a-b, Distances of MP-SVs to the membrane and PD per tethered category. MP-SVs are found at similar distances from the AZ membrane regardless the genotype and activity state. The distance of tethered MP-SVs to the PD was significantly smaller upon inhibition than stimulation in wild-type ribbon synapses. Kruskal-Wallis followed by Dunn's post-test, *, $p < 0.05$. Values: Table 5.2.8. Each sample point of the violin plot corresponds to the average distance measurement of a SVs. Data are show in mean ± S.E.M. **c-d**, Summary scheme of the effects of activity in $RBE^{wt/wt}$ and $RBE^{KO/KO}$ synapses. Stimulated (50 mM K^+) wild-type ribbon synapses show a mild increase in docked SVs, while in mutant synapses non-tethered, tethered and docked SVs remain comparable to the resting condition (5 mM K^+). In addition, the distance to the membrane and the PD from each category of MP-SVs remains similar for stimulated and resting states.

.

3.2.1.4 Endocytic structures

Loss of the synaptic ribbon has been shown to slightly reduce the replenishment of SVs (Jean et al., 2018), in which the synaptic ribbon might required to capture newly formed SVs (Chakrabarti et al., 2018). I quantified the endocytic structures present in the proximity of the synaptic ribbon/PD (see section 2.3.12) and categorised them into ELVs and CCVs.

Similar numbers of endocytic structures were found in wild-type and mutant synapses regardless the activity state (Fig. 3.2.1.4a, Table 5.2.3). Moreover, these endocytic structures were subcategorised into CCVs and ELVs. An accumulation of either one of the structures could hint towards a hindered SV recycling. Stimulation of $RBE^{wt/wt}$ ribbon synapses results in a decrease in ELVs and an increase of CCVs, since during rest only ELVs were found. These data are preliminary and therefore conclusions can only be drawn very carefully (ELVs: $RBE^{wt/wt}$ resting, 1.00 ± 0.00; $RBE^{wt/wt}$ stimulation, 0.57 ± 0.13. Kruskal-Wallis followed by Dunn’s post-test, *, $p < 0.05$. CCVs: $RBE^{wt/wt}$ resting, 0.00 ± 0.00; $RBE^{wt/wt}$ stimulation, 0.43 ± 0.13. Kruskal-Wallis, *, $p < 0.05$) (Fig. 3.2.1.4b, Table 5.2.10).

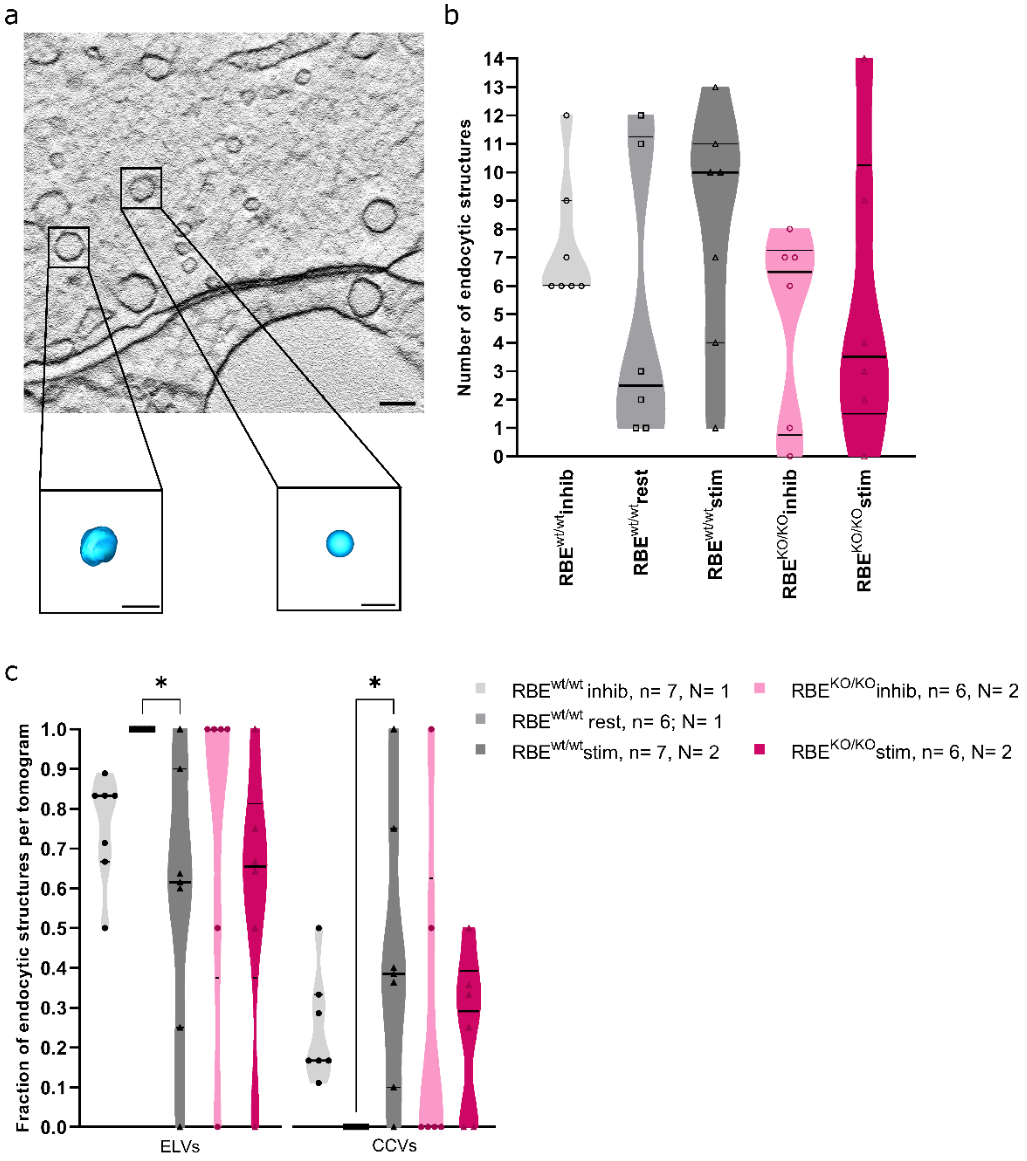

Fig. 3.2.1.4: Quantification of endocytic structures. a, Average number of endocytic structures in a ≤400 nm distance from the ribbon/PD surface. Non-significant differences are shown between wild-type and mutant regardless of the activity state. Kruskal-Wallis followed by Dunn's post-test, ns, $p > 0.05$. **b**, Fractions of endocytic structures. The proportion of ELVs significantly decrease, while the fraction of CCVs significantly increases in stimulated ribbon-occupied synapses compared to rest in wild-type ribbon synapses. Kruskal-Wallis followed by Dunn's post-test, *, $p < 0.05$. Values: Table 5.2.3, Table 5.2.10. Data are show in mean ± S.E.M.

3.2.2 Ultrastructural effects of RBE$^{KO/KO}$ synapses following conventional synapse analysis criteria

Quantification of SVs from the AZ membrane in certain synapse area is a method for ultrastructural analysis of activity and age-related changes in conventional synapses (Hintze et al., 2021; Imig et al., 2014; Maus et al., 2020). Typically, the focus of this analysis is made in the docked SVs, since they represent the RRP in conventional synapses (Imig et al., 2014). Application of conventional synapse analysis criteria – like for example Hintze et al. (2021) and others (Imig et al., 2014; Maus et al., 2020) – in ribbon-occupied and ribbon-less synapses might give insight into the SV distribution at the AZ on the basis of their distance to the membrane. SVs were categorised into bins within a volume of 200 x 200 x 400 nm (see section 2.4.12) and their relative abundance was plotted. These criteria might reveal any polarised distribution of SVs as a consequence of activity. Then, we focused on the quantification and frequency distribution of SVs found up to 40 nm from the AZ membrane, which include also docked SVs, to study what is considered membrane proximal in conventional synapses (Hintze et al., 2021).

3.2.2.1 SV organisation in 40 nm bins

First, general activity-based changes in the architecture of ribbon-occupied and ribbon-less synapses were studied by quantifying SVs into 40 nm bins (Fig. 3.2.2.1.1a; also see section 2.4.12). An accumulation SVs was found in close proximity to the AZ (0-40 nm) regardless of genotype and condition. Upon stimulation ribbon-less synapses contain more SVs between 40-80 nm from the AZ than in wild-type ([40-80]: *RBE*$^{wt/wt}$ stimulation, 0.16 ± 0.038; *RBE*$^{KO/KO}$ stimulation, 0.32 ± 0.043. Kruskal-Wallis followed by Dunn's post-test, *, $p < 0.05$). Moreover, inhibited and stimulated *RBE*$^{KO/KO}$ synapses harbored significantly more SVs at 80-120 nm from the membrane than in inhibitory and stimulatory conditions in *RBE*$^{wt/wt}$ ribbon synapses ([80-120]: *RBE*$^{wt/wt}$ inhibition, 0.069 ± 0.015; *RBE*$^{KO/KO}$ inhibition, 0.22 ± 0.038; *RBE*$^{KO/KO}$ stimulation, 0.20 ± 0.020. Kruskal-Wallis followed by Dunn's post-test, *, $p < 0.05$). Wild-type tomograms showed significantly fewer SVs between 120-160 nm upon rest than upon inhibition ([120-160]: *RBE*$^{wt/wt}$ inhibition, 0.14 ± 0.023; *RBE*$^{wt/wt}$ rest, 0.034 ± 0.017. One-way ANOVA followed by Šidák's post-test, *, $p < 0.05$) (Fig. 3.2.2.2.1b, Table 5.2.11).

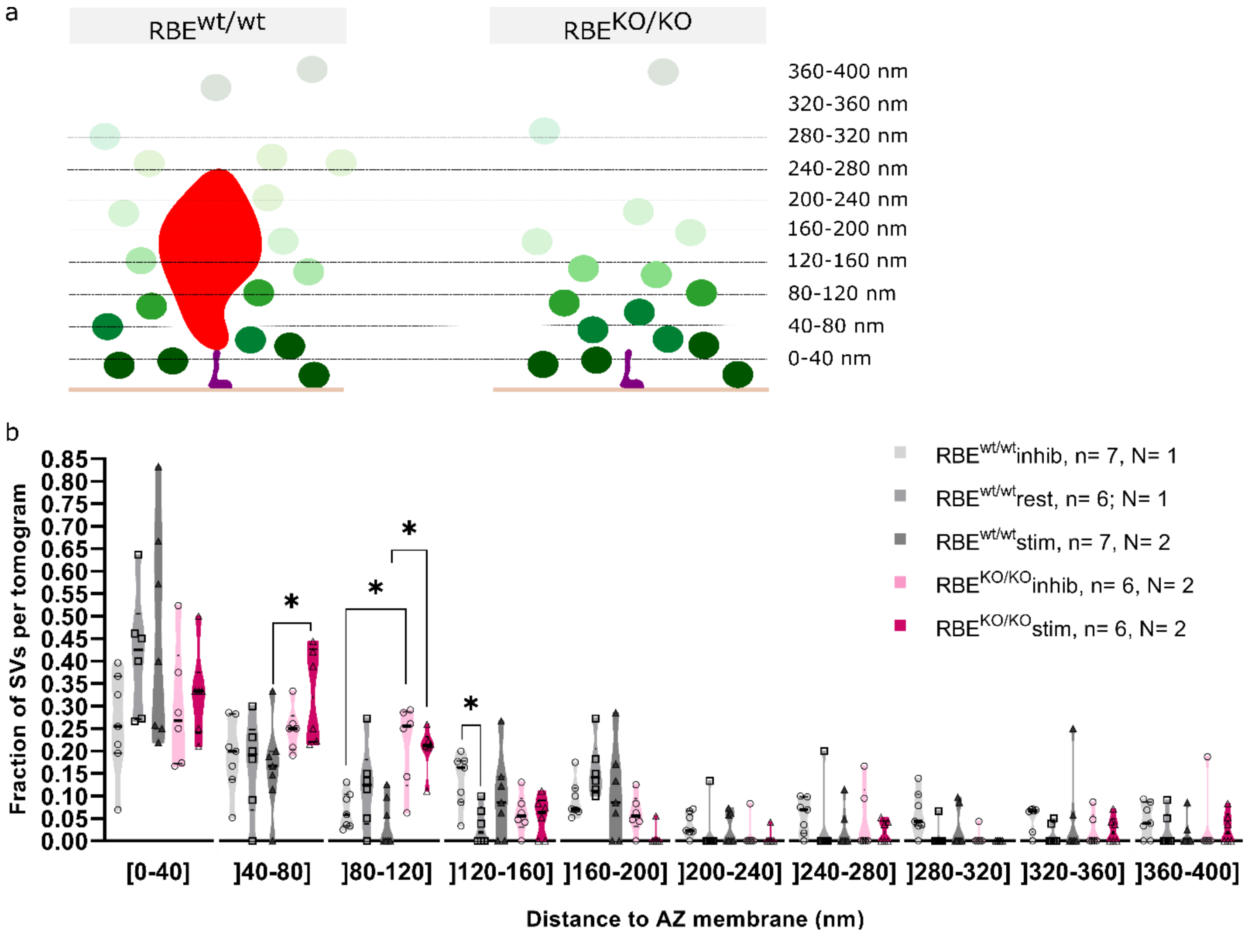

Fig. 3.2.2.1: Fractions of SVs per bin in *RBE*$^{wt/wt}$ and *RBE*$^{KO/KO}$ upon 15 minutes of stimulation. a, Diagram of the analysis criteria for conventional synapses in *RBE*$^{wt/wt}$ and *RBE*$^{KO/KO}$. SVs were measured ≤ 100 nm from the PD surface and ≤ 400 nm from the AZ membrane, which is subdivided in 40 nm bins. **b**, Fractions of SVs in 40 nm bins. Statistically significant differences are found within 40-80 nm, 80-120 nm and within 120-160 nm. One-way ANOVA followed by Šidák's post-test and Kruskal-Wallis followed by Dunn's post-test, *, p< 0.05. Values: Table 5.2.11. Data are show in mean ± S.E.M.

3.2.2.2 *Organisation of SVs in the proximity of the AZ membrane*

SVs in the proximity of the plasma membrane (≤ 40 nm) include docked SVs, which potentially represent the RRP.Stimulated *RBE*$^{wt/wt}$ synapses present a significantly higher ratio of docked-to-40-nm-SVs than upon inhibition (*RBE*$^{wt/wt}$ inhib, 0.030 ± 0.024; *RBE*$^{wt/wt}$ stim, 0.30 ± 0.0066. Kruskal-Wallis, *, p< 0.05); but these proportion remains similar to *RBE*$^{KO/KO}$ synapses (Fig. 3.2.2.2.1, Table 5.2.12).

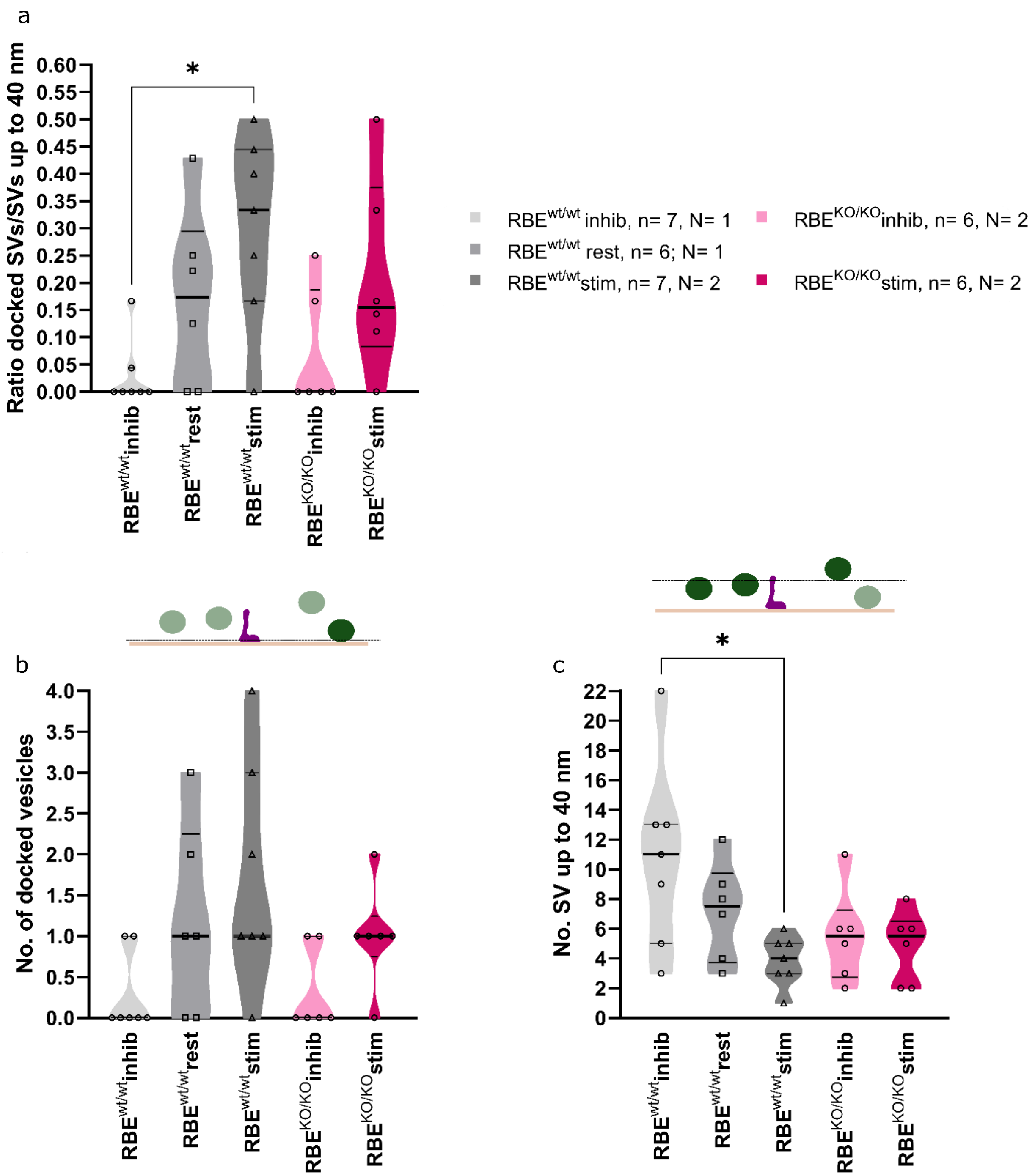

Fig. 3.2.2.2.1: Quantification of SVs found up to 40 nm from the AZ membrane. a, Ratio of docked SVs over the total SVs in 40 nm from the AZ membrane. Statistically significant differences are found in wild-type upon stimulation versus inhibition. **b**, Docked SV quantification. No statistically significant differences are found between genotypes in any condition. **c**, Quantification of SVs up to 40 nm from the AZ membrane. Significantly fewer SVs are found in stimulated wild-type synapses compared to inhibited ones. Kruskal-Wallis, *, $p < 0.05$. Values: Table 5.2.12. All data are shown as mean ± S.E.M.

Moreover, SVs might be susceptible to subtle changes in their vertical distribution upon ribbon lack or stimulation, which is reflected via their distance to the AZ. This was analysed by further subdividing the first 40 nm bin (Fig. 3.2.2.2.2a). No significant changes were observed in SV distribution in *RBE*$^{KO/KO}$ tomograms. Conversely, stimulated wild-type data reveal a decrease in SVs between 5-10 nm from the AZ membrane compared to rest, in addition to the changes in docked SVs (docked: *RBE*$^{wt/\ wt}$ inhibition, 0.030 ± 0.024; *RBE*$^{wt/wt}$ stimulation, 0.30 ± 0.066.]5-10] nm: *RBE*$^{wt/wt}$ resting, 0.27 ± 0.092; *RBE*$^{wt/wt}$ stimulation, 0.016 ± 0.016. Kruskal-Wallis followed bu Dunn's post-test, *, $p < 0.05$) (Fig. 3.2.2.2.3; Table 5.2.13).

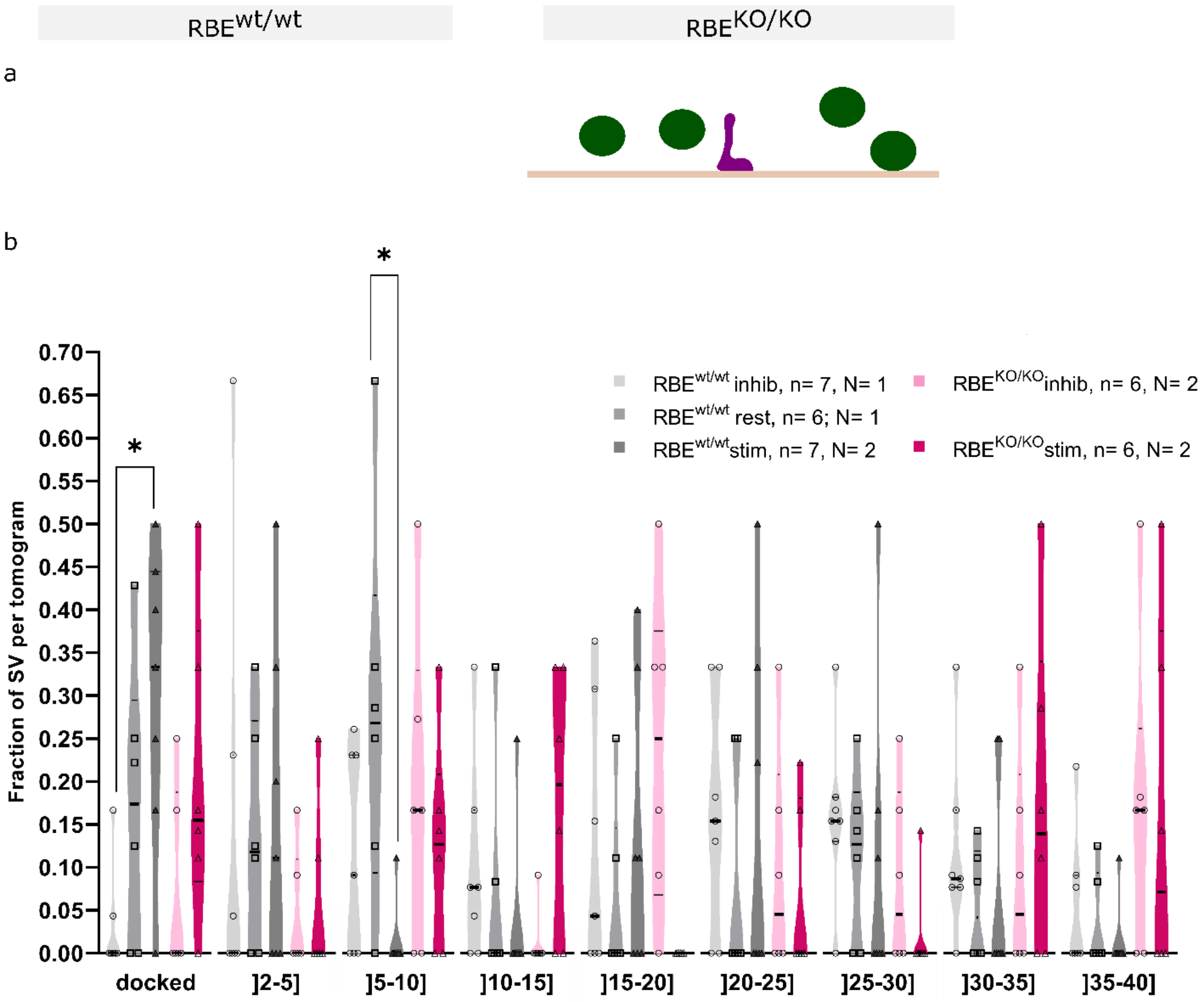

Fig. 3.2.2.2.3: Fractions of SVs found up to 40 nm from the AZ membrane. a, SVs found in the first 40 nm bin are subclassified into 5 nm bins, except for docked SVs whose distance to the AZ membrane is 0-2 nm. **b**, Fractions of SVs in the first 40 nm bin. Stimulated RBE$^{wt/wt}$ ribbon synapses present significantly more docked SVs than inhibited ribbon synapses. Significantly more SVs in 5-10 nm from the membrane are found upon resting than stimulated wild-type ribbon synapses. Kruskal-Wallis, *, $p < 0.05$. Values: Table 5.2.13. Data are show in mean ± S.E.M.

3.2.3 Summary

This section reveals some minor ultrastructural changes in the MP pool under different stimulations between *RBE*$^{wt/wt}$ and *RBE*$^{KO/KO}$ synapses. Special focus has been placed in the analysis of docked SVs following ribbon synapse criteria, as well as conventional synapse-like criteria.

To summarise, stimulated *RBE*$^{KO/KO}$ synapses show little differences in the quantification of the different SV pool and endocytic structures, which may be due to the low sample size. Notably, MP-SV show longer distances to the AZ membrane in stimulated *RBE*$^{KO/KO}$ than in *RBE*$^{wt/wt}$ synapses.

Briefly, the results from this section are not enough to draw any definitive conclusions, since a bigger sample size is needed to that end. Overall, the ribbon appears to contribute to the recruitment of SVs to the AZ membrane. Furthermore, the morphological correlates of endocytosis seem to indicate that the lack of ribbon has no effect in endocytosis or SV replenishment.

3.3 EFFECTS OF CHR2 EXPRESSION IN THE RIBBON SYNAPSE ULTRASTRUCTURE FOR AN OPTOGENETIC MODEL

Classically, the effects of activity on the ribbon synapse ultrastructure have been studied via minutes-long, chemical stimulation (Chakrabarti et al., 2018), which has a coarse temporal resolution. Implementing optical stimulation coupled with high-pressure freezing in *C. elegans* neuromuscular junctions (Watanabe et al., 2013a) and murine hippocampal tissue (Imig et al., 2020, 2014; Maus et al., 2020; Watanabe et al., 2013b) opened the door for establishing similar approaches for cochlear ribbon synapses. The challenge for successfully stimulating IHCs during milliseconds was tackled in two fronts: (1) modifying the high-pressure freezing machine (HPM) to precisely stimulated and allow the user to measure the light stimulation interval (Chakrabarti et al., 2022), its onset and temporal correlation to freezing of the sample; and (2) obtaining transgenic mouse lines whose IHCs are light sensitive (Ai32VC and Ai32KI) (Chakrabarti et al., 2022) (see section 2.3.3). Importantly, the temporal precision optogenetic stimulation might allow to address questions such as the identification of the RRP and the type of SV release mode (Chapochnikov et al., 2014) in IHCs. Recently, a study on short optogenetic stimulation of IHCs focusing on the electrophysiological output of different light intensities and the ultrastructural analysis of the stimulated ribbon synapse has been made public. I contributed to this publication by verifying the expression of ChR2 and the synaptic progression along adulthood via immunohistochemistry. Immunofluorescence data presented in this section can be also found in Chakrabarti et al. (2022). Figure arrangement and description have been tailored to fit this thesis.

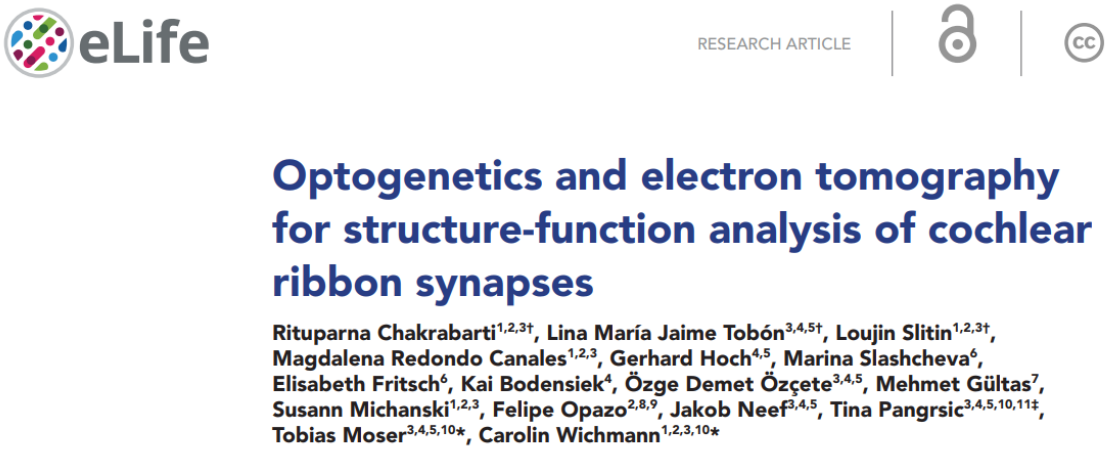

eLife RESEARCH ARTICLE

Optogenetics and electron tomography for structure-function analysis of cochlear ribbon synapses

Rituparna Chakrabarti[1,2,3†], Lina María Jaime Tobón[3,4,5†], Loujin Slitin[1,2,3†], Magdalena Redondo Canales[1,2,3], Gerhard Hoch[4,5], Marina Slashcheva[6], Elisabeth Fritsch[6], Kai Bodensiek[4], Özge Demet Özçete[3,4,5], Mehmet Gültas[7], Susann Michanski[1,2,3], Felipe Opazo[2,8,9], Jakob Neef[3,4,5], Tina Pangrsic[3,4,5,10,11‡], Tobias Moser[3,4,5,10*], Carolin Wichmann[1,2,3,10*]

As a follow up study, I established a longer (~ 440 ms) stimulation paradigm to analysed the ultrastructural changes in the ribbon synapse upon sustained stimulation, as well as the changes triggered by the the putative Ca^{2+} influx through ChR2 upon stimulation. Therefore, I used Ai32VC *cre*$^{+}$ ribbon synapses (see section 2.3) to analyse the architectural modifications upon sustained stimulation. Part of the data presented in the ultrastructural subsections were part of the Masters' dissertation project of Julius Bahr, which I supervised. He contributed to the results of this thesis with 5 tomograms from Ai32VC *cre*$^{+}$ inhibition, 5 tomograms from Ai32VC *cre*$^{+}$ isradipine and 4 tomograms from Ai32VC *cre*$^{+}$ opto-stimulation. The analysis for these tomograms was done by Julius Bahr and extended for this thesis.

Below I leave the information about tomogram orientation to show the skewness of these data (Table 5.3.1).

Values of quantifications and fractions from *cre*$^{+}$ data can be found in section 5.3.

3.3.1 ChR2 expression in the inner hair cell plasma membrane

The expression of ChR2 in IHC plasma membrane was verified via immunohistochemistry using Ai32KI mouse line (see section 2.3.3), in which animals expressing ChR2 were called Ai32KI *cre*$^{+}$, while animals without ChR2 expression were called wild-type (WT). Three age groups were used to determine ChR2 expression and synapse progression with age, namely 4-5 months old, 6-7 months old and 9-12 months old. A decrease in the number of ribbon synapses per IHC was expected to happen with age, as previously shown by Sergeyenko et al. (2013). Therefore, IHCs were stained against the eYFP label from the ChR2 construct (Nagel et al., 2003), myo6 as a counterstaining marker and CtBP2 to identify synaptic ribbons. Confocal microscopy images showed membrane expression of ChR2 over the three age groups in Ai32KI *cre*$^{+}$ IHCs (Fig. 3.4.1a, b). Next, the number of ribbon synapses per IHC was quantified in each aging group to determine whether ChR2 expression influenced the normal aging process of *cre*$^{+}$ mice. WT data showed statistically significant differences between the youngest and eldest age groups (WT 4-5 months, 9.77 ± 0.65; WT 6-7 months, 7.61 ± 1.00; WT 9-12 months, 6.39 ± 0.56. Two-way ANOVA followed by Tukey's post-test). Similarly, Ai32KI *cre*$^{+}$ inner hair cells also showed a significant reduction in the number of ribbons over time (Ai32KI *cre*$^{+}$ 4-5 months, 9.28 ± 0.44; Ai32KI *cre*$^{+}$ 6-7 months, 5.32 ± 0.43; Ai32KI *cre*$^{+}$ 9-12 months, 5.69 ± 0.42. Two-way ANOVA followed by Tukey's post-test) (Fig. 3.3.1c, Table 5.3.2). Importantly, similarities between WT and Ai32KI *cre*$^{+}$ synapse progression along adulthood, which indicate the lack of impact of ChR2 in this process. This result is a contribution to the publication of Chakrabarti et al. (2022).

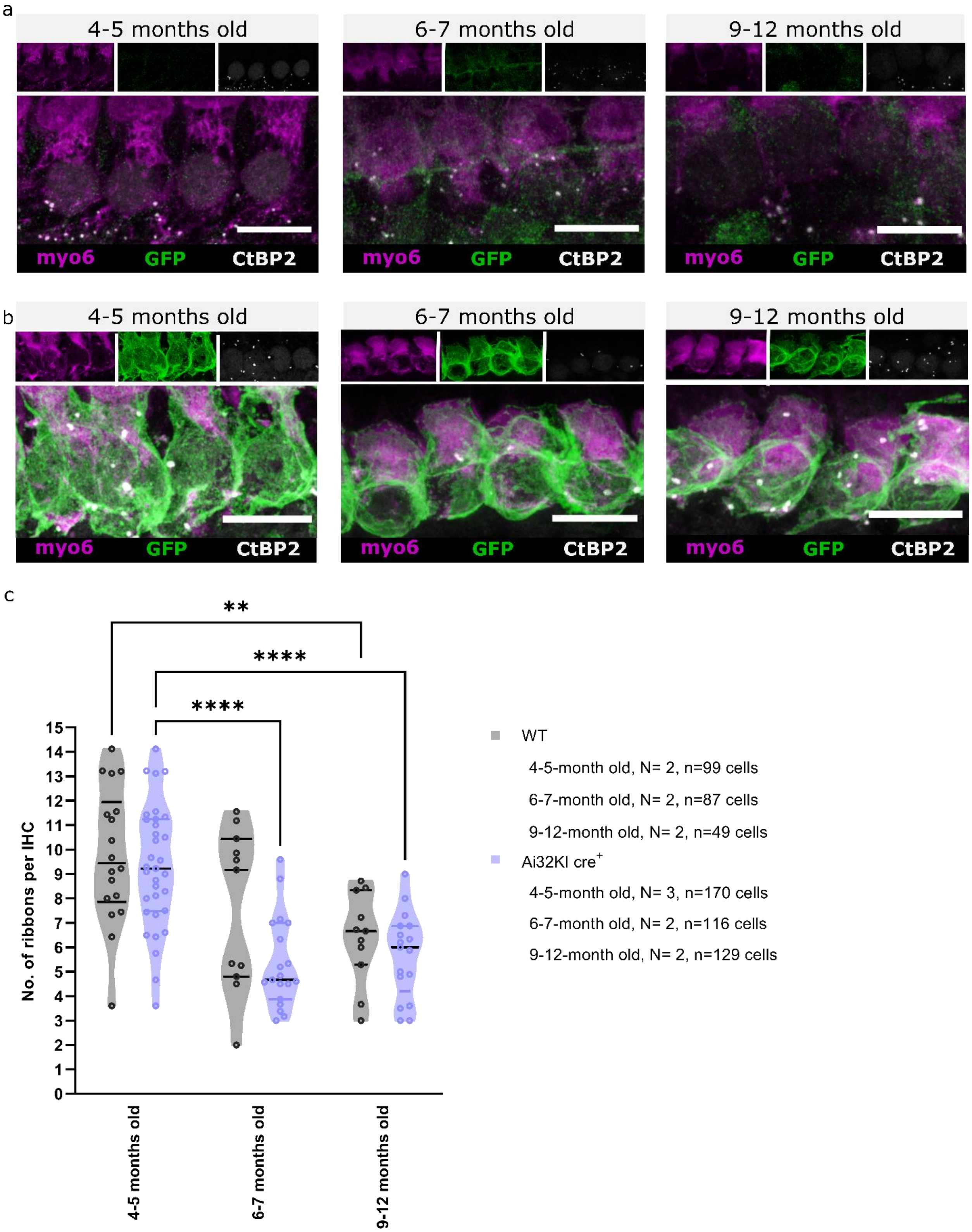
a
4-5 months old
6-7 months old
9-12 months old
myo6
GFP
CtBP2
b
4-5 months old
6-7 months old
9-12 months old
myo6
GFP
CtBP2
c
**
****
****
No. of ribbons per IHC
0
1
2
3
4
5
6
7
8
9
10
11
12
13
14
15
4-5 months old
6-7 months old
9-12 months old
WT
4-5-month old, N= 2, n=99 cells
6-7-month old, N= 2, n=87 cells
9-12-month old, N= 2, n=49 cells
Ai32KI cre$^+$
4-5-month old, N= 3, n=170 cells
6-7-month old, N= 2, n=116 cells
9-12-month old, N= 2, n=129 cells

Fig. 3.4.1: ChR2 expression in inner hair cell plasma membrane. a-c, Representative confocal microscopy images of WT (left) and Ai32KI *cre*$^+$ (right) IHCs. ChR2 expression (green) is found in the three age groups in Ai32KI *cre*$^+$ cells. Additional staining was performed to label the synaptic ribbons (white) with CtBP2 antibody and counterstaining to label the cytoskeleton (magenta) with myo6 antibodies. Scale bar, 10 µm. **d**, Quantification of the number of ribbons per inner hair cell in WT and Ai32KI *cre*$^+$ samples. Statistically significant differences are found between in WT at 4-5 months old and 9-12 months-old, as well as in Ai32KI *cre*$^+$ at 4-5 months old and the other two aging groups. Two-way ANOVA followed by Tukey's post-test, **, $p< 0.01$; ****, $p< 0.0001$. Values: Table 5.3.2**.** Data are presented as mean ± S.E.M. Figure (above) modified from Chakrabarti et al. (2022)**.**

3.3.2 Ribbon-associated and membrane-proximal pools characteristics

Availability of Ca^{2+} constitutes a dependent variable for exocytosis, whose buffering has been used to study the SV cycle dynamics (Beutner and Moser, 2001; Goutman and Glowatzki, 2007; Moser and Beutner, 2000). The addition of a light sensitive cation channel with low Ca^{2+} permeability to the IHC plasma membrane, such as ChR2, might impact in the morphological SV pools upon stimulation due to a potentially larger influx of Ca^{2+} via ChR2 and $Ca_V1.3$ channels. Therefore, isolating the effect of ChR2 in SV exocytosis was performed by using three stimulation paradigms: inhibitory condition, whereby there is no Ca^{2+} influx through $Ca_V1.3$ channels and ChR2 due to the presence of EGTA that chelates the extracellular Ca^{2+}; isradipine plus opto-stimulation condition, in which $Ca_V1.3$ channels are blocked so that whichever changes in the SV pools must be due to the influx of Ca^{2+} through ChR2; and opto-stimulation condition, where $Ca_V1.3$ and ChR2 are active and open upon light stimulation and subsequent IHC depolarisation (Fig. 3.4.2.1a).

In this context, sustained light stimulation (~ 442 ms) might help distinguish the effects of the potential Ca^{2+} influx through ChR2 in SV exocytosis. Prolonged stimulation requires active RA and MP pools to ultimately replenish the released SVs. Replenishment alterations might be observed by quantifying the SVs in the RA and MP pools. Comparable number of SVs were found in both pools regardless the activity state (Fig. 3.4.2.1b, Table 5.3.3). Recruitment of SVs to the ribbon and the AZ membrane was assessed by measuring the distance of a given SV to either structure. In addition, Ca^{2+} coupling of MP-SVs might be altered upon use of isradipine, since Ca^{2+} only passes to the cell by ChR2 channels. Distance measurements showed RA and MP-SVs to be found at similar distances from the reference structures in all conditions (Fig. 3.4.2.2, Table 5.3.4).

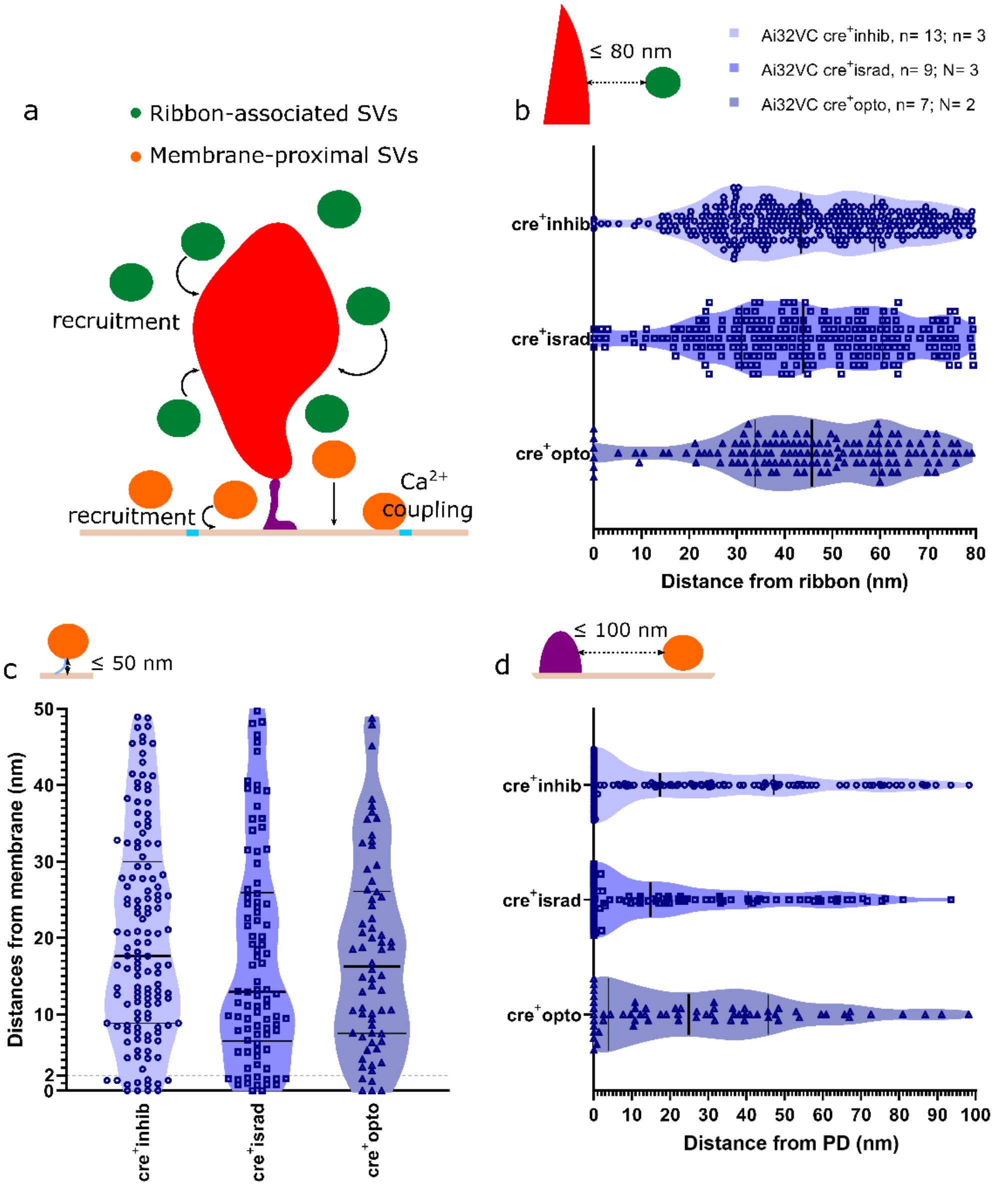

Fig. 3.4.2.2: Quantification of the distances of RA and MP SVs in Ai32VC *cre*$^+$ ribbon synapses. a, Quantification of RA and MP-SVs permits to verify differences in recruitment to the ribbon and the AZ membrane, as well as in Ca^{2+} coupling. **b-d**, Distances of RA-SVs to the ribbon surface, and MP-SVs to the AZ membrane and the PD surface. Comparable distances were found in all activity states. Kruskal-Wallis followed by Dunn's post-test, ns, $p > 0.05$. Values: Table 5.3.4. Each sample point of the violin plot corresponds to the average distance measurement of a SVs. All data are presented as mean ± S.E.M.

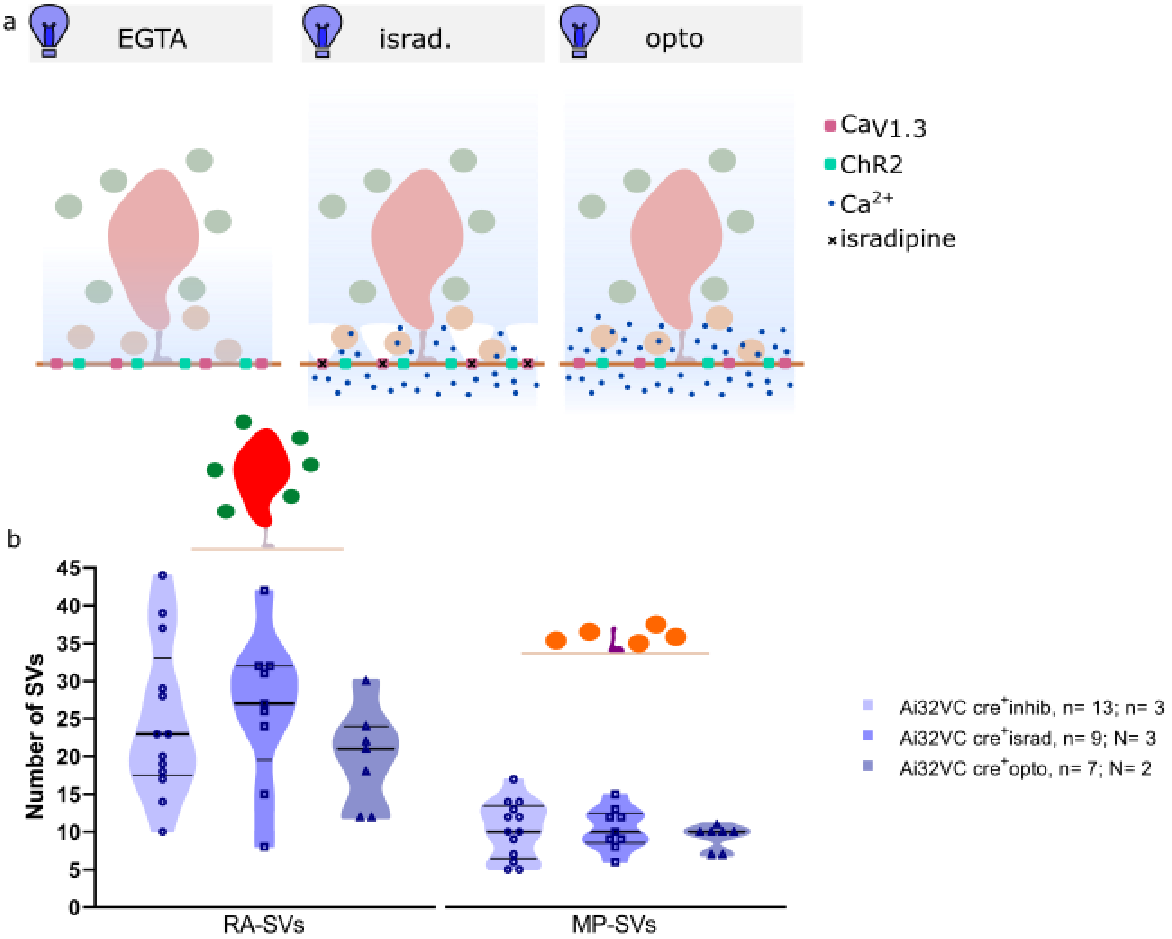

Fig. 3.4.2.1: RA and MP pool quantification. a, Summary diagram of the solutions used to test the impact of ChR2 in Ca^{2+} influx upon sustained light stimulation. EGTA, a slow Ca^{2+} buffer, sequesters extracellular Ca^{2+} (blue) preventing SV release (left). The opto solution (right) contains Ca^{2+} to normally trigger SV exocytosis upon light stimulation. The addition of 5 mM of isradipine to the opto solution blocks the Ca$_V$1.3 channels (magenta), which results in ChR2 (green) being the only entry pathway of Ca^{2+} to the ribbon synapse. **b**, Quantification of the RA and MP pools. No statistically significant differences are observed in any pool regardless the activity state. Kruskal-Wallis followed by Dunn's multiple comparisons test, ns, p> 0.05. Values: Table 5.3.3. All data are presented as mean ± S.E.M.

Recently, ~50 ms stimulation has been shown to increase the number docked SVs at the AZ membrane (Chakrabarti et al., 2022). Reducing the Ca^{2+} influx to the AZ membrane might also reduce the number of docked SVs at the AZ. This quantification revealed similar number for docked and non-docked SVs in all three conditions (Fig. 3.4.2.3, Table 5.3.5).

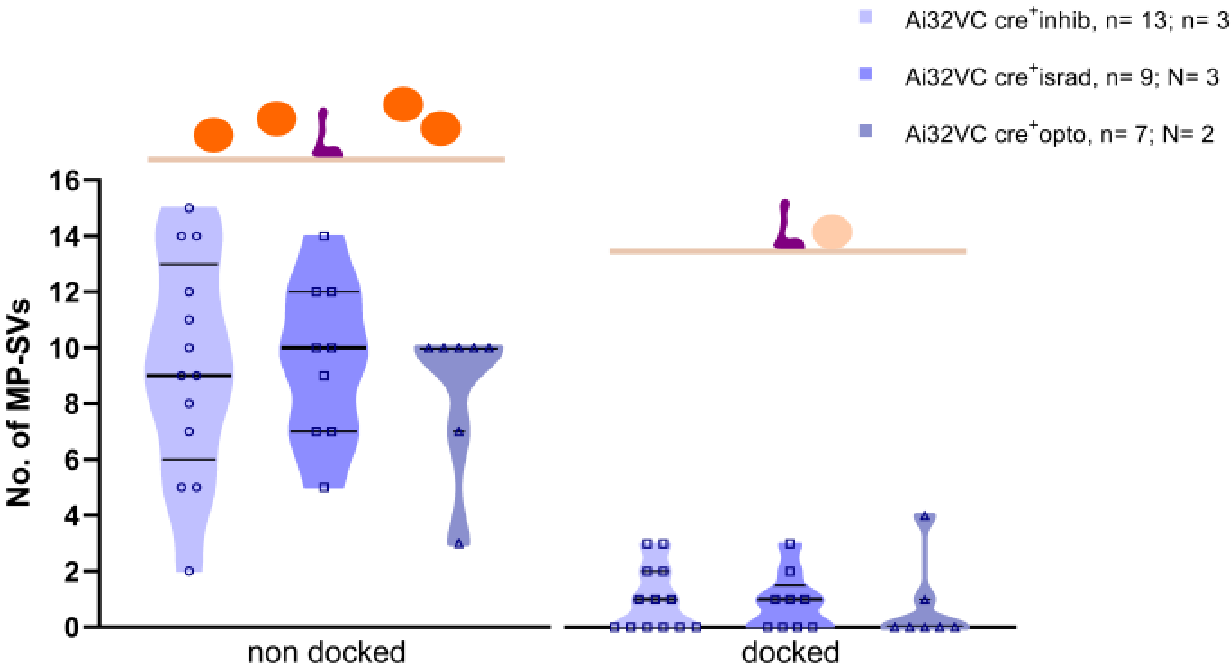

Fig. 3.4.2.3: Non-docked and docked MP-SV quantification. Average number of non-docked (orange) and docked (light orange) SVs per tomogram. Comparable numbers of non-docked and docked SVs are found in all conditions. Kruskal-Wallis, ns, $p > 0.05$. Values: Table 5.3.5. All data are shown as mean ± S.E.M.

Speed of SV recruitment to the AZ membrane and Ca^{2+} access was inferred from the distances of the MP-SVs to the plasma membrane and the PD surface. Blockage of $Ca_V1.3$ channels results in less Ca^{2+} available, which might be reflected in a decrease in SV engagement to the AZ membrane. Non-docked SVs were located at comparable distances from the plasma membrane and the PD surface. Similarly, docked SVs presented no statistically significant differences in under any stimulation paradigm (Fig. 3.4.2.4, Table 5.3.6). However, the importance of Ca^{2+} for SV recruitment might be observed in non-docked SVs in isradipine, since non-docked SVs show a slight increase in the distance to the membrane and a decrease in the distance to the PD surface compared to stimulated condition.

This subsection shows comparable sizes for the RA and MP pools, as well as the distances of these SVs to a prominent structure.

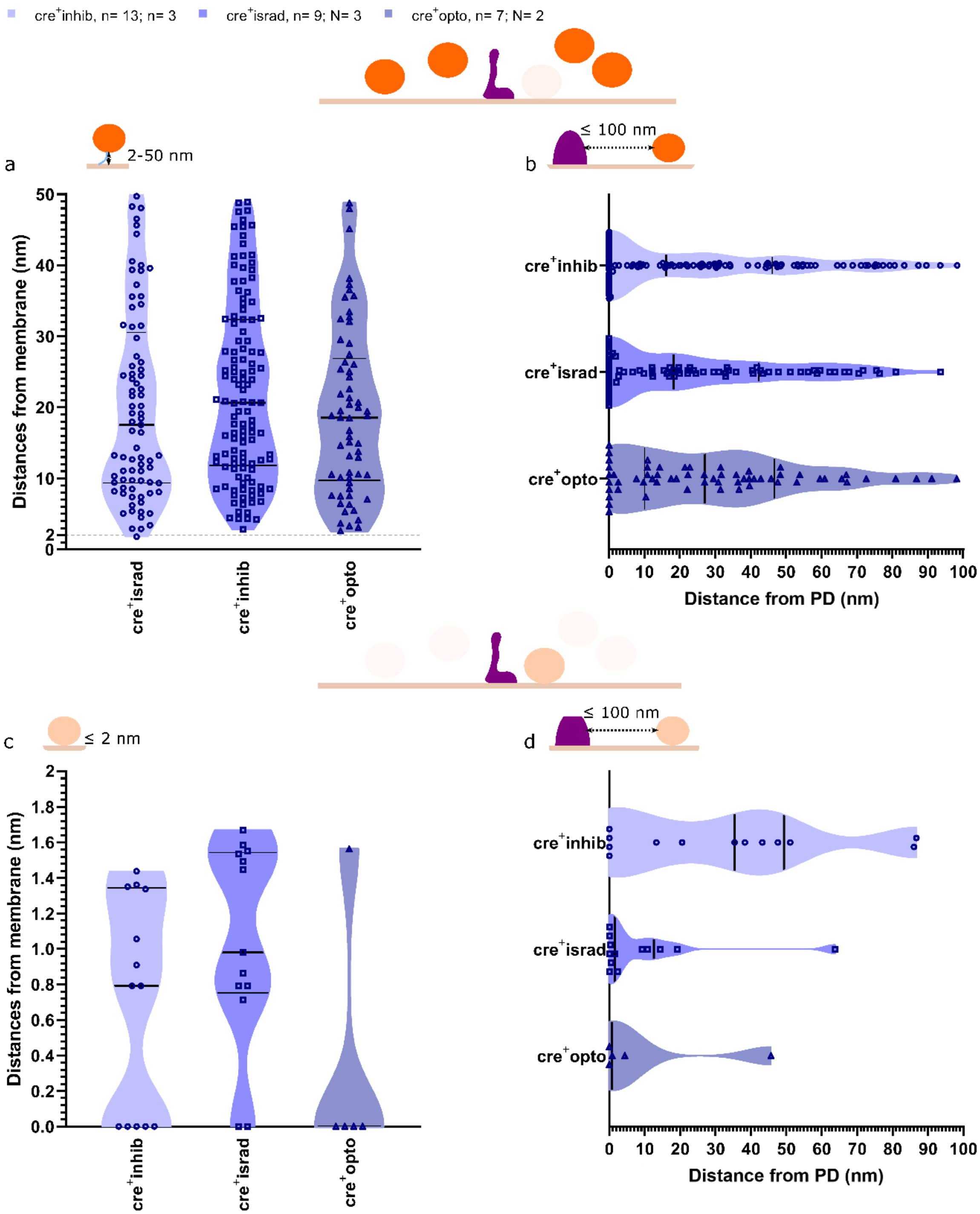

Fig. 3.4.2.4: Distances of non-docked and docked MP-SVs to the AZ membrane and the PD surface. a-b, Measurements the distance of non-docked SVs to the AZ membrane and to the PD surface. No statistically significant differences are found among any activity state. Kruskal-Wallis followed by Dunn's post-test, ns, $p > 0.05$. **c-d**, Average distance of docked SVs to the plasma membrane and the PD surface. Docked SVs are found at similar distances from the AZ membrane and the PD surface regardless the activity state. Kruskal-Wallis followed by Dunn's post-test, ns, $p > 0.05$. Values: Table 5.3.6. All data are shown as mean ± S.E.M.

3.3.3 MP-SV analysis based on the presence of tethers

Changes in the SV subpool organisation upon short and phasic light stimulation has shown an increase in the recruitment of SVs by the formation of tethers (Chakrabarti et al., 2022). Moreover, functional data showed a reduction in exocytosis upon application of isradipine in IHCs (Brandt et al., 2003). Therefore, fewer tethered and docked SVs are expected to be observed upon $Ca_V1.3$ blockage. The data presented no statistically significant changes in any of the SV subpool regardless of the activity state (Fig. 3.4.3.1b, Table 5.3.7). Nevertheless, a reduction of Ca^{2+} influx seemed to prevent the engagement of non-tethered SVs to the release sequence, although docked SVs appeared more abundantly at the AZ membrane. Furthermore, a reduced entry of Ca^{2+} to the ribbon synapse brings non-tethered SV significantly closer to the AZ membrane compared to inhibitory condition (Ai32VC *cre*$^+$ inhib, 24.25 ± 1.92; Ai32VC *cre*$^+$ israd, 15.65 ± 1.85. Kruskal-Wallis followed by Dunn's post-test) (Fig. 3.4.3.2, Table 5.3.8).

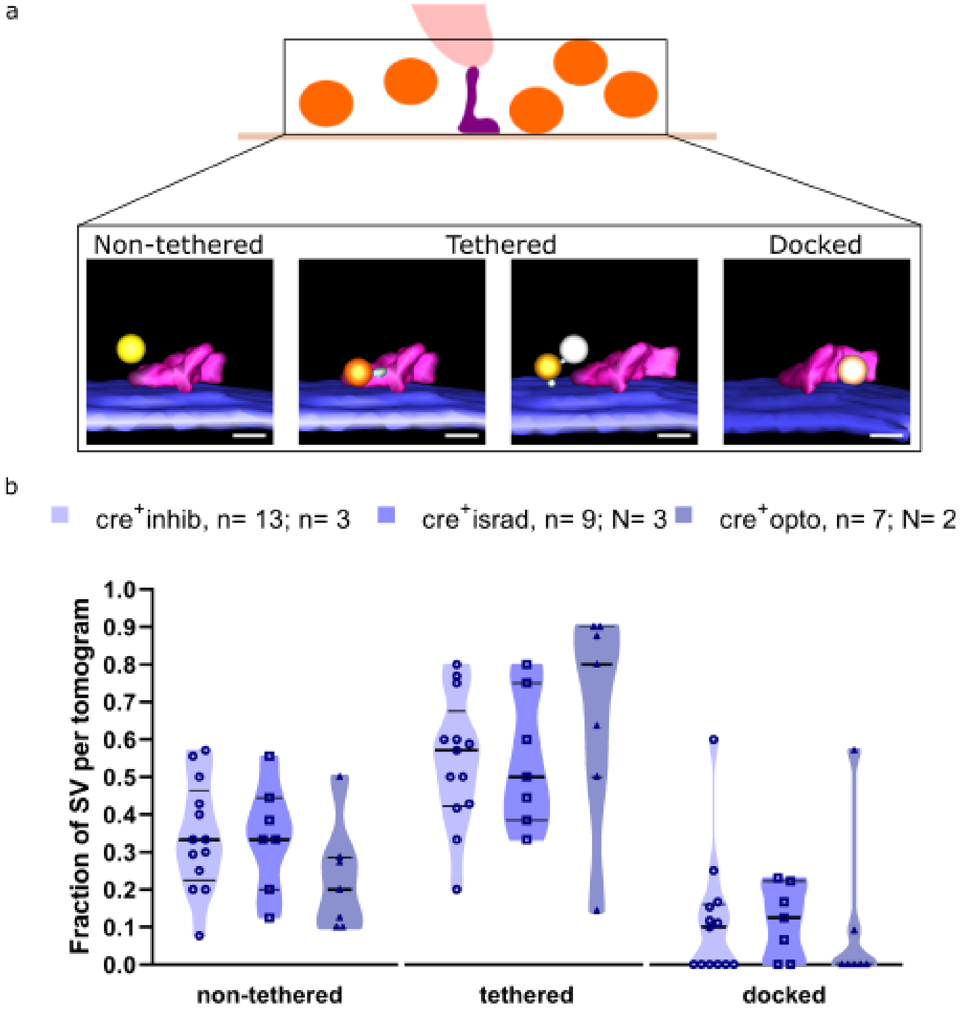

Fig. 3.4.3.1: Tethering states of MP-SVs. a, Presence of tethers and distance to the AZ membrane makes possible to classify MP-SVs into non-tethered, tethered and docked. Scale bar, 50 nm. **b**, Fraction of MP-SVs according to the presence of tethers. Similar fractions are found per tether category regardless of the activity state. One-way ANOVA followed by Šidák's post-test and Kruskal-Wallis followed by Dunn's post-test, ns, p> 0.05. Values: Table 5.3.7. Data are presented as mean ± S.E.M.(Figure above)

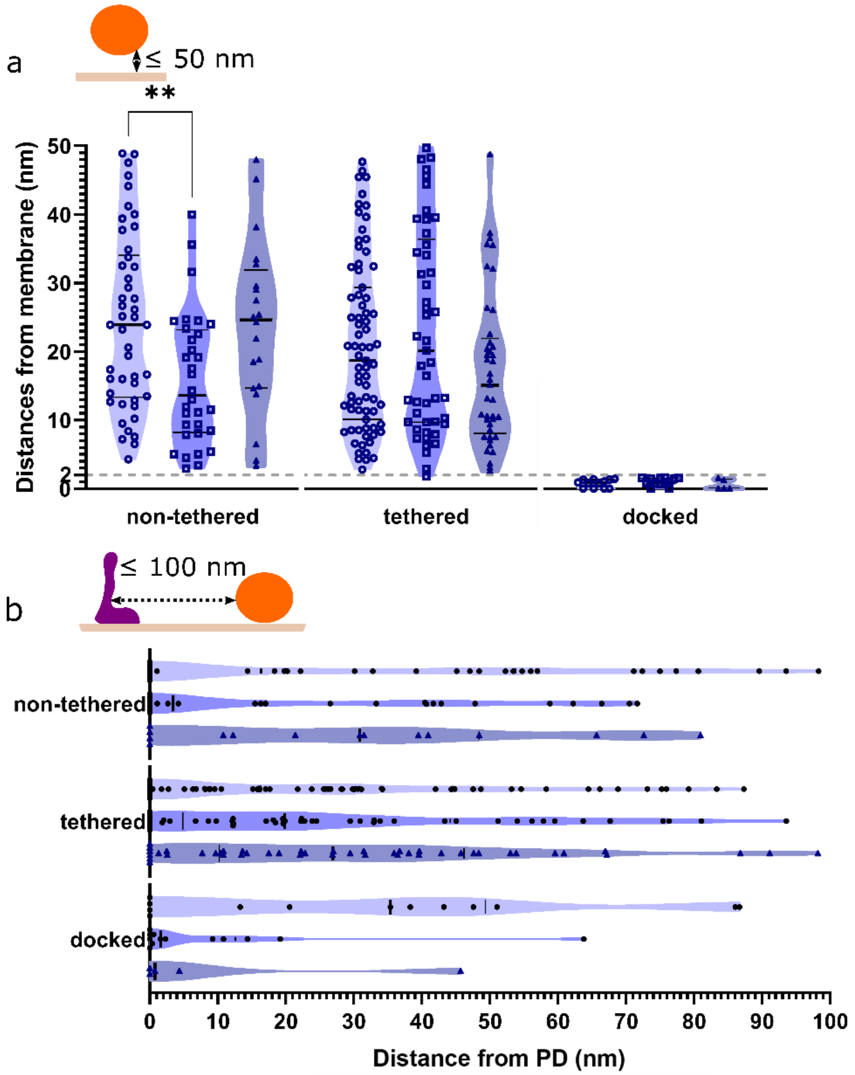

Fig. 3.4.3.2: Distances to AZ membrane and PD of MP subpools. a, Distance of MP-SVs to the AZ membrane. Non-tethered SVs are found significantly closer to the plasma membrane in the presence of isradipine compared to inhibitory condition. Kruskall-Wallis followed by Dunn's post-test, *, p< 0.05. **b**, Distance of MP-SVs to the PD surface. Comparable distances to the PD are found in non-tethered, tethered and docked SVs. Kruskall-Wallis followed by Dunn's post-test, ns, p> 0.05. Each sample point of the violin plot corresponds to the average distance measurement of a SVs. Values: Table 5.3.8. All data are presented as mean ± S.E.M.

3.3.4 Summary

This section shows that ChR2 is expressed in the IHC plasma membrane along the life of the mice without interfering with the normal progression of synapse decline with aging. No statistically significant differences could be observed in any SV pool or subpool, although the trends seem to indicate that the Ca^{2+} influx through ChR2 is quite small. Further experiments are necessary to increase the sample size and confirm the trends observed.

4 DISCUSSION

This thesis focuses on the ultrastructural changes triggered by prolonged activity in IHC ribbon synapses, mainly upon the lack of Otof and the loss of the synaptic ribbon, and to a lesser extent upon milliseconds of light stimulation. I investigated the ultrastructural correlates of exocytosis and endocytosis in *Otof*$^{KO/KO}$ and *RBE*$^{KO/KO}$ synapses to understand how these proteins are involved in these processes. Furthermore, the contribution of the Ca^{2+} influx via ChR2 to exocytosis was assessed in optogenetically-stimulated IHCs. Therefore, analysis of SV pools and subpools, as well as the endocytic structures was performed under different activity-states, namely EGTA-inhibited, resting and stimulatory conditions. Loss of Otof revealed longer distances of tethered MP-SVs to the AZ membrane upon stimulation, as well as a decrease in the number of endocytic structures in the stimulated state compared to resting. Lack of synaptic ribbons results in seemingly small PDA and MP pools, whereby MP-SVs were found further away from the AZ membrane upon stimulation. Finally, optogenetically stimulated IHCs present comparable ribbon synapse SV pools and subpools in the different activity states, although some trends some can be observed and will be discussed. In the following subsections I assess the previously presented results to (I) elucidate the role of Otof and (II) the synaptic ribbon/RBE upon sustained chemical stimulation; and (III) the contribution of ChR2 to optogenetically-triggered exocytosis.

4.1 TOPOGRAPHY OF STIMULATED RIBBON SYNAPSE AZS IN OTOF AND RBE MUTANTS

Otof and RBE mutants might show impaired MP pool dynamics, since disruption of Otof severely impairs exocytosis (Pangšrič et al., 2010; Roux et al., 2006; Vogl et al., 2015) and deletion of RBE produces a reduction in SV replenishment (Jean et al., 2018). MP-SVs are thought to be replenished with RA-SVs via the PD, but the lack of ribbon in *RBE*$^{KO/KO}$ synapses point towards a different mechanism in recruiting SVs to the MP pool. In the following subsections I discuss the MP pool replenishment and MP-SV recruitment to the AZ with special focus on the role of docked SVs.

4.1.1 Resupply of the membrane proximal pool seems independent of RBE and Otof

Initial work on the effects of activity in saccular frog ribbon synapses revealed a depletion of the SVs in the proximity of the membrane and the formation of a vesicle gradient towards the base of the ribbon (Lenzi et al., 1999). More recently, Chakrabarti et al. (2018) showed in murine cochlear IHCs that the MP pool seems efficiently replenished upon prolonged, strong stimulation (15 min, 50 mM K^+ solution) by RA-SVs (Lenzi et al., 1999). Functionally, the loss of the synaptic ribbon produces a mild reduction in SV replenishment (Jean et al., 2018), which might be portrayed as smaller

PD-associated (PDA) and MP pools upon stimulation. Previous ultrastructural data showed a considerable decrease in the number of PDA-SVs compared to RA-SVs in unstimulated conditions (Jean et al., 2018). However, the size of the PDA and MP pool I found upon stimulation remains comparable to the inhibited and resting conditions, as well as the published data (Jean et al., 2018).

An additional factor to consider is the distance of SVs to the ribbon or PD, since it indicates the engagement of SVs for exocytosis. For instance, changes in the proportions of SVs found at different distances from the AZ membrane in hippocampal synapses has been observed in different high frequency light stimulation paradigms (Imig et al., 2020). Furthermore, tethering of SVs also plays a role in SV exocytosis in conventional (Maus et al., 2020; Watanabe et al., 2013b) and ribbon synapses (Chakrabarti et al., 2018). Studying the interplay between structural changes in the SV pools at the ribbon and the membrane contributes to understand the function of the synaptic ribbon. Chakrabarti et al. (2018) revealed that stimulation triggers an increase in the number of tethered RA-SVs and a shortening of the tether length in ribbon synapses. Therefore, disruption of the ribbon might produce an increase in the distance of PDA-SVs to the PD. Conversely, the data in section 3.2.1 show that the average distance between PDA-SVs and the PD is comparable to the distance of RA-SVs to the ribbon regardless of the activity state. This observation might reflect a difference in tethering components, whereby filaments connecting RA-SVs might involve RBE and piccolino (Chakrabarti and Wichmann, 2019), while SVs connecting to the PD might be mediated by Bsn (Chakrabarti et al., 2018). Notably, I measured the distance of a SV to the ribbon or PD to infer its recruitment for MP replenishment, although this prevents me from making a direct comparison with the reported tether length data. Therefore, subcategorising RA/PDA-SVs into SV subpools might help to elucidate if the comparability in measured distances is due to a change in tethering.

Furthermore, MP pool replenishment relies on the descent of SVs towards the AZ membrane, whereby the PD is proposed to act as a bridge towards the AZ membrane (Chakrabarti et al., 2018). Therefore, the main component of the PD, Bsn (Dick et al., 2003; Regus-Leidig et al., 2009; Wong et al., 2014), might constitute the tethers emanating from the PD (Chakrabarti et al., 2018). Wild-type data from this thesis suggests that SV tethering to the PD is a transitory stage that becomes less frequent upon stimulation (Table 5.1.10, Table 5.2.9), as similarly reported in Chakrabarti et al. (2018). Moreover, mutation in Otof C_2F domain (*Otof*$^{pga/pga}$) does not alter the fraction of MP-SVs establishing tethers with the PD, indicating normal recruitment of SVs via the PD to the AZ membrane (Chakrabarti et al., 2018). Similarly, full disruption of Otof does not alter the proportion of SVs tethered to the PD, nor the size of the MP pool (Table 5.1.3, Table 5.1.10). In contrast, disruption of the ribbon seems to slightly favour the formation of tethers with the PD over the membrane

(Table 5.2.9). Overall, these findings suggest that RBE and Otof are not required for an initial recruitment step to the MP pool; instead, the PD seems to play an important role in providing SVs for further steps towards SV release.

4.1.2 Effective engagement of membrane proximal vesicles at the AZ membrane for release requires the presence of Otof and the synaptic ribbon

MP-SV recruitment to the AZ membrane is a Ca^{2+}-dependent process (Chakrabarti et al., 2018) in which Otof plays an important role (see section 3.1). Ablation of the synaptic ribbon has been observed to disrupt the clustering of $Ca_V1.3$ (Jean et al., 2018), while the deletion of Otof alters the tether length, which might indicate a direct interference in the tether composition. Thus, loss of Otof and the ribbon might affect the transition along the various morphological SV subpools that render MP-SVs fusion competent. A few questions can be posed in this context: is the proposed SV release sequence (i.e., single-tethered to multiple-tethered to docked) affected? Can SVs normally approach the AZ membrane? Can we indicate which step(s) of release is impaired? What information can we extract from docked SV data?

Steps for MP-SV release: A previous ultrastructural study in young, mature IHC ribbon synapses showed that MP-SVs are organised into subpools, in which the number and connections of the tethers are the main classificatory feature (Chakrabarti et al., 2018). Otof has been proposed to participate in MP-SV tethering (Chakrabarti et al., 2018; Vogl et al., 2015), while RBE/the ribbon appears involved in $Ca_V1.3$ channel distribution at the AZ membrane (Jean et al., 2018). Hence, the coupling distance between Ca^{2+} influx and SVs might be altered in both mutants, resulting in an impairment of different severities of the steps required for SV release.

Tether formation at the AZ membrane is an extremely important step in the SV release, whereby long single tethers are first established and followed by the formation of multiple short tethers until SV docking (Chakrabarti et al., 2018; Fernández-Busnadiego et al., 2010). Deletion of Otof results in quite unresponsive ribbon synapses, which might be caused by severe defects in MP-SV tethering that ultimately results in few docked SVs. Wild-type data (see section 3.1) shows that normal MP-SV recruitment upon stimulation is mediated by a reduction in the fraction of non-tethered SVs, while tethered and docked SV subpools increase. In contrast, stimulated *Otof*$^{KO/KO}$ ribbon synapses present unaltered fractions of non-tethered, tethered and docked SVs (Fig. 3.1.1.4.1). Consequently, docked SVs are scarcer in mutants than in wild-type stimulated ribbon synapses. Thus, deletion of Otof appears to severely impair the SV subpool progression culminating in docked SVs.

Functional studies in IHCs revealed the importance of the ribbon for fast exocytosis (Becker et al., 2018; Jean et al., 2018; Khimich et al., 2005), whereby strong IHC depolarisation in the absence of ribbons produces a delay in SV release likely due to a decrease in the available SVs competent for fusion (Becker et al., 2018; Jean et al., 2018). This phenomenon might ultrastructurally correlate with changes in the SV subpools, which lead to few docked SVs in ribbon-less synapses. The lack of synaptic ribbon results in a mild increase in non-tethered and a decrease in docked SVs compared to wild-type (Fig. 3.2.1.3.1), which can be interpreted as a slight impairment in MP-SV recruitment upon strong and prolonged stimulation. In contrast, stimulated wild-type ribbon synapses show an increase of docked SVs to the AZ membrane, while the proportion of non-tethered SVs decreases (Chakrabarti et al., 2018) (also see section 3.1). Therefore, deletion of RBE/the ribbon seems to mildly impair the progression of MP-SVs towards docking at the AZ membrane.

Approach of MP-SV to the AZ membrane: Activity triggers a shortening of the MP-SV tethers in wild-type IHC ribbon synapses, which permits the approach of the SVs to the AZ membrane (Chakrabarti et al., 2018). Despite that the tether length was not measured in my work, the distance of MP-SVs to the AZ membrane was quantified as way to infer the readiness for SV release, as done in conventional synapses (Hintze et al., 2021; Imig et al., 2020, 2014; Maus et al., 2020). These measurements in stimulated *Otof*$^{KO/KO}$ synapses show an invariably large distance of tethered SVs to the AZ membrane, specially of single tethered SVs, compared to wild-type (Table 5.1.9). These data support the involvement of Otof in the formation of short tethers (< 20nm) upon stimulation (Vogl et al., 2015).

Moreover, the reduction (not absence) in short tethers in *Otof*$^{KO/KO}$ (Vogl et al., 2015) might be pointing towards an Otof-independent mechanism for SVs to closely approach the plasma membrane. However, candidate proteins involved in forming short tethers in neuronal synapses, such as Rab3-interacting molecule (RIM) 1α (Fernández-Busnadiego et al., 2013), Munc13 (Vogl et al., 2015), neuronal SNARE proteins (Nouvian et al., 2006; Uthaiah and Hudspeth, 2010) and complexins (Uthaiah and Hudspeth, 2010), are absent from mature IHC ribbon synapses. Notably, IHCs present RIM2α and RIM binding protein (BP) 2, that are needed for normal synaptic function (Jung et al., 2015b; Krinner et al., 2021, 2017). These proteins control the SV release probability in conventional synapses (Butola et al., 2021; Zarebidaki et al., 2020) by regulating Ca^{2+} channel clustering (Butola et al., 2021; Kaeser et al., 2011). Ultrastructural observations of unstimulated IHC ribbon synapses have revealed that RIM2α seems necessary for tether formation (Jung et al., 2015b), while RIM-BP2 regulates SV distance distribution to the AZ (Krinner et al., 2017). In this regard, I could observe that tethered MP-SVs from *Otof*$^{wt/wt}$ ribbon synapses approach the membrane (~ 18 nm) upon stimulation, while in *Otof*$^{KO/KO}$ they remained as distant (~ 25 nm) as in non-stimulated conditions. Altogether, even though Otof disruption seemingly interferes with necessary steps for MP-

SV release, the function of other proteins, such as RIM2α and RIM-BP2, might contribute to tether formation leading to sparse SV docking.

The long distance of MP-SVs to the AZ membrane in *Otof*$^{KO/KO}$ ribbon synapses might also indicate the importance of Otof for docking. Electron tomography data from *Otof*$^{pga/pga}$ ribbon synapses have shown that single and multiple tethers in the MP pool are still present, although they present abnormal lengths upon stimulation (Chakrabarti et al., 2018). According to SV simulations in retinal ribbon synapses, tethers of up to 10 nm would hold SVs within the docking region (Graydon et al., 2014). Therefore, the combination of the overall increased distance of MP-SVs to the AZ membrane (see section 3.1.1.3) and the reported lack of short (<20 nm) tethers (Vogl et al., 2015) suggests that holding MP-SVs in their docking sites might be impaired in *Otof*$^{KO/KO}$ ribbon synapses.

In addition, an impairment in the release site clearance has been proposed to happen in *Otof*$^{pga/pga}$ synapses (Pangšrič et al., 2010), which was later correlated with an accumulation of multiple tethered and docked SV at the AZ hypothetically near $Ca_V1.3$ channels (Chakrabarti et al., 2018). Notably, despite the sparsity in the presence of docked SVs in stimulated *Otof*$^{KO/KO}$ ribbon synapses, these are found very close (~ 17 nm) to the PD compared to resting condition (~ 38 nm) (Fig.3.1.1.3.4). This supports the hypothesis that Otof might promote the removal of vesicular material from the AZ membrane, although the scarcity of docked SVs in *Otof*$^{KO/KO}$ ribbon synapses muddle this proposal.

Conversely, the approach of MP-SVs in stimulated *RBE*$^{KO/KO}$ ribbon synapses seems mildly impaired, specially the approach of the tethered SVs (~ 26 nm), compared to wild-type (~ 19 nm) (Fig. 3.2.1.2.2, Fig. 3.2.1.3.2). Experiments in IHC ribbon synapses have shown that the deletion of RBE results in spot-like channel distribution (Becker et al., 2018; Jean et al., 2018), which produces a wider Ca^{2+} spread than in *RBE*$^{wt/wt}$ ribbon synapses (Jean et al., 2018). The distant SVs and the disruption of $Ca_V1.3$ channel clusters in ribbon-less synapses (Becker et al., 2018; Jean et al., 2018) might functionally correlate with the decrease in the peak firing rate of SGNs (Jean et al., 2018). This is in line with data from retinal ribbon-less synapses that showed that Ca^{2+} buffering heavily impaired *RBE*$^{KO/KO}$ synapses ability to spontaneously fire miniature EPSCs, which suggests a deterioration in the coupling of Ca^{2+} influx and SV release (Maxeiner et al., 2016). Therefore, strong and prolonged stimulation shows that ribbon loss might cause a decrease in the efficiency of MP-SVs to be recruited to the plasma membrane.

Electron microscopy observations in hippocampal synapses have shown that the process of SV docking to the AZ membrane is reversible and, at high Ca^{2+} concentrations, location-independent (Kusick et al., 2020). In contrast, docked SVs in IHC ribbon synapses have been observed polarised from the PD within the AZ membrane (Chakrabarti et al., 2018), under the Ca^{2+} nanodomain-like coupling model (Moser et al., 2019). The altered $Ca_V1.3$ channel distribution in *RBE*$^{KO/KO}$ synapses translates into a decoupling between $Ca_V1.3$ channels and the release sites (Lv et al., 2016; Maxeiner et al., 2016), whereby the nanodomain-like exocytosis model might be disrupted.

Normally, $Ca_V1.3$ channels localise close (~ 60 nm) to the PD (Jean et al., 2018; Wong et al., 2014) and very close (15-30 nm) to docked SVs (Moser et al., 2019), in such way that the Ca^{2+} influx from few channels triggers SV fusion (Moser et al., 2019). Docked SVs in stimulated *Otof*$^{wt/wt}$ ribbon synapses are usually found at ~ 26 nm (see section 3.1.1.3, Table 5.1.5) from the PD, which is similar (~ 30 nm) to the *RBE*$^{wt/wt}$ measurements (see section 3.2.1.2, Table 5.2.4). In contrast, docked SVs from stimulated *RBE*$^{KO/KO}$ synapses are found extremely close (~ 7 nm) to the PD, whose distance is even closer to the PD than docked SVs from EGTA-inhibited *RBE*$^{wt/wt}$ ribbon synapses (~ 20 nm) (see section 3.2.1.2, Table 5.2.4). Altogether, the role of RBE in $Ca_V1.3$ channel cluster distribution might affect the docking sites of MP-SVs.

Overall, I propose that MP-SVs from *Otof*$^{KO/KO}$ and *RBE*$^{KO/KO}$ ribbon synapses might go through the different steps for SV release more slowly than in wild-types. Despite that data about SV subpools and their distances to the AZ membrane have low temporal resolution, the sense of speed in the SVs undergoing different recruitment steps prior to docking and fusion stems from the combination of data regarding the relative abundances of each SV subpool, as well as their distances to the AZ membrane. However, the causes for the differences in impairment severities in MP-SV transitioning towards release vary: the loss of Otof – likely an important Ca^{2+} sensor and participating in the MP tether machinery (Pangšrič et al., 2010; Vogl et al., 2015) – produces seemingly unchanging MP subpools; while the loss of ribbon – a structure partially controlling the SV-to-Ca^{2+} coupling (Jean et al., 2018) – results in a mild increase in non-tethered SVs. Furthermore, both mutants display defects in tethered MP-SVs approaching the AZ membrane, specially the single tethered SVs in *Otof*$^{KO/KO}$ AZs. Therefore, the need for Otof and RBE in IHC ribbon synapses relies on the correct Ca^{2+} sensing/coupling by the tethering machinery.

Finally, the above-described processes might be the reason that docked SVs in *Otof*$^{KO/KO}$ and *RBE*$^{KO/KO}$ IHCs are sparser than in wild-type ribbon synapses. Despite that the molecular causes for this phenomenon differ in both mutants, tethered MP-SVs were mainly affected from the disruption of Otof and RBE. In addition, normal docking site occupancy is also abolished likely due to the lack of short tethers in *Otof*$^{KO/KO}$ or the disruption of $Ca_V1.3$ channels in *RBE*$^{KO/KO}$ mutants. Therefore, the presence of Otof and the synaptic ribbon seem necessary for MP-SVs to normally achieve the docking stage.

4.1.3 General considerations about the RRP in Otof mutants and wild type IHC ribbon synapses

Much has been debated about morphological correlates of the RRP in IHC ribbon synapses, since ultrastructural and electrophysiological data seem to point to different sizes (Beutner et al., 2001; Chakrabarti et al., 2018). While in conventional synapses the morphological correlates of the RRP are the docked SVs (Imig et al., 2014; Maus et al., 2020), new ultrastructural evidence suggests that docked SVs might also represent the RRP in ribbon synapses (Chakrabarti et al., 2018). However, IHC electrophysiological data indicates that ~15-21 SVs per ribbon synapse would form the RRP (Beutner et al., 2001; Meyer et al., 2009; Pangšrič et al., 2010; Wong et al., 2014), which ultrastructurally correlates to the number of MP-SVs (Chakrabarti et al., 2022, 2018). Therefore, disruption of Otof would result in a smaller MP pool compared to wild-type. However, the MP pool is found in similar average sizes in *Otof*$^{KO/KO}$ (9 SVs) and *Otof*$^{wt/wt}$ (8 SVs) (Table 5.1.3). In addition, only a smaller MP pool is found in *Otof*$^{KO/KO}$ (9 SVs) compared to *Otof*$^{pga/pga}$ (11 SVs) ribbon synapses (Fig. 3.1.1.3.1, Table 5.1.18), which might be due to the accumulation of SVs in the *pachanga* mutant (Chakrabarti et al., 2018). In contrast, docked SVs are fewer in stimulated *Otof*$^{KO/KO}$ (0.7 SVs) than in *Otof*$^{wt/wt}$ (1.6 SVs) upon stimulation, while they are comparable to the already reported docked SVs for stimulated *Otof*$^{pga/pga}$ ribbon synapses (Chakrabarti et al., 2018). Altogether, the RRP might be represented by the morphologically docked SVs, but very short (~ 20 ms) optogenetic stimulation of wild-type organs of Corti is necessary to evaluate the size of the RRP before SV replenishment mechanisms start to act.

Under the premise that the RRP corresponds to docked SVs, the mechanism of SV release in IHC ribbon synapses is still unclear, although increasingly ultrastructural evidence points against homotypic fusion events of SVs (Chakrabarti et al., 2022, 2018). Three modes for SV release have been proposed to happen in IHC ribbon synapses, namely uniquantal release (Takago et al., 2019), coordinated multiquantal release (Fuchs et al., 2003) and multiquantal release (Edmonds et al., 2004). It has been suggested that multiquantal release might involve the fusion of SVs before and/or after fusion with the membrane (Edmonds et al., 2004). A structural outcome of SV compound fusion is the formation of cisternae near the ribbon, as reported for retinal ribbon synapses (Matthews and Sterling, 2008); another outcome of compound fusion, is an increase in the size of MP-SVs. Disruption of Otof results in smaller monophasic EPSCs (Takago et al., 2019), which might indicate smaller SVs. However, similar sizes of MP-SVs were found in wild-type and mutant, which points against multiquantal release.

4.1.4 A model summarising the contribution of RBE and Otof to the ribbon synapse

The joint review of data from the MP pool and its subpools from Otof and RBE mutants indicate that normal synaptic transmission of IHC ribbon synapse relies on correct sensing and coupling to Ca^{2+}, which relates to the progression of MP-SV through the different subpools that make SVs fusion competent.

Briefly, these data depict the structure-functional landscape of the MP pool in IHC ribbon synapses. The distribution of $Ca_V1.3$ channels, as a background actor that RBE/the ribbon presence regulates, is involved in the spread of Ca^{2+}-influx wave (Jean et al., 2018) and might be involved the docking positions of the SVs. Usually, entry of Ca^{2+} to the AZ immediately triggers SV release, followed by fast replenishment. Otof seems essential to make single tethered SVs competent to approach the plasma membrane that culminates with the formation of very short tethers, which may hold SVs in their docking sites. Therefore, normal MP subpool dynamics need appropriate Ca^{2+} access, as well as functional Ca^{2+} sensing mechanisms and tether formation.

4.2 THE ROLE OF OTOF IN ENDOCYTOSIS

Prolonged chemical stimulation combined with HPF was used to study the function of Otof in exocytosis and endocytosis. Otof interaction with Ca^{2+} (Dominguez et al., 2022; Michalski et al., 2017; Pangršič et al., 2012), lipids (Dominguez et al., 2022) and proteins from the endocytic pathway (Dulon et al., 2009; Heidrych et al., 2009; Jung et al., 2015a) indicates its importance for several steps within the SV cycle. Otof has been hypothesised to be essential for release site clearance, which contributes to the normal progression of the last steps of exocytosis (Chakrabarti et al., 2018) and also connects to endocytosis (Duncker et al., 2013). I hypothesised that the endocytic pathway is altered in *Otof*$^{KO/KO}$ ribbon synapses, which might be reflected by changes in the types of endocytic structures and their sizes.

4.2.1 The effects of Otof in the endocytic pathway remain unclear

Data in this thesis indicates that disruption of Otof has unclear effects on the endocytic pathway, even though it is thought to have a role in plasma membrane uptake and SV reformation from endosomes (Heidrych et al., 2009; Jung et al., 2015a). An early electron tomography study in saccular ribbon synapses revealed that 30 minutes of strong stimulation increased the formation of tubular and cisternae-like structures, while coated vesicles remained in similar abundance as in non-stimulated tissue (Lenzi et al., 2002). Recycling in IHCs mostly happens at their basal zone (Kamin et al., 2014), where CME and bulk endocytosis have been identified by ultrastructural methods (Neef et al., 2014). CCVs were distinguished by the clathrin coat, that presents an electron-dense, spiky appearance; while morphological correlates of bulk endocytosis called endosomal-like vacuoles (ELVs) are large (diameter > 70 nm), clear core round or oval vesicles. Moreover, they can also be found as large invaginations from the plasma membrane (Kroll et al., 2019; Neef et al., 2014). Analysis of these structures was performed to assess the involvement of Otof in endocytosis.

Types of endocytic structures: Given that Otof has been shown to participate in CME and SV reformation by interacting with AP-2 (Duncker et al., 2013; Jung et al., 2015a), one would expect that CME and reformation of SVs from ELVs would be impaired upon mutation/deletion of Otof, hence finding a reduction in CCVs and an accumulation of ELVs. Notably, similar proportions of CCVs and ELVs were found in mutant and wild-type (Fig. 3.1.1.5.3, Fig. 3.1.2.2). In addition to these structures, I noticed that many tomograms of *Otof*$^{wt/wt}$ upon rest presented what it seemed *de visu* extremely abundant tubular "endocytic" structures (TESs), which were not in contact with the plasma membrane and I proceeded to quantify. However, the TESs were found in comparable proportions in both mutants compared to their controls (Fig. 3.1.1.5.3, Fig. 3.1.2.2). Similar cisternae-like structures have been previously seen in IHCs using photo-oxidation of styryl dyes to track endocytic processes, where they are more abundant in the nuclear region of the IHCs (Kamin et al., 2014). These structures were also observed in the basal region of IHCs, where they became less abundant upon strong, prolonged stimulation (1 min, 65.36 mM KCl) (Kamin et al., 2014). Micrographs of unstimulated IHC ribbon synapses have shown that these tubular structures appear surrounded by what might be ribosomes, suggesting rough endoplasmic reticulum identity (Vogl et al., 2016). Recently, a high-resolution confocal study showed that cisternae-like structures in the nuclear region of IHCs had neither Golgi apparatus nor endoplasmic reticulum origin, but suggested that these might be involved in the traffic of material from the membrane to the Golgi apparatus (Revelo and Rizzoli, 2016). The fact is that the molecular origin of these tubular structures (TESs) observed and quantified in the Otof tomograms cannot be determined yet since only visual information is available. However, implementing correlative light and electron microscopy in the organ of Corti might help clarify their identity in future experiments.

ELVs or not? A striking anatomical aspect of *Otof*$^{KO/KO}$ and *Otof*$^{pga/pga}$ ribbon synapses is that some of them contain clusters of vesicles of different sizes (Chakrabarti, 2018), whose molecular origin remains unknown. This is a limitation of this type of ultrastructural studies because the origin of structures that look alike may not always be determined. Disparities between *Otof*$^{KO/KO}$ and *Otof*$^{pga/pga}$ in the ELV quantification (Table 5.1.20) might be caused by the presence of these unknown vesicles that might be taken for endocytic structures according to their morphology.

Ultrastructural studies in conventional synapses have revealed SV clusters whose appearance can be regulated by phosphorylation-dephosphorylation of proteins in the SVs surface such as synapsin (Milovanovic and De Camilli, 2017). In addition, morphological correlates of endocytosis are relegated to the edges of these clusters, where reformed SVs join and mingle with other SVs (Rizzoli and Betz, 2004; Wu et al., 2014). In contrast, clusters of large vesicles have been observed in IHC ribbon synapses upon disruption of the pathway for protein insertion, such as Otof, in membranes (Vogl et al., 2016), as well as in the *pachanga* mutant (Chakrabarti, 2018). Young wild-type ribbon synapses neither show such vesicle clusters, nor large numbers of ELVs; conversely, the numbers of ELVs are doubled in *Otof*$^{KO/KO}$ ribbon synapses, while other endocytic structures remain in comparable numbers (Table 5.4.1). This hints that sparse large vesicles may gather at *Otof*$^{KO/KO}$ synapses without necessarily being compartmentalised. Notably, these large vesicles of unknown origin may be ELVs (Vogl et al., 2016), lysosomes or intermediate vesicles from recycling pathway. If these vesicles had endosomal origin, their accumulation might hypothetically happen due to the lack of interaction between Otof with myo6 (Heidrych et al., 2009) and protein kinase (PK) Cα (Cepeda et al., 2019), thereby impairing retrograde transport and endocytosis dynamics.

Effects of activity on endocytic structures: Otof is proposed to be necessary for endocytosis (Duncker et al., 2013; Jung et al., 2015a; Strenzke et al., 2016), although its mechanism remains unclear. I hypothesised that defects in SV reformation could be tracked by an accumulation of ELVs, although the actual molecular identity of the structures classified as ELVs calls for caution on the interpretation of this data. Resting *Otof*$^{KO/KO}$ ribbon synapses have significantly more endocytic structures than other *Otof*$^{KO/KO}$ conditions, resting *Otof*$^{wt/wt}$ and *Otof*$^{pga/pga}$, which does not fulfil the hypothesis (Fig. 3.1.1.5.1, Fig. 3.1.3.3). Furthermore, strong and prolonged stimulation of *Otof*$^{KO/KO}$ ribbon synapses decreases almost by half the amount of quantified ELVs compared to resting condition (Table 5.4.1), which might actually be sparse, large vesicles. Conversely, there is no striking increase in endocytic structures nor ELVs upon mutation of the C_2F domain of Otof. This might be caused by the presence of the FerB domain in *Otof*$^{pga/pga}$, which has been proposed to interact with PKCα controlling endocytosis dynamics (Cepeda et al., 2019). The actual endocytosis dynamics in stimulated *Otof*$^{KO/KO}$ and *Otof*$^{pga/pga}$ ribbon synapses might be masked by the presence of these large vesicles. Still, the determination of the vesicle identity with molecular markers and correlative electron microscopy experiments in stimulated *Otof*$^{KO/KO}$ and *Otof*$^{pga/pga}$ are necessary to clarify the involvement of Otof in endocytosis and SV reformation.

4.2.2 SV reformation may be maintained despite Otof deletion

SV reformation from endocytic structures is a key step to resupply the synaptic ribbon for sustained exocytosis (Kamin et al., 2014; Kroll et al., 2019). However, lack of Otof has been shown to almost abolish exocytosis (Pangšrič et al., 2010; Roux et al., 2006; Vogl et al., 2015), and possibly only very few SVs might fuse upon strong exocytosis justifying non-flat EPSC recordings (Takago et al., 2019). The number of docked SVs that might fuse in 15 minutes of strong stimulation in *Otof*$^{KO/KO}$ ribbon synapses is unknown, but their presence implies that some residual SV reformation might be needed. Therefore, defects in this step of the SV cycle might be reflected in the size of the endocytic structures or the size of RA-SVs, as suggested in temperature-sensitive Otof mutant (Strenzke et al., 2016).

On the one hand, bigger than normal endocytic structures might be caused by a defective interaction between Otof and AP-2µ needed for SV reformation (Duncker et al., 2013; Jung et al., 2015a; Strenzke et al., 2016). However, the effective radii of the endocytic structures, even when subdividing them into ELVs, CCVs and TES, is comparable across activity states in *Otof*$^{wt/wt}$ and *Otof*$^{KO/KO}$ mice. Notably, the endocytic origin of TESs or ELVs cannot be ensured, which represents one limitation of this study (see previous subsection).

On the other hand, RA-SVs of abnormal size might indicate a fault in SV reformation. A recent ultrastructural study of stimulation in *Otof*$^{pga/pga}$ ribbon synapses showed that RA-SVs had more variability in their size compared to wild-type (Chakrabarti et al., 2018), which partially resulted from large vesicles that intermixed with the RA-SVs. However, these data cannot be compared to *Otof*$^{KO/KO}$ data because of the difference in analysis criteria. *Otof*$^{pga/pga}$ RA-SVs were classified as such on only the basis of distance criterion (Chakrabarti et al., 2018); while *Otof*$^{KO/KO}$ RA-SVs were quantified excluding vesicles ≥ 70 nm in diameter, which were treated as ELVs (see section 2.4.12), as done in Kroll et al. (2019). Lack of Otof shows that the diameter of RA-SVs is ~ 48 nm, which is fairly comparable to *Otof*$^{wt/wt}$ RA-SVs. However, a number of big vesicles were excluded in *Otof*$^{wt/wt}$ and *Otof*$^{KO/KO}$ synapses from the RA pool quantification due to their size (Table 5.4.2), which might have impacted on the homogeneity of the RA-SV diameters if they had been taken as RA-SVs. Therefore, clarification of the molecular origin of the big, clustered vesicles may provide a reliable assessment of the RA-SV size as proxy of correct SV reformation and how it is altered upon mutation or disruption of Otof.

4.2.3 A model for Otof function in IHC ribbon synapses

The ultrastructural study done in section 3.1 on the role of Otof indicates the need of Otof for (I) SVs to normally achieve the docking stage; (II) release site clearance; and (III) the incidence of ELV or ELV-like structures.

There are also technical caveats that must be considered regarding data reliability: first, certainty in endocytic structure identification solely relies on visual data, since no technique combining molecular and structural data has been applied in my thesis. And second, statistical comparison of the two Otof mutants partially relied on published information, making sometimes unable to compare certain parameters such as the SV subpools.

Below I present a model for the action of Otof in IHC ribbon synapses summarising my *Otof*$^{KO/KO}$ and *Otof*$^{wt/wt}$ data (Fig.4.1.6): strong and prolonged stimulation of wild-type ribbon synapses produces an increase in docked SVs, while tethered MP-SVs become close to the AZ membrane. Subsequently, bulk endocytosis and CME (not shown in the model) occur steadily in the wild-type. Conversely, lack of Otof results in a quite unresponsive MP pool, whereby upon stimulation very few SVs achieve docking. In turn, endocytosis might be triggered, although its extent and the involvement of Otof is difficult to assess.

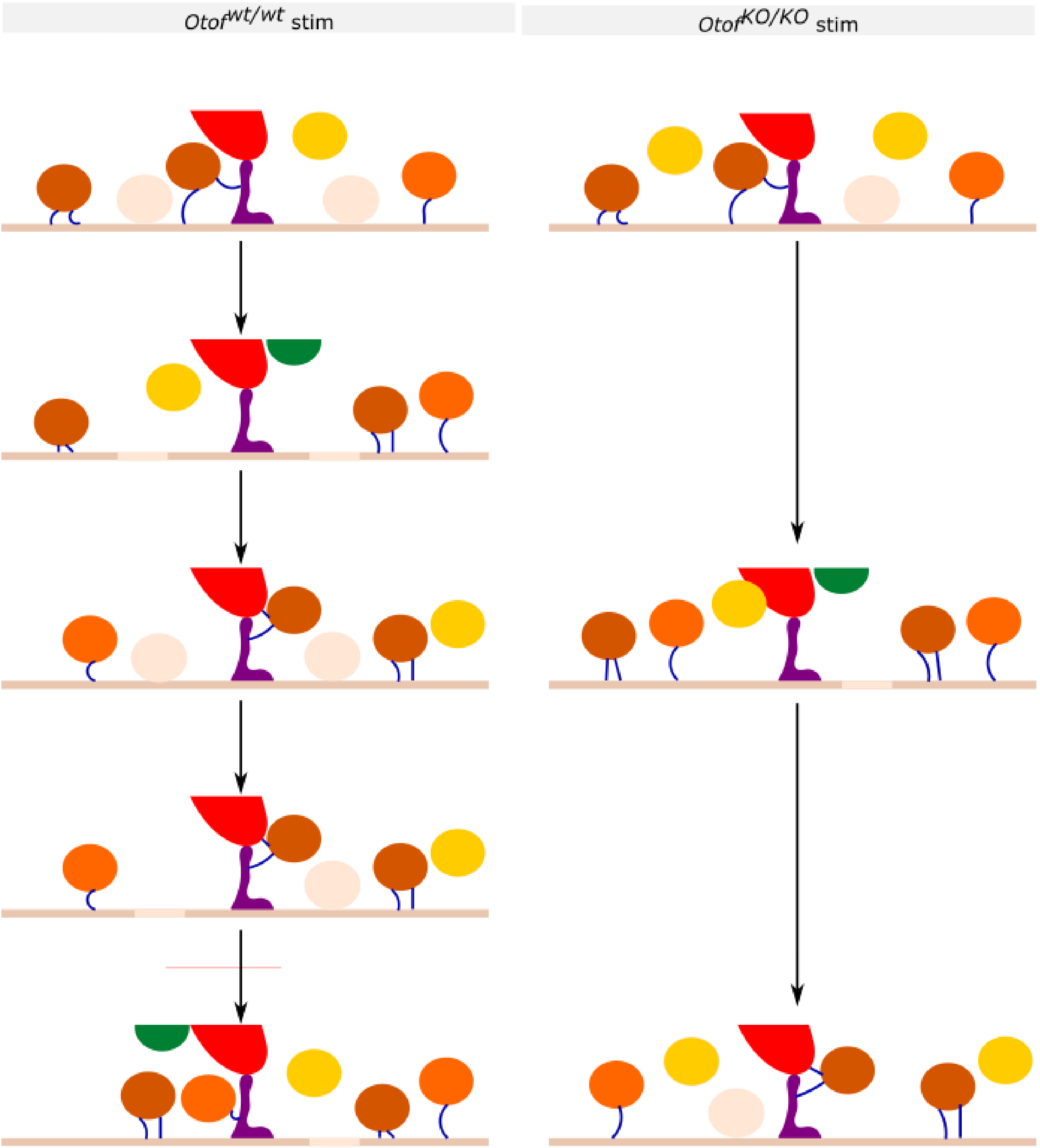

Fig. 4.2.3: Model for the role of Otof. In stimulated wild-type ribbon synapses (left), MP-SVs undergo the proposed tethering stages (single and multiple tethered), which approach the AZ membrane, until docking and fusing. SVs descending from the ribbon through the PD replenish the MP pool to sustain release. In contrast, prolonged stimulation of *Otof*$^{KO/KO}$ ribbon synapses (right) prevents tethered MP-SVs from approaching the AZ membrane, which leads to sparse docking of SVs.

Colour code for SVs: green, RA-SV; yellow, non-tethered MP-SVs; orange, single-tethered MP-SV; brown, multiple-tethered MP-SVs; light orange, docked SV.

4.3 THE ROLE OF RBE IN THE SV CYCLE

The role of the synaptic ribbon remains elusive to date, since its deletion produces only a slight decrease in the performance of ribbon synapses (Becker et al., 2018; Jean et al., 2018). 15-minute chemical stimulation of IHC ribbon-less synapses followed by HPF was utilised to study the role of the ribbon in the SV cycle. A prominent quality of the ribbon is its role in the distribution of $Ca_V1.3$ channels at the plasma membrane (Jean et al., 2018), which regulates the coupling of SVs to Ca^{2+}. In this study (see section 3.2) I focused on the structure-function effects of the deletion of the ribbon in SV release and endocytosis pathway. I hypothesised that ribbon-less synapses display (I) a redistribution of SVs in SV pools and (II) an alteration in the readiness of SVs for release. I discussed the MP pool and its subpools in subsection 4.1, which allowed me to propose that the ribbon is required for timely recruitment of SVs to the AZ membrane. In the following subsections I will discuss aspects related to synaptic transmission and the endocytic pathway in IHC ribbon-less synapses, although no final conclusion can be made due to the preliminary nature of these data.

The main caveats of this part of my thesis are the lack of a resting $RBE^{KO/KO}$ dataset and the small sample size, although $RBE^{wt/wt}$ data means fall into the lower end of the distribution of the other wild-type data (Table 5.4.3, Table 5.4.4).

4.3.1 The presence of the synaptic ribbon might be important for synaptic adaptation during the same stimulus

Quantification of docked SVs from wild-type IHC ribbon synapses might give insight in synaptic behaviour. Previous studies in conventional synapses have shown that tonic and phasic synaptic behaviours (Neher and Brose, 2018) are dependent in the proportion docked-to-tethered SVs found in the terminal (Maus et al., 2020). For instance, tonic conventional synapses, such as mossy fibre synapses, contain a low proportion of docked SVs at rest (Maus et al., 2020), hence displaying a low probability of vesicle release (Maus et al., 2020; Neher and Brose, 2018). Moreover, the increase or decrease in the proportion of docked SVs is thought to be regulating short term plasticity (Maus et al., 2020; Neher and Brose, 2018). Alternatively, IHC electrophysiological recordings point that at physiological membrane potentials ribbon synapses work in a facilitated state (Goutman and Glowatzki, 2011). Therefore, I hypothesise that adaptation to a prolonged stimulus in IHC ribbon synapses might be observed as an increase of docked SVs relative to other MP-SVs. In this regard, ribbon-occupied synapses show an increase in the fraction of docked SVs upon stimulation compared to inhibited wild-type synapses. Conversely, $RBE^{KO/KO}$ data revealed a smaller proportion of docked SVs upon stimulation than in $RBE^{wt/wt}$ ribbon synapses (Fig. 3.2.1.3.1, Fig. 3.2.2.2.1). Therefore, a milder adaptation might occur in *RBE*$^{KO/KO}$ synapses during a single strong and prolonged stimulus. However, first analysis of resting *RBE*$^{KO/KO}$ synapses is required to verify whether synaptic adaptation happens in ribbon-less synapses using 15-minute stimulation paradigm. To resolve the low temporal resolution that the currently used paradigm provides, performing optogenetic stimulation of the *RBE*$^{KO/KO}$ organ of Corti may further help dissect the temporal order of exocytic events

4.3.2 The synaptic ribbon might modulate endocytosis

The role of the ribbon in the endocytic pathway is still unclear, even though the RBE B-domain has been hypothesised to interact with an enzyme involved in SV reformation (Dembla et al., 2014). That study suggests that retinal synaptic ribbons modulate the access of the protein to its substrate, which steers the endocytic pathway (Dembla et al., 2014). Therefore, deletion of the ribbon might affect the retrieval of material and SV reformation. Indeed, a mild reduction in endocytic structures was observed in ribbon-less synapses, specially of CCVs. An increase in the sample size will contribute to verify the observed trend.

4.3.3 A model of RBE role in stimulated IHC ribbon synapses

The results presented in section 3.2 indicate that the synaptic ribbon is needed to recruit (I) numerous SVs to the synapse and (II) MP-SVs for release. In addition, the synaptic ribbon might control endocytosis.

Here I present a model for the role of the synaptic ribbon upon stimulation comparing ribbon-less and ribbon-occupied synapses (Fig. 4.2.5): strong and prolonged stimulation of wild-type ribbon synapses triggers the approach of MP-SVs to the AZ membrane, culminating in an increase in the number of docked SVs. SV fusion is followed by bulk endocytosis and CME, from which new SVs are formed and resupplied to the ribbon. In contrast, the engagement of SVs to the AZ membrane is mildly impaired, possibly due to mislocalised $Ca_V1.3$ channels, resulting in few SVs docking. Then, vesicular material is retrieved and reformed SVs approach the PD, which harbours a handful of them (not shown in the model below).

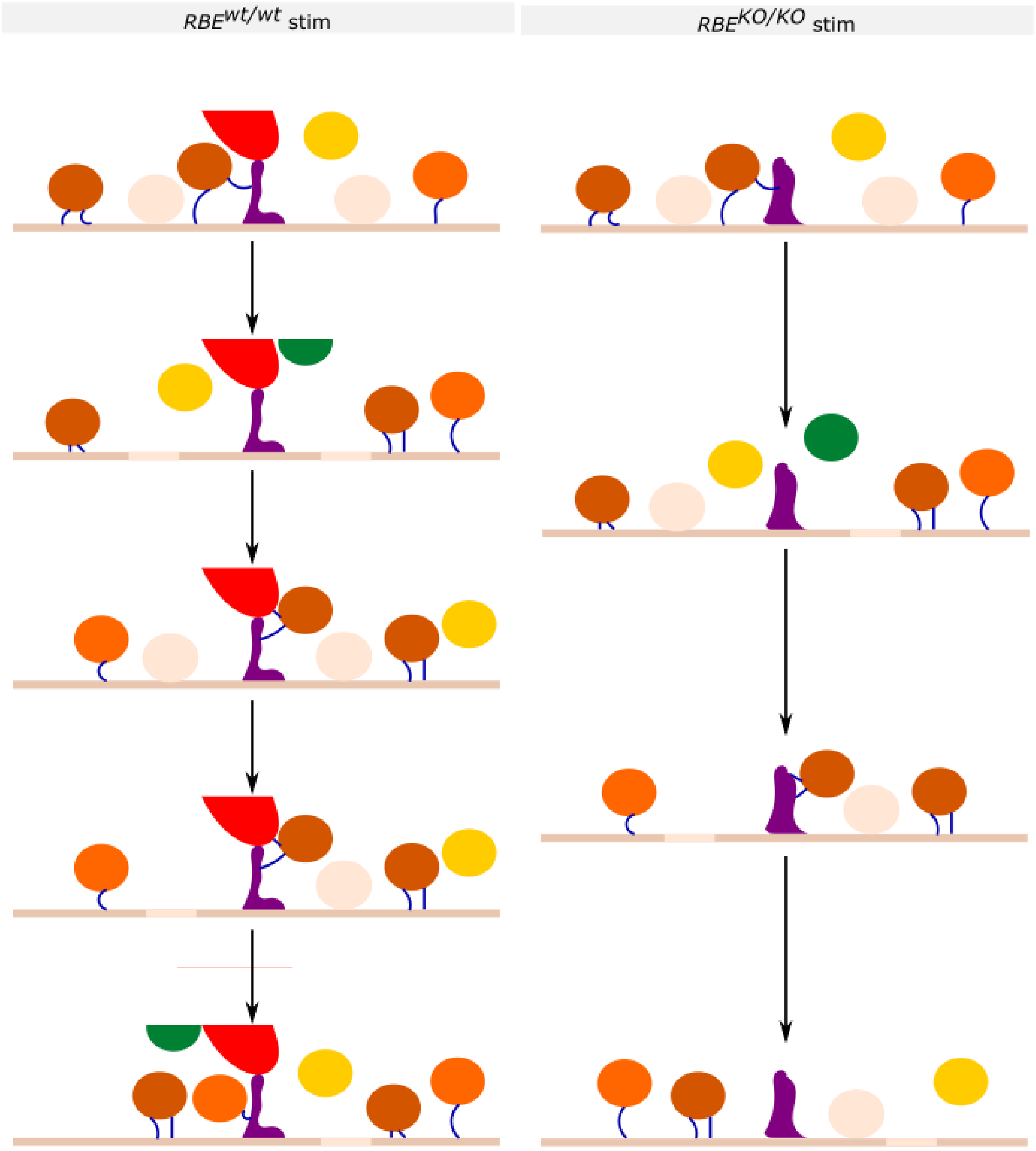

Fig. 4.3.3: Model for the role of the ribbon. MP-SVs go through the different tethering stages until docking in stimulated *RBE*$^{wt/wt}$ and *RBE*$^{KO/KO}$ ribbon synapses. Loss of ribbon produces a mild impairment in the approach of MP-SVs to the AZ membrane, which lead to fewer docked SVs. These docked SVs are found closer to the PD in mutants than in wild-type, maybe pointing to a change in the Ca$_V$1.3 channel distribution.

Colour code for SVs: green, RA-SV; yellow, non-tethered MP-SVs; orange, single-tethered MP-SV; brown, multiple-tethered MP-SVs; light orange, docked SV.

4.4 SUSTAINED OPTOGENETIC STIMULATION OF IHCS

Sustained optogenetic stimulation of IHC ribbon synapses in the presence and absence of isradipine was done to elucidate whether the Ca^{2+} influx through ChR2 is sufficient to trigger any SV pool changes. Recently, a reliable method for short and precise stimulation of IHC ribbon synapses was established, which has allowed to uncover the earlier stages of exocytosis (Chakrabarti et al., 2022). In that study, 17-26 ms and 48-76 ms light-stimulation produce an increase of docked SVs (Chakrabarti et al., 2022). I hypothesised that ChR2 (I) has a negligible effect in triggering SV subpool changes upon stimulation and (II) is expressed towards adulthood without any major effects on IHC health. The preliminary, collected data seem to support these two hypotheses, and they also allow to draw a preliminary model of sustained (~ 442 ms) physiological-like stimulation. However, the results of this section are verified with a higher sample size.

However, the main pitfalls of the presented preliminary data are the lack of Ai32VC *cre*$^-$ ribbon synapses to use as control, the disparity in sample size, and the germline recombination of the Ai32 construct causing constitutive expression of ChR2 regardless of the presence of the cre recombinase in all tissue used in the isradipine condition. The recombination of the Ai32 construct happened in Ai32VC *cre*$^+$ samples, whereby ChR2 is expressed despite the presence of cre.

4.4.1 Refinement of the experimental design

No result presented in this section presented significant changes; only mild trends could be observed. The cause for the lack of significance in the findings, that is whether it is biological or a consequence of the number of replicates and/or experimental design, remains to be addressed. Some of the major concerns in the current experimental design include the low sample size for all conditions, the lack of Ai32VC *cre*$^-$ controls, a potential failure in light stimulation and the nature of the chosen stimulation paradigm. First, the disparity in the sample size per condition (e.g., 13 tomograms in inhibited condition versus 7 tomograms in opto-stimulated condition) and the lack of Ai32VC *cre*$^-$ controls ask for these data to be interpreted with caution. The next possibility involves the failure in stimulation, but I am inclined to reject this option because before every experiment the optical fibre was tested and the graph obtained from *HPManalyse* allow to visualise whether light stimulation happened (see section 2.4.12, Fig. 2.4.12.1). Finally, the long light stimulation paradigm might result in a convergence of docked SV release ($\tau \approx$ 20-30 ms) (Beutner and Moser, 2001; Goutman and Glowatzki, 2007) and the action of fast endocytosis mechanisms ($\tau \approx$ 300 ms) (Beutner et al., 2001). Based on these electrophysiologically estimated parameters, at least 15-20 exocytic and 6-7 fast endocytic events might happen within

442 ms of light stimulation. However, reaching a sample size of 15-20 for Ai32VC *cre*$^+$ and Ai32VC *cre*$^-$ tomograms is essential to assess the events happening in 442 ms of stimulation.

In the following subsections I will discuss changes in ribbon synapse architecture upon 442 ms of light stimulation and the effects of Ca^{2+} influx through ChR2 under the assumption that the trends describe real biological phenomena.

4.4.2 Possible changes in ribbon synapse architecture upon milliseconds of sustained stimulation

Studying the early steps of exocytosis in IHC ribbon synapses became possible recently, in a study that outlined the changes in MP-SV subpools upon tens of millisecond of light stimulation (Chakrabarti et al., 2022). Despite that stimulation generally increases the proportion of docked SVs in IHC ribbon synapses, sustained stimulation (48-76 ms) produced an increase in docked SVs on the detriment of tethered SVs (Chakrabarti et al., 2022). In this context, stimulation for hundreds of milliseconds (~ 442 ms) produces a subtle increase in tethered SVs with a depletion in docked SVs (Fig. 3.3.3.1). This comparative reduction in the proportion of docked SVs might be indicative of SV fusion upon stimulation in the absence of isradipine, in such way that only through the opening $Ca_V1.3$ channels Ca^{2+} influx is enough to produce SV fusion. Alternatively, the decrease in docked SVs upon stimulation without isradipine might also happen due to the activation of fast endocytosis mechanisms, such as kiss-and-run events ($\tau \approx 300$ ms) (Beutner et al., 2001), whereby transiently fusing SVs are quickly retrieved without the mediation of clathrin (Milosevic, 2018). However, morphological evidence of kiss-and-run events (i.e., docked SVs with little neurotransmitter) in IHC ribbon synapses is yet to be found.

4.4.3 Assessing the contribution of ChR2-related Ca^{2+} influx upon light stimulation

Addition of the H134R ChR2 variant to the IHC plasma membrane might have an effect in the Ca^{2+} influx into the cells, since this opsin is an unspecific cation transporter (Nagel et al., 2003). Despite that the presence of ChR2 does not interfere with the normal synaptic progression in aging IHCs (Table 5.3.2), the presence of ChR2 might interfere with the SV cycle due to the influx of Ca^{2+} ions via ChR2 into IHCs. Therefore, stimulating ribbon synapses while blocking $Ca_V1.3$ channels contributes to determine the extent of the changes in SV subpools driven by Ca^{2+} influx via ChR2.

Assessing the likelihood for SV subpools changes upon Ca^{2+} entry through ChR2: Capacitance measurements in IHC ribbon synapses showed low Ca^{2+} affinity for exocytosis, whereby measurable SV release happens with at least 12 µM of intracellular Ca^{2+} concentration (Beutner et al., 2001). In addition, IHCs have robust mechanisms for Ca^{2+} buffering such as the action of the endoplasmic reticulum (Tucker and Fettiplace, 1995), modulation of $Ca_V1.3$ channel activation and inactivation dynamics (Frank et al., 2009; Issa and Hudspeth, 1996) and the action of mobile Ca^{2+}-binding proteins (i.e., parvalbumin, calbindin and calretinin) (Pangršič et al., 2015). The expression of ChR2 at the plasma membrane might alter the exocytic response and reduce the efficiency of the Ca^{2+} buffering mechanisms. However, ChR2 permeability to Ca^{2+} influx upon stimulation is lower than other ChR2 mutants like CatCh or Chronos (Duan et al., 2019), thereby over 90 mM Ca^{2+} in the extracellular solutions would be necessary to reach intracellular Ca^{2+} levels that elicit exocytosis (Kleinlogel et al., 2011; Mager et al., 2018). Notably, the extracellular solution used for optogenetic stimulation contained 1.3 mM of Ca^{2+} (see Table 2.2.8). Therefore, and based on these preliminary results, I am inclined to think that the overall effect of Ca^{2+} influx via ChR2 may not be sufficient to trigger ultrastructural changes in the SV subpools upon light stimulation.

Furthermore , blockage of $Ca_V1.3$ channels with isradipine is expected to block Ca^{2+} influx and, hence, block exocytosis (Brandt et al., 2003). I found that light stimulation in the presence of isradipine results in slightly (non-significant) more non-tethered SVs than upon light stimulation without isradipine, which might correlate with a reduction in SV recruitment to the AZ membrane. Confirmation of these data might suggest that Ca^{2+} entering through ChR2 is not enough to trigger an exocytic response upon sustained light stimulation.

Docked SVs: Ultrastructural data lack information about the direction of travel of docked SVs, that is whether SVs are primed for immediate neurotransmitter release, or they correspond to a fast, endocytic pathway. In the previous subsections, docked SVs have been considered the morphological correlates of primed SVs (Imig et al., 2014), whereby strong stimulation of ribbon synapses triggers an increase in their abundance (see section 3.1 and section 3.2). Notably, blockage of $Ca_V1.3$ channels appears to result in more docked SVs compared to optogenetically stimulation in absence of isradipine. The presence of isradipine makes one expect few docked SVs due to a reduced entry of Ca^{2+} to the ribbon synapse. The rejection of this hypothesis might indicate that an increase in docked SVs upon stimulation in presence of isradipine might be the product of impaired fusion. In this regard, the intracellular Ca^{2+} levels upon exclusive ChR2-driven Ca^{2+} influx might not be sufficient for Otof, which was suggested to regulate the SV pore dynamics for glutamate release (Takago et al., 2019), to induce SV fusion.

4.4.4 A preliminary model for 442 ms optogenetic stimulation of IHC ribbon synapses

Data from section 3.3 indicate that $Ca_V1.3$ channels are required to elicit a normal exocytic response upon sustained light stimulation, in which fast endocytosis pathways seem to be active.

Here I present a preliminary model for the changes in ribbon synapse architecture upon sustained optogenetic stimulation accounting for the possibly slim contribution of ChR2 in cation influx (Fig. 4.3.3). Under the premise that the observed trends are confirmed with a larger sample size, I porpose that 442 ms of light stimulation of ribbon synapses results in an increase of tethered SV, while docked SVs decrease maybe due to fast endocytic mechanisms. Conversely, blockage of $Ca_V1.3$ channels reveals more non-tethered SVs and docked SVs, although its cause remains to be clarified.

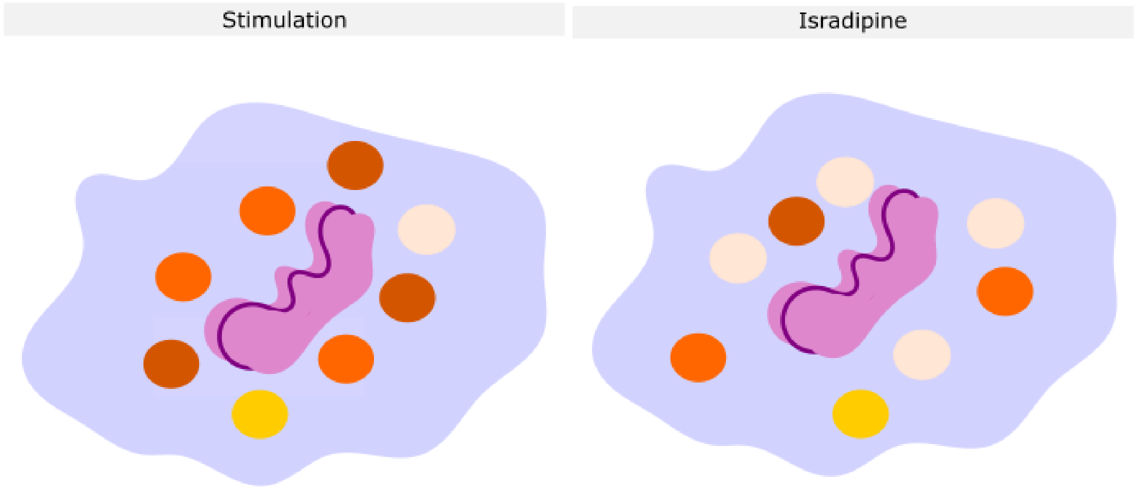

Fig. 4.4.4: Model of the effect of ChR2 in Ca^{2+} influx. The most striking morphological feature of optically stimulated ribbon synapses for 442 ms is the lack of docked SVs compared to stimulated synapses upon blockage of $Ca_V1.3$ channels.

Colour code for SVs: yellow, non-tethered MP-SVs; orange, single-tethered MP-SV; brown, multiple-tethered MP-SVs; light orange, docked SV.

4.5 CONCLUSION AND OUTLOOK

In this thesis I mainly reported ultrastructural changes in SV subpools and in the endocytic structures in ribbon synapses lacking Otof and RBE/the synaptic ribbon. These data reveal the importance of Otof for the approach of tethered SVs, specially of single tethered, to the AZ membrane; and they hint the importance of the ribbon in the release site occupancy of docked SVs.

I found ultrastructural evidence of the need for Otof in IHC ribbon synapses for the progression of SVs along the different tether states culminating in docking. Deletion of Otof severely disrupts the approach of MP-SVs to the AZ membrane, although docked SVs still appear maybe due to the action of other proteins, such as RIM2α and RIM-BP2 (Jung et al., 2015b; Krinner et al., 2021, 2017). Conversely, the involvement of Otof in the endocytic pathway and SV reformation is not clear, since visual data obtained in this thesis cannot offer clues about the molecular origin of what I classified as TESs and ELVs. Implementing correlative light and electron microscopy for IHC ribbon synapses is necessary to identify the molecular identity of these structures.

I observed that RBE predominantly affects the abundance of docked SVs and their distribution along the AZ membrane. I used two different methods for quantification to be able to compare to discern SV changes in a ribbon synapse SV pool or based on the criteria of distance to the AZ membrane. Regardless of the analysis criteria, docked SVs were scarce upon ribbon loss in stimulated conditions. In addition, docked SVs were found extremely close to the PD upon stimulation in the mutant, which might be the ultrastructural consequence of the disruption of $Ca_V1.3$ channel clusters (Becker et al., 2018; Jean et al., 2018). In contrast, the loss of the ribbon does not seem to alter the endocytic pathway.

Ultrastructural data from stimulated Otof and RBE mutants describe a synaptic landscape where the sequence for SV release, with special emphasis in the position of docked SVs, is subject to $Ca_V1.3$ channel location – controlled by RBE/the ribbon (Becker et al., 2018; Jean et al., 2018) – and Otof. Despite that the data show an impairment in the approach of tethered SVs to the AZ membrane in both mutants, the coarse temporal resolution of this study prevents me from correlating the impairment in the MP-SV progression with the speed needed for SVs to be released precisely and indefatigably upon sustained stimulation. Therefore, optogenetic stimulation of wild-type, *Otof*$^{KO/KO}$ and *RBE*$^{KO/KO}$ synapses under different stimulation times will help obtain a sequence of events in the SV cycle with high temporal resolution. Moreover, it will help narrowing down the temporal consequences of the deletion of Otof and the ribbon.

5 APPENDIX

5.1 TABLES: COMPARATIVE STUDY OF ACTIVITY-BASED CHANGES IN SYNAPTIC VESICLE ORGANISATION IN RIBBON SYNAPSES FROM TWO OTOFERLIN MUTANTS

Experimental condition		Cross-section	Longitudinal	In-between
Otof$^{wt/wt}$ inhibition	N= 4, n = 23	10	8	5
Otof$^{wt/wt}$ resting	N= 2, n= 20	7	6	7
Otof$^{wt/wt}$ stimulation	N= 3, n= 18	6	6	6
Otof$^{KO/KO}$ inhibition	N= 2, n= 20	11	3	6
Otof$^{KO/KO}$ resting	N= 3, n= 20	7	4	9
Otof$^{KO/KO}$ stimulation	N= 2, n= 17	7	1	9

Table 5.1.1: orientation of tomogram acquisition.

	Sample size	Endocytic structures	periRA-SVs	RA-SVs	MP-SVs
Otof$^{wt/wt}$ inhibition	N= 4, n = 23	0.1495 ± 0.01086	0.1935 ± 0.01816	0.4721 ± 0.01757	0.1849 ± 0.01222
Otof$^{wt/wt}$ resting	N= 2, n= 20	0.1654 ± 0.0205	0.2061 ± 0.0198	0.4470 ± 0.0190	0.1815 ± 0.0167
Otof$^{wt/wt}$ stimulation	N= 3, n= 18	0.1422 ± 0.0149	0.1669 ± 0.0145	0.4986 ± 0.0242	0.1923 ± 0.0160
Otof$^{KO/KO}$ inhibition	N= 2, n= 20	0.1432 ± 0.0174	0.1831 ± 0.0115	0.5220 ± 0.0190	0.1517 ± 0.0081
Otof$^{KO/KO}$ resting	N= 2, n= 20	0.2818 ± 0.0209	0.1479 ± 0.0136	0.4260 ± 0.0174	0.1443 ± 0.0091
Otof$^{KO/KO}$ stimulation	N= 2, n= 17	0.1562 ± 0.0258	0.1903 ± 0.0172	0.4976 ± 0.0220	0.1558 ± 0.0122
	Statistical test and significances	*Otof*$^{wt/wt}$ rest. vs. *Otof*$^{KO/KO}$ rest.: **, p= 0.0053, Kruskal-Wallis *Otof*$^{KO/KO}$ inhib. vs *Otof*$^{KO/KO}$ rest.: ***, p= 0.0001, Kruskal-Wallis *Otof*$^{KO/KO}$ stim. vs *Otof*$^{KO/KO}$ rest.: **, p=0.0036, Kruskal-Wallis	**ns**, One-way ANOVA	*Otof*$^{KO/KO}$ inhib. vs. *Otof*$^{KO/KO}$ rest.: ******, p= 0.0066, One-way ANOVA	**ns**, Kruskal-Wallis

Table 5.1.2: Fraction of analysed structures in *Otof*$^{wt/wt}$ and *Otof*$^{KO/KO}$ ribbon synapses.

	Sample size	Endocytic structures	periRA-SVs	RA-SVs	MP-SVs
Otof$^{wt/wt}$ inhibition	N= 4, n = 23	6.870 ± 0.7009	9.174 ± 1.061	21.43 ± 1.946	8.00 ± 0.5728
Otof$^{wt/wt}$ resting	N= 2, n= 20	9.750 ± 1.467	11.85 ± 1.534	24.65 ± 2.427	9.550 ± 0.8287
Otof$^{wt/wt}$ stimulation	N= 3, n= 18	6.056 ± 0.7252	7.500 ± 0.8565	23.22 ± 2.772	8.056 ± 0.6129
Otof$^{KO/KO}$ inhibition	N= 2, n= 20	9.500 ± 1.812	11.20 ± 1.461	31.85 ± 3.388	8.650 ± 0.6168
Otof$^{KO/KO}$ resting	N= 2, n= 20	21.85 ± 2.294	11.20 ± 1.256	31.90 ± 2.030	10.55 ± 0.6939
Otof$^{KO/KO}$ stimulation	N= 2, n= 17	10.47 ± 2.118	10.82 ± 1.082	29.35 ± 2.270	8.882 ± 0.6907
	Statistical test and significances	*Otof*$^{wt/wt}$ rest. vs. *Otof*$^{KO/KO}$ rest.: **, p = 0.0031, Kruskal-Wallis *Otof*$^{KO/KO}$ inhib. vs *Otof*$^{KO/KO}$ rest.: ***, p = 0.0008, Kruskal-Wallis *Otof*$^{KO/KO}$ stim. vs *Otof*$^{KO/KO}$ rest.: **, p = 0.0029, Kruskal-Wallis	**ns**, Kruskal-Wallis	**ns**, Kruskal-Wallis	**ns**, Kruskal-Wallis

Table 5.1.3: Quantification of analysed structures in *Otof*$^{wt/wt}$ and *Otof*$^{KO/KO}$ ribbon synapses.

	Sample size	RA-SVs	MP-SVs
Otof$^{wt/wt}$ inhibition	N= 4, n = 23	46.51 ± 0.1566	44.34 ± 0.2440
Otof$^{wt/wt}$ resting	N= 2, n= 20	47.76 ± 0.1616	45.82 ± 0.2805
Otof$^{wt/wt}$ stimulation	N= 3, n= 18	47.14 ± 0.1627	45.85 ± 0.2072
Otof$^{KO/KO}$ inhibition	N= 2, n= 20	48.49 ± 0.1706	45.18 ± 0.2910
Otof$^{KO/KO}$ resting	N= 2, n= 20	48.78 ± 0.1775	46.58 ± 0.2869
Otof$^{KO/KO}$ stimulation	N= 2, n= 17	48.85 ± 0.1889	47.47 ± 0.2909
	Statistical test and significances	*Otof*$^{wt/wt}$ rest. vs. *Otof*$^{wt/wt}$ inhib.: ****, p< 0.0001, Kruskal-Wallis *Otof*$^{wt/wt}$ rest. vs. *Otof*$^{KO/KO}$ rest.: **, p= 0.056, Kruskal-Wallis *Otof*$^{KO/KO}$ inhib. vs. *Otof*$^{wt/wt}$ inhib.: ****, p< 0.0001, Kruskal-Wallis *Otof*$^{KO/KO}$ stim. vs. *Otof*$^{wt/wt}$ stim.: ****, p< 0.0001, Kruskal-Wallis	*Otof*$^{wt/wt}$ rest. vs. *Otof*$^{wt/wt}$ inhib.: ***, p= 0.0004, Kruskal-Wallis *Otof*$^{KO/KO}$ inhib. vs. *Otof*$^{wt/wt}$ inhib.: **, p = 0.0031, Kruskal-Wallis *Otof*$^{KO/KO}$ stim. vs. *Otof*$^{KO/KO}$ inhib.: *, p = 0.0152, Kruskal-Wallis

Table 5.1.4: Quantification of RA and MP-SV diameters in *Otof*$^{wt/wt}$ and *Otof*$^{KO/KO}$ ribbon synapses.

	Sample size	Distances of RA-SVs to the ribbon (nm)	Distances of MP-SVs to the membrane (nm)	Distances of MP-SVs to the PD (nm)
Otof$^{wt/wt}$ inhibition	N= 4, n = 23	43,34 ± 0.8944	22.78 ± 1.096	35.65 ± 1.956
Otof$^{wt/wt}$ resting	N= 2, n= 20	45.79 ± 0.8526	22.20 ± 1.044	42.46 ± 1.997
Otof$^{wt/wt}$ stimulation	N= 3, n= 18	44.42 ± 0.8376	15.49 ± 1.065	34.61 ± 2.073
Otof$^{KO/KO}$ inhibition	N= 2, n= 20	44.22 ± 0.7126	27.04 ± 1.001	30.03 ± 1.636
Otof$^{KO/KO}$ resting	N= 2, n= 20	47.27 ± 0.7238	23.13 ± 1.046	23.13 ± 1.046
Otof$^{KO/KO}$ stimulation	N= 2, n= 17	44.69 ± 0.8439	23.32 ± 1.144	29.12 ± 2.219
	Statistical test and significances	*Otof*$^{KO/KO}$ inhib. vs. *Otof*$^{KO/KO}$ rest.: *, p = 0.0298, Kruskal-Wallis	*Otof*$^{wt/wt}$ inhib. vs. *Otof*$^{wt/wt}$ stim.: ****, p < 0.0001, Kruskal-Wallis *Otof*$^{wt/wt}$ inhib. vs. *Otof*$^{KO/KO}$ inhib.: *, p = 0.0371, Kruskal-Wallis *Otof*$^{wt/wt}$ rest. vs. *Otof*$^{wt/wt}$ stim.: ***, p = 0.0002, Kruskal-Wallis *Otof*$^{KO/KO}$ stim. vs. *Otof*$^{wt/wt}$ stim.: ****, p < 0.0001, Kruskal-Wallis	*Otof*$^{KO/KO}$ inhib. vs. *Otof*$^{KO/KO}$ rest.: **, p = 0.0088, Kruskal-Wallis *Otof*$^{KO/KO}$ stim. vs. *Otof*$^{KO/KO}$ rest.: ****, p < 0.0001, Kruskal-Wallis

Table 5.1.5: Quantification of distances to ribbon or PD and membrane of RA and MP-SV in *Otof*$^{wt/wt}$ and *Otof*$^{KO/KO}$ and ribbon synapses.

	Sample size	Non-docked MP-SVs	Docked SVs
Otof$^{wt/wt}$ inhibition	N= 4, n = 23	7.217 ± 0.5551	0.7826 ± 0.2081
Otof$^{wt/wt}$ resting	N= 2, n= 20	8.500 ± 0.7763	1.050 ± 0.2760
Otof$^{wt/wt}$ stimulation	N= 3, n= 18	6.444 ± 0.6169	1.611 ± 0.2003
Otof$^{KO/KO}$ inhibition	N= 2, n= 20	8.150 ± 0.6459	0.500 ± 0.1987
Otof$^{KO/KO}$ resting	N= 2, n= 20	9.150 ± 0.6210	1.400 ± 0.2847
Otof$^{KO/KO}$ stimulation	N= 2, n= 17	8.176 ± 0.6138	0.7059 ± 0.2389
	Statistical test and significances	**ns**, Kruskal-Wallis	*Otof*$^{KO/KO}$ stim. vs. *Otof*$^{KO/KO}$ stim.: *, p = 0.0482, Kruskal-Wallis

Table 5.1.6: Quantification of non-docked and docked SVs in *Otof*$^{wt/wt}$ and *Otof*$^{KO/KO}$ ribbon synapses.

	Sample size	Distances of non-docked MP-SVs to the membrane (nm)	Distances of non-docked SVs to the PD (nm)	Distances of docked MP-SVs to the membrane (nm)	Distances of docked SVs to the PD (nm)
Otof$^{wt/wt}$ inhibition	N= 4, n = 23	25.11 ± 1.065	34.88 ± 2.008	1.080 ± 1.412	41.72 ± 7.814
Otof$^{wt/wt}$ resting	N= 2, n= 20	24.85 ± 0.9990	43.51 ± 2.104	0.8111 ± 0.1294	36.99 ± 6.190
Otof$^{wt/wt}$ stimulation	N= 3, n= 18	19.13 ± 1.095	36.91 ± 2.272	0.8628 ± 0.1066	25.65 ± 5.208
Otof$^{KO/KO}$ inhibition	N= 2, n= 20	28.60 ± 0.9256	30.59 ± 1.651	1.209 ± 0.1634	20.90 ± 8.697
Otof$^{KO/KO}$ resting	N= 2, n= 20	26.59 ± 0.9953	39.82 ± 1.651	0.9623 ± 0.1171	38.63 ± 5.097
Otof$^{KO/KO}$ stimulation	N= 2, n= 17	25.21 ± 1.103	30.18 ± 2.308	1.264 ± 0.1084	16.91 ± 7.484
	Statistical test and significances	*Otof*$^{wt/wt}$ inhib. vs. *Otof*$^{wt/wt}$ stim.: ******, p= 0.0015, Kruskal-Wallis *Otof*$^{wt/wt}$ rest. vs. *Otof*$^{wt/wt}$ stim.: ******, p = 0.0024, Kruskal-Wallis *Otof*$^{KO/KO}$ stim. Vs. *Otof*$^{wt/wt}$ stim.: ******, p =0.020, Kruskal-Wallis	*Otof*$^{wt/wt}$ inhib. vs. *Otof*$^{wt/wt}$ rest.: *****, p= 0.0243, Kruskal- Wallis *Otof*$^{KO/KO}$ inhib. vs. *Otof*$^{KO/KO}$ rest.: *****, p = 0.0296, Kruskal-Wallis *Otof*$^{KO/KO}$ stim. vs. *Otof*$^{KO/KO}$ rest.: ******, p = 0.0014, Kruskal-Wallis	**ns**, Kruskal- Wallis	*Otof*$^{KO/KO}$ rest. vs. *Otof*$^{KO/KO}$ stim.: *****, p = 0.0285, Kruskal-Wallis

Table 5.1.7: Quantification of the distance to the membrane and PD of non-docked and docked SVs in *Otof*$^{wt/wt}$ and *Otof*$^{KO/KO}$ ribbon synapses.

	Sample size	Non-tethered SVs	Tethered SVs			Docked SVs
				Single	Multiple	
Otof$^{wt/wt}$ inhibition	N= 4, n = 23	0,1607 ± 0.0363	0.7450 ± 0.04461	0.4221 ± 0.04389	0.3100 ± 0.05302	0.09431 ± 0.02421
Otof$^{wt/wt}$ resting	N= 2, n= 20	0.3917 ± 0.04487	0.5799 ± 0.04375	0.3047 ± 0.03878	0.2586 ± 0.05249	0.1005 ± 0.02863
Otof$^{wt/wt}$ stimulation	N= 3, n= 18	0.1359 ± 0.04487	0.6470 ± 0.03261	0.3762 ± 0.04853	0.2505 ± 0.03694	0.2171 ± 0.03370
Otof$^{KO/KO}$ inhibition	N= 2, n= 20	0.1421 ± 0.03564	0.7983 ± 0.03773	0.4391 ± 0.04089	0.3293 ± 0.3757	0.05964 ± 0.02244
Otof$^{KO/KO}$ resting	N= 2, n= 20	0.1609 ± 0.03236	0.7109 ± 0.02633	0.4038 ± 0.03285	0.2944 ± 0.03333	0.1282 ± 0.2359
Otof$^{KO/KO}$ stimulation	N= 2, n= 17	0.1812 ± 0.03533	0.7483 ± 0.03963	0.4165 ± 0.04461	0.3089 ± 0.04212	0.07043 ± 0.02347
	Statistical test and significances	*Otof*$^{wt/wt}$ inhib. vs. *Otof*$^{wt/wt}$ rest.: *, p = 0.0263, Kruskal-Wallis *Otof*$^{wt/wt}$ rest vs. *Otof*$^{wt/wt}$ stim.: *, p = 0.0265, Kruskal-Wallis	*Otof*$^{wt/wt}$ rest. vs. *Otof*$^{wt/wt}$ inhib.: *, p = 0.272, Kruskal-Wallis	**ns**, Kruskal-Wallis	**ns**, Kruskal-Wallis	*Otof*$^{wt/wt}$ inhib. vs. *Otof*$^{wt/wt}$ stim.: *, p = 0.0188, Kruskal-Wallis *Otof*$^{wt/wt}$ stim. vs. *Otof*$^{KO/KO}$ stim.: *, p = 0.0109, Kruskal-Wallis

Table 5.1.8: Fraction of the MP subpools in *Otof*$^{wt/wt}$ and *Otof*$^{KO/KO}$ ribbon synapses.

	Sample size	Distances of non-tethered SVs to the membrane (nm)	Distances of non-tethered SVs to the PD (nm)	Distances of tethered SVs to the membrane (nm)			Distances of tethered SVs to the PD (nm)			Distances of docked SVs to the membrane (nm)	Distances of docked SVs to the PD (nm)
					Single	Multiple		Single	Multiple		
Otof$^{wt/wt}$ inhibition	N= 4, n = 23	27.55 ± 2.621	33.67 ± 5.316	24.60 ± 1.166	26.80 ± 1.586	22.35 ± 1.682	35.12 ± 2.171	36.68 ± 3.041	33.50 ± 3.110	1.080 ± 0.1575	41.72 ± 7.814
Otof$^{wt/wt}$ resting	N= 2, n= 20	29.92 ± 1.602	48.69 ± 3.575	22.14 ± 1.199	24.91 ± 1.542	18.93 ± 1.783	40.72 ± 2.574	41.49 ± 3.559	39.84 ± 3.759	0.8111 ± 0.1294	36.99 ± 6.190
Otof$^{wt/wt}$ stimulation	N= 3, n= 18	25.97 ± 3.006	39.77 ± 6.884	17.79 ± 1.128	18.32 ± 1.558	17.17 ± 1.649	36.35 ± 2.374	39.35 ± 3.250	32.88 ± 3.441	0.8628 ± 0.1066	25.65 ± 5.208
Otof$^{KO/KO}$ inhibition	N= 2, n= 20	32.73 ± 2.603	38.67 ± 5.399	27.89 ± 0.9794	28.87 ± 1.450	27.16 ± 1.335	29.20 ± 1.679	31.48 ± 2.506	27.46 ± 2.251	1.209 ± 0.1634	20.90 ± 8.697
Otof$^{KO/KO}$ resting	N= 2, n= 20	30.19 ± 1.958	50.29 ± 5.036	25.77 ± 1.130	27.71 ± 1.503	23.53 ± 1.679	37.43 ± 2.136	35.48 ± 2.732	39.68 ± 3.354	0.9623 ± 0.1171	38.63 ± 5.097
Otof$^{KO/KO}$ stimulation	N= 2, n= 17	25.60 ± 2.857	34.58 ± 6.927	25.12 ± 1.190	26.87 ± 1.638	23.49 ± 1.704	29.12 ± 2.336	32.96 ± 3.534	25.54 ± 3.041	1.350 ± 0.1402	16.91 ± 7.484
	Statistical test and significances	**ns**, Kruskal-Wallis	**ns**, Kruskal-Wallis	*Otof*$^{wt/wt}$ inhib. vs. *Otof*$^{wt/wt}$ stim.: *******, p= 0.0003, Kruskal-Wallis *Otof*$^{KO/KO}$ stim. vs. *Otof*$^{wt/wt}$ stim.: *******, p= 0.0002,	*Otof*$^{wt/wt}$ inhib. vs. *Otof*$^{wt/wt}$ stim.: ******, p= 0.0017, Kruskal-Wallis *Otof*$^{KO/KO}$ stim. vs. *Otof*$^{wt/wt}$ stim.: ******, p= 0.0037,	**ns**, Kruskal-Wallis	**ns** Kruskal-Wallis	**ns**, Kruskal-Wallis	**ns**, Kruskal-Wallis	**ns**, Kruskal-Wallis	*Otof*$^{wt/wt}$ inhib. vs. *Otof*$^{wt/wt}$ rest.: *, $p < 0.05$, Kruskal-Wallis

				Kruskal-Wallis	Kruskal-Wallis						

Table 5.1.9: Quantification of the distances to the AZ membrane and PD surface from MP subpools in *Otof*$^{wt/wt}$ and *Otof*$^{KO/KO}$ ribbon synapses.

	Sample size	Tethered to membrane	Tethered to PD/Rb.	Interconnected	Other multiple tethered
Otof$^{wt/wt}$ inhibition	N= 4, n = 23	0.3725 ± 005877	0.2381 ± 0.03910	0.1682 ± 0.04478	0.2213 ± 0.04052
Otof$^{wt/wt}$ resting	N= 2, n= 20	0.3738 ± 0.06449	0.2861 ± 0.05213	0.09187 ± 0.03488	0.2482 ± 0.06699
Otof$^{wt/wt}$ stimulation	N= 3, n= 18	0.4679 ± 0.06871	0.2225 ± 0.05115	0.09112 ± 0.03117	0.2185 ± 0.04978
Otof$^{KO/KO}$ inhibition	N= 2, n= 20	0.1980 ± 0.04813	0.3381 ± 0.05055	0.1026 ± 0.02523	0.3613 ± 0.04245
Otof$^{KO/KO}$ resting	N= 2, n= 20	0.2572 ± 0.04574	0.3602 ± 0.05448	0.1306 ± 0.02987	0.2521 ± 0.03656
Otof$^{KO/KO}$ stimulation	N= 2, n= 17	0.2949 ± 0.06014	0.2279 ± 0.03984	0.1691 ± 0.03519	0.3091 ± 0.04801
	Statistical test and significances	**ns**, Kruskal-Wallis	**ns** Kruskal-Wallis	**ns** Kruskal-Wallis	**ns** Kruskal-Wallis

Table 5.1.10: Fraction of MP-SVs according to the tethering partner in *Otof*$^{wt/wt}$ and *Otof*$^{KO/KO}$ and ribbon synapses.

	Sample size	All endocytic structures	Non-round endocytic structures (nm)	Round endocytic structures (nm)
Otof$^{wt/wt}$ inhibition	N= 4, n = 23	50.18 ± 1.922	57.26 ± 2.792	39.22 ± 1.481
Otof$^{wt/wt}$ resting	N= 2, n= 20	47.19 ± 1.261	49.23 ± 2.001	44.42 ± 1.238
Otof$^{wt/wt}$ stimulation	N= 3, n= 18	48.11 ± 1.674	50.64 ± 2.221	42.04 ± 1.570
Otof$^{KO/KO}$ inhibition	N= 2, n= 20	43.50 ± 0.9696	42.97 ± 1.915	43.94 ± 0.9224
Otof$^{KO/KO}$ resting	N= 2, n= 20	43.71 ± 0.5439	44.36 ± 1.124	43.26 ± 0.4856
Otof$^{KO/KO}$ stimulation	N= 2, n= 17	44.85 ± 1.209	47.88 ± 2.128	41.53 ± 0.9268
	Statistical test and significances	**ns**, Kruskal-Wallis	*Otof*$^{wt/wt}$ inhib. vs. *Otof*$^{KO/KO}$ inhib.: ******, $p = 0.0011$, Kruskal-Wallis	*Otof*$^{wt/wt}$ inhib. vs. *Otof*$^{KO/KO}$ inhib.: *****, $p = 0.0493$, Kruskal-Wallis

Table 5.1.11: Quantification of radii of endocytic structures in *Otof*$^{wt/wt}$ and *Otof*$^{KO/KO}$ ribbon synapses.

	Sample size	ELVs	CCVs	TESs
Otof$^{wt/wt}$ inhibition	N= 4, n = 23	0.7674 ± 0.03832	0.1316 ± 0.04193	0.1010 ± 0.02306
Otof$^{wt/wt}$ resting	N= 2, n= 20	0.6882 ± 0.05477	0.1162 ± 0.03335	0.1456 ± 0.03702
Otof$^{wt/wt}$ stimulation	N= 3, n= 18	0.8005 ± 0.06538	0.07738 ± 0.05645	0.1221 ± 0.04081
Otof$^{KO/KO}$ inhibition	N= 2, n= 20	0.7622 ± 0.03798	0.1014 ± 0.02837	0.1365 ± 0.03587
Otof$^{KO/KO}$ resting	N= 2, n= 20	0.7754 ± 0.04347	0.09862 ± 0.02106	0.1260 ± 0.04165
Otof$^{KO/KO}$ stimulation	N= 2, n= 17	0.8754 ± 0.05920	0.4276 ± 0.01990	0.02302 ± 0.01129
	Statistical test and significances	**ns**, Kruskal-Wallis	**ns**, Kruskal-Wallis	**ns**, Kruskal-Wallis

Table 5.1.12: Fraction of the types of endocytic structures in *Otof*$^{wt/wt}$ and *Otof*$^{KO/KO}$ ribbon synapses.

	Sample size	Round ELVs	Non-round ELVs	Round CCVs	Non-round CCVs	Non-round TESs
Otof$^{wt/wt}$ inhibition	N= 4, n= 23	44.46 ± 1.710	58.50 ± 3.350	31.41 ± 1.752	29.57 ± 3.130	56.11 ± 4.787
Otof$^{wt/wt}$ resting	N= 2, n= 20	47.67 ± 1.466	47.49 ± 2.414	36.53 ± 1.420	47.26 ± 13.29	54.13 ± 3.643
Otof$^{wt/wt}$ stimulation	N= 3, n= 18	42.20 ± 1.621	48.31 ± 2.403	39.68 ± 8.554	47.95 ± 0.00	61.12 ± 5.312
Otof$^{KO/KO}$ inhibition	N= 2, n= 20	43.92 ± 1.005	39.24 ± 2.156	43.72 ± 2.371	36.83 ± 0.00	55.07 ± 2.998
Otof$^{KO/KO}$ resting	N= 2, n= 20	43.58 ± 0.5164	42.17 ± 1.079	41.30 ± 1.376	0.00 ± 0.00	49.60 ± 2.695
Otof$^{KO/KO}$ stimulation	N= 2, n= 17	41.58 ± 1.015	47.70 ± 2.318	41.10 ± 1.810	0.00 ± 0.00	51.39± 4.428
	Statistical test and significances	**ns**, Kruskal-Wallis	*Otof*$^{wt/wt}$ inhib. vs *Otof*$^{KO/KO}$ inhib.: ********, p< 0.0001, Kruskal-Wallis *Otof*$^{KO/KO}$ stim. vs *Otof*$^{KO/KO}$ inhib.: *****, p= 0.0223, Kruskal-Wallis	*Otof*$^{wt/wt}$ inhib. vs *Otof*$^{KO/KO}$ inhib.: *******, p= 0.0005, Kruskal-Wallis	n too small for statistics	**ns**, Kruskal-Wallis

Table 5.1.13: Quantification of the radii of the various types of endocytic structures in *Otof*$^{wt/wt}$ and *Otof*$^{KO/KO}$ ribbon synapses.

	Sample size	Endocytic structures	periRA-SVs	RA-SVs	MP-SVs
B6J inhibition	N= 3, n= 10	0.06150 ± 0.01440	0.1283 ± 0.02275	0.6130 ± 0.02921	0.2224 ± 0.02525
B6J resting	N= 2, n= 7	0.04545 ± 0.01175	0.1657 ± 0.02742	0.5930 ± 0.03162	0.1959 ± 0.01289
B6J stimulation	N= 3, n= 10	0.07782 ± 0.01353	0.1707 ± 0.05363	0.5289 ± 0.07371	0.2225 ± 0.03309
Otof$^{pga/pga}$ inhibition	N= 2, n= 10	0.03833 ± 0.008210	0.1361 ± 0.03636	0.6610 ± 0.05373	0.1646 ± 0.02574
Otof$^{pga/pga}$ resting	N= 2, n= 8	0.06075 ± 0.009739	0.1408 ± 0.02714	0.5895 ± 0.02289	0.1690 ± 0.01693
Otof$^{pga/pga}$ stimulation	N= 2, n= 10	0.07949 ± 0.01143	0.1545 ± 0.03112	0.5995 ± 0.03968	0.1665 ± 0.01474
	Statistical test and significances	**ns**, Kruskal-Wallis	**ns**, Kruskal-Wallis	**ns**, One-way ANOVA	**ns**, One-way ANOVA

Table 5.1.14: Fraction of analysed structures in C57*B6/J* and *Otof*$^{pga/pga}$ ribbon synapses.

	Sample size	Endocytic structures	periRA-SVs
B6J inhibition	N= 3, n= 10	5.556 ± 1.002	5.556 ± 1.002
B6J resting	N= 2, n= 7	6.429 ± 1.088	10.29 ± 1.874
B6J stimulation	N= 3, n= 10	6.125 ± 1.505	7.750 ± 2.282
Otof$^{pga/pga}$ inhibition	N= 2, n= 10	6.200 ± 0.7272	10.50 ± 2.813
Otof$^{pga/pga}$ resting	N= 2, n= 8	8.000 ± 2.130	7.750 ± 1.461
Otof$^{pga/pga}$ stimulation	N= 2, n= 10	7.700 ± 0.9315	10.00 ± 1.783
	Statistical test and significances	**ns**, Kruskal-Wallis	**ns**, Kruskal-Wallis

Table 5.1.15: Quantification of endocytic structures and peripherally RA-SVs in C57B6/J and *Otof*$^{pga/pga}$ ribbon synapses.

	Sample size	ELVs	CCVs	TESs
B6J inhibition	N= 3, n= 10	0.8036 ± 0.01072	0.1409 ± 0.05849	0.05556 ± 0.05556
B6J resting	N= 2, n= 7	0.7544 ± 0.08173	0.2456 ± 0.08173	0.00 ± 0.00
B6J stimulation	N= 3, n= 10	0.5688 ± 0.01411	0.1667 ± 0.08333	0.1396 ± 0.06711
Otof$^{pga/pga}$ inhibition	N= 2, n= 10	0.8007 ± 0.06547	0.1243 ± 0.04606	0.0750 ± 0.05336
Otof$^{pga/pga}$ resting	N= 2, n= 8	0.8681 ± 0.04841	0.07847 ± 0.02783	0.5347 ± 0.02305
Otof$^{pga/pga}$ stimulation	N= 2, n= 10	0.7536 ± 0.06090	0.1619 ± 0.04609	0.08459 ± 0.02403
	Statistical test and significances	**ns**, Kruskal-Wallis	**ns**, Kruskal-Wallis	**ns**, Kruskal-Wallis

Table 5.1.16: Fraction of the various endocytic structures in C57B6/J and *Otof*$^{pga/pga}$ ribbon synapses.

	Sample size	Endocytic structures	periRA-SVs	RA-SVs	MP-SVs
Otof$^{KO/KO}$ inhibition	N= 2, n= 20	0.1432 ± 0.0174	0.1831 ± 0.0115	0.5220 ± 0.0190	0.1517 ± 0.0081
Otof$^{KO/KO}$ resting	N= 2, n= 20	0.2818 ± 0.0209	0.1479 ± 0.0136	0.4260 ± 0.0174	0.1443 ± 0.0091
Otof$^{KO/KO}$ stimulation	N= 2, n= 17	0.1562 ± 0.0258	0.1903 ± 0.0172	0.4976 ± 0.0220	0.1558 ± 0.0122
Otof$^{pga/pga}$ inhibition	N= 2, n= 10	0.03833 ± 0.008210	0.1361 ± 0.03636	0.6610 ± 0.05373	0.1646 ± 0.02574
Otof$^{pga/pga}$ resting	N= 2, n= 8	0.06075 ± 0.009739	0.1408 ± 0.02714	0.5895 ± 0.02289	0.1690 ± 0.01693
Otof$^{pga/pga}$ stimulation	N= 2, n= 10	0.07949 ± 0.01143	0.1545 ± 0.03112	0.5995 ± 0.03968	0.1665 ± 0.01474
	Statistical test and significances	*Otof*$^{KO/KO}$ inhib. vs *Otof*$^{KO/KO}$ rest.: *****, p= 0.0222, Kruskal-Wallis *Otof*$^{KO/KO}$ inhib. vs Otof$^{pga/pga}$ inhib.: ******, p= 0.0051, Kruskal-Wallis, *Otof*$^{KO/KO}$ stim. vs Otof$^{KO/KO}$ rest.: *****, p= 0.0223, Kruskal-Wallis *Otof*$^{pga/pga}$ rest. vs *Otof*$^{KO/KO}$ rest.: ********, $p< 0.0001$, Kruskal-Wallis	**ns**, Kruskal-Wallis	*Otof*$^{KO/KO}$ inhib. Vs *Otof*$^{KO/KO}$ rest.: *****, p= 0.0257, Kruskal-Wallis *Otof*$^{KO/KO}$ inhib. vs *Otof*$^{pga/pga}$ inhib.: ******, p= 0.0055 Kruskal-Wallis *Otof*$^{pga/pga}$ rest. vs *Otof*$^{KO/KO}$ rest.: ******, $p< 0.0022$, Kruskal-Wallis	*Otof*$^{pga/pga}$ rest. vs *Otof*$^{KO/KO}$ rest.: *****, $p< 0.00337$, Kruskal-Wallis

Table 5.3.17: Fraction of analysed structures in *Otof*$^{KO/KO}$ and *Otof*$^{pga/pga}$ ribbon synapses.

	Sample size	Endocytic structures	periRA-SVs	RA-SVs	MP-SVs
Otof$^{KO/KO}$ inhibition	N= 2, n= 20	9.500 ± 1.812	11.20 ± 1.461	31.85 ± 3.388	8.650 ± 0.6168
Otof$^{KO/KO}$ resting	N= 2, n= 20	21.85 ± 2.294	11.20 ± 1.256	31.90 ± 2.030	10.55 ± 0.6939
Otof$^{KO/KO}$ stimulation	N= 2, n= 17	10.47 ± 2.118	10.82 ± 1.082	29.35 ± 2.270	8.882 ± 0.6907
Otof$^{pga/pga}$ inhibition	N= 2, n= 10	6.200 ± 0.7272	10.50 ± 2.813	53.60 ± 7.60	12.30 ± 1.82
Otof$^{pga/pga}$ resting	N= 2, n= 8	8.000 ± 2.130	7.750 ± 1.461	33.50 ± 3.00	12.00 ± 1.650
Otof$^{pga/pga}$ stimulation	N= 2, n= 10	7.700 ± 0.9315	10.00 ± 1.783	41.80 ± 5.00	11.10 ± 0.92
	Statistical test and significances	*Otof*$^{KO/KO}$ inhib. vs. *Otof*$^{KO/KO}$ rest.: ***, p = 0.0008, Kruskal-Wallis *Otof*$^{KO/KO}$ stim. vs. *Otof*$^{KO/KO}$ rest.: **, p = 0.0029, Kruskal-Wallis	**ns**, Kruskal-Wallis	**ns**, Brown-Forsythe and Welch ANOVA	*Otof*$^{KO/KO}$ inhib. vs. *Otof*$^{pga/pga}$ inhib.: ***, p= 0.0003, Brown-Forsythe and Welch ANOVA *Otof*$^{KO/KO}$ stim. vs. *Otof*$^{pga/pga}$ stim.: ****, p< 0.0001, Brown-Forsythe and Welch ANOVA

Table 5.1.18: Quantification of analysed structures in *Otof*$^{KO/KO}$ and *Otof*$^{pga/pga}$ ribbon synapses.

Otof$^{pga/pga}$ data acquired from Chakrabarti et al. (2018).

	Sample size	Non-docked MP-SVs	Docked SVs
Otof$^{KO/KO}$ inhibition	N= 2, n= 20	8.150 ± 0.6459	0.500 ± 0.1987
Otof$^{KO/KO}$ resting	N= 2, n= 20	9.150 ± 0.6210	1.400 ± 0.2847
Otof$^{KO/KO}$ stimulation	N= 2, n= 17	8.176 ± 0.6138	0.7059 ± 0.2389
Otof$^{pga/pga}$ inhibition	N= 2, n= 10	11.5 ± 1.839	0.8 ± 0.4163
Otof$^{pga/pga}$ resting	N= 2, n= 8	11.75 ± 1.567	0.25 ± 0.4629
Otof$^{pga/pga}$ stimulation	N= 2, n= 10	9.4 ± 0.7916	1.7 ± 0.6155
	Statistical test and significances	**ns**, Kruskal-Wallis	**ns**, Kruskal-Wallis

Table 5.1.19: Quantification of non-docked and docked MP-SVs in *Otof*$^{KO/KO}$ and *Otof*$^{pga/pga}$ ribbon synapses.

	Sample size	ELVs	CCVs	TESs
Otof$^{KO/KO}$ inhibition	N= 2, n= 20	0.7622 ± 0.03798	0.1014 ± 0.02837	0.1365 ± 0.03587
Otof$^{KO/KO}$ resting	N= 2, n= 20	0.7754 ± 0.04347	0.09862 ± 0.02106	0.1260 ± 0.04165
Otof$^{KO/KO}$ stimulation	N= 2, n= 17	0.8754 ± 0.05920	0.4276 ± 0.01990	0.02302 ± 0.01129
Otof$^{pga/pga}$ inhibition	N= 2, n= 10	0.8007 ± 0.06547	0.1243 ± 0.04606	0.0750 ± 0.05336
Otof$^{pga/pga}$ resting	N= 2, n= 8	0.8681 ± 0.04841	0.07847 ± 0.02783	0.5347 ± 0.02305
Otof$^{pga/pga}$ stimulation	N= 2, n= 10	0.7536 ± 0.06090	0.1619 ± 0.04609	0.08459 ± 0.02403
	Statistical test and significances	**ns**, Kruskal-Wallis	**ns**, Kruskal-Wallis	**ns**, Kruskal-Wallis

Table 5.1.20: Quantification of the types of endocytic structures MP-SVs in *Otof*$^{KO/KO}$ and *Otof*$^{pga/pga}$ ribbon synapses.

5.2 TABLES: ULTRASTRUCTURAL CORRELATES OF EXOCYTOSIS AND ENDOCYTOSIS IN RIBBON-OCCUPIED AND RIBBON-LESS SYNAPSES

Experimental condition		Cross-section	Longitudinal	In-between
RBE$^{wt/wt}$ inhibition	N= 1, n= 7	3	1	3
RBE$^{wt/wt}$ resting	N= 1, n= 6	2	0	3
RBE$^{wt/wt}$ stimulation	N= 2, n= 7	2	3	2

Table 5.2.1: orientation of tomogram acquisition.

	Sample size	Endocytic structures	periRA-SVs	RA-SVs	MP-SVs
$RBE^{wt/wt}$ inhibition	N= 1, n= 7	0.1244 ± 0.01266	0.1681 ± 0.03352	0.4967 ± 0.04035	0.2108 ± 0.03064
$RBE^{wt/wt}$ resting	N= 1, n= 6	0.1137 ± 0.03535	0.1569 ± 0.02254	0.4993 ± 0.04891	0.2300 ± 0.02038
$RBE^{wt/wt}$ stimulation	N= 2, n= 7	0.2114 ± 0.03688	0.2465 ± 0.04660	0.3736 ± 0.04104	0.1684 ± 0.01416
$RBE^{KO/KO}$ inhibition	N= 2, n= 6	0.2156 ± 0.04490	0.1829 ± 0.04172	0.3092 ± 0.0257	0.2924 ± 0.06103
$RBE^{KO/KO}$ stimulation	N= 2, n= 6	0.2285 ± 0.07967	0.1425 ± 0.03652	0.3274 ± 0.05059	0.3016 ± 0.06261
	Statistical test and significances	**ns**, One-way ANOVA	**ns**, One-way ANOVA	$RBE^{wt/wt}$ inhib. vs. $RBE^{KO/KO}$ inhib.: *****, p= 0.0150, One-way ANOVA	**ns**, Kruskal-Wallis

Table 5.2.2: Fraction of analysed structures in $RBE^{wt/wt}$ and $RBE^{KO/KO}$ ribbon synapses.

	Sample size	Endocytic structures	periRA-SVs	RA-SVs	MP-SVs
$RBE^{wt/wt}$ inhibition	N= 1, n= 7	7.429 ± 0.8690	10.29 ± 2.124	30.71 ± 4.046	12.57 ± 1.998
$RBE^{wt/wt}$ resting	N= 1, n= 6	5.000 ± 2.082	5.500 ± 0.6708	18.17 ± 2.227	8.667 ± 1.498
$RBE^{wt/wt}$ stimulation	N= 2, n= 7	8.000 ± 1.604	9.429 ± 2.181	14.14 ± 3.128	6.143 ± 1.100
$RBE^{KO/KO}$ inhibition	N= 2, n= 6	4.833 ± 1.400	4.500 ± 1.384	7.000 ± 0.6831	6.500 ± 1.310
$RBE^{KO/KO}$ stimulation	N= 2, n= 6	5.333 ± 2.124	3.167 ± 0.8333	7.333 ± 1.174	6.167 ± 1.014
	Statistical test and significances	**ns**, Kruskal-Wallis	**ns**, One-way ANOVA	$RBE^{wt/wt}$ inhib. vs. $RBE^{KO/KO}$ inhib.: *******, p= 0.0007, Kruskal-Wallis	$RBE^{wt/wt}$ stim. vs. $RBE^{wt/wt}$ inhib.: *****, p= 0.0181, one-way ANOVA $RBE^{KO/KO}$ inhib. vs. $RBE^{wt/wt}$ inhib.: *****, p= 0.0379, one-way ANOVA

Table 5.2.3: Quantification of analysed structures in $RBE^{wt/wt}$ and $RBE^{KO/KO}$ ribbon synapses.

	Sample size	Distances of RA-SVs to the ribbon (nm)	Distances of MP-SVs to the membrane (nm)	Distances of MP-SVs to the PD (nm)
RBE$^{wt/wt}$ inhibition	N= 1, n= 7	47.82 ± 1.156	23.81 ± 1.463	30.40 ± 2.729
RBE$^{wt/wt}$ resting	N= 1, n= 6	42.53 ± 1.926	17.07 ± 2.225	33.39 ± 4.399
RBE$^{wt/wt}$ stimulation	N= 2, n= 7	48.56 ± 1.777	15.16 ± 2.161	41.25 ± 4.333
RBE$^{KO/KO}$ inhibition	N= 2, n= 6	50.71 ± 2.827	23.15 ± 2.213	24.68 ± 3.250
RBE$^{KO/KO}$ stimulation	N= 2, n= 6	43.31 ± 2.819	24.77 ± 2.507	30.08 ± 4.258
	Statistical test and significances	*RBE*$^{KO/KO}$ stim. vs. *RBE*$^{KO/KO}$ rest: ******, p= 0.0025, Kruskal-Wallis	*RBE*$^{wt/wt}$ inhib. vs. *RBE*$^{wt/wt}$ stim.: *****, p= 0.0026, Kruskal-Wallis *RBE*$^{wt/wt}$ inhib. vs. *RBE*$^{wt/wt}$ rest.: *****, p= 0.0025, Kruskal-Wallis *RBE*$^{KO/KO}$ stim. vs. *RBE*$^{wt/wt}$ stim.: *****, p= 0.0104, Kruskal-Wallis	**ns**, Kruskal- Wallis

Table 5.2.4: Distances of RA and MP-SVs to a prominent structure.

	Sample size	Non-docked MP-SVs	Docked SVs
RBE$^{wt/wt}$ inhibition	N= 1, n= 7	7.548 ± 1.936	0.2857 ± 0.1844
RBE$^{wt/wt}$ resting	N= 1, n= 6	7.167 ± 1.701	1.500 ± 0.4282
RBE$^{wt/wt}$ stimulation	N= 2, n= 7	4.429 ± 0.7190	1.714 ± 0.516
RBE$^{KO/KO}$ inhibition	N= 2, n= 6	6.167 ± 1.327	0.3333 ± 0.2108
RBE$^{KO/KO}$ stimulation	N= 2, n= 6	5.500 ± 0.8466	0.6667 ± 0.3333
	Statistical test and significances	*RBE*$^{wt/wt}$ inhib. vs. *RBE*$^{wt/wt}$ stim.: ******, p= 0.0045, Kruskal-Wallis	**ns**, Kruskal-Wallis

Table 5.2.5: Quantification of non-docked and docked SVs.

	Sample size	Distances of non-docked MP-SVs to the membrane (nm)	Distances of non-docked SVs to the PD (nm)	Distances of docked MP-SVs to the membrane (nm)	Distances of docked SVs to the PD (nm)
RBE$^{wt/wt}$ inhibition	N= 1, n= 7	24.32 ± 1.452	25.11 ± 2.770	1.844 ± 0.1504	1.844 ± 0.1504
RBE$^{wt/wt}$ resting	N= 1, n= 6	20.04 ± 2.125	39.56 ± 4.495	0.5484 ± 0.2298	11.79 ± 5.275
RBE$^{wt/wt}$ stimulation	N= 2, n= 7	20.68 ± 2.326	48.04 ± 4.883	0.8774 ± 0.2441	29.84 ± 9.453
RBE$^{KO/KO}$ inhibition	N= 2, n= 6	24.30 ± 2.176	25.24 ± 3.3398	1.561 ± 0.008033	1.849 ± 0.2950
RBE$^{KO/KO}$ stimulation	N= 2, n= 6	26.83 ± 2.425	33.35 ± 4.867	1.443 ± 0.09468	1.443 ± 0.09468
	Statistical test and significances	**ns**, Kruskal- Wallis	*RBE*$^{wt/wt}$ inhib. vs. *RBE*$^{wt/wt}$ stim.: *****, p= 0.0128, Kruskal- Wallis	-	-

Table 5.2.6: Distances of non-docked and docked SVs to the AZ membrane and PD surface.

No statistical analysis was performed for docked SVs due to the reduced SV numbers.

	Sample size	Non-tethered SVs	Tethered SVs			Docked SVs
				Single	Multiple	
$RBE^{wt/wt}$ inhibition	N= 1, n= 7	0.1370 ± 0.03953	0.8389 ± 0.05303	0.3836 ± 0.05256	0.4349 ± 0.07548	0.02407 ± 0.01790
$RBE^{wt/wt}$ resting	N= 1, n= 6	0.1940 ± 0.09050	0.5926 ± 0.02794	0.2631 ± 0.1190	0.4349 ± 0.07548	0.2133 ± 0.07631
$RBE^{wt/wt}$ stimulation	N= 2, n= 7	0.1861 ± 0.09210	0.5467 ± 0.1105	0.2219 ± 0.08338	0.2962 ± 0.09734	0.2672 ± 0.05808
$RBE^{KO/KO}$ inhibition	N= 2, n= 6	0.1389 ± 0.07954	0.8095 ± 0.1005	0.3869 ± 0.1166	0.4226 ± 0.1313	0.05159 ± 0.1358
$RBE^{KO/KO}$ stimulation	N= 2, n= 6	0.2108 ± 0.08427	0.7045 ± 0.08025	0.4439 ± 0.1183	0.2606 ± 0.07275	0.08466 ± 0.04594
	Statistical test and significances	**ns**, Kruskal-Wallis	$RBE^{wt/wt}$ inhib. vs. $RBE^{wt/wt}$ stim.: *****, p= 0.0286, Kruskal-Wallis	**ns**, Kruskal-Wallis	**ns**, Kruskal-Wallis	**ns**, Kruskal-Wallis

Table 5.2.7: Fraction of MP subpools in $RBE^{wt/wt}$ and $RBE^{KO/KO}$ ribbon synapses.

	Sample size	Distances of non-tethered SVs to the membrane (nm)	Distances of non-tethered SVs to the PD (nm)	Distances of tethered SVs to the membrane (nm)			Distances of tethered SVs to the PD (nm)			Distances of docked SVs to the membrane (nm)	Distances of docked SVs to the PD (nm)
					Single	Multiple		Single	Multiple		
RBE$^{wt/wt}$ inhibition	N= 1, n = 7	27.29 ± 3.647	34.49 ± 8.604	23.79 ± 1.585	29.83 ± 2.208	19.51 ± 2.028	29.93 ± 2.904	30.40 ± 4.376	30.50 ± 4.075	1.844 ± 0.1504	20.82 ± 19.15
RBE$^{wt/wt}$ resting	N= 1, n= 6	23.06 ± 3.837	38.93 ± 9.641	19.45 ± 2.894	24.87 ± 4.437	14.03 ± 3.255	38.16 ± 5.685	39.14 ± 7.951	37.18 ± 8.418	0.4932 ± 0.2530	9.102 ± 5.146
RBE$^{wt/wt}$ stimulation	N= 2, n= 7	28.80 ± 4.261	43.02 ± 12.27	18.73 ± 2.581	24.24 ± 3.853	15.64 ± 3.230	46.30 ± 5.063	45.59 ± 7.460	46.71 ± 6.881	0.8774 ± 0.2441	29.84 ± 9.453
RBE$^{KO/KO}$ inhibition	N= 2, n= 6	32.25 ± 4.758	32.76 ± 11.09	22.76 ± 2.358	22.74 ± 2.902	22.78 ± 3.980	23.79 ± 3.483	27.56 ± 5.612	18.90 ± 3.236	1.849 ± 0.2950	14.29 ± 4.816
RBE$^{KO/KO}$ stimulation	N= 2, n= 6	25.62 ± 5.308	15.65 ± 6.001	26.26 ± 2.785	29.67 ± 3.111	21.63 ± 5.318	35.64 ± 5.040	42.19 ± 6.632	22.71 ± 5.301	1.443 ± 0.09468	7.055 ± 5.127
	Statistical test and significances	**ns**, One-way ANOVA	**ns**, Kruskal-Wallis	**ns**, Kruskal-Wallis	**ns**, Kruskal-Wallis	**ns**, Kruskal-Wallis	**ns**, Kruskal-Wallis	**ns**, Kruskal-Wallis	**ns**, Kruskal-Wallis	**ns**, Kruskal-Wallis	**ns**, Kruskal-Wallis

Table 5.2.8: Distances of MP-SV subpools to the AZ membrane and the PD surface.

	Sample size	Tethered to membrane	Tethered to PD/Rb.	Interconnected	Other multiple tethered
RBE$^{wt/wt}$ inhibition	N= 1, n = 7	0.4122 ± 0.08371	0.2527 ± 0.08179	0.09946 ± 0.05216	0.2356 ± 0.06672
RBE$^{wt/wt}$ resting	N= 1, n= 6	0.3833 ± 0.1232	0.2600 ± 0.1461	0.1400 ± 0.05788	0.2167 ± 0.08878
RBE$^{wt/wt}$ stimulation	N= 2, n= 7	0.4524 ± 0.1026	0.09524 ± 0.04611	0.1071 ± 0.07435	0.2024 ± 0.07684
RBE$^{KO/KO}$ inhibition	N= 2, n= 6	0.2000 ± 0.09309	0.2667 ± 0.1036	0.1611 ± 0.08407	0.3722 ± 0.1454
RBE$^{KO/KO}$ stimulation	N= 2, n= 6	0.2292 ± 0.09607	0.4028 ± 0.1497	0.1250 ± 0.05990	0.2431 ± 0.09527
	Statistical test and significances	**ns**, One-way ANOVA	**ns**, Kruskal-Wallis	**ns**, Kruskal-Wallis	**ns**, One-way ANOVA

Table 5.2.9: Fraction of MP-SVs per tethering partner.

	Sample size	ELVs	CCVs
RBE$^{wt/wt}$ inhibition	N= 1, n= 7	0.7528 ± 0.05136	0.2472 ± 0.05136
RBE$^{wt/wt}$ resting	N= 1, n= 6	1.000 ± 0.000	0.000 ± 0.000
RBE$^{wt/wt}$ stimulation	N= 2, n= 7	0.5717 ± 0.1317	0.4283 ± 0.1317
RBE$^{KO/KO}$ inhibition	N= 2, n= 6	0.7500 ± 0.1708	0.2500 ± 0.1708
RBE$^{KO/KO}$ stimulation	N= 2, n= 6	0.5933 ± 0.1364	0.2401 ± 0.08273
	Statistical test and significances	*RBE*$^{wt/wt}$ rest. vs. *RBE*$^{wt/wt}$ stim.: *****, p= 0.0278, Kruskal-Wallis	*RBE*$^{wt/wt}$ rest. vs. *RBE*$^{wt/wt}$ stim.: *****, p= 0.210, Kruskal-Wallis

Table 5.2.10: Fraction of the various endocytic structures.

	Sample size	[0-40]	]40-80]	]80-120]	]120-160]	]160-200]	]200-240]	]240-280]	]280-320]	]320-360]	]360-400]
$RBE^{wt/wt}$ inhibition	N= 1, n= 7	0.2604 ± 0.04273	0.1905 ± 0.0311	0.06854 ± 0.01540	0.1352 ± 0.02290	0.09297 ± 0.01608	0.03635 ± 0.01020	0.05654 ± 0.01488	0.06199 ± 0.01806	0.5166 ± 0.01104	0.04593 ± 0.01452
$RBE^{wt/wt}$ resting	N= 1, n= 6	0.4145 ± 0.05623	0.1672 ± 0.04349	0.1202 ± 0.003818	0.03419 ± 0.01723	0.1589 ± 0.02555	0.02222 ± 0.02222	0.03333 ± 0.03333	0.01111 ± 0.01111	0.01474 ± 0.000944	0.02348 ± 0.01576
$RBE^{wt/wt}$ stimulation	N= 2, n= 7	0.4569 ± 0.09012	0.1640 ± 0.03786	0.03996 ± 0.02026	0.09710 ± 0.03507	0.1054 ± 0.03842	0.02754 ± 0.01311	0.02330 ± 0.01665	0.02618 ± 0.01695	0.04388 ± 0.03528	0.01573 ± 0.01216
$RBE^{KO/KO}$ inhibition	N= 2, n= 6	0.2959 ± 0.05538	0.2488 ± 0.02028	0.2156 ± 0.03771	0.06093 ± 0.01788	0.06032 ± 0.01713	0.01389 ± 0.01389	0.04365 ± 0.02911	0.007246 ± 0.007246	0.02243 ± 0.01507	0.03125 ± 0.03125
$RBE^{KO/KO}$ stimulation	N= 2, n= 6	0.3268 ± 0.04064	0.3235 ± 0.04321	0.2043 ± 0.02015	0.05353 ± 0.01858	0.009259 ± 0.009259	0.006945 ± 0.006945	0.02189 ± 0.01001	0.0 ± 0.0	0.02502 ± 0.01218	0.02883 ± 0.01426
	Statistical test and significances	**ns**, One-way ANOVA	$RBE^{wt/wt}$ stim. vs $RBE^{KO/KO}$ stim.: *, p= 0.0246 One-way ANOVA	$RBE^{wt/wt}$ inhib. vs $RBE^{KO/KO}$ inhib.: **, p= 0.0044, Kruskal-Wallis $RBE^{wt/wt}$ stim. vs $RBE^{KO/KO}$ stim.: ***, p= 0.0009, Kruskal-Wallis	$RBE^{wt/wt}$ inhib. vs $RBE^{wt/wt}$ rest.: *, p= 0.0388 One-way ANOVA	**ns**, Kruskal-Walli	**ns**, Kruskal-Walli	**ns**, Kruskal-Walli	**ns**, Kruskal-Walli	**ns**, Kruskal-Walli	**ns**, Kruskal-Walli

Table 5.2.11: Fraction of SVs found up to 400 nm from the AZ membrane.

	Sample size	SVs up-to-40nm	Docked SVs	Ratio docked SVs/ SVs up-to-40nm
$RBE^{wt/wt}$ inhibition	N= 1, n= 7	10.86 ± 2.355	0.2857 ± 0.1844	0.03002 ± 0.02358
$RBE^{wt/wt}$ resting	N= 1, n= 6	7.167 ± 1.352	1.167 ± 0.4773	0.1710 ± 0.06728
$RBE^{wt/wt}$ stimulation	N= 2, n= 7	3.857 ± 0.6335	1.714 ± 0.5216	0.2992 ± 0.06587
$RBE^{KO/KO}$ inhibition	N= 2, n= 6	0.5.500 ± 1,285	0.3333 ± 0.2108	0.06944 ± 0.04522
$RBE^{KO/KO}$ stimulation	N= 2, n= 6	4.833 ± 0.09804	1.000 ± 0.2582	0.2090 ± 0.07293
	Statistical test and significances	$RBE^{wt/wt}$ inhib. vs $RBE^{wt/wt}$ stim.: *, p= 0.0404, Kruskal-Wallis	**ns**, Kruskal- Wallis	$RBE^{wt/wt}$ inhib. vs $RBE^{wt/wt}$ stim.: *, p= 0.0228, Kruskal-Wallis

Table 5.2.12: Quantification of SVs up to 40 nm from the AZ membrane.

	Sample size	[0-2]	]2-5]	]5-10]	]10-15]	]15-20]	]20-25]	]25-30]	]30-35]	]35-40]
$RBE^{wt/wt}$ inhibition	N= 1, n= 7	0.03002 ± 0.02358	0.1344 ± 0.09425	0.1162 ± 0.04586	0.09962 ± 0.04449	0.1241 ± 0.05869	0.01618 ± 0.05179	0.1600 ± 0.03688	0.01188 ± 0.04016	0.05503 ± 0.03095
$RBE^{wt/wt}$ resting	N= 1, n= 6	0.1710 ± 0.06728	0.1366 ± 0.05467	0.2768 ± 0.09231	0.06944 ± 0.05450	0.06019 ± 0.04208	0.08333 ± 0.05270	0.1118 ± 0.04003	0.05622 ± 0.02629	0.03472 ± 0.02261
$RBE^{wt/wt}$ stimulation	N= 2, n= 7	0.2992 ± 0.06587	0.1635 ± 0.07341	0.01587 ± 0.01587	0.03571 ± 0.03571	0.1365 ± 0.06275	0.1508 ± 0.07736	0.1111 ± 0.06964	0.07143 ± 0.04611	0.01587 ± 0.01587
$RBE^{KO/KO}$ inhibition	N= 2, n= 6	0.06944 ± 0.04522	0.04293 ± 0.02886	0.1843 ± 0.07660	0.1843 ± 0.07660	0.2374 ± 0.07532	0.09848 ± 0.05445	0.08460 ± 0.04305	0.09848 ± 0.05445	0.1692 ± 0.07458
$RBE^{KO/KO}$ stimulation	N= 2, n= 6	0.2090 ± 0.07293	0.06019 ± 0.04208	0.1257 ± 0.05063	0.1257 ± 0.05063	0.0 ± 0.0	0.06481 ± 0.04162	0.02381 ± 0.02381	0.1772 ± 0.07816	0.1627 ± 0.08616
	Statistical test and significances	$RBE^{wt/wt}$ inhib. vs $RBE^{wt/wt}$ stim.: *****, p= 0.0228, Kruskal-Wallis	**ns**, Kruskal-Wallis	$RBE^{wt/wt}$ rest. vs $RBE^{wt/wt}$ stim: *****, p= 0.0214, Kruskal-Wallis	**ns**, Kruskal-Wallis	**ns**, Kruskal-Wallis	**ns**, Kruskal-Wallis	**ns**, Kruskal-Wallis	**ns**, Kruskal-Wallis	**ns**, Kruskal-Wallis

Table 5.2.13: Fraction of SVs found within 40 nm from the AZ membrane.

5.3 TABLES: EFFECTS OF CHR2 EXPRESSION IN THE RIBBON SYNAPSE ULTRASTRUCTURE FOR AN OPTOGENETIC MODEL

Experimental condition		Cross-section	Longitudinal	In-between
Ai32VC *cre*$^+$ inhibition	N= 3, n= 13	4	6	3
Ai32VC *cre*$^+$ isradipine	N= 2, n= 9	3	4	2
Ai32VC *cre*$^+$ opto-stimulation	N= 2, n= 7	1	2	4

Table 5.3.1: orientation of tomogram acquisition.

	Sample size	Ribbon count/IHC
WT 4-5 months	N= 2; n= 99	9.773 ± 0.6533
WT 6-7 months	N= 2; n= 87	7.605 ± 0.9884
WT 9-12 months	N= 2; n= 49	6.392 ± 0.5600
Ai32KI cre$^+$ 4-5 months	N= 3; n= 170	9.281 ± 0.4383
Ai32KI cre$^+$ 6-7 months	N= 2; n= 116	5.324 ± 0.4263
Ai32KI cre$^+$ 9-12 months	N= 2; n= 129	5.691 ± 0.4231
	Statistical test and significances	*WT* 4-5 months vs. *WT* 9-12 months: ******, p= 0.0077, Two-way ANOVA *Ai32KI cre*$^+$ 4-5 months vs. *Ai32KI cre*$^+$ 6-7 months: ********, p< 0.0001, Two-way ANOVA *Ai32KI cre*$^+$ 4-5 months vs. *Ai32KI cre*$^+$ 9-12 months: ********, p< 0.0001, Two-way ANOVA

Table 5.3.2: Average number of synaptic ribbons per IHC.

	Sample size	RA-SVs	MP-SVs
Ai32VC cre$^+$ inhibition	N= 3; n= 13	24.69 ± 2.834	10.31 ± 1.052
Ai32VC cre$^+$ opto + isradipine	N= 3; n= 9	26.33 ± 3.337	10.44 ± 0.9296
Ai32VC cre$^+$ opto	N= 2; n= 7	19.86 ± 2.454	9.286 ± 0.6061
	Statistical test and significances	**ns**, one-way ANOVA	**ns**, Kruskal-Wallis

Table 5.3.3: Quantification of RA and MP pool sizes.

	Sample size	Distances of periRA-SVs to the ribbon (nm)	Distances of RA-SVs to the ribbon (nm)	Distances of MP-SVs to the membrane (nm)	Distances of MP-SVs to the PD (nm)
Ai32VC cre$^+$ inhibition	N= 3; n= 13	111.3 ± 2.123	44.61 ± 1.283	20.26 ± 1.172	26.00 ± 2.443
Ai32VC cre$^+$ opto + isradipine	N= 3; n= 9	109.4 ± 2.065	44.55 ± 1.021	17.61 ± 1.463	22.47 ± 2.577
Ai32VC cre$^+$ opto	N= 2; n= 7	118.7 ± 2.886	45.38 ± 1.623	17.86 ± 1.534	28.81 ± 3.195
	Statistical test and significances	*Ai32VC cre*$^+$ inhibition vs. cre$^+$ opto: *****, p= 0.0378, Kruskal-Wallis	**ns**, Kruskal-Wallis	**ns**, Kruskal-Wallis	**ns**, Kruskal-Wallis

Table 5.3.4: Distances of periRA, RA and MP-SVs to a prominent structure.

	Sample size	Non-docked MP-SVs	Docked SVs
Ai32VC cre$^+$ inhibition	N= 3; n= 13	9.308 ± 1.088	1.000 ± 0.3203
Ai32VC cre$^+$ opto + isradipine	N= 3; n= 9	9.556 ± 0.9590	0.8889 ± 0.3514
Ai32VC cre$^+$ opto	N= 2; n= 7	8.571 ± 1.020	0.7143 ± 0.5654
	Statistical test and significances	**ns**, Kruskal-Wallis	**ns**, Kruskal-Wallis

Table 5.3.5: Quantification of non-docked and docked SVs.

	Sample size	Distances of non-docked MP-SVs to the membrane (nm)	Distances of non-docked SVs to the PD (nm)	Distances of docked MP-SVs to the membrane (nm)	Distances of docked SVs to the PD (nm)
Ai32VC cre^{+} inhibition	N= 3; n= 13	22.20 ± 1.147	25.30 ± 2.551	0.6951 ± 0.3126	32.47 ± 8.500
Ai32VC cre^{+} opto + isradipine	N= 3; n= 9	20.27 ± 1.498	24.57 ± 2.827	1.033 ± 0.1600	9.407 ± 4.873
Ai32VC cre^{+} opto	N= 2; n= 7	19.28 ± 1.522	30.34 ± 3.320	0.3126 ± 0.3126	10.17 ± 8.916
	Statistical test and significances	**ns**, Kruskal-Wallis	**ns**, Kruskal-Wallis	**ns**, Kruskal-Wallis	**ns**, Kruskal-Wallis

Table 5.3.6: Distances of non-docked and docked SVs to the AZ membrane and PD surface.

	Sample size	Non-tethered SVs	Tethered SVs			Docked SVs
				Single	Multiple	
Ai32VC cre^{+} inhibition	N= 3; n= 13	0.3418 ± 0.04061	0.5429 ± 0.04829	0.3577 ± 0.03660	0.1758 ± 0.03293	0.1153 ± 0.04649
Ai32VC cre^{+} opto + isradipine	N= 3; n= 9	0.3395 ± 0.05461	0.5446 ± 0.06774	0.3466 ± 0.06354	0.2843 ± 0.09929	0.1159 ± 0.03666
Ai32VC cre^{+} opto	N= 2; n= 7	0.2262 ± 0.05422	0.6792 ± 0.1060	0.3628 ± 0.04686	0.09462 ± 0.08049	0.08279 ± 0.07071
	Statistical test and significances	**ns**, One-way ANOVA	**ns**, One-way ANOVA	**ns**, Kruskal-Wallis	**ns**, Kruskal-Wallis	**ns**, Kruskal-Wallis

Table 5.3.7: Fraction of MP-SV subpools.

	Sample size	Distances of non-tethered SVs to the membrane (nm)	Distances of non-tethered SVs to the PD (nm)	Distances of tethered SVs to the membrane (nm)			Distances of tethered SVs to the PD (nm)			Distances of docked SVs to the membrane (nm)	Distances of docked SVs to the PD (nm)
					Single	Multiple		Single	Multiple		
Ai32VC cre$^+$ inhibition	N= 3; n= 13	24.25 ± 1.915	28.22 ± 4.816	20.99 ± 1.422	25.26 ± 2.484	16.10 ± 2.154	23.57 ± 2.900	26.15 ± 3.742	18.89 ± 4.479	0.6951 ± 0.1689	32.47 ± 8.500
Ai32VC cre$^+$ opto + isradipine	N= 3; n= 9	15.65 ±1.845	21.49 ± 4.810	22.39 ± 2.061	23.68 ± 2.484	18.57 ± 3.378	26.08 ± 3.567	27.93 ± 4.746	23.61 ± 5.495	1.033 ± 0.1600	12.66 ± 5.297
Ai32VC cre$^+$ opto	N= 2; n= 7	24.10 ± 3.429	30.72 ± 6.656	17.56 ± 1.613	18.75 ± 2.388	16.32 ± 2.181	30.20 ± 3.873	26.24 ± 4.020	34.35 ± 6.706	0.3126 ± 0.3126	10.17 ± 8.916
	Statistical test and significances	*Ai32VC cre*$^+$ inhib. vs. cre$^+$ israd.: ******, p= 0.0058, Kruskal-Wallis	**ns**, Kruskal-Wallis	**ns**, Kruskal-Wallis	**ns**, Kruskal-Wallis	**ns**, Kruskal-Wallis	**ns**, Kruskal-Wallis	**ns**, Kruskal-Wallis	**ns**, Kruskal-Wallis	**ns**, Kruskal-Wallis	**ns**, Kruskal-Wallis

Table 5.3.8: Distances of MP-SVs to the AZ membrane and the PD surface.

5.4 TABLES: DISCUSSION

	Sample size	ELVs	CCVs	TESs
Otof$^{wt/wt}$ inhibition	N= 3, n= 23	4.913 ± 0.4070	1.217 ± 0.4444	0.7391 ± 0.2010
Otof$^{wt/wt}$ resting	N= 2, n= 20	7.000 ± 1.095	1.300 ± 0.3980	1.450 ± 0.3439
Otof$^{wt/wt}$ stimulation	N= 3, n= 17	5.111 ± 0.7135	0.1667 ± 0.09039	0.7778 ± 0.2499
Otof$^{KO/KO}$ inhibition	N= 2, n= 20	7.600 ± 1.557	0.9500 ± 0.2562	0.9500 ± 0.2458
Otof$^{KO/KO}$ resting	N= 2, n= 20	17.40 ± 1.557	1.800 ± 0.3524	2.650 ± 0.8774
Otof$^{KO/KO}$ stimulation	N= 2, n= 17	9.471 ± 1.900	0.5291 ± 0.2443	0.4706 ± 0.2589
Otof$^{pga/pga}$ inhibition	N= 2, n= 10	5.400 ± 0.8192	0.8000 ± 0.2906	0.4000 ± 0.3055
Otof$^{pga/pga}$ resting	N= 2, n= 8	7.375 ± 1.731	0.7500 ± 0.2500	0.5000 ± 0.1890
Otof$^{pga/pga}$ stimulation	N= 2, n= 10	6.700 ± 0.6675	1.800 ± 0.5925	0.9000 ± 0.3145

Table 5.4.1: Quantification of the various endocytic structures in *Otof*$^{wt/wt}$, *Otof*$^{KO/KO}$ and *Otof*$^{pga/pga}$ ribbon synapses.

		Otof$^{wt/wt}$ inhibition	*Otof*$^{wt/wt}$ resting	*Otof*$^{wt/wt}$ stimulation	*Otof*$^{KO/KO}$ inhibition	*Otof*$^{KO/KO}$ resting	*Otof*$^{KO/KO}$ stimulation
No. tomograms		23	20	18	20	20	17
Number of vesicles		7	1	3	19	11	2
Location	Distal	6	0	3	16	9	2
	Proximal	1	1	0	3	2	0

Table 5.4.2: Number of big vesicles of over 70 nm in diameter excluded from the RA pool.

These big vesicles are counted as endosomal-like vacuoles due to their size and clear core.

	Sample size	Endocytic structures	periRA-SVs	RA-SVs	MP-SVs
B6J inhibition	N= 3, n= 10	0.06150 ± 0.01440	0.1283 ± 0.02275	0.6130 ± 0.02921	0.2224 ± 0.02525
B6J resting	N= 2, n= 7	0.04545 ± 0.01175	0.1657 ± 0.02742	0.5930 ± 0.03162	0.1959 ± 0.01289
B6J stimulation	N= 3, n= 10	0.07782 ± 0.01353	0.1707 ± 0.05363	0.5289 ± 0.07371	0.2225 ± 0.03309
Otof$^{wt/wt}$ inhibition	N= 4, n = 23	0.1495 ± 0.01086	0.1935 ± 0.01816	0.4721 ± 0.01757	0.1849 ± 0.01222
Otof$^{wt/wt}$ resting	N= 2, n= 20	0.1654 ± 0.0205	0.2061 ± 0.0198	0.4470 ± 0.0190	0.1815 ± 0.0167
Otof$^{wt/wt}$ stimulation	N= 3, n= 18	0.1422 ± 0.0149	0.1669 ± 0.0145	0.4986 ± 0.0242	0.1923 ± 0.0160
RBE$^{wt/wt}$ inhibition	N= 1, n = 7	0.1244 ± 0.01266	0.1681 ± 0.03352	0.4967 ± 0.04035	0.2108 ± 0.03064
RBE$^{wt/wt}$ resting	N= 1, n= 6	0.1137 ± 0.03535	0.1569 ± 0.02254	0.4993 ± 0.04891	0.2300 ± 0.02038
RBE$^{wt/wt}$ stimulation	N= 2, n= 7	0.2114 ± 0.03688	0.2465 ± 0.04660	0.3736 ± 0.04104	0.1684 ± 0.01416
	Statistical test and significances	B6J rest. vs. *Otof*$^{wt/wt}$ rest.: *, p= 0.0187, One-way ANOVA B6J rest. vs. *RBE*$^{wt/wt}$ rest.: **, p= 0.0055, One-way ANOVA B6J stim. vs. *RBE*$^{wt/wt}$ stim.: **, p= 0.0055, One-way ANOVA	**ns**, One-way ANOVA	B6J stim.vs. *RBE*$^{wt/wt}$ stim.: **, p= 0.0079, One-way ANOVA B6J inhib. vs. *Otof*$^{wt/wt}$ inhib.: *, p= 0.0201, One-way ANOVA B6J rest. vs. *Otof*$^{wt/wt}$ rest.: *, p= 0.0296, One-way ANOVA B6J rest. vs. *RBE*$^{wt/wt}$ stim.: ***, p= 0.0003, One-way ANOVA *Otof*$^{wt/wt}$ stim. vs. *RBE*$^{wt/wt}$ stim.: *, p=	**ns**, One-way ANOVA

				0.0055, One-way ANOVA *RBE*$^{wt/wt}$ inhib. vs. *RBE*$^{wt/wt}$ rest.: *, p= 0.0477, One-way ANOVA	

Table 5.4.3: Fractions of analysed structures in all wild-type ribbon synapses.

	Sample size	Endocytic structures	periRA-SVs	RA-SVs	MP-SVs
B6J inhibition	N= 3, n= 10	5.556 ± 1.002	5.556 ± 1.002	26.40 ± 1.8	10.20 ± 1.60
B6J resting	N= 2, n= 7	6.429 ± 1.088	10.29 ± 1.874	6.429 ± 1.088	5.556 ± 1.002
B6J stimulation	N= 3, n= 10	6.125 ± 1.505	7.750 ± 2.282	36.6 ± 4.2	11.71 ± 0.75
Otof$^{wt/wt}$ inhibition	N= 4, n = 23	6.870 ± 0.7009	9.174 ± 1.061	21.43 ± 1.946	8.00 ± 0.5728
Otof$^{wt/wt}$ resting	N= 2, n= 20	9.750 ± 1.467	11.85 ± 1.534	24.65 ± 2.427	9.550 ± 0.8287
Otof$^{wt/wt}$ stimulation	N= 3, n= 18	6.056 ± 0.7252	7.500 ± 0.8565	23.22 ± 2.772	8.056 ± 0.6129
RBE$^{wt/wt}$ inhibition	N= 1, n= 7	7.429 ± 0.8690	10.29 ± 2.124	30.71 ± 4.046	12.57 ± 1.998
RBE$^{wt/wt}$ resting	N= 1, n= 6	5.000 ± 2.082	5.500 ± 0.6708	18.17 ± 2.227	8.667 ± 1.498
RBE$^{wt/wt}$ stimulation	N= 2, n= 7	8.000 ± 1.604	9.429 ± 2.181	14.14 ± 3.128	6.143 ± 1.100

Table 5.4.4: Quantification of analysed structures in all wild-type ribbon synapses.

B6J data acquired from Chakrabarti et al., (2018)

BIBLIOGRAPHY

Becker, L., Schnee, M.E., Niwa, M., Sun, W., Maxeiner, S., Talaei, S., Kachar, B., Rutherford, M.A., Ricci, A.J., 2018. The presynaptic ribbon maintains vesicle populations at the hair cell afferent fiber synapse. eLIFE 1–26. https://doi.org/10.7554/eLife.30241.001

Beutner, D., Moser, T., 2001. The Presynaptic Function of Mouse Cochlear Inner Hair Cells during Development of Hearing. J. Neurosci. 21, 4593–4599.

Beutner, D., Voets, T., Neher, E., Moser, T., 2001. Calcium Dependence of Exocytosis and Endocytosis at the Cochlear Inner Hair Cell Afferent Synapse and anchored to the presynaptic density. It has often been suggested that the ability of sensory cells to pro-duce both rapid and sustained phases of neurotransmit, Neuron.

Borges-Merjane, C., Kim, O., Jonas, P., 2020. Functional Electron Microscopy, “Flash and Freeze,” of Identified Cortical Synapses in Acute Brain Slices. Neuron 105, 992-1006.e6. https://doi.org/10.1016/j.neuron.2019.12.022

Brandt, A., Striessnig, J., Moser, T., 2003. Ca V 1.3 Channels Are Essential for Development and Presynaptic Activity of Cochlear Inner Hair Cells. J. Neurosci. 23, 10832–10840.

Bullen, A., West, T., Moores, C., Ashmore, J., Fleck, R.A., MacLellan-Gibson, K., Forge, A., 2015. Association of intracellular and synaptic organization in cochlear inner hair cells revealed by 3D electron microscopy. J. Cell Sci. 128, 2529–2540. https://doi.org/10.1242/jcs.170761

Butola, T., Alvanos, T., Hintze, A., Koppensteiner, P., Kleindienst, D., Shigemoto, R., Wichmann, C., Moser, T., 2021. RIM-Binding Protein 2 Organizes Ca(2+) Channel Topography and Regulates Release Probability and Vesicle Replenishment at a Fast Central Synapse. J. Neurosci. Off. J. Soc. Neurosci. 41, 7742–7767. https://doi.org/10.1523/JNEUROSCI.0586-21.2021

Byczkowicz, N., Ritzau-Jost, A., Delvendahl, I., Hallermann, S., 2018. How to maintain active zone integrity during high-frequency transmission. Neurosci. Res. 127, 61–69. https://doi.org/10.1016/j.neures.2017.10.013

Ceccarelli, B., Hurlbut, W.P., Mauro, A., 1972. Depletion of vesicles from frog neuromuscular junctions by prolonged tetanic stimulation. J. Cell Biol. 54, 30–38. https://doi.org/10.1083/jcb.54.1.30

Cepeda, A.P., Al-Moyed, H., Lenz, C., Urlaub, H., Reisinger, E., 2019. PKCα-dependent interaction of otoferlin and calbindin: evidence for regulation of endocytosis in inner hair cells. bioRxiv. https://doi.org/10.1101/779520

Chakrabarti, R., 2018. Investigation of Vesicle Pool Dynamics at Activity Modulated Inner Hair Cell Ribbon Synapses.

Chakrabarti, R., Michanski, S., Wichmann, C., 2018. Vesicle sub-pool organization at inner hair cell ribbon synapses. EMBO Rep. 19. https://doi.org/10.15252/embr.201744937

Chakrabarti, R., Tobon, L.M.J., Slitin, L., Redondo-Canales, M., Hoch, G., Slashcheva, M., Fritsch, E., Bodensiek, K., Özçete, Ö.D., Gültas, M., Michanski, S., Opazo, F., Neef, J., Pangrsic, T., Moser, T., Wichmann, C., 2022. Optogenetics and electron tomography for structure-function analysis of cochlear ribbon synapses. eLife 11. https://doi.org/10.7554/eLife.79494

Chakrabarti, R., Wichmann, C., 2019. Nanomachinery Organizing Release at Neuronal and Ribbon Synapses. Int. J. Mol. Sci. 20, 2147. https://doi.org/10.3390/ijms20092147

Chapochnikov, N.M., Takago, H., Huang, C.H., Pangršič, T., Khimich, D., Neef, J., Auge, E., Göttfert, F., Hell, S.W., Wichmann, C., Wolf, F., Moser, T., 2014. Uniquantal release through a dynamic fusion pore is a candidate mechanism of hair cell exocytosis. Neuron 83, 1389–1403. https://doi.org/10.1016/j.neuron.2014.08.003

Clayton, E.L., Cousin, M.A., 2009. The molecular physiology of activity-dependent bulk endocytosis of synaptic vesicles. J. Neurochem. 111, 901–914. https://doi.org/10.1111/j.1471-4159.2009.06384.x

Clayton, E.L., Evans, G.J.O., Cousin, M.A., 2008. Bulk synaptic vesicle endocytosis is rapidly triggered during strong stimulation. J. Neurosci. Off. J. Soc. Neurosci. 28, 6627–6632. https://doi.org/10.1523/JNEUROSCI.1445-08.2008

Dallos, P., 1992. The active cochlea. J. Neurosci. 12, 4575–4585. https://doi.org/10.1523/JNEUROSCI.12-12-04575.1992

Dembla, M., Wahl, S., Katiyar, R., Schmitz, F., 2014. ArfGAP3 is a component of the photoreceptor synaptic ribbon complex and forms an NAD(H)-regulated, Redox-sensitive complex with RIBEYE that is important for endocytosis. J. Neurosci. 34, 5245–5260. https://doi.org/10.1523/JNEUROSCI.3837-13.2014

Denker, A., Rizzoli, S.O., 2010. Synaptic vesicle pools: an update. Front. Synaptic Neurosci. 2, 135. https://doi.org/10.3389/fnsyn.2010.00135

Dick, O., Dieck, S. tom, Altrock, W.D., Ammermüller, J., Weiler, R., Garner, C.C., Gundelfinger, E.D., Brandstätter, J.H., 2003. The Presynaptic Active Zone Protein Bassoon Is Essential for Photoreceptor Ribbon Synapse Formation in the Retina. Neuron 37, 775–786. https://doi.org/10.1016/S0896-6273(03)00086-2

Dieter, A., Keppeler, D., Moser, T., 2020. Towards the optical cochlear implant: optogenetic approaches for hearing restoration. EMBO Mol. Med. 12, e11618. https://doi.org/10.15252/emmm.201911618

Dominguez, M.J., McCord, J.J., Sutton, R.B., 2022. Redefining the architecture of ferlin proteins: Insights into multi-domain protein structure and function. PloS One 17, e0270188. https://doi.org/10.1371/journal.pone.0270188

Dresbach, T., Qualmann, B., Kessels, M.M., Garner, C.C., Gundelfinger, E.D., 2001. The presynaptic cytomatrix of brain synapses. Cell. Mol. Life Sci. CMLS 58, 94–116. https://doi.org/10.1007/PL00000781

Duan, X., Nagel, G., Gao, S., 2019. Mutated Channelrhodopsins with Increased Sodium and Calcium Permeability. Appl. Sci. 9. https://doi.org/10.3390/app9040664

Dubochet, J., 1995. High-pressure freezing for cryoelectron microscopy. Trends Cell Biol. 5, 366–368. https://doi.org/10.1016/S0962-8924(00)89071-6

Dulon, D., Safieddine, S., Jones, S.M., Petit, C., 2009. Otoferlin is critical for a highly sensitive and linear calcium-dependent exocytosis at vestibular hair cell ribbon synapses. J. Neurosci. 29, 10474–10487. https://doi.org/10.1523/JNEUROSCI.1009-09.2009

Duncker, S.V., Franz, C., Kuhn, S., Schulte, U., Campanelli, D., Brandt, N., Hirt, B., Fakler, B., Blin, N., Ruth, P., Engel, J., Marcotti, W., Zimmermann, U., Knipper, M., 2013. Otoferlin couples to clathrin-mediated endocytosis in mature cochlear inner hair cells. J. Neurosci. 33, 9508–9519. https://doi.org/10.1523/JNEUROSCI.5689-12.2013

Edmonds, B.W., Gregory, F.D., Schweizer, F.E., 2004. Evidence that fast exocytosis can be predominantly mediated by vesicles not docked at active zones in frog saccular hair cells. J. Physiol. 560, 439–450. https://doi.org/10.1113/jphysiol.2004.066035

Eggermann, E., Bucurenciu, I., Goswami, S.P., Jonas, P., 2011. Nanodomain coupling between Ca^{2+} channels and sensors of exocytosis at fast mammalian synapses. Nat. Rev. Neurosci. 13, 7–21. https://doi.org/10.1038/nrn3125

Fernández-Busnadiego, R., Asano, S., Oprisoreanu, A.-M., Sakata, E., Doengi, M., Kochovski, Z., Zürner, M., Stein, V., Schoch, S., Baumeister, W., Lucić, V., 2013. Cryo-electron tomography reveals a critical role of RIM1α in synaptic vesicle tethering. J. Cell Biol. 201, 725–740. https://doi.org/10.1083/jcb.201206063

Fernández-Busnadiego, R., Zuber, B., Maurer, U.E., Cyrklaff, M., Baumeister, W., Lučić, V., 2010. Quantitative analysis of the native presynaptic cytomatrix by cryoelectron tomography. J. Cell Biol. 188, 145–156. https://doi.org/10.1083/jcb.200908082

Frank, T., Khimich, D., Neef, A., Moser, T., 2009. Mechanisms contributing to synaptic Ca signals and their heterogeneity in HCs. PNAS 106, 4483–4488.

Frank, T., Rutherford, M.A., Strenzke, N., Neef, A., Pangršič, T., Khimich, D., Fetjova, A., Gundelfinger, E.D., Liberman, M.C., Harke, B., Bryan, K.E., Lee, A., Egner, A., Riedel, D., Moser, T., 2010. Bassoon and the synaptic ribbon organize Ca2+ channels and vesicles to add release sites and promote refilling. Neuron 68, 724–738. https://doi.org/10.1016/j.neuron.2010.10.027

Fuchs, P.A., Evans, M.G., Murrow, B.W., 1990. Calcium currents in hair cells isolated from the cochlea of the chick. J. Physiol. 429, 553–568. https://doi.org/10.1113/jphysiol.1990.sp018272

Fuchs, P.A., Glowatzki, E., Moser, T., 2003. The afferent synapse of cochlear hair cells. Curr. Opin. Neurobiol. 13, 452–458. https://doi.org/10.1016/S0959-4388(03)00098-9

Gersdorff, H.V., Vardi, E., Matthews, G., 1996. Evidence That Vesicles on the Synaptic Ribbon of Retinal Bipolar Neurons Can Be Rapidly Released, Neuron.

Ginzberg, R.D., Gilula, N.B., 1980. Synaptogenesis in the vestibular sensory epithelium of the chick embryo. J. Neurocytol. 9, 405–424. https://doi.org/10.1007/BF01181545

Goutman, J.D., Glowatzki, E., 2011. Short-term facilitation modulates size and timing of the synaptic response at the inner hair cell ribbon synapse. J. Neurosci. Off. J. Soc. Neurosci. 31, 7974–7981. https://doi.org/10.1523/JNEUROSCI.0604-11.2011

Goutman, J.D., Glowatzki, E., 2007. Time course and calcium dependence of transmitter release at a single ribbon synapse. PNAS 104, 16341–16346.

Granseth, B., Lagnado, L., 2008. The role of endocytosis in regulating the strength of hippocampal synapses. J. Physiol. 586, 5969–5982. https://doi.org/10.1113/jphysiol.2008.159715

Granseth, B., Odermatt, B., Royle, S.J., Lagnado, L., 2006. Clathrin-mediated endocytosis is the dominant mechanism of vesicle retrieval at hippocampal synapses. Neuron 51, 773–786. https://doi.org/10.1016/j.neuron.2006.08.029

Graydon, C.W., Zhang, J., Oesch, N.W., Sousa, A.A., Leapman, R.D., Diamond, J.S., 2014. Passive diffusion as a mechanism underlying ribbon synapse vesicle release and resupply. J. Neurosci. 34, 8948–8962. https://doi.org/10.1523/JNEUROSCI.1022-14.2014

He, L., Wu, L.-G., 2007. The debate on the kiss-and-run fusion at synapses. Trends Neurosci. 30, 447–455. https://doi.org/10.1016/j.tins.2007.06.012

Heidrych, P., Zimmermann, U., Kuhn, S., Franz, C., Engel, J., Duncker, S.V., Hirt, B., Pusch, C.M., Ruth, P., Pfister, M., Marcotti, W., Blin, N., Knipper, M., 2009. Otoferlin interacts with myosin VI: Implications for maintenance of the basolateral synaptic structure of the inner hair cell. Hum. Mol. Genet. 18, 2779–2790. https://doi.org/10.1093/hmg/ddp213

Heuser, E., Reese, T.S., 1973. EVIDENCE FOR RECYCLING OF SYNAPTIC VESICLE MEMBRANE DURING TRANSMITTER RELEASE AT THE FROG NEUROMUSCULAR JUNCTION, THE JOURNAL OF CELL BIOLOGY.

Heuser, J.E., Reese, T.S., 1981. Structural changes after transmitter release at the frog neuromuscular junction. J. Cell Biol. 88, 564–580. https://doi.org/10.1083/jcb.88.3.564

Hintze, A., Gültas, M., Semmelhack, E.A., Wichmann, C., 2021. Ultrastructural maturation of the endbulb of Held active zones comparing wild-type and otoferlin-deficient mice. iScience 24, 102282. https://doi.org/10.1016/j.isci.2021.102282

Holt, M., Cooke, A., Neef, A., Lagnado, L., 2004. High Mobility of Vesicles Supports Continuous Exocytosis at a Ribbon Synapse. Curr. Biol. 14, 173–183. https://doi.org/10.1016/j.cub.2003.12.053

Hua, Y., Ding, X., Wang, H., Wang, F., Lu, Y., Neef, J., Gao, Y., Moser, T., Wu, H., 2021. Electron Microscopic Reconstruction of Neural Circuitry in the Cochlea. Cell Rep. 34, 108551. https://doi.org/10.1016/j.celrep.2020.108551

Imig, C., López-Murcia, F.J., Maus, L., García-Plaza, I.H., Mortensen, L.S., Schwark, M., Schwarze, V., Angibaud, J., Nägerl, U.V., Taschenberger, H., Brose, N., Cooper, B.H., 2020. Ultrastructural Imaging of Activity-Dependent Synaptic Membrane-Trafficking Events in Cultured Brain Slices. Neuron 108, 843-860.e8. https://doi.org/10.1016/j.neuron.2020.09.004

Imig, C., Min, S.W., Krinner, S., Arancillo, M., Rosenmund, C., Südhof, T.C., Rhee, J.S., Brose, N., Cooper, B.H., 2014. The Morphological and Molecular Nature of Synaptic Vesicle Priming at Presynaptic Active Zones. Neuron 84, 416–431. https://doi.org/10.1016/j.neuron.2014.10.009

Issa, N.P., Hudspeth, A.J., 1996. The entry and clearance of Ca2+ at individual presynaptic active zones of hair cells from the bullfrog’s sacculus. Proc. Natl. Acad. Sci. 93, 9527–9532. https://doi.org/10.1073/pnas.93.18.9527

Jean, P., Morena, D.L. de la, Michanski, S., Tobón, L.M.J., Chakrabarti, R., Picher, M.M., Neef, J., Jung, S.Y., Gültas, M., Maxeiner, S., Neef, A., Wichmann, C., Strenzke, N., Grabner, C., Moser, T., 2018. The synaptic ribbon is critical for sound encoding at high rates and with temporal precision. eLife 7. https://doi.org/10.7554/eLife.29275

Jung, S., Maritzen, T., Wichmann, C., Jing, Z., Neef, A., Revelo, N.H., Al-Moyed, H., Meese, S., Wojcik, S.M., Panou, I., Bulut, H., Schu, P., Ficner, R., Reisinger, E., Rizzoli, S.O., Neef, J., Strenzke, N., Haucke, V., Moser, T., 2015a. Disruption of adaptor protein 2μ (AP -2μ) in cochlear hair cells impairs vesicle reloading of synaptic release sites and hearing. EMBO J. 34, 2686–2702. https://doi.org/10.15252/embj.201591885

Jung, S., Oshima-Takago, T., Chakrabarti, R., Wong, A.B., Jing, Z., Yamanbaeva, G., Picher, M.M., Wojcik, S.M., Göttfert, F., Predoehl, F., Michel, K., Hell, S.W., Schoch, S., Strenzke, N., Wichmann, C., Moser, T., 2015b. Rab3-interacting molecules 2α and 2β promote the abundance of voltage-gated CaV1.3 Ca2+ channels at hair cell active zones. Proc. Natl. Acad. Sci. U. S. A. 112, E3141–E3149. https://doi.org/10.1073/pnas.1417207112

Kaeser, P.S., Deng, L., Wang, Y., Dulubova, I., Liu, X., Rizo, J., Südhof, T.C., 2011. RIM proteins tether Ca2+ channels to presynaptic active zones via a direct PDZ-domain interaction. Cell 144, 282–295. https://doi.org/10.1016/j.cell.2010.12.029

Kamin, D., Revelo, N.H., Rizzoli, S.O., 2014. FM dye photo-oxidation as a tool for monitoring membrane recycling in inner hair cells. PLoS ONE 9. https://doi.org/10.1371/journal.pone.0088353

Kanno, H., Speedy, R.J., Angell, C.A., 1975. Supercooling of Water to -92°C Under Pressure. Science 189, 880–881. https://doi.org/10.1126/science.189.4206.880

Khimich, D., Nouvian, R., Pujol, R., tom Dieck, S., Egner, A., Gundelfinger, E.D., Moser, T., 2005. Hair cell synaptic ribbons are essential for synchronous auditory signalling. Nature 434, 889–894. https://doi.org/10.1038/nature03418

Kleinlogel, S., Feldbauer, K., Dempski, R.E., Fotis, H., Wood, P.G., Bamann, C., Bamberg, E., 2011. Ultra light-sensitive and fast neuronal activation with the Ca2+-permeable channelrhodopsin CatCh. Nat. Neurosci. 14, 513–518. https://doi.org/10.1038/nn.2776

Kremer, J.R., Mastronarde, D.N., McIntosh, J.R., 1996. Computer Visualization of Three-Dimensional Image Data Using IMOD. J. Struct. Biol. 116, 71–76. https://doi.org/10.1006/jsbi.1996.0013

Krinner, S., Butola, T., Jung, S., Wichmann, C., Moser, T., 2017. RIM-Binding Protein 2 Promotes a Large Number of Ca(V)1.3 Ca(2+)-Channels and Contributes to Fast Synaptic Vesicle Replenishment at Hair Cell Active Zones. Front. Cell. Neurosci. 11, 334. https://doi.org/10.3389/fncel.2017.00334

Krinner, S., Predoehl, F., Burfeind, D., Vogl, C., Moser, T., 2021. RIM-Binding Proteins Are Required for Normal Sound-Encoding at Afferent Inner Hair Cell Synapses. Front. Mol. Neurosci. 14. https://doi.org/10.3389/fnmol.2021.651935

Kroll, J., Tobón, L.M.J., Vogl, C., Neef, J., Kondratiuk, I., König, M., Strenzke, N., Wichmann, C., Milosevic, I., Moser, T., 2019. Endophilin-A regulates presynaptic Ca 2+ influx and synaptic vesicle recycling in auditory hair cells. EMBO J. 38. https://doi.org/10.15252/embj.2018100116

Kusick, G.F., Chin, M., Raychaudhuri, S., Lippmann, K., Adula, K.P., Hujber, E.J., Vu, T., Davis, M.W., Jorgensen, E.M., Watanabe, S., 2020. Synaptic vesicles transiently dock to refill release sites. Nat. Neurosci. 23, 1329–1338. https://doi.org/10.1038/s41593-020-00716-1

Lagnado, L., Gomis, A., Job, C., 1996. Continuous Vesicle Cycling in the Synaptic Terminal of Retinal Bipolar Cells. Neuron 17, 957–967. https://doi.org/10.1016/S0896-6273(00)80226-3

Leitz, J., Kavalali, E.T., 2011. Ca^{2+} influx slows single synaptic vesicle endocytosis. J. Neurosci. Off. J. Soc. Neurosci. 31, 16318–16326. https://doi.org/10.1523/JNEUROSCI.3358-11.2011

Lenzi, D., Crum, J., Ellisman, M.H., Roberts, W.M., 2002. Depolarization Redistributes Synaptic Membrane and Creates a Gradient of Vesicles on the Synaptic Body at a Ribbon Synapse (2 mM EGTA with no added Ca 2) before fixing and, Neuron.

Lenzi, D., Runyeon, J.W., Crum, J., Ellisman, M.H., Roberts, W.M., 1999. Synaptic vesicle populations in saccular hair cells reconstructed by electron tomography. J. Neurosci. Off. J. Soc. Neurosci. 19, 119–132. https://doi.org/10.1523/JNEUROSCI.19-01-00119.1999

Lenzi, D., von Gersdorff, H., 2001. Structure suggests function: the case for synaptic ribbons as exocytotic nanomachines. BioEssays 23, 831–840. https://doi.org/10.1002/bies.1118

Leunissen, J.L.M., Yi, H., 2009. Self-pressurized rapid freezing (SPRF): a novel cryofixation method for specimen preparation in electron microscopy. J. Microsc. 235, 25–35. https://doi.org/10.1111/j.1365-2818.2009.03178.x

Liberman, M.C., Kujawa, S.G., 2017. Cochlear synaptopathy in acquired sensorineural hearing loss: Manifestations and mechanisms. Hear. Res. 349, 138–147. https://doi.org/10.1016/j.heares.2017.01.003

Lou, S., Duan, B., Vong, L., Lowell, B.B., Ma, Q., 2013. Runx1 Controls Terminal Morphology and Mechanosensitivity of VGLUT3-expressing C-Mechanoreceptors. J. Neurosci. 33, 870–882. https://doi.org/10.1523/JNEUROSCI.3942-12.2013

Lv, C., Stewart, W.J., Akanyeti, O., Frederick, C., Zhu, J., Santos-Sacchi, J., Sheets, L., Liao, J.C., Zenisek, D., 2016. Synaptic Ribbons Require Ribeye for Electron Density, Proper Synaptic Localization, and Recruitment of Calcium Channels. Cell Rep. 15, 2784–2795. https://doi.org/10.1016/j.celrep.2016.05.045

Madisen, L., Mao, T., Koch, H., Zhuo, J.M., Berenyi, A., Fujisawa, S., Hsu, Y.W.A., Garcia, A.J., Gu, X., Zanella, S., Kidney, J., Gu, H., Mao, Y., Hooks, B.M., Boyden, E.S., Buzsáki, G., Ramirez, J.M., Jones, A.R., Svoboda, K., Han, X., Turner, E.E., Zeng, H., 2012. A toolbox of Cre-dependent optogenetic transgenic mice for light-induced activation and silencing. Nat. Neurosci. 15, 793–802. https://doi.org/10.1038/nn.3078

Mager, T., Lopez de la Morena, D., Senn, V., Schlotte, J., D´Errico, A., Feldbauer, K., Wrobel, C., Jung, S., Bodensiek, K., Rankovic, V., Browne, L., Huet, A., Jüttner, J., Wood, P.G., Letzkus, J.J., Moser, T., Bamberg, E., 2018. High frequency neural spiking and auditory signaling by ultrafast red-shifted optogenetics. Nat. Commun. 9, 1750. https://doi.org/10.1038/s41467-018-04146-3

Magupalli, V.G., Schwarz, K., Alpadi, K., Natarajan, S., Seigel, G.M., Schmitz, F., 2008. Multiple RIBEYE–RIBEYE Interactions Create a Dynamic Scaffold for the Formation of Synaptic Ribbons. J. Neurosci. 28, 7954. https://doi.org/10.1523/JNEUROSCI.1964-08.2008

Marty, N.J., Holman, C.L., Abdullah, N., Johnson, C.P., 2013. The C2 domains of otoferlin, dysferlin, and myoferlin alter the packing of lipid bilayers. Biochemistry 52, 5585–5592. https://doi.org/10.1021/bi400432f

Mastronarde, D.N., 2005. Automated electron microscope tomography using robust prediction of specimen movements. J. Struct. Biol. 152, 36–51. https://doi.org/10.1016/j.jsb.2005.07.007

Matthews, G., Sterling, P., 2008. Evidence that vesicles undergo compound fusion on the synaptic ribbon. J. Neurosci. 28, 5403–5411. https://doi.org/10.1523/JNEUROSCI.0935-08.2008

Maus, L., Lee, C., Altas, B., Sertel, S.M., Weyand, K., Rizzoli, S.O., Rhee, J., Brose, N., Imig, C., Cooper, B.H., 2020. Ultrastructural Correlates of Presynaptic Functional Heterogeneity in Hippocampal Synapses. Cell Rep. 30, 3632-3643.e8. https://doi.org/10.1016/j.celrep.2020.02.083

Maxeiner, S., Luo, F., Tan, A., Schmitz, F., Südhof, T.C., 2016. How to make a synaptic ribbon: RIBEYE deletion abolishes ribbons in retinal synapses and disrupts neurotransmitter release. EMBO J. 35, 1098–1114. https://doi.org/10.15252/embj.201592701

McNulty, J.A., Fox, L.M., 1992. Pinealocyte synaptic ribbons and neuroendocrine function. Microsc. Res. Tech. 21, 175–187. https://doi.org/10.1002/jemt.1070210302

Meyer, A.C., Frank, T., Khimich, D., Hoch, G., Riedel, D., Chapochnikov, N.M., Yarin, Y.M., Harke, B., Hell, S.W., Egner, A., Moser, T., 2009. Tuning of synapse number, structure and function in the cochlea. Nat. Neurosci. 12, 444–453. https://doi.org/10.1038/nn.2293

Michalski, N., Goutman, J.D., Auclair, S.M., Monvel, J.B. de, Tertrais, M., Emptoz, A., Parrin, A., Nouaille, S., Guillon, M., Sachse, M., Ciric, D., Bahloul, A., Hardelin, J.P., Sutton, R.B., Avan, P., Krishnakumar, S.S., Rothman, J.E., Dulon, D., Safieddine, S., Petit, C., 2017. Otoferlin acts as a Ca2+ sensor for vesicle fusion and vesicle pool replenishment at auditory hair cell ribbon synapses. eLife 6. https://doi.org/10.7554/eLife.31013

Michanski, S., Smaluch, K., Steyer, A.M., Chakrabarti, R., Setz, C., Oestreicher, D., Fischer, C., Möbius, W., Moser, T., Vogl, C., Wichmann, C., 2019. Mapping developmental maturation of inner hair cell ribbon synapses in the apical mouse cochlea. Proc. Natl. Acad. Sci. U. S. A. 116, 6415–6424. https://doi.org/10.1073/pnas.1812029116

Milosevic, I., 2018. Revisiting the Role of Clathrin-Mediated Endoytosis in Synaptic Vesicle Recycling. Front. Cell. Neurosci. 12, 27. https://doi.org/10.3389/fncel.2018.00027

Milovanovic, D., De Camilli, P., 2017. Synaptic Vesicle Clusters at Synapses: A Distinct Liquid Phase? Neuron 93, 995–1002. https://doi.org/10.1016/j.neuron.2017.02.013

Moser, T., Beutner, D., 2000. Kinetics of exocytosis and endocytosis at the cochlear inner hair cell afferent synapse of the mouse. PNAS 97, 883–888.

Moser, T., Grabner, C.P., Schmitz, F., 2019. Sensory processing at ribbon synapses in the retina and the cochlea. Physiol Rev 100, 103–144.

Moser, T., Starr, A., 2016. Auditory neuropathy--neural and synaptic mechanisms. Nat. Rev. Neurol. 12, 135–149. https://doi.org/10.1038/nrneurol.2016.10

Müller, T.M., Gierke, K., Joachimsthaler, A., Sticht, H., Izsvák, Z., Hamra, F.K., Fejtová, A., Ackermann, F., Garner, C.C., Kremers, J., Brandstätter, J.H., Regus-Leidig, H., 2019. A multiple piccolino-RIBEYE interaction supports plate-shaped synaptic ribbons in retinal neurons. J. Neurosci. 39, 2606–2619. https://doi.org/10.1523/JNEUROSCI.2038-18.2019

Nagel, G., Szellas, T., Huhn, W., Kateriya, S., Adeishvili, N., Berthold, P., Ollig, D., Hegemann, P., Bamberg, E., 2003. Channelrhodopsin-2, a directly light-gated cation-selective membrane channel. PNAS 100, 13940–13945.

Neef, A., Khimich, D., Pirih, P., Riedel, D., Wolf, F., Moser, T., 2007. Probing the Mechanism of Exocytosis at the Hair Cell Ribbon Synapse. J. Neurosci. 27, 12933–12944. https://doi.org/10.1523/JNEUROSCI.1996-07.2007

Neef, J., Jung, S.Y., Wong, A.B., Reuter, K., Pangršič, T., Chakrabarti, R., Kügler, S., Lenz, C., Nouvian, R., Boumil, R.M., Frankel, W.N., Wichmann, C., Moser, T., 2014. Modes and regulation of endocytic membrane retrieval in mouse auditory hair cells. J. Neurosci. 34, 705–716. https://doi.org/10.1523/JNEUROSCI.3313-13.2014

Neher, E., 2010. What is Rate-Limiting during Sustained Synaptic Activity: Vesicle Supply or the Availability of Release Sites. Front. Synaptic Neurosci. 2. https://doi.org/10.3389/fnsyn.2010.00144

Neher, E., Brose, N., 2018. Dynamically Primed Synaptic Vesicle States: Key to Understand Synaptic Short-Term Plasticity. Neuron 100, 1283–1291. https://doi.org/10.1016/j.neuron.2018.11.024

Neuroscience, 3rd ed., 2004. , Neuroscience, 3rd ed. Sinauer Associates, Sunderland, MA, US.

Nouvian, R., Beutner, D., Parsons, T.D., Moser, T., 2006. Structure and function of the hair cell ribbon synapse. J. Membr. Biol. 209, 153–165. https://doi.org/10.1007/s00232-005-0854-4

Nouvian, R., Neef, J., Bulankina, A.V., Reisinger, E., Pangršié, T., Frank, T., Sikorra, S., Brose, N., Binz, T., Moser, T., 2011. Exocytosis at the hair cell ribbon synapse apparently operates without neuronal SNARE proteins. Nat. Neurosci. 14, 411–413. https://doi.org/10.1038/nn.2774

Oghalai, J.S., 2004. The cochlear amplifier: augmentation of the traveling wave within the inner ear. Curr. Opin. Otolaryngol. Head Neck Surg. 12, 431–438. https://doi.org/10.1097/01.moo.0000134449.05454.82

Padmanarayana, M., Hams, N., Speight, L.C., Petersson, E.J., Mehl, R.A., Johnson, C.P., 2014. Characterization of the lipid binding properties of Otoferlin reveals specific interactions between PI(4,5)P2 and the C2C and C2F domains. Biochemistry 53, 5023–5033. https://doi.org/10.1021/bi5004469

Paillart, C., Li, J., Matthews, G., Sterling, P., 2003. Endocytosis and Vesicle Recycling at a Ribbon Synapse. J. Neurosci. 23, 4092–4099.

Pangršič, T., Gabrielaitis, M., Michanski, S., Schwaller, B., Wolf, F., Strenzke, N., Moser, T., 2015. EF-hand protein Ca2+ buffers regulate Ca2+ influx and exocytosis in sensory hair cells. Proc. Natl. Acad. Sci. U. S. A. 112, E1028–E1037. https://doi.org/10.1073/pnas.1416424112

Pangršič, T., Reisinger, E., Moser, T., 2012. Otoferlin: a multi-C2 domain protein essential for hearing. Trends Neurosci. 35, 671–680. https://doi.org/10.1016/j.tins.2012.08.002

Pangšrič, T., Lasarow, L., Reuter, K., Takago, H., Schwander, M., Riedel, D., Frank, T., Tarantino, L.M., Bailey, J.S., Strenzke, N., Brose, N., Müller, U., Reisinger, E., Moser, T., 2010. Hearing requires otoferlin-dependent efficient replenishment of synaptic vesicles in hair cells. Nat. Neurosci. 13, 869–876. https://doi.org/10.1038/nn.2578

Payne, S.A., Joens, M.S., Chung, H., Skigen, N., Frank, A., Gattani, S., Vaughn, K., Schwed, A., Nester, M., Bhattacharyya, A., Iyer, G., Davis, B., Carlquist, J., Patel, H., Fitzpatrick, J.A.J., Rutherford, M.A., 2021. Maturation of Heterogeneity in Afferent Synapse Ultrastructure in the Mouse Cochlea. Front. Synaptic Neurosci. 13. https://doi.org/10.3389/fnsyn.2021.678575

Pelassa, I., Zhao, C., Pasche, M., Odermatt, B., Lagnado, L., 2014. Synaptic vesicles are â€œprimedâ€� for fast clathrin-mediated endocytosis at the ribbon synapse. Front. Mol. Neurosci. 7. https://doi.org/10.3389/fnmol.2014.00091

Platzer, J., Engel, J., Schrott-Fischer, A., Stephan, K., Bova, S., Chen, H., Zheng, H., Striessnig, J., 2000. Congenital Deafness and Sinoatrial Node Dysfunction in Mice Lacking Class D L-Type Ca2+ Channels. Cell 102, 89–97. https://doi.org/10.1016/S0092-8674(00)00013-1

Ramakrishnan, N.A., Drescher, M.J., Drescher, D.G., 2009. Direct Interaction of Otoferlin with Syntaxin 1A, SNAP-25, and the L-type Voltage-gated Calcium Channel CaV1.3*. J. Biol. Chem. 284, 1364–1372. https://doi.org/10.1074/jbc.M803605200

Rao-Mirotznik, R., Harkins, A.B., Buchsbaum, G., Sterling, P., 1995. Mammalian rod terminal: Architecture of a binary synapse. Neuron 14, 561–569. https://doi.org/10.1016/0896-6273(95)90312-7

Regus-Leidig, H., Fuchs, M., Löhner, M., Leist, S.R., Leal-Ortiz, S., Chiodo, V.A., Hauswirth, W.W., Garner, C.C., Brandstätter, J.H., 2014. In vivo knockdown of Piccolino disrupts presynaptic ribbon morphology in mouse photoreceptor synapses. Front. Cell. Neurosci. 8. https://doi.org/10.3389/fncel.2014.00259

Regus-Leidig, H., tom Dieck, S., Specht, D., Meyer, L., Brandstätter, J.H., 2009. Early steps in the assembly of photoreceptor ribbon synapses in the mouse retina: The involvement of precursor spheres. J. Comp. Neurol. 512, 814–824. https://doi.org/10.1002/cne.21915

Reisinger, E., Bresee, C., Neef, J., Nair, R., Reuter, K., Bulankina, A., Nouvian, R., Koch, M., Bückers, J., Kastrup, L., Roux, I., Petit, C., Hell, S.W., Brose, N., Rhee, J.S., Kügler, S., Brigande, J.V., Moser, T., 2011. Probing the functional equivalence of otoferlin and synaptotagmin 1 in exocytosis. J. Neurosci. 31, 4886–4895. https://doi.org/10.1523/JNEUROSCI.5122-10.2011

Revelo, N.H., Rizzoli, S.O., 2016. The membrane marker mCLING reveals the molecular composition of trafficking organelles. Curr. Protoc. Neurosci. 2016, 2.25.1-2.25.21. https://doi.org/10.1002/0471142301.ns0225s74

Rizzoli, S.O., 2014. Synaptic vesicle recycling: steps and principles. EMBO J. 33, 788–822. https://doi.org/10.1002/embj.201386357

Rizzoli, S.O., Betz, W.J., 2004. The Structural Organization of the Readily Releasable Pool of Synaptic Vesicles. Science 303, 2037–2039. https://doi.org/10.1126/science.1094682

Rodríguez-Ballesteros, M., Reynoso, R., Olarte, M., Villamar, M., Morera, C., Santarelli, R., Arslan, E., Medá, C., Curet, C., Völter, C., Sainz-Quevedo, M., Castorina, P., Ambrosetti, U., Berrettini, S., Frei, K., Tedín, S., Smith, J., Cruz Tapia, M., Cavallé, L., Gelvez, N., Primignani, P., Gómez-Rosas, E., Martín, M., Moreno-Pelayo, M.A., Tamayo, M., Moreno-Barral, J., Moreno, F., del Castillo, I., 2008. A multicenter study on the prevalence and spectrum of mutations in the otoferlin gene (OTOF) in subjects with nonsyndromic hearing impairment and auditory neuropathy. Hum. Mutat. 29, 823–831. https://doi.org/10.1002/humu.20708

Rosenmund, C., Stevens, C.F., 1996. Definition of the Readily Releasable Pool of Vesicles at Hippocampal Synapses. Neuron 16, 1197–1207. https://doi.org/10.1016/S0896-6273(00)80146-4

Roux, I., Safieddine, S., Nouvian, R., Grati, M., Simmler, M.-C., Bahloul, A., Perfettini, I., Le Gall, M., Rostaing, P., Hamard, G., Triller, A., Avan, P., Moser, T., Petit, C., 2006. Otoferlin, Defective in a Human Deafness Form, Is Essential for Exocytosis at the Auditory Ribbon Synapse. Cell 127, 277–289. https://doi.org/10.1016/j.cell.2006.08.040

Safieddine, S., El-Amraoui, A., Petit, C., 2012. The Auditory Hair Cell Ribbon Synapse: From Assembly to Function. Annu. Rev. Neurosci. 35, 509–528. https://doi.org/10.1146/annurev-neuro-061010-113705

Safieddine, S., Wenthold, R.J., 1999. SNARE complex at the ribbon synapses of cochlear hair cells: analysis of synaptic vesicle- and synaptic membrane-associated proteins. Eur. J. Neurosci. 11, 803–812. https://doi.org/10.1046/j.1460-9568.1999.00487.x

Schmitz, F., Königstorfer, A., Südhof, T.C., 2000. RIBEYE, a Component of Synaptic Ribbons: A Protein's Journey through Evolution Provides Insight into Synaptic Ribbon Function. Neuron 28, 857–872. https://doi.org/10.1016/S0896-6273(00)00159-8

Schnee, M.E., Lawton, D.M., Furness, D.N., Benke, T.A., Ricci, A.J., 2005. Auditory Hair Cell-Afferent Fiber Synapses Are Specialized to Operate at Their Best Frequencies. Neuron 47, 243–254. https://doi.org/10.1016/j.neuron.2005.06.004

Schwander, M., Sczaniecka, A., Grillet, N., Bailey, J.S., Avenarius, M., Najmabadi, H., Steffy, B.M., Federe, G.C., Lagler, E.A., Banan, R., Hice, R., Grabowski-Boase, L., Keithley, E.M., Ryan, A.F., Housley, G.D., Wiltshire, T., Smith, R.J.H., Tarantino, L.M., Müller, U., 2007. A forward genetics screen in mice identifies recessive deafness traits and reveals that pejvakin is essential for outer hair cell function. J. Neurosci. 27, 2163–2175. https://doi.org/10.1523/JNEUROSCI.4975-06.2007

Schwarz, K., Natarajan, S., Kassas, N., Vitale, N., Schmitz, F., 2011. The synaptic ribbon is a site of phosphatidic acid generation in ribbon synapses. J. Neurosci. Off. J. Soc. Neurosci. 31, 15996–16011. https://doi.org/10.1523/JNEUROSCI.2965-11.2011

Sergeyenko, Y., Lall, K., Liberman, M.C., Kujawa, S.G., 2013. Age-related cochlear synaptopathy: An early-onset contributor to auditory functional decline. J. Neurosci. 33, 13686–13694. https://doi.org/10.1523/JNEUROSCI.1783-13.2013

Smith, C.A., Sjöstrand, F.S., 1961. Structure of the nerve endings on the external hair cells of the guinea pig cochlea as studied by serial sections. J. Ultrastruct. Res. 5, 523–556. https://doi.org/10.1016/S0022-5320(61)80025-7

Sobkowicz, H., Rose, J., Scott, G., Slapnick, S., 1982. Ribbon synapses in the developing intact and cultured organ of Corti in the mouse. J. Neurosci. 2, 942–957. https://doi.org/10.1523/JNEUROSCI.02-07-00942.1982

Spassova, M.A., Avissar, M., Furman, A.C., Crumling, M.A., Saunders, J.C., Parsons, T.D., 2004. Evidence that rapid vesicle replenishment of the synaptic ribbon mediates recovery from short-term adaptation at the hair cell afferent synapse. JARO - J. Assoc. Res. Otolaryngol. 5, 376–390. https://doi.org/10.1007/s10162-004-5003-8

Stahlberg, M.A., Ramakrishnan, C., Willig, K.I., Boyden, E.S., Deisseroth, K., Dean, C., 2019. Investigating the feasibility of channelrhodopsin variants for nanoscale optogenetics. Neurophotonics 6, 1. https://doi.org/10.1117/1.nph.6.1.015007

Stamataki, S., Francis, H.W., Lehar, M., May, B.J., Ryugo, D.K., 2006. Synaptic alterations at inner hair cells precede spiral ganglion cell loss in aging C57BL/6J mice. Hear. Res. 221, 104–118. https://doi.org/10.1016/j.heares.2006.07.014

Stevens, C.F., Tsujimoto, T., 1995. Estimates for the pool size of releasable quanta at a single central synapse and for the time required to refill the pool. Proc. Natl. Acad. Sci. 92, 846–849. https://doi.org/10.1073/pnas.92.3.846

Strenzke, N., Chakrabarti, R., Al-Moyed, H., Müller, A., Hoch, G., Pangrsic, T., Yamanbaeva, G., Lenz, C., Pan, K.-T., Auge, E., Geiss-Friedlander, R., Urlaub, H., Brose, N., Wichmann, C., Reisinger, E., 2016. Hair cell synaptic dysfunction, auditory fatigue and thermal sensitivity in otoferlin Ile515Thr mutants. EMBO J. 35, 2519–2535. https://doi.org/10.15252/embj.201694564

Takago, H., Oshima-Takago, T., Moser, T., 2019. Disruption of otoferlin alters the mode of exocytosis at the mouse inner hair cell ribbon synapse. Front. Mol. Neurosci. 11. https://doi.org/10.3389/fnmol.2018.00492

tom Dieck, S., Brandstätter, J.H., 2006. Ribbon synapses of the retina. Cell Tissue Res. 326, 339–346. https://doi.org/10.1007/s00441-006-0234-0

tom Dieck, S., Sanmartí-Vila, L., Langnaese, K., Richter, K., Kindler, S., Soyke, A., Wex, H., Smalla, K.-H., Kämpf, U., Fränzer, J.-T., Stumm, M., Garner, C.C., Gundelfinger, E.D., 1998. Bassoon, a Novel Zinc-finger CAG/Glutamine-repeat Protein Selectively Localized at the Active Zone of Presynaptic Nerve Terminals. J. Cell Biol. 142, 499–509. https://doi.org/10.1083/jcb.142.2.499

Tucker, T., Fettiplace, R., 1995. Confocal imaging of calcium microdomains and calcium extrusion in turtle hair cells. Neuron 15, 1323–1335. https://doi.org/10.1016/0896-6273(95)90011-X

Uthaiah, R.C., Hudspeth, A.J., 2010. Molecular anatomy of the hair cell's ribbon synapse. J. Neurosci. Off. J. Soc. Neurosci. 30, 12387–12399. https://doi.org/10.1523/JNEUROSCI.1014-10.2010

Vogl, C., Cooper, B.H., Neef, J., Wojcik, S.M., Reim, K., Reisinger, E., Brose, N., Rhee, J.-S., Moser, T., Wichmann, C., 2015. Unconventional molecular regulation of synaptic vesicle replenishment in cochlear inner hair cells. J. Cell Sci. 128, 638. https://doi.org/10.1242/jcs.162099

Vogl, C., Panou, I., Yamanbaeva, G., Wichmann, C., Mangosing, S., Vilardi, F., Indzhykulian, A.A., Pangršič, T., Santarelli, R., Rodriguez-Ballesteros, M., Weber, T., Jung, S., Wu, X., Wojcik, S.M., Kwan, K.Y., Castillo, I.D., Schwappach, B., Strenzke, N., Corey, D.P., Lin, S.-Y., Moser, T., 2016. Tryptophan-rich basic protein (WRB) mediates insertion of the tail-anchored protein otoferlin and is required for hair cell exocytosis and hearing. EMBO J. 35, 2436–2552.

Voorn, R.A., Vogl, C., 2020. Molecular Assembly and Structural Plasticity of Sensory Ribbon Synapses-A Presynaptic Perspective. Int. J. Mol. Sci. 21. https://doi.org/10.3390/ijms21228758

Wan, G., Corfas, G., Stone, J.S., 2013. Inner ear supporting cells: rethinking the silent majority. Semin. Cell Dev. Biol. 24, 448–459. https://doi.org/10.1016/j.semcdb.2013.03.009

Wangemann, P., 2006. Supporting sensory transduction: cochlear fluid homeostasis and the endocochlear potential. J. Physiol. 576, 11–21. https://doi.org/10.1113/jphysiol.2006.112888

Wangemann, P., 2002. K+ cycling and the endocochlear potential. Hear. Res. 165, 1–9.

Watanabe, S., Davis, M.W., Jorgensen, E.M., 2014. Flash-and-freeze electron microscopy: Coupling optogenetics with high-pressure freezing. Neuromethods 84, 43–57. https://doi.org/10.1007/978-1-4614-9179-8_3

Watanabe, S., Liu, Q., Davis, M.W., Hollopeter, G., Thomas, N., Jorgensen, N.B., Jorgensen, E.M., 2013a. Ultrafast endocytosis at Caenorhabditis elegans neuromuscular junctions. eLife 2013. https://doi.org/10.7554/eLife.00723

Watanabe, S., Rost, B.R., Camacho-Pérez, M., Davis, M.W., Söhl-Kielczynski, B., Rosenmund, C., Jorgensen, E.M., 2013b. Ultrafast endocytosis at mouse hippocampal synapses. Nature 504, 242–247. https://doi.org/10.1038/nature12809

Wichmann, C., Moser, T., 2015. Relating structure and function of inner hair cell ribbon synapses. Cell Tissue Res. 361, 95–114. https://doi.org/10.1007/s00441-014-2102-7

Wong, A.B., Rutherford, M.A., Gabrielaitis, M., Pangršič, T., Göttfert, F., Frank, T., Michanski, S., Hell, S., Wolf, F., Wichmann, C., Moser, T., 2014. Developmental refinement of hair cell synapses tightens the coupling of Ca2+ influx to exocytosis. EMBO J. 33, 247–264. https://doi.org/10.1002/embj.201387110

Wu, Y., O'Toole, E.T., Girard, M., Ritter, B., Messa, M., Liu, X., McPherson, P.S., Ferguson, S.M., De Camilli, P., 2014. A dynamin 1-, dynamin 3- and clathrin-independent pathway of synaptic vesicle recycling mediated by bulk endocytosis. eLife 3, e01621. https://doi.org/10.7554/eLife.01621

Xu, W., Lipscombe, D., 2001. Neuronal CaV1.3α1 L-Type Channels Activate at Relatively Hyperpolarized Membrane Potentials and Are Incompletely Inhibited by Dihydropyridines. J. Neurosci. 21, 5944–5951. https://doi.org/10.1523/JNEUROSCI.21-16-05944.2001

Yasunaga, ichiro, Grati, hamed, Chardenoux, S., Smith, T.N., Friedman, T.B., Lalwani, A.K., Wilcox, E.R., Petit, C., 2000. OTOF Encodes Multiple Long and Short Isoforms: Genetic Evidence That the Long Ones Underlie Recessive Deafness DFNB9, Am. J. Hum. Genet.

Zarebidaki, F., Camacho, M., Brockmann, M.M., Trimbuch, T., Herman, M.A., Rosenmund, C., 2020. Disentangling the Roles of RIM and Munc13 in Synaptic Vesicle Localization and Neurotransmission. J. Neurosci. 40, 9372–9385. https://doi.org/10.1523/JNEUROSCI.1922-20.2020

Zenisek, D., Horst, N.K., Merrifield, C., Sterling, P., Matthews, G., 2004. Visualizing synaptic ribbons in the living cell. J. Neurosci. Off. J. Soc. Neurosci. 24, 9752–9759. https://doi.org/10.1523/JNEUROSCI.2886-04.2004

Zhai, R.G., Vardinon-Friedman, H., Cases-Langhoff, C., Becker, B., Gundelfinger, E.D., Ziv, N.E., Garner, C.C., 2001. Assembling the Presynaptic Active Zone: A Characterization of an Active Zone Precursor Vesicle ulating the mobilization of SVs and the refilling of release sites (Garner et al The assembly of functional active zones is a key event during the formation of synapses in CNS. The formation of synapses presumably begins with the protrusive ac, Ziv and Smith. Ahmari.

Zheng, J., Shen, W., He, D.Z., Long, K.B., Madison, L.D., Dallos, P., 2000. Prestin is the motor protein of cochlear outer hair cells. Nature 405, 149–155. https://doi.org/10.1038/35012009

ACKNOWLEDGEMENTS

I would like to thank my supervisor, Prof. Dr. Carolin Wichamnn, for her support, patience, feedback and mentoring along my PhD. I would like to thank her for seeing potential and offering me the opportunity to develop as a researcher in the beautiful world of electron microscopy and activity changes. I would also like to thank the members of my thesis committee, Prof. Dr. Tim Gollisch and Prof. Dr. Nils Brose, for the valuable feedback provided over these years.

I am thankful of all the members of the Wichmann lab not only for sharing with me their technical and scientific knowledge, but also for their warmth and openness to quickly make me feel a part of the group. I specially want to thank Lujane Slitin, my office, freezing and event organiser buddy, for her friendship, candor and support. The long HPF days and the analysis time wouldn't have been the same without her! I also want to thank Julius Bahr for his work during his Masters' rotation and dissertation.

I would also like to express my gratitude to all members of the Inner Ear Lab for their suggestions during the lab meetings and the retreats. In particular, I would like to thank Roos Voorn for the scientific input, her friendship, the decompression walks and all the random podcasts.

I am also grateful to Sandra Gerke, Christiane Senger-Freitag, Anna Goldak and Sina Langer for their valuable technical support and kindness. I would like to particularly thank Anna for her handy knowledge of every piece of equipment (specially the HPM!) and preparation of experiments. Thanks also to Gerhard Hoch for his help and advice during opto-HPF; Dr. Jakob Neef for his patience and support while teaching me to use the STED microscope; and Prof. Dr. Michael Hopfert for his technical support when I had problems with the TEM. I am also thankful to Omar Díaz for all the computer support in the office and remotely. I would like to thank too the animal caretakers, specially Daniela, for caring for the mice and the suggestions while planning for the breeding pairs.

I am thankful to the SFB889 research fund and the GGNB Bridging Fund for having provided financial support during the course if the PhD.

I would also like to thank Mary Xylaki and Carmina Warth Pérez for being such nice office mates, as well as for their friendship, their support and wisdom, and all the good times (of course!).

A big thanks goes to all my friends, some of them already mentioned, some of them not. Thank you for being there in person and on the phone; for reaching when I was silent and making my life colourful. May we have many more good moments to come!

Finally, I would also like to deeply thank my family, from now and before; from here and there. I only have a few truthful words full of gratitude: thank you for your support along my life and being my role models. I specially would like to thank Floyd Chitalu, Jr. for being such an amazing partner. Thank you for your love, your encouragement, your morning rambling full of ideas… and life together. Thank you for entering the craziest years of your life so far and walking together with me all this time. Cheers to all of you! ¡A vosotros!

LIST OF PUBLICATIONS

Rituparna Chakrabarti, Lina María Jaime Tobón, Loujin Slitin, Magdalena Redondo Canales, Gerhard Hoch, Marina Slashcheva, Elisabeth Fritsch, Kai Bodensiek, Özge Demet Özçete, Mehmet Gültas, Susann Michanski, Felipe Opazo, Jakob Neef, Tina Pangrsic, Tobias Moser, Carolin Wichmann (2022) **Optogenetics and electron tomography for structure-function analysis of cochlear ribbon synapses** *eLife* 11:e79494. https://doi.org/10.7554/eLife.79494